Novel Transition Metal Dichalcogenide Semiconductors and Heterostructures

Hart, Lewis

Award date:
2018

Awarding institution:
University of Bath

Novel Transition Metal Dichalcogenide Semiconductors and Heterostructures

Lewis Stephen Hart

A thesis submitted for the degree of Doctor of Philosophy

University of Bath

Department of Physics

May 2018

Abstract

Rhenium diselenide and rhenium disulphide are layered semiconductors that belong to the transition metal dichalcogenide (TMD) family. Like graphene and other TMDs, these materials can be exfoliated down to a few atomic layers. However, unlike other TMDs, the rhenium dichalcogenides are only stable in a triclinic structure that exhibits in-plane anisotropy. This anisotropy manifests itself in the vibrational, optical and electronic transport properties of these crystals.

Ab initio calculations and experimental results are presented to describe the Raman spectra of the rhenium dichalcogenides. From Raman spectroscopy the anisotropy of these crystals can be observed. Flipping a flake (a C_2 rotation about an axis in the layer plane) is not a symmetry of the system. Therefore, there are two non-equivalent vertical orientations. Raman spectroscopy can be used to identify whether a flake is facing "up" or "down". The lattice dynamics of these crystals are described using a simple ball and spring model. It is shown that low mass impurities, such as sulphur, in $ReSe_2$ can occupy four non-equivalent positions of the unit cell; there are four local vibrational modes corresponding to these four positions and Raman spectroscopy can be used to find them. An unusual experimental geometry (edge-on excitation) helps enhance these signals.

The electronic band structures of bulk $ReSe_2$ and ReS_2 are explored using angle-resolved photoemission spectroscopy (ARPES). From the measurements and complementary DFT calculations it is shown that: (i) there is anisotropy in the electronic dispersions; (ii) the valence band maxima are not located along any of the high symmetry directions; and (iii) both of these crystals have indirect band gaps. The rhenium dichalcogenides were thought to act as electronically decoupled monolayers; it is demonstrated that this is not the case and that there is significant electronic coupling between the layers. Finally, ARPES results of a monolayer of $ReSe_2$ are presented; again, anisotropy in the electronic band structure is observed.

Contents

Acknowledgements

The work in this thesis is due in no small part to the people I have been lucky enough to work with over the last 3 years. Firstly, I would like to thank my beamline collaborators at the ANTARES beamline in Paris for their tireless support:

Maria Carmen-Asensio, Chayou Chen, Jose Avila and Stephane Lorcy

Secondly, I would to acknowledge the PhD and postdoctoral researchers I have worked alongside during my studies. They have assisted me through fruitful conversations and invaluable equipment training:

James Webb, Sara Dale, Charles Sayers, Liam Farrar, Surani Gunasekera

Finally, I would like to thank my supervisor Dr Daniel Wolverson, for his guidance and support. It is as a result of his expert teachings I have been able to hone the skills necessary to produce this body of work.

Abbreviations

TMD	Transition metal dichalcogenide
VDWH	van der Waals heterostructure
ARPES	Angle-resolved photoemission spectroscopy
DFT	Density functional theory
LDA	Local density approximation
GGA	General gradient approximation
AFM	Atomic force microscopy
CVD	Chemical vapour deposition
FET	Field effect transistor
XPS	X-ray photoemission spectroscopy
STM	Scanning tunnelling microscopy
CCD	Charge-coupled device
HDS	Hydrodesulfurisation
FZP	Fresnel zone plate
OSA	Order sorting aperture
UHV	Ultra-high vacuum

Chapter 1

Introduction

1.1 History

1.1.1 Graphene

At the start of the 21st century, graphene, a single layer of graphite, was first isolated and graphene has since been named in the press as a "wonder material" [1]. The reasoning for this name is due to its remarkable properties. Graphene has the highest mobility amongst all known crystals, with the mobility being reported as high as $15\,000\,\mathrm{cm^2Vs^{-1}}$ [2]. Graphene is stronger than steel with a Young's modulus of 1 TPa [3]. It is hoped with all these amazing properties graphene can have a great commercial value [4, 5] .

One desirable application of graphene is in field effect transistors (FETs). However, for a material to be used in an FET, a band gap is required. Pristine, non-strained graphene lacks a band gap. There has been a considerable amount of research into introducing a band gap in graphene with some success but the introduction of this band gap usually diminishes the mobility [6, 7]. This started the search for other layered materials that too have large conductances when exfoliated to a monolayer but also have a band gap.

1.1.2 2D materials

It is clear why the discovery of the "wonder material" was very exciting to the condensed matter physics community, with the large number of superlatives that can be used to describe graphene. However, graphite is not the only layered material that can be exfoliated to create a monolayer that has interesting physical properties. In 2005 a paper was published where monolayers of h-BN, MoS_2 and $NbSe_2$ were prepared [8]. Since this paper, there have been thousands of publications on 2D materials and over a hundred different crystals explored so far. There is now a large catalogue of 2D materials, including superconductors [9], semimetals [1], semiconductors [10] and conventional insulators [8] to name a few. With the isolation of a monolayer of a new material comes about a new playground of physics.

One might ask, why is it interesting to measure monolayers and bilayers of these materials? Simply, many of the physical properties of a crystal can be tuned by varying the thickness. In strongly correlated materials the charge density wave transition temperature depends upon thickness [11]. In semiconductors the mobility, band gap and exciton binding energy all vary with layer thickness [12]. The reason for this change in excitonic binding energy will be described in Sec. 2.1.3.

Perhaps the most exciting family of layered materials are the transition metal dichalcogenides (TMDs). Unlike graphene, some of these crystals have a band gap, suggesting applications as field effect transistors. However, like graphene, the mobilities of these materials can be very large with the mobility of one of the TMDs, MoS_2, reported as high as $700\,\mathrm{cm^2V^{-1}s^{-1}}$.

1.2 Outline of thesis

This thesis will look at two of the more unusual members of the TMD family, ReS_2 and $ReSe_2$. These materials are conventional semiconductors but are unique amongst the TMDs as they have a triclinic structure and exhibit electronic and vibrational in-plane anisotropy. This anisotropy is investigated in this body of work.

A background of what is currently known about the transition metal dichalcogenides and

in particular, the rhenium dichalcogenides, will be given in the next chapter followed by a section on the key experimental techniques used in this work.

There are three chapters of this thesis that give a detailed description of the lattice dynamics of the rhenium dichalcogenides utilising Raman spectroscopy and ab initio DFT calculations. Chapter 4 describes how Raman spectroscopy can be used to identify the vertical orientation of the rhenium dichalcogenides. In Chapter 5, the lattice dynamics of $ReSe_2$ and ReS_2 are explored using a simple ball and spring model. Chapter 6 shows, using the rhenium dichalcogenides as examples, how Raman spectroscopy can be used to identify low mass impurities in the TMDs.

The following four chapters look at the electronic properties using angle-resolved photoemission spectroscopy. Chapter 7 gives an in-depth description of the electronic properties of bulk $ReSe_2$, Chapter 8 investigates monolayer $ReSe_2$ and Chapter 9 explores the band structure of ReS_2. Ab initio DFT calculated band structures of the bulk rhenium dichalcogenides are presented in Chapter 10.

Finally, a conclusion of the results given in this thesis is provided alongside a description of the direction future studies can take.

Chapter 2

Background

2.1 Transition metal dichalcogenides

Before introducing the rhenium dichalcogenides in detail, this thesis will describe some of the better known members of the transition metal dichalcogenides (TMDs). The group VI TMDs include MoS_2, $MoSe_2$, WS_2 and WSe_2, and these materials are the focus of this section.

2.1.1 Structure

TMDs are made up of transition metals such as molybdenum and the chalcogens sulphur, selenium and tellurium. The transition metal atoms lie in a plane sandwiched between two layers of chalcogen atoms, as shown in Fig. 2.1. The c crystal axis is along the direction perpendicular to the layer plane for the group VI TMDs.

A monolayer is defined as a single chalcogen-metal-chalcogen sandwich. A bilayer and a trilayer consist of two or three monolayers respectively, stacked along the c crystal axis direction. These monolayers are held together by van der Waals forces. A bulk TMD contains a sufficient number of layers such that the characteristics of the crystal are not perturbed when an extra monolayer is added. For this thesis a crystal that contains more than ten layers is considered bulk-like.

Within a monolayer, there are covalent bonds between the atoms. The metal atom lies in the middle of six chalcogen atoms in either the trigonal prismatic or octahedral coordination. When in the trigonal prismatic arrangement the chalcogens in the bottom plane lie directly below the chalcogens in the top plane. This differs to the octahedral configuration where the positions of the chalcogens in the different planes are staggered.

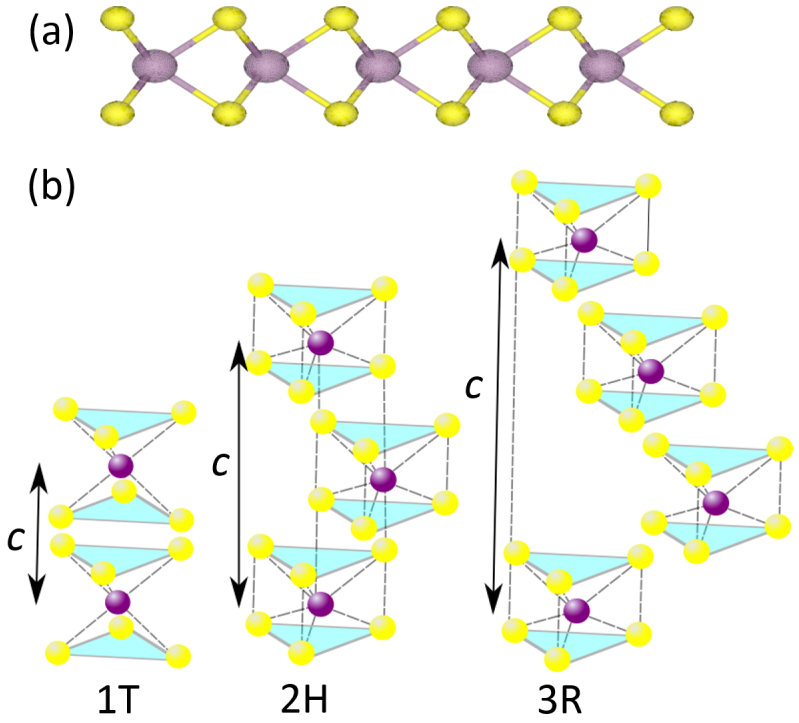

Figure 2.1: Diagrams showing three different polytypes of MoS_2, with the purple spheres representing molybdenum atoms and the yellow balls are sulphur. (a) The chalcogen-transition metal-chalcogen sandwich of MoS_2. (b) Diagrams of the three most common polytypes of transition metal dichalcogenides from left to right 1T (tetragonal symmetry with octahedral coordination), 2H (hexagonal symmetry with trigonal prismatic coordination) and 3R (rhombohedral symmetry with trigonal prismatic coordination). This diagram was made using the crystal structure data from Ref. [13].

The TMDs are usually found in three different polymorphs as shown in Fig. 2.1. These polymorphs are named 1-tetragonal (1T), 2-hexagonal (2H) and 3-rhombohedral (3R). The numbers in these labels describe how many monolayers are required to make a unit cell.

The 1T polymorph has octahedral coordination and the 2H and 3R polmorphs have trigonal prismatic coordination [14].

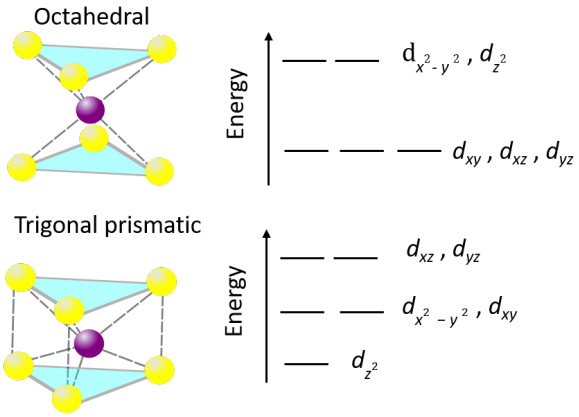

Figure 2.2: Energy diagram of the d-orbitals from the transition metal in a TMD with the octahedral and trigonal prismatic coordination. Each orbital has a two-fold spin degeneracy [14].

There are 5 d-orbitals originating from the transition metal in a TMD. Figure. 2.2 shows the energy levels for each of these 5 orbitals for the octahedral and trigonal prismatic coordination. A group VI transition metal in a TMD has 2 electrons available to occupy the d-orbitals. When in the trigonal prismatic coordination these 2 electrons fill the d_{z^2} orbital. Therefore the group VI TMDs are semiconductors when in the 2H polymorph with a filled valence band and an empty conduction band [14].

2.1.2 Electronic properties

One of the most interesting features of the group VI TMDs is that, in the bulk form, they have an indirect band gap, but the monolayers of these materials are direct band gap semiconductors [15].

To understand the cause of this indirect to direct transition it is first imperative to describe the chemical make-up of the bands. The Brillouin zone of a TMD is hexagonal with high symmetry points Γ, K and M which are at the centre, the corners and the middle of the edges of this hexagon respectively. The bands at and around Γ contain a large contribution from

the p_z states of the chalcogen elements. The interlayer hopping integral is particularly large for the chalcogen p_z states. Therefore, the bands at and around Γ are strongly dependent on the interlayer coupling. In contrast, the bands at K mostly consist of orbitals localised in the x-y plane, which are relatively unaffected by interlayer coupling [16].

A monolayer TMD has a direct band gap at K and a slightly larger indirect gap in the region near to the Γ point. There are no interlayer interactions for a monolayer. For crystals with two or more layers, the interlayer interaction strength increases with layer number because the interlayer distance becomes smaller. The indirect gap at Γ reduces with an increase in thickness, due to the change in interlayer coupling strength. However, the gap at K does not change with layer number. The size of the indirect gap at Γ is smaller than the direct gap at K for a bilayer. The indirect gap remains smaller than the direct gap for all layers from bilayer to bulk [17].

Another interesting property of the TMDs is they exhibit relatively large spin-orbit coupling (SOC) compared to graphene and silicon. SOC is a relativistic effect that originates from the interaction of the spin of an electron and its motion in a potential. The strength of the SOC tends to be greater for materials that contain elements with larger atomic numbers, which is the reason the heavy transition metal-based compounds exhibit strong SOC effects. For a monolayer TMD in the 2H structure, spin-orbit splitting can be observed as a result of spin-orbit coupling and the lack of inversion symmetry [14]. In a material that lacks inversion symmetry, such as the aforementioned monolayer, the crystal potential is asymmetric and will interact with opposing spins differently, thus leading to spin-orbit splitting [18].

2.1.3 Excitons

An electron in the valence band that is excited by a photon can make a transition to a conduction band. This will create a hole in the valence band; the electron and hole can then interact via the Coulomb force. An exciton is a quasiparticle which describes a bound state formed from this electron-hole interaction.

The properties of excitons depend upon the material in which they are situated. This

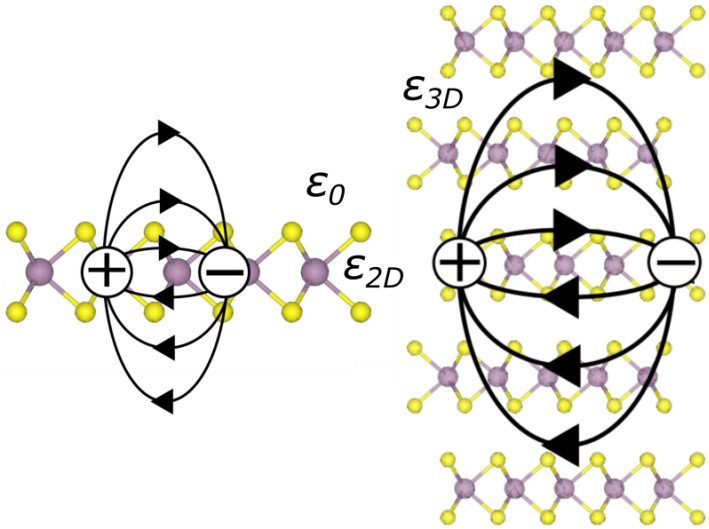

Figure 2.3: A schematic picture of how the excitons are bound within a monolayer (left), and a bulk TMD (right). The labels ϵ_0, ϵ_{2D} and ϵ_{3D} are the dielectric constants of air, a 2D material and a 3D crystal respectively. This diagram was made using the crystal structure data from [13].

section will describe two types of excitons, Frenkel and Wannier-Mott. A Wannier-Mott exciton can be found in a material that has a large dielectric constant. As a result of this large dielectric constant there will be a significant amount of screening from valence electrons from within the material. The interaction between the electron and the hole that make up the Wannier-Mott exciton is weakened by this screening. The binding energy of this type of exciton is weak, typically 0.01 eV, and the radius of this exciton can be a few nanometres. In contrast, a Frenkel exciton exists in a material with a small dielectric constant, where the screening from valence electrons is poor. This exciton has a larger binding energy than a Wannier-Mott exciton, typically 0.1-1 eV. The electron and hole that make up this exciton are usually found in the same unit cell or neighbouring unit cells of a crystal [19].

The excitons within bulk TMDs are of Wannier-Mott type. However, monolayers have excitons that exhibit both Wannier-Mott and Frenkel properties. Excitons in monolayers are strongly bound to the layer plane and can be a few nanometres in size.

The excitons in a monolayer TMD experience screening from neighbouring atoms in the in-plane directions. However, in the direction perpendicular to the layer plane there is only

vacuum (or air). The poor screening in the vacuum allows for very high binding energies, typically an order of magnitude higher than conventional quantum well structures. For example, the binding energy of an exciton in monolayer MoS_2 has been calculated to be 0.224 eV [12]. The dielectric constant of the monolayer is large, this means that the screening within the monolayer is substantial. This screening results in the wavefunction of the exciton extending over a few nanometres within the layer plane. Figure 2.3 compares the sizes of excitons in bulk and monolayer crystal, whilst showing how the field lines of the Coulomb interaction extend into a vacuum for a monolayer.

The binding energy of an exciton depends on dimensionality, α, as given below:

$$E_n = \frac{-E_0}{(n + \frac{\alpha-3}{2})^2}, \tag{2.1}$$

where E_0 is the exciton Rydberg and n is the principal quantum number [20]. From this equation it can be deduced that an exciton in a two-dimensional material, like a monolayer, should have a larger binding energy than one in a 3D, or bulk, crystal.

In addition to neutral excitons, trions have been observed in monolayer TMDs. A trion is a quasiparticle that is a bound state of two electrons and a hole or two holes and an electron. Quasiparticles of two electrons bound to two holes, bi-excitons, have also been observed in TMDs [21].

2.2 Rhenium dichalcogenides

Unlike the group VI TMDs, fairly little is known about $ReSe_2$ and ReS_2. Indeed, many fundamental questions surrounding them remained unanswered until recently. For example, it was not known whether the rhenium dichalcogenides are direct or indirect band gap semiconductors or if there is an indirect/direct band gap transition as these materials are exfoliated down from bulk to monolayer. This thesis will address and try to answer these questions initially through a literature review on recent progress and finally using experimental evidence.

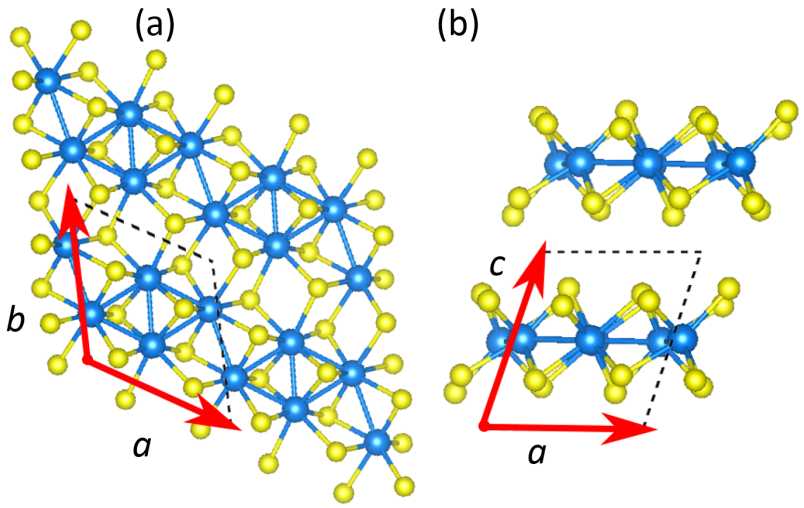

Figure 2.4: Crystal structure of $ReSe_2$ with the rhenium atoms represented by blue spheres and the selenium atoms by yellow balls. (a) A view along the direction perpendicular to the layer plane. The image in (b) shows the chalcogen-metal-chalcogen sandwiches and the corrugated surfaces of the selenium planes. This diagram was made using the crystal structure data from Ref. [24].

2.2.1 Structure

Similar to other TMDs, $ReSe_2$ and ReS_2 monolayers are chalcogen-metal-chalcogen sandwiches and the bulk consists of stacks of these monolayers held together by van der Waals forces. However, unlike the group VI TMDs, the rhenium dichalcogenides are not stable in the 1T, 2H or 3R structures. Instead, they are commonly found in a distorted 1T structure, 1T'. The origin of this distortion is thought to be Peierls-like [22].

Peierls' theorem states that a 1D chain of atoms which each have one free electron is unstable. These atoms will undergo a distortion such that each atom will move closer to one neighbour but further away from the other. These atoms are now in groups of two. The energy cost of having a long bond is outweighed by the benefits of having a short bond. The one-dimensional structure would act like a metal with a half filled band before the distortion and after would be a semiconductor with a filled valence band and an empty conduction band. The rhenium dichalcogenides are unstable in the 1T polymorph, therefore they undergo a two-dimensional Peierls-like distortion along the layer plane [23].

The structure of $ReSe_2$ is triclinic, with the space group $P\bar{1}$. The $P\bar{1}$ group has no symmetry except inversion symmetry. The first report of the crystal structure of $ReSe_2$ claimed it has a $Cd(OH)_2$ structure and that the unit cell has four rhenium and eight selenium atoms, consisting of just one Se-Re-Se sandwich [25]. This was refuted by Wildervanck et al. who described $ReSe_2$ as having a $Cd(Cl)_2$ like structure [26]. It is now thought a single unit cell of $ReSe_2$ contains one monolayer, four formula units and has a $Cd(Cl)_2$ structure [27, 24].

All reports on the structure of $ReSe_2$ agree on a few very important points. Firstly, there are rhenium-rhenium bonds, as shown in Fig. 2.4a. Each rhenium atom is bonded with three other rhenium atoms, forming a chain of 'diamond-like' units. $ReSe_2$ exhibits in-plane anisotropy as a consequence of this quasi-one dimensional structure. This anisotropy is exemplified in the electronic characteristics of this crystal; the mobility of the charge carriers is largest along the direction of the rhenium chains [28]. This will be explored in more detail in Sec. 2.2.5.

Secondly, it has been noted that the rhenium atoms are surrounded by six selenium atoms in a slightly distorted octahedron. The rhenium atom sits closer to three of these selenium atoms than the other three. This leaves three short Re-Se bonds and three longer Re-Se bonds. In the group VI TMDs the chalcogen planes lie flat above and below the metal plane. However, due to the distortion in the rhenium dichalcogenides, the chalcogen plane is corrugated with a vertical amplitude of 0.34 Å, as can be seen in Fig.2.4b [29].

The rhenium-rhenium bonds can be observed to form a parallelogram-like shape along the crystal axis labelled a in Fig. 2.4. The angle, γ, between the in-plane crystal axes, a and b, is 118.94°[26]. In a hypothetical undistorted hexagonal 1T polymorph the angle between a and b is 120°. The Peierls distortion does not significantly change γ. Therefore the shape of the 2D Brillouin zone is only weakly perturbed and in this thesis will be described as quasi-hexagonal.

ReS_2 is thought to be isostructural with $ReSe_2$ [26]. There has, however, been a report of the contrary; Lamfers et al. stated that two monolayers are required to make up a single unit cell of ReS_2 [30]. The lattice parameters of ReS_2 are displayed in Table 2.1.

	a (Å)	b (Å)	c (Å)	α°	β°	γ°
			$ReSe_2$			
Wildervanck et al. [26]	6.716	6.602*	6.728	104.9	91.82	118.94
Lamfers et al. [30]	6.597*	6.71	6.721	91.84	104.9	118.91
Ho et al. [27]	6.713	6.623*	6.740	104.59	92.28	118.70
Jariwala et al. [24]	5.5791*	6.690	6.702	91.747	105.019	118.946
			ReS_2			
Wildervanck et al. [26]	6.455	6.362*	6.401	105.04	91.60	118.97
Lamfers et al. [30]	6.352*	6.446	12.779	91.84	104.90	118.91
Ho et al. [27]	6.450	6.390*	6.403	105.49	91.32	119.03

Table 2.1: Lattice parameters of the rhenium dichalcogenides. The asterisk (*) denotes the direction of the rhenium chains. α, β and γ correspond to the angles between b and c, a and c, and a and b respectively.

Alternative phases of the rhenium dichalcogenides

The vast majority of research on ReS_2 and $ReSe_2$ has been done on the 1T' phase. Although few in number, there have been reports of other phases of these materials.

Shortly after the first monolayer of ReS_2 was isolated in 2014, work began on trying to create a 1T phase of ReS_2. If this structure existed, it would be metallic. However this phase has been predicted to be thermodynamically unstable [31]. Chemical exfoliation has been shown to induce phase changes in the group VI TMDs [32]. Wu et al. investigated whether chemical exfoliation could induce a structural transition in ReS_2. Their work resulted in flakes which contain both the 1T and 1T' phase. This 1T phase can exist as a metastable structure alongside the 1T' [33].

As mentioned above, the conventional distorted 1T structure of ReS_2 contains rhenium diamond-like chains. Lin et al. found an alternative 1T' structure of ReS_2 which too contains diamond-like rhenium chains, but with slightly different lattice parameters. Using aberration-corrected TEM the conventional 1T' structure was observed; the electron beam introduced chalcogen deficiencies and these defects induced a phase change where the rhenium-rhenium bond lengths were altered [34].

Lithium intercalation also has been predicted to induce a phase change in ReS_2. From

DFT calculations Sun et al. predict a magnetic phase of ReS_2, where instead of the rhenium atoms forming dimers they form trimers. There is currently no experimental evidence for this magnetic phase of ReS_2 [35].

At high pressures ReS_2 is found to exhibit a phase transition. Hou et al. find a structure with the space group $P\bar{6}m2$ when the pressure exceeds 11.3 GPa [36]. Zhou et al. performed DFT calculation to determine the phase transition of ReS_2 as a function of pressure. They start by stating the structure, that is labelled 1T' in this thesis and throughout literature, is best described as a distorted 3R structure. At a pressure of 0.1 GPa ReS_2 transforms to a different triclinic structure and at 90 GPa ReS_2 becomes tetragonal $I4_1/amd$ [37].

Finally, there has been a high pressure study of $ReSe_2$. A phase transition at 9.98 GPa was observed by Kao et al. [38]. It was found by doping the $ReSe_2$ with gold that this phase transition occurs at lower pressures.

Exfoliation

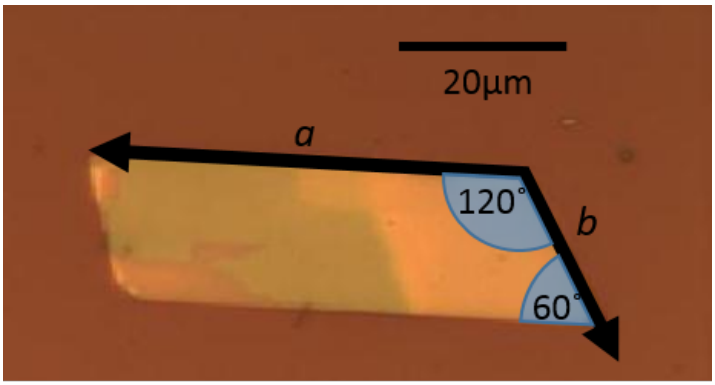

Figure 2.5: An image of an exfoliated flake of ReS_2.

The isolation of a single layer of graphite was first achieved using micromechanical exfoliation [1]. This technique has been used since on various other crystals. The layers in a TMD are held together by weak van der Waals bonds; to produce a monolayer these bonds need to be broken. Micromechanical exfoliation involves peeling layers off of a bulk crystal using

scotch tape, and this peeling action is strong enough to break the van der Waals bonds.

Following micromechanical exfoliation, the tape containing the flakes is placed upon a substrate. Light pressure is then placed upon the tape using a cotton bud. The tape is slowly peeled away from the substrate, leaving behind thin flakes.

An example of a commonly used substrate is silicon with a 290 nm layer of silicon oxide on top. Monolayers placed upon Si/SiO_2 are visible due to interference between light reflected from the Si/SiO_2, SiO_2/TMD and TMD/air interface [39].

When 2D crystals are exfoliated they tend to cleave along the in-plane crystal axes. The rhenium dichalcogenides typically exfoliate as long parallelograms. The edges of these parallelograms are the in-plane crystal axes a and b. The longest edge of the exfoliated flakes usually follows the direction of the rhenium chains. This, however, is not always the case and the shape of a flake should not be used as a proof of the orientation of a flake. Figure 2.5 is an image of a flake of ReS_2; note the parallelogram shape with the rhenium chain direction, a, the long edge. The orientation of this sample was determined using angle-resolved polarised Raman spectroscopy, which is described in Chapter 4.

2.2.2 Crystal growth

The rhenium dichalcogenides can be grown using a Bridgman method. Jariwala et al. were able to grow ReS_2 using this procedure, by placing high purity rhenium and sulphur powder into a quartz tube and heating these materials in a Bridgman furnace for 10 days at a maximum temperature of 1100°C [40]. Alternatively, these crystals can be grown similar to the procedure mentioned but also utilising a transport agent such as iodine or bromine [26]. Both of these processes involve growth over such a long time that it can be assumed that the crystal is made in thermal equilibrium. The ReS_2 and $ReSe_2$ crystals used in this thesis were grown by HQ Graphene and 2D Semiconductors by chemical vapour transport.

Mechanical exfoliation can be used to produce high quality and clean monolayers; however, this technique can only produce small flakes, with lengths in the order of microns. For many commercial applications large monolayers that can be mass produced are desirable. An

alternative approach to making monolayers is to grow them using a technique called chemical vapour deposition (CVD). In CVD growth, precursors react over the surface of a heated substrate to form thin layers of a desired material. The thickness of the material can be controlled by tuning the flow rate of the precursors, the temperature of the substrate and the growth time [14].

$ReSe_2$ is grown by CVD using ReO_3 and selenium powder. Substrates that this crystal has been grown on include silicon with a silicon dioxide layer [41], sapphire [42] and gold foil [43, 44]. $ReSe_2$ has also been grown between two layers of mica [45]. There is a range of growth temperatures reported, varying from 625°C to 750°C [46, 42].

The precursors ReO_3 and sulphur are commonly used to grow ReS_2. Ammonium perrhenate has also been used as a source for rhenium [47]. Like $ReSe_2$, ReS_2 has been grown on silicon dioxide, sapphire [48] and mica [49]. The growth temperatures for ReS_2, given in the literature, vary from 450°C to 800°C [50, 51]

2.2.3 Electronic properties

Electronic coupling

This section will look at some of the novel electronic properties that belong to the rhenium dichalcogenides. In 2014, Tongay et al. made the claim that the multilayer rhenium dichalcogenides act like electronically decoupled monolayers. The argument for weak coupling between the layers is as follows. The distorted structure of these crystals results in ordered stacking not being beneficial. As a consequence, the wavefunctions that describe the behaviour of electrons in these crystals have minimal interlayer overlap. It is this lack of the interlayer overlap of wavefunctions that results in the electronic decoupling of the layers [52].

There is a considerable amount of evidence in support of weak interlayer coupling in the rhenium dichalcogenides. Firstly, from DFT calculations with a GGA pseudopotential, Tongay et al. predict the band structure of monolayer ReS_2 to be very similar to the bulk [52]. In Sec. 2.1.2, the difference between the band structures of monolayer and bulk group

VI TMDs was described in terms of interlayer hopping. The interlayer hopping strength for the rhenium dichalcogenides is small. Therefore, the electronic dispersions depend weakly on the layer number.

Secondly, optical absorption measurements have been done on ReS_2 under pressure. No change in the optical spectra was observed before and after the pressure was applied. For large pressures, the interlayer distance is expected to decrease. The probability that an electron hops from one layer to another increases if the distance needed to hop is decreased in most layered crystals. Therefore, when pressure is applied to a crystal the optical spectra, which depends upon these electron transitions, would usually change. However, it is thought the interlayer hopping strength in the rhenium dichalcogenides is so weak that even under pressure the electrons are trapped within individual layers [52].

Finally, from DFT+GdW calculations, Arora et al. find that 68% of the excitons are confined to the layer plane in bulk $ReSe_2$ [53]. This is due to weak coupling between the layers. Similar results have been found for MoS_2, with the authors stating this confinement is due to the large interlayer distances in the TMDs [54].

In contrast to the aforementioned work, there is now a substantial amount of evidence for significant interlayer coupling in the rhenium dichalcogenides, including the angle-resolved photoemission spectroscopy (APRES) results in Chapter 7 and Chapter 9. There has also been other ARPES results on the rhenium dichalcogenides that agree there is non-negligible interlayer coupling between the layers [55, 56]. Echeverrey et al. have calculated the van der Waals interactions between the layers of bilayer ReS_2 using a PBE pseudopotential and find the layer coupling energy is similar to MoS_2 [57].

Anisotropic electronic band structure

The rhenium dichalcogenides have anisotropic electronic properties, which will be described in this section. The Brillouin zone of bulk $ReSe_2$ is shown in Fig. 2.6a. As a result of the triclinic structure of the crystal, the reciprocal lattice vectors a^* and b^* are not perpendicular to c^*, but instead are situated in a plane represented by an orange hexagon in Fig. 2.6a.

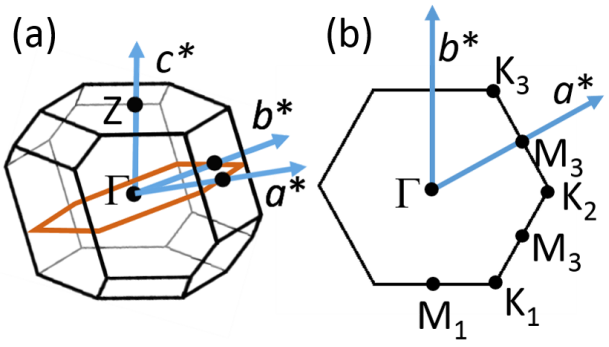

Figure 2.6: The Brillouin zone of bulk $ReSe_2$ (a), with the reciprocal lattice plane that contains the basis vectors a^* and b^* represented by an orange hexagon, and (b) the Brillouin zone of monolayer $ReSe_2$. This figure was made using XCrySDen [58] from the crystal structure calculated by Miss Gunasekera (PhD student) with the atomic coordinates from Lamfers et al. [30].

Figure 2.7 presents the electronic band structure of bulk $ReSe_2$ calculated by Wolverson et al. using DFT [59]. The Γ-x and the Γ-y paths correspond to the high symmetry directions from Γ to the edge of the Brillouin zone in the plane containing a^* and b^*. The uppermost valence band along Γ-x is much more dispersive than along Γ-y. The change in the structures of the bands for these two cuts in the Brillouin zone demonstrate the electronic anisotropy in this material.

Figure 2.6b shows the Brillouin zone of monolayer $ReSe_2$. Similar to the group VI TMDs the high symmetry points at the edge of the Brillouin zone are labelled K and M. However unlike other TMDs, there are three inequivalent K and M points, due to the in-plane anisotropy. The uppermost valence band along Γ-K_2 has been predicted, using DFT calculations, to be parabolic whereas the highest valence band along Γ-M_1 is expected to be very flat [60].

The Brillouin zone of ReS_2 has the same shape as $ReSe_2$ for both the bulk and monolayer forms of these crystals. Similar to $ReSe_2$ the bands of monolayer ReS_2 in the Γ-K_2 direction are predicted to be more dispersive than along Γ-M_1 [60].

In chapters 7, 8 and 9 ARPES measurements showing the anisotropy in the electronic band structures of the rhenium dichalcogenides are presented.

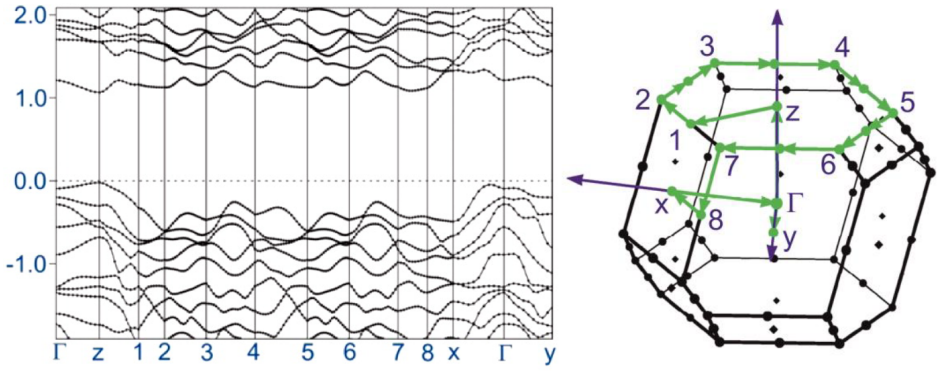

Figure 2.7: The DFT calculated band structure of bulk $ReSe_2$ (left), with the vertical axis in units of eV. The top of the valence bands is used as the zero of energy. The high symmetry point labels are defined using the Brillouin zone diagram (right). This figure was reproduced from Ref [59].

Nature of band gap

There is a considerable amount of controversy surrounding the nature of the band gaps of the rhenium dichalcogenides. Firstly, whether the bulk forms of these crystals are direct or indirect still remains to be answered definitively. Secondly, as mentioned in the earlier section, there is disagreement as to whether the layers in the rhenium dichalcogenides are electronically decoupled. The reports that state these crystals are electronically decoupled also find the nature of the band gap does not change with layer number.

$ReSe_2$ - bulk

The vast majority of results in the literature support the idea that bulk $ReSe_2$ has an indirect band gap. There have been a few DFT calculations that predict the band gap to be 0.98 eV, 0.92 eV and 0.99 eV [59, 53, 61]. In these publications the conduction band minimum (CBM) is found at the Γ point. Wolverson et al. and Arora et al. locate the VBM at the Z point whereas Zhao et al. predict the VBM to be near to Γ. The band structure calculated by Wolverson et al. is presented in Fig. 2.7.

There is a considerable amount of experimental evidence for an indirect band gap in $ReSe_2$. Ho et al. measured an indirect band gap of 1.387 eV using piezoreflectance [62]. Zelewski et

al. used photoacoustic measurements to determine the smallest direct band gap of $ReSe_2$ and modulated reflectance to measure the smallest indirect band gap. The indirect band gap is 1.18 eV, which is 0.13 eV smaller than the direct gap [63].

However, there are two reports that predict $ReSe_2$ has a direct band gap located at the Z point, with the size of this gap expected to be 1.49 eV and 1.38 eV [53, 57]. These band gaps are calculated using DFT+GdW and DFT with GW self-energy corrections respectively.

The results in Chapter 7 will show that $ReSe_2$ is an indirect band gap semiconductor and that the VBM is not found along any of the high symmetry directions. This band gap has been missed in all previous DFT calculations, which have only considered the bands along the high symmetry directions. There has been one other paper on ARPES of bulk $ReSe_2$, which comes to the same conclusions as those given above [64].

$ReSe_2$ - monolayer/bilayer

Monolayer $ReSe_2$ has a very flat uppermost valence band. The lowest lying conduction band is also not strictly dispersive. These flat bands make it very difficult to determine where the VBM and CBM are. Nevertheless, there have been a number of calculations to determine the nature of the band gap. From DFT calulations, the band gap has been found to be indirect, with the magnitude reported to be 1.34 eV, 1.22 eV and 1.348 eV [59, 53, 65]. All these calculations show the VBM is near to Γ and the CBM is at Γ. There have been a few reports of a direct band gap at Γ. Using GW self-energy corrected DFT this direct gap has been predicted to be 2.09 eV and 2.05 eV [60, 57], and a gap of 2.44 eV has been calculated from DFT+GdW [53].

There has only been one calculation of bilayer $ReSe_2$. Echeverry et al. predict bilayer $ReSe_2$ has an indirect band gap with the CBM at Γ and the VBM near to Γ. This is interesting because, according to the calculations in this paper the nature of the band gap changes from direct in the bulk, to indirect in bilayer, and finally to direct again in the monolayer [57].

ReS_2 - bulk

Since 2014, there has been a lot of work that indicates ReS_2 is a direct band gap semiconductor. There have been numerous first principles calculations of the band structure that indicate ReS_2 has a direct band gap [28, 52]. Most of these calculations show a direct gap at Γ. Echeverry et al. predict a direct gap of 1.6 eV at Z using GW self-energy corrected DFT [57]. Table 2.2 shows the predicted size of this band gap from a number of different sources.

There has also been experimental evidence for a direct band gap. Tongay et al. measured an intense photoluminescence (PL) peak from bulk ReS_2. PL is the light emitted from the relaxation of an electron, that has previously been excited by absorbing a photon, from the bottom of a conduction band to the top of a valence band. If the band gap is indirect the PL is expected to be weak because, to fulfil conservation of momentum, the electron transition from the CBM to the VBM needs to be phonon mediated. It is a fair assumption that the strong PL peak Tongay et al. observed is as a consequence of a direct gap [52]. Further affirmation of a direct gap comes from electron energy loss spectroscopy measurements that show a gap of 1.42 eV [66].

However, despite all the aforementioned evidence of a direct band gap, it is now thought that ReS_2 is an indirect band gap semiconductor. Aslan et al. discovered a weak PL peak at 1.4 eV, 0.7 eV lower in energy than the intense PL peak first observed by Tongay et al. Given that this peak is weak the authors deduced that it is likely to be from a phonon mediated transition, therefore from an indirect gap [67]. Electroluminescence measurements show that there is indeed an indirect band gap at 1.41 eV [68]. Furthermore, Zelewski et al. measure an indirect band gap of 1.37 eV from modulated reflectance results and a direct gap of 1.55 eV from photoacoustic measurements [63]. These band gaps are within reasonable agreement of the electroluminescence and PL measured band gaps.

In Chapter 9 ARPES measurements and results from DFT calculations will be presented that show the smallest direct band gap is at Z and that there is a smaller indirect gap. In Chapter 10 DFT calculated band structures will be displayed that indicate ReS_2 has an

	Bulk (eV)	Monolayer (eV)
Liu et al.[28]	1.35(d)*	1.44(d)*
Tongay et al. [52]	1.35(d)*	1.43(d)*
Zhong et al. [60]	-	1.36(d)*
Zhong et al. [60]	-	2.38(d)†
Echeverry et al. [57]	1.6(d)†	2.38(d)†
Gehlmann et al. [56]	1.57(i)†	1.85(i)†
Sun et al. [35]	-	2.1(d)†
Liu et al. [65]	-	1.553(i) ‡
Liu et al. [65]	-	1.448(i)*

Table 2.2: Comparison of the calculated values for the band gap of ReS_2. The label (d) indicates a direct gap and (i) represents an indirect gap. The choice of pseudopotential is indicated by (‡) for LDA and (*) for GGA. The symbol (†) denotes DFT calculations with GW self-energy corrections.

indirect band gap, which similar to $ReSe_2$, does not exist along any of the high symmetry directions. Two other groups have shown ARPES results of bulk ReS_2 which agree that ReS_2 could be an indirect semiconductor [55, 56].

ReS_2 - monolayer/bilayer

Monolayer ReS_2 is predicted to have a direct band gap at Γ [28]. The band gap increases in magnitude from the bulk. Table 2.2 shows the size of the band gap of monolayer ReS_2 predicted from DFT calculations. In 2014, Tongay et al. reported strong PL from monolayer ReS_2 which could indicate a direct band gap. In addition to this, they state the intensity of the PL signal increases with layer number. From this they deduce that the band gap is direct for monolayer, bilayer and bulk [52].

The uppermost valence band of monolayer ReS_2 is very flat. This makes it difficult to accurately determine the position of the VBM. There has been a prediction of an indirect band gap with the VBM near to Γ and the CBM at Γ [65]. The difference in energy between the narrowest direct and indirect band gaps in ReS_2, from these calculations made by Liu et al., is very small, and it is thought that a weak perturbation, such as strain, would be strong enough to change the direct/indirect nature of the gap [69].

There have only been two calculations of the band structure of bilayer ReS_2. Gehlmann et al. have predicted the bilayer to be direct with a gap of 1.7 eV. They state that the bulk is indirect, the bilayer is direct and the monolayer is indirect. This indirect/direct transition is indicative of electronic coupling between the layers. This group also obtained ARPES measured bands which agree with their calculations [56]. In contrast Echeverry et al. predict a direct gap of 2.0 eV for the bilayer [57].

Spin-orbit coupling

The spin-orbit coupling in the rhenium dichalcogenides, like the group VI TMDs, is very strong. The SOC modifies the bands containing the rhenium d orbitals. The uppermost valence bands in these materials contain contributions from the rhenium states. Therefore, any calculation that intends to predict the valence band maximum needs to correctly incorporate spin-orbit coupling [70].

Unlike the group VI TMDs, there is no spin-orbit splitting (SOS) in the band structures of the rhenium dichalcogenides. This is because both ReS_2 and $ReSe_2$ have a centre of inversion within the unit cell and this exists for any number of layers, including a monolayer. As described in Sec 2.2.3 an asymmetric potential is required for SOS. The centre of inversion can be removed by selectively doping the crystal.

2.2.4 Excitons

Similar to the group VI TMDs, the monolayer rhenium dichalcogenides have tightly bound excitons. This strong binding energy comes from the weak screening of the excitons, as described in Sec 2.1.3. In fact, the binding energy of monolayer ReS_2 is predicted to be 0.74 eV [57], larger than the calculated binding energy of monolayer MoS_2, 0.224 eV [12]. Much like ReS_2, the excitons in $ReSe_2$ are predicted to have a large binding energy which is 0.57 eV [57].

Five excitonic transitions have been observed in monolayer $ReSe_2$ using absorption measurements. The group responsible for this measurement state that monolayer $ReSe_2$ has a

direct gap at Γ. The first four excitons, found over the range of 1.49 eV to 1.54 eV, come from interband transitions at the high symmetry point Γ [53]. The five excitons found in the monolayer have also been observed in bulk $ReSe_2$. The first four excitons are detected at energies ranging from 1.37 eV to 1.4 eV. There is a redshift due to the bandgap in the bulk being smaller than in the monolayer. This redshift could also occur because the exciton binding energy in the bulk is weaker than in the monolayer. The origin of these excitons is from transitions at Z, which is also the position of the Brillouin zone where the direct band gap is predicted [53].

Excitonic transitions in monolayer ReS_2 have been observed at energies of 1.61 eV, 1.68 eV and 1.88 eV. In bulk ReS_2, three excitonic transitions have been detected by Aslan et al. at 1.47 eV, 1.51 eV and 1.58 eV [67]. This is in agreement with a previous report which finds excitons at 1.48 eV and 1.52 eV [71]. In Chapter 4 photoreflectivity measurements are presented that show an excitonic transition in bulk ReS_2.

An interesting consequence of the low symmetry of the rhenium dichalcogenides is, the excitons are anisotropic and have different orientation and optical selection rules for light that is linearly polarised [72].

2.2.5 Electronic transport

The semiconductor TMDs have many exciting applications, with perhaps the most promising use of these materials being in transistors. To make a good digital transistor there are two essential requirements; the first is a band gap and the second is high mobility. MoS_2 has a band gap of 1.20 eV and extremely high mobility 700 cm^2Vs^{-1} [73]. This is comparable to the mobility of silicon, the material most commonly used in transistors [74]. The TMDs are flexible, meaning that these materials can be used on a surface that needs to bend such as a watch, or in flexible screens [75].

Field effect transistors (FETs) have been made using thin flakes of exfoliated ReS_2. Mobilities ranging from 0.1 $cm^2V^{-1}s^{-1}$ to 79.1 $cm^2V^{-1}s^{-1}$ [76, 34, 40, 77, 78, 79, 80, 81] have been found at room temperature and at low temperature, (<100K), the mobility can be as

large as $350\,\mathrm{cm^2V^{-1}s^{-1}}$ [77]. The reason there is such a large range of conductances reported in the literature is likely to be because the measurements have been done on crystals of different purity. Defects in ReS_2 are expected to significantly hinder the mobility of the charge carriers. These defects could be from sulphur vacancies [82].

To make an efficient FET, the current that can pass through the transistor when in an off state needs to be very low compared to the on state. The largest on/off ratio measured for a ReS_2 FET is 10^8 [78], which is comparable to an FET made using MoS_2 [73].

TMDs grown using CVD are usually of poorer crystal quality than exfoliated flakes. Therefore, the resistance in CVD grown ReS_2 is expected to be large. However, there have been reports of CVD grown ReS_2 crystals with mobilities over a range from $0.0072\,\mathrm{cm^2V^{-1}s^{-1}}$ to $4.01\,\mathrm{cm^2V^{-1}s^{-1}}$, comparable to that of exfoliated flakes [82, 49, 51]. This could mean the CVD-grown ReS_2 is of good quality. Alternatively the exfoliated materials may be of low quality. There has been a theoretical calculation that predicts the mobility in pristine ReS_2 can be $799.64\,\mathrm{cm^2V^{-1}s^{-1}}$ [69].

Anisotropic conduction

As mentioned in Sec 2.2.1, the rhenium dichalcogenides have a triclinic structure, which is of low symmetry. Due to this low symmetry, these materials exhibit anisotropic conduction along the in-plane directions.

The conductance of the charge carriers is largest along the direction of the rhenium chains. The ratio of mobilities parallel to the rhenium chains, the a crystal axis, and perpendicular to the chains have been measured to be 1.506 and 3.01 [34, 49]. Furthermore, Liu et al. find that the ratio of the mobilities along the a direction and b direction is 3:1 [28].

The charge carries in $ReSe_2$ are not able to move as freely as those in the other TMDs. The mobility of FETs made using $ReSe_2$ range from $0.8\,\mathrm{cm^2V^{-1}s^{-1}}$ to $9.78\,\mathrm{cm^2V^{-1}s^{-1}}$ [40, 83, 84]. Unfortunately, the high resistance in $ReSe_2$ makes it a poor candidate for use in transistors. $ReSe_2$, much like ReS_2, exhibits in-plane anisotropy. The ratio of the resistivities along and perpendicular to the rhenium chains found by Tiong et al. is approximately 4 [85]. Therefore,

there may still be applications of $ReSe_2$ in future electronics which utilise this anisotropy.

2.2.6 Optics

The anisotropy in these crystals manifests itself in more ways than just in the mobility of the charge carriers. The way in which light interacts with these materials is also affected by the in-plane anisotropy. The rhenium dichalcogenides have both linear and circular birefringence and these optical properties may have useful applications.

The rhenium dichalcogendies can be used to detect the polarisation of light. Due to anisotropy induced linear dichroism, light of one polarisation (defined with respect to the rhenium chains) is absorbed more. The free carrier concentration within a rhenium dichalcogenide flake is increased when illuminated, which can result in a larger current flowing across a flake that has a voltage applied across it. This property makes these crystals useful as photodetectors. Moreover, as certain polarisations of light are absorbed more efficiently, there will be polarisations which result in larger amplification of the conductivity of the charge carriers [81].

The birefringence of these crystals can be utilised to make optical waveplates. Yang et al. measured the birefringence of ReS_2 using a 642 nnm laser and found a phase shift of 0.051 and 0.082 for ReS_2 and $ReSe_2$ respectively [86].

2.2.7 Applications

The rhenium dichalcogenides have significant commercial promise. Applications for these materials include catalysts for reactions that reduce pollutants from industrial emissions [87], catalysts for hydrogen evolution reactions [88], energy storage [89], photo and humidity detectors [90], and field effect transistors [76].

One of the big challenges in modern science is to find ways of producing energy in an environmentally clean way. Hydrodesulfurisation (HDS) is a chemical reaction that reduces pollutants from oil and gas. ReS_2 is thought to be a very good catalyst for HDS reactions, perhaps better than the current industrial standard, MoS_2 [87, 91, 92, 93, 94].

Another of the key areas for scientific advancement, is to replace fossil fuels. Hydrogen, can be used as an alternative fuel. ReS_2, can be used as a catalyst in hydrogen evolution reactions [88, 95, 96].

There is a considerable amount of work ongoing into energy storage. ReS_2 can be used as a component in a battery. Lithium-ion batteries are commonly used for energy storage due to their high energy density and long cycle life. It is thought the weak interlayer coupling and large interlayer distance between the layers of ReS_2 would facilitate intercalation of a large number of lithium ions [89, 97, 98, 99].

2.3 Van der Waals heterostructures

Over 100 different types of 2D crystals have been discovered. These materials have a variety of different properties; for instance, phosphorene is a small band gap semiconductor, graphene is a semi-metal and h-BN is an insulator.

By placing 2D materials one above the other, similar to how one would stack Lego bricks, new electronic devices can be fabricated that utilise the different properties of these crystals. Such a device is called a van der Waals heterostructure (VDWH) [100]. There is now a rather extensive list of VDWHs. These include: light emitting diodes made using graphene, MoS_2 and h-BN [101], field effect tunnelling resistors containing graphene and h-BN [102], and p-n junctions that utilise MoS_2 and WSe_2 [103].

The rhenium dichalcogenides have in-plane anisotropy, are stable in air and have reasonably large mobilities [40]. It is hoped that these qualities may be of use in future VDWHs. There has been some progress in the development of VDWHs that contain the rhenium dichalcogenides. ReS_2 has been incorporated in devices with MoS_2 [104, 105], phosphorene [106], WS_2 [107], h-BN [108] and $ReSe_2$ [109]. Likewise, VDWH have been made with $ReSe_2$ alongside MoS_2 [110] and WS_2 [111].

Chapter 3

Experimental techniques

3.1 Raman spectroscopy

Raman spectroscopy is an experimental technique that can be used to measure light that has been inelastically scattered from some medium of interest. A Raman scattering event involves a photon interacting with an excitation of a material. This excitation can be a phonon and, by measuring the scattered light, the properties of the phonon can be probed.

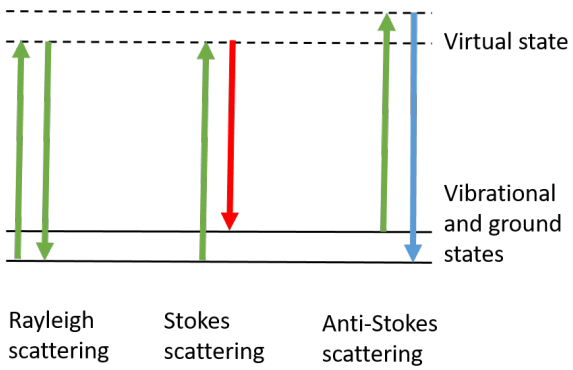

Figure 3.1: Energy diagram that shows the difference between Rayleigh, Stokes and anti-Stokes scattering. The excitation and emission processes are represented by the left-hand and right-hand arrows respectively.

By measuring the intensity of scattering events as a function of detected photon energy a Raman spectrum can be obtained. The independent axis of the spectrum is given in a

specialist unit, called the Raman shift. The Raman shift is the energy that is lost or gained by a photon in a scattering event, given in wavenumbers,

$$1\,\mathrm{cm}^{-1} = 0.124\,\mathrm{meV}. \tag{3.1}$$

There are two different ways in which light can be Raman scattered: Stokes scattering occurs when a photon loses energy to the material it is scattered from and anti-Stokes scattering occurs when a photon gains energy. An energy diagram describing Stokes and anti-Stokes scattering is given in Fig. 3.1. This section will use a semi-classical derivation, which follows the tutorial introduction of Raman in [112], to show where these two forms of scattering originate.

Raman scattering occurs when the polarisation of a material is perturbed by the electric field, E, from a light source. The polarisation of a crystal can be described by the following equation,

$$\vec{P} = \epsilon_0 \chi \vec{E}, \tag{3.2}$$

where ϵ_0 is the permittivity of free space. The electric field from the incident light source, has a periodic dependence on time,

$$\vec{E}(\vec{r}, t) = \vec{E}(\vec{k}_I, \omega_I)\cos(\vec{k}_I \cdot \vec{r} - \omega_I t), \tag{3.3}$$

where ω_I is the angular frequency and $\vec{k}_I$ is the wave vector. The final variable in eq. 3.2 is χ, the dielectric susceptibility, which describes the response of the material to an electric field. The dielectric susceptibility contains an oscillatory component as a consequence of the vibration of the atoms in the material.

The vibrations in a crystal can be described as periodic variations in the displacement of the atoms about an equilibrium position (with angular frequency ω_{ph} and wave vector $\vec{q}$),

$$\vec{u}(\vec{r}, t) = \vec{u}(\vec{q}, \omega_{ph})\cos(\vec{q} \cdot \vec{r} - \omega_{ph} t). \tag{3.4}$$

Should these displacements be small, χ can be expanded in a Taylor series as a function of displacement, u, and from this expansion, to first order, χ is

$$\chi_{jk}(\vec{k}_I, \omega_I) \approx \chi_{jk}(\vec{k}_I, \omega_I) + \frac{\partial \chi_{jk}(\vec{k}_I, \omega_I)}{\partial u_l} u_l. \tag{3.5}$$

The labels j, k and l run over the spatial coordinates x, y and z. Raman scattering occurs as a result of the dielectric susceptibility changing, therefore it is only the second term of this expansion that concerns this derivation. By substituting eq. 3.4, eq. 3.3 and the second term of eq. 3.5 into eq. 3.2, and utilising some simple trigonometric identities, the following equation can be derived,

$$\begin{aligned} P_j(\vec{r}, t, \vec{u}) = \frac{1}{2}\epsilon_0 \frac{\partial \chi_{jk}(\vec{k}_I, \omega_I)}{\partial u_l} u_l(\vec{q}, \omega_{ph}) E_k(\vec{k}_I, \omega_I) \\ \times (\cos[(\vec{k}_I + \vec{q}) \cdot \vec{r} - (\omega_I + \omega_{ph})t] + \cos[(\vec{k}_I - \vec{q}) \cdot \vec{r} - (\omega_I - \omega_{ph})t]). \end{aligned} \tag{3.6}$$

This equation shows that the interaction of light with a crystal will result in the polarisation oscillating at two frequencies,

$$\omega_S = \omega_I \pm \omega_{ph}. \tag{3.7}$$

These frequencies correspond to the cases where the scattered photon has gained or lost energy from the medium, known as anti-Stokes and Stokes scattering respectively. Eq. 3.6 also shows there is momentum transfer between the photon and the sample,

$$\vec{k}_S = \vec{k}_I \pm \vec{q}. \tag{3.8}$$

The momentum of the photon, $\vec{q}$, is very small compared to the dimensions of a Brillouin zone. Therefore, it is usually only phonons near the Brillouin zone centre, Γ, that are measured.

The component at the start of eq. 3.6 is known as the Raman tensor. The definition of

the Raman tensor is given below,

$$R_{jk,l} = \frac{\partial \chi_{jk}}{\partial u_l} u_l(\vec{q}, \omega_{ph}). \tag{3.9}$$

The intensity of a Raman mode for a particular vibrational mode, l, can be determined using the Raman tensor,

$$I \propto |e_j^I \cdot R_{jk,l} \cdot e_k^S|^2, \tag{3.10}$$

where e_j^I and e_k^S describe the polarisation of the incident and scattered light.

3.1.1 Selection rules

Raman spectroscopy can be used to identify the vibrational modes in crystals (and molecules). However, not all vibrational modes are Raman active. There are some selection rules to describe whether a mode can be Raman active.

For a vibrational mode to be Raman active the polarisability must change during the vibration. This selection rule can be explained using the equations derived in the semi-classical description of Raman scattering. It will be shown that if the polarisability does not change then no Raman scattering is expected. Eq. 3.2 states that the polarisation is proportional to the dielectric susceptibility, therefore the susceptibility must also change during vibration. It can be seen from eq. 3.9 that if $\frac{\partial \chi_{jk}}{\partial u_l} = 0$ then the Raman tensor will too be zero. From eq. 3.10 it can be deduced that the intensity will go to zero when the Raman tensor is 0. Therefore, for a vibrational mode to be Raman active the polarisability must change.

Group theory gives a way of predicting whether the vibration of the atoms will perturb the polarisation of the crystal or molecule. The Raman active modes will be those which correspond to the irreducible representations of the crystal point group which transform quadratically e.g. (xy, x^2). By looking at the irreducible representations for a particular point group it is possible to: (i) learn which modes are Raman active; (ii) determine whether any modes are degenerate; and (iii) predict the form of the Raman tensor [112].

The Raman active modes are usually labelled using Mulliken symbols which describe the

Mulliken Symbol	Description
A	Non-degenerate mode that is symmetric about a principal axis
B	Non-degenerate mode that is asymmetric about a principal axis
E	Doubly degenerate mode
T	Triply degenerate mode
g (subscript)	Symmetric about a centre of symmetry
u (subscript)	Asymmetric about a centre of symmtery

Table 3.1: Descriptions of the Mulliken symbols.

symmetry species of point groups. Table 3.1 gives a description of the Mulliken labels.

An example of a Raman tensor is given below:

$$R = \begin{bmatrix} u & v & r \\ v & w & s \\ r & s & t \end{bmatrix} \tag{3.11}$$

This is the Raman tensor for the A_g mode of a crystal that belongs to the $P\bar{1}$ space group. Group theory can tell us which elements of the Raman tensor are non-zero, and which elements are equal; for the triclinic $P\bar{1}$ space group all A_g tensors elements are non-zero in principle.

3.1.2 Raman spectroscopy experimental configuration

A Raman spectrum can be obtained using an excitation source and a spectrometer. In this thesis all Raman measurements have been made using a Renishaw In-Via spectrometer.

Approximately one in ten million of the incident photons are inelastically scattered. To detect a significant number of Raman scattered photons an intense light source is required, and lasers are used normally.

Raman spectroscopy can be a microscopy technique. The Renishaw spectrometer can focus the incident light to a spot size of approximately one micron. This is done by utilising objective lenses. By collecting the light over a large solid angle, a good collection efficiency can be achieved, which is necessary given the small probability of inelastic scattering events.

Most of the light scattered by the sample is Rayleigh scattered (that is, without any frequency shift). In a Raman spectroscopy experiment, it is only the inelastically scattered light that is of interest. Therefore, the elastically scattered light needs to be rejected. Before the photons are measured by a detector they pass through a holographic notch filter. This prevents photons that have frequencies similar to the laser from passing.

Finally, the light is detected by a CCD. A CCD is a silicon based device capable of detecting light over an array of pixels. Before the light is detected by the CCD it is dispersed by a diffraction grating. This dispersion results in photons of different wavelengths being spatially separated. The different pixels in the CCD count photons of differing frequency [112].

3.1.3 Raman of 2D materials

Raman spectroscopy has been shown to be a very useful tool when studying 2D materials. This technique can be used to identify the structure [113], thickness [114], dopant concentration [115] and strain [116] of a material and the orientation of anisotropic crystals [59].

Raman spectroscopy is a popular tool for measuring the thickness of a 2D material because this technique is easy and the measurement is quick. A monolayer of graphene can be identified by comparing the intensity ratio of two Raman modes and its crystalline quality can be assessed as well [114]. In the group VI TMDs, the high frequency Raman modes (the modes at Raman shifts greater than $100\,\mathrm{cm}^{-1}$) change frequency with layer number giving again a means of detecting monolayers [117].

Layered crystals also have vibrational modes in the region of $5\mathrm{cm}^{-1}$ to $60\,\mathrm{cm}^{-1}$. These are known as the ultra-low frequency modes and correspond to rigid layer vibrations. The layers can move in a compression-like motion, known as the layer breathing mode, and the layers can oscillate along the in-plane direction, which corresponds to an interlayer shear mode. The frequency and number of these Raman modes depend upon layer number and thus can be used to identify the thickness of a flake [118].

Raman spectroscopy is a quick, non-invasive technique which allows for the easy identification of a monolayer and is therefore an ideal tool in 2D material research. Unfortunately,

in the case of ReS_2, the frequencies of the modes with a Raman shift greater than $100\,cm^{-1}$ do not change significantly with layer number [119] and there has been no change observed for $ReSe_2$ [59]. The thickness of the rhenium dichalcogenides can be determined using the ultra-low frequency modes [120]. However, at the University of Bath the equipment to observe Raman modes of microscopic objects at frequencies below $80\,cm^{-1}$ is not available. Therefore all measurements of thickness in this thesis have been done using atomic force microscopy (AFM). AFM will be described in Sec 3.5.

The orientation of the rhenium dichalcogenides can be measured by observing how the intensity of the Raman modes change with polarisation [59]. This is also the case in other anisotropic 2D materials [121, 122].

3.2 Angle-resolved photoemission spectroscopy

3.2.1 Basic principles

Angle-resolved photoemission spectroscopy (ARPES) is an experimental technique designed to measure the electronic band structure of a material. This section will introduce the physics behind this very useful tool.

In a photoemission spectroscopy experiment monochromatic light, typically of soft X-ray energy (20-120 eV), will be shone upon a material. This light will result in an electron, that is initially bound in the crystal with binding energy E_B, being liberated from the sample as described by the photoelectric effect [123]. The photoelectron will be emitted with a kinetic energy described by the following equation,

$$E_{\text{kin}} = h\nu - \phi_{WF} - |E_B|, \tag{3.12}$$

where ϕ_{WF} is the work function of the material, h is Planck's constant and ν is the frequency of X-ray. The kinetic energy of the photoelectron is detected by an analyser. If the work function is known, then the binding energy, E_B, can be calculated using eq. 3.12.

The emitted electron can be from the core level of an atom or can be from the valence band of a crystal. ARPES is an experimental technique that is used to look at the valence bands of a material.

In an ARPES experiment the direction that the electron is emitted from the material is measured by the analyser. From the emission angle the momentum wave vector of the photoelectron can be calculated using the following equations,

$$\vec{K}_x = \frac{1}{\hbar}\sqrt{2mE_{\text{kin}}}\sin(\theta)\cos(\phi), \tag{3.13}$$

$$\vec{K}_y = \frac{1}{\hbar}\sqrt{2mE_{\text{kin}}}\sin(\theta)\sin(\phi), \tag{3.14}$$

$$\vec{K}_z = \frac{1}{\hbar}\sqrt{2mE_{\text{kin}}}\cos(\theta). \tag{3.15}$$

where ϕ and θ are spherical polar coordinates used to describe the direction the photoelectrons are travelling, defined in Fig. 3.2. E_{kin} and m are the kinetic energy and mass of the photoelectron. In an ARPES experiment the in-plane crystal momenta of electrons are conserved (see Sec 3.2.2 for more detail). A consequence of this conservation is, the in-plane momenta of the detected photoelectrons can be used to find the in-plane crystal momenta of the bound electrons [124].

By measuring the kinetic energy and the emission angle of a photoelectron it is possible to determine the binding energy and crystal momentum of a bound electron. From these two quantities an electronic band structure can be formed.

3.2.2 Conservation laws

An ARPES experiment relies on the conservation of energy and momentum. The following section gives a description into how the conservation laws can be used to determine the electronic band structure of a crystal.

The momentum of a low energy photon can be neglected because it is much smaller than the Brillouin zone dimensions. Thus $\vec{k}_i$ - $\vec{k}_{\text{f}}$ = 0 in the reduced zone scheme or $\vec{k}_i$ - $\vec{k}_f$ =

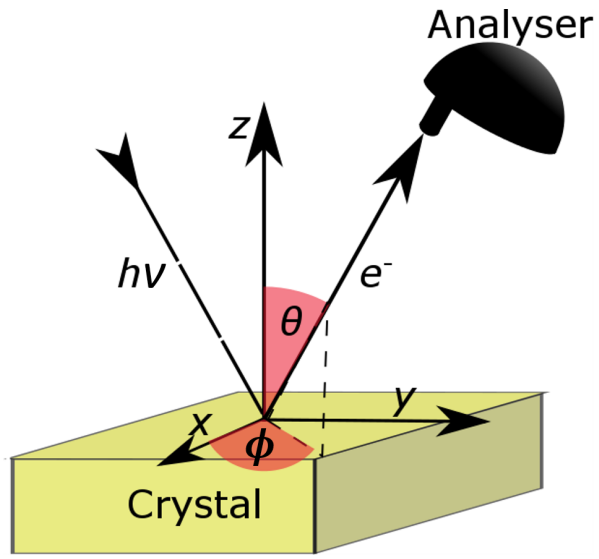

Figure 3.2: A diagram depicting the photoemission process.

$\vec{G}$ in the extended zone scheme, where $\vec{k}_i$ and $\vec{k}_f$ represent the crystal momentum before and after interaction with the photon and $\vec{G}$ is a reciprocal lattice vector. As the electron exits the material it must travel past the surface. The surface has no effect on the potential along the x-y plane. The potential at $\vec{k}_x$ is equal to $\vec{k}_x + \vec{G}$, therefore the crystal momentum in this plane, $\vec{k}_\parallel$, is conserved to within a reciprocal lattice vector $\vec{G}$. However the crystal momentum in the perpendicular direction, $\vec{k}_\perp$, is not conserved. This is due to the large variation in potential perpendicular to the surface. Nevertheless, it is possible to calculate $\vec{k}_\perp$ by making a few approximations. Firstly, an assumption is made that the final state of the detected photoelectron can be described by a free electron state. Secondly, it is assumed the bound electron comes from a parabolic valence band that has a minimum E_0. Using these approximations the following equation is derived,

$$\vec{k}_\perp = \frac{\sqrt{2m(V_0 + \cos^2(\theta)E_{\text{kin}})}}{\hbar}, \tag{3.16}$$

where m is the mass of the photoelectron, θ is the polar angle defined by the geometry of the experiment and V_0 is the inner potential. Figure. 3.3a and b show that V_0 is the difference in

energy between the bottom of the valence band, E_0, and the vacuum level, E_V, which is the energy of a stationary electron in a vacuum. From this equation it can be deduced that by changing the incident photon energy, which is proportional to E_{kin} as described in eq. 3.12, one can explore different $\vec{k}_z$ points in the Brillouin zone [124].

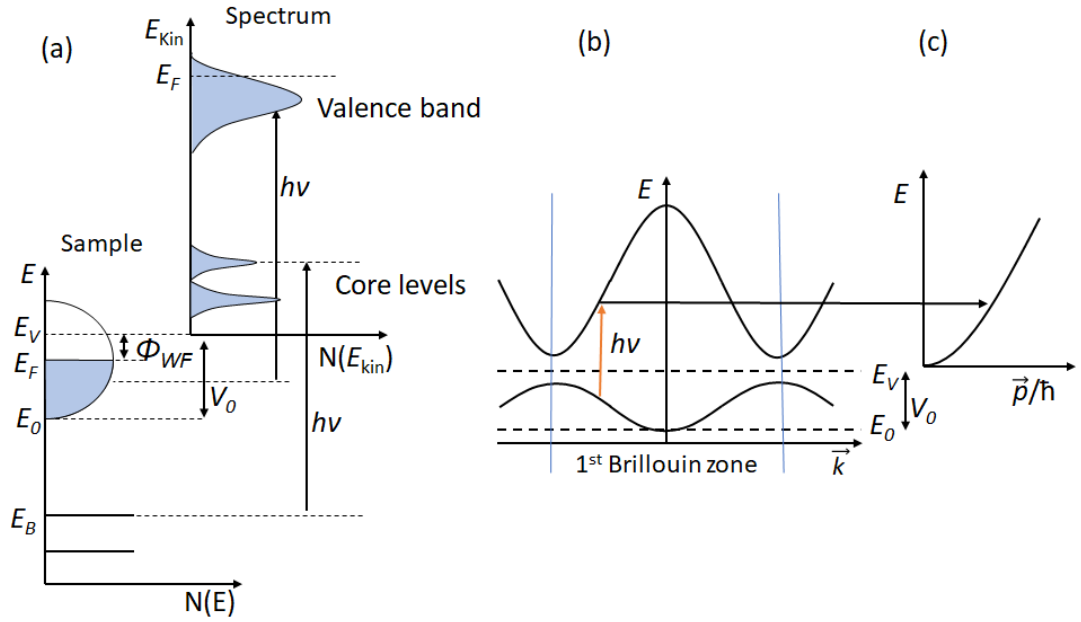

Figure 3.3: (a) Energy levels that are involved in the photoemission process, with the kinetic energies of the photoelectrons on the right and the initial states of the sample on the left. In this figure E_F is the Fermi energy. (b) A diagram describing the photoemission in the sample from an initial state of a crystal to a nearly-free electron state. (c) The free electron dispersion of the final state in vacuum, given as a function of the photoelectron momentum, $\vec{p}$ [124].

Eq. 3.16 states that $\vec{k}_\perp$ is a function of the polar angle. Eq. 3.13 and Eq. 3.14 shows that $\vec{k}_x$ and $\vec{k}_y$ also depend on the polar angle. From these equation it can be seen that as the value of θ increases, which corresponds to $\vec{k}_x$ and $\vec{k}_y$ increasing, $\vec{k}_\perp$ decreases. As a consequence, the plane in reciprocal space measured by ARPES is not completely flat, but is instead curved.

3.2.3 Three step model and sudden approximation

A photoemission event involves the excitation of an electron in an N-particle system by a photon. The discussion in this section is based upon that of Damascelli et al. [124]. The

probability of a transition from an initial state Ψ_i^N to a final state Ψ_f^N is given by Fermi's golden rule,

$$w_{fi} = \frac{2\pi}{\hbar} |\langle \Psi_f^N | \hat{H} | \Psi_i^N \rangle|^2 \delta(E_f^N - E_i^N - h\nu). \tag{3.17}$$

In this equation E_i^N and E_f^N are the energies of the initial and final state of the N-body system and $\hat{H}$ is

$$\hat{H} = \frac{e}{2mc}(\vec{A} \cdot \vec{P} + \vec{P} \cdot \vec{A}), \tag{3.18}$$

where e and m are the electron charge and mass respectively, c is the speed of light, $\vec{P}$ is the electronic momentum operator and $\vec{A}$ is the electromagnetic vector operator [124].

The photoemission process can be described by three independent steps: (i) the excitation of an electron following stimulation from a light source; (ii) the transport of an electron through the material; and (iii) the escape of an electron from the material. The photoemission intensity depends on the probability of an optical transition in step (i), the chance that an electron can travel across the crystal without being scattered in step (ii), and whether an electron has enough kinetic energy to overcome the work function, ϕ_{WF}, and leave the material in step (iii). The second step involves the motion of an excited electron across the crystal. It is only electrons that are near to the surface that can escape the crystal without being inelastically scattered (i.e., with no change in momentum and energy). In a typical ARPES experiment, using a photon energy of 100 eV, the photoelectrons that are measured come from the top couple of nanometres of the sample, therefore ARPES is a surface sensitive technique [125].

The previous description of the photoemission of an electron uses an independent particle approach that does not consider many-body effects. When the photoelectron is emitted the system left behind will be in an energetically unfavourable state, and will thus relax. During this relaxation, interactions between the system and the photoelectron are possible. In the sudden approximation the photoelectron is emitted in an instant, before any relaxation can occur. A consequence of the sudden approximation is the final state of the N-particle system, Ψ_f^N, can be given as a product of the photoelectron final state which has momentum $\vec{k}$, $\phi_f^{\vec{k}}$,

and the final state of the remaining $(N-1)$-particle system, Ψ_m^{N-1},

$$\Psi_f^N = \mathcal{A}\phi_f^{\vec{k}}\Psi_m^{N-1}. \tag{3.19}$$

In this equation $\mathcal{A}$ is an antisymmetric operator. By assuming that the initial state of the N-particle system, Ψ_i^N, is a single Slater determinant, it can be given in terms of the product of the initial states of the photoelectron, $\phi_i^{\vec{k}}$, and the $(N-1)$-particle system, Ψ_i^{N-1},

$$\Psi_i^N = \mathcal{A}\phi_i^{\vec{k}}\Psi_i^{N-1}. \tag{3.20}$$

The matrix elements in eq. 3.17 can now be given as,

$$\langle\Psi_f^N|\hat{H}|\Psi_i^N\rangle = \langle\phi_f^{\vec{k}}|\hat{H}|\phi_i^{\vec{k}}\rangle\,\langle\Psi_m^{N-1}|\Psi_i^{N-1}\rangle\,. \tag{3.21}$$

The photoemission intensity as a function of $\vec{k}$ and E_{kin}, which is $I(\vec{k}, E_{\text{kin}}) = \sum_{fi} w_{fi}$, can be described by the following equation,

$$I(\vec{k}, E_{\text{kin}}) \propto \sum_{fi} |M_{fi}^{\vec{k}}|^2 \sum_m |c_{m,i}|^2 \delta(E_{\text{kin}} + E_m^{N-1} - E_i^N - h\nu), \tag{3.22}$$

where $|c_{m,i}|^2 = |\,\langle\Psi_m^{N-1}|\hat{H}|\Psi_i^{N-1}\rangle\,|^2$ is the probability that the $(N-1)$-particle system will be in state m, after an electron has left state i. $M_{fi}^{\vec{k}} = \langle\phi_f^{\vec{k}}|\hat{H}|\phi_i^{\vec{k}}\rangle$ is the one-electron dipole matrix element. The terms E_m^{N-1} and E_i^N are the energies of the final state of the $(N-1)$-particle system and the initial state of the N-particle system respectively [124].

3.2.4 Nano-ARPES experimental set-up

An ARPES experiment where the spot-size of the X-ray beam is smaller than a micron is called nano-ARPES. The lateral resolution offered by nano-ARPES facilitates measurements of small objects, such as exfoliated flakes of TMDs. The ARPES results in this thesis are produced using the nano-ARPES equipment at the ANTARES beamline at the Synchrotron

Soleil in Paris.

For an ARPES experiment an intense, highly monochromated source of X-rays is needed. The light produced at the Synchrotron Soleil fulfils all of these requirements. A synchrotron produces light by passing a high energy beam of electrons through a series of magnets that force the electrons to continuously change direction and follow a sinusoidal path. The change of direction results in the electrons being accelerated. An accelerating charged particle will emit light. The light is then passed through a monochromator. A synchrotron source can supply photons of tunable energies. This is useful when studying a 3D crystal because, by using a particular photon energy the plane in $\vec{k}_z$ can be chosen (as described in Sec 3.2.2). At the ANTARES beamline X-rays with energies that range from 10 eV to 900 eV are produced. The photon flux measured on a sample for a nano-spot experiment is typically 5.4×10^{10} photons per second in a 0.01% bandwidth [126].

To focus the beam to a spot size of approximately 100 nm, a set of Fresnel zone plates (FZP) are used. A FZP focusses light using diffraction. The FZP is illuminated using a pinhole as depicted in Fig. 3.4. To suppress unwanted diffraction orders an order sorting aperture (OSA) is placed between the FZP and the sample [127].

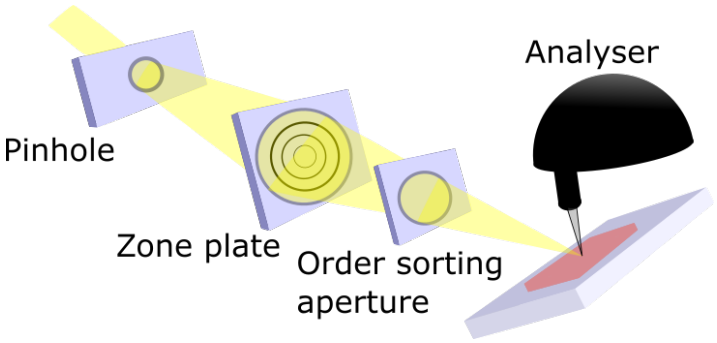

Figure 3.4: A schematic picture of how the X-ray beam is focussed at the ANTARES beamline.

The sample stage can rotate in the polar (θ) and the azimuthal angles (ϕ), with an angular resolution of $\sim$0.2°. These angles are defined in Fig. 3.2. By rotating the sample different cuts in the Brillouin zone can be measured. To position the sample on the X-ray spot, the stage can also be moved in the x, y and z directions with nanoscale precision.

ARPES experiments need to be performed in ultra-high vacuum (UHV). The main chamber of the equipment at the ANTARES beamline can get to pressures of 10^{-12} mbar. In this UHV the emitted photoelectron can travel from the surface of the sample to the detector unimpeded.

To measure the kinetic energies and momenta of the photoelectrons a Scienta detector is used. When inside the detector the photoelectrons are acted upon by an electric field which results in the photoelectrons following a hemispherical path. This electric field acts to disperse the particles by kinetic energy. The photoelectrons are focussed onto a charge-coupled device CCD, which is a two-dimensional array of pixels, with each pixel a photodetector. The pixels in one direction count the photoelectrons as a function of kinetic energy. The pixels in the other direction count the particles as a function of emission angle. Before the CCD the photoelectrons pass through an entrance slit which is used to selectively choose a range of momenta of electrons. The energy resolution of the detector at the ANTARES beamline is approximately 10 meV and has an in-plane momentum resolution of 0.02 Å^{-1}.

Due to recent progress in the design of Scienta detectors the kinetic energy of the photoelectrons can now be measured as a function of $\vec{k}_x$ and $\vec{k}_y$ simultaneously without rotating the sample stage. This is made possible by the use of deflectors that redirect the photoelectrons before they are detected. Using this instrument the k-space can be electronically scanned. The elimination of the need to rotate the sample is advantageous for a nano-ARPES experiment because, when the flake rotates it may also move in x or y if it is not exactly in the centre of rotation [128]. This new model of detector was used to obtain the valence band dispersions of a monolayer of $ReSe_2$ in Chapter 8, but was not used for any of the measurements of the bulk crystals, in Chapter 7 and Chapter 9.

3.3 Dry transfer

There is a considerable amount of interest in building new electronic devices by stacking 2D materials. To facilitate the production of such structures, the flakes need to be placed upon

each other with micrometer precision. This section will describe an easy way of building van der Waals heterostructures by utilising a technique called dry transfer.

The first van der Waals heterostructures were built using wet transfer of flakes. This involves picking up a flake using a sacrificial polymer and then placing it on a recipient substrate. The polymer is then removed using a solvent wash [129]. It is not always possible to completely dispose of the residue, therefore this way of transfer is not considered to be clean.

Castellanos-Gomez et al. proposed an alternative way of deterministic transfer of a 2D material. The method they mention involves using a viscoelastic polymer, PDMS [130]. A viscoelastic polymer becomes less adhesive when deformed slowly. The dry transfer procedure is described below.

The first stage involves carefully placing a PDMS thin film onto a glass slide, whilst trying to avoid wrinkling the PDMS. A layered crystal is then micromechanically exfoliated using the scotch tape method. This tape is placed upon the PDMS film and subsequently peeled away. In this step some of the flakes are transferred from the tape to the PDMS film.

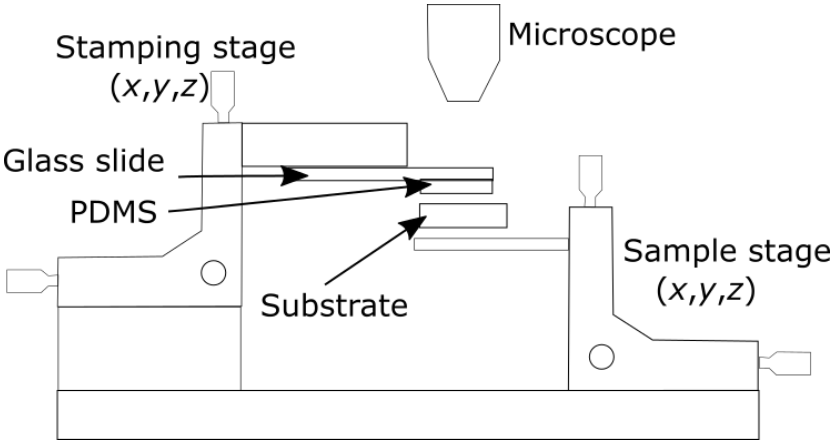

Figure 3.5: A schematic picture of the dry transfer set-up.

Next, the glass slide is connected a translation stage which has three degrees of freedom x, y and z. Beneath this glass slide is the sample holder that contains the recipient substrate. The sample stage can also be translated in the x, y and z directions as shown in Fig. 3.5.

Whilst looking through a microscope, the flake on the PDMS is aligned with the substrate. Following this, the PDMS stamp is carefully brought into contact with the substrate. When contact is made, the PDMS will change colour from clear to yellow. The PDMS film can now be slowly peeled off the substrate. During the peeling process the flakes should preferentially adhere to the substrate and detach from the viscoelastic polymer. It is possible to see a change in colour of the flake as the sample is transferred. This process of dry transfer is used in Chapter 8 to place monolayers of $ReSe_2$ onto graphite. The PDMS films used in this thesis were bought from Gel-Pak®.

3.4 Density functional theory

All the physics required to obtain the wavefunction of a hydrogen or helium atom is contained within the Schrödinger equation. In principle, the Schrödinger equation can be used for a system of any number of electrons. However, both the Hamiltonian operator and the wavefunction depend on the spatial coordinates of the electrons. For an atom with more than ten electrons it becomes impractical to solve the Schrödinger equation even with the use of supercomputers. In contrast, density functional theory (DFT) uses the electron density which only depends on three spatial variables to solve a modified Schrödinger equation. The electron density is defined as follows

$$n(\vec{r}) = \int d\vec{r}_2 ... \int d\vec{r}_N |\Psi(\vec{r}_1, \vec{r}_2, ..., \vec{r}_N)|^2. \tag{3.23}$$

In the DFT framework it is assumed that electrons in a solid behave as if they are in an external potential, ν_{ext}. This potential could be due to the nucleus of an atom. DFT was built from the work of Hohenberg-Kohn [131] and Kohn-Sham [132].

3.4.1 Hohenberg-Kohn theroem

The Hohenberg-Kohn theorem states that it is possible to predict the ground state characteristics of a many-body system, such as electrons in a static external potential, using the electron density. Within the seminal paper by Hohenberg et al. it was first showed that there is a unique map between the external potential ν_{ext}, the wavefunction of the electrons in this potential Ψ and the electron density n. This means that if the ground state density is known it is possible to uniquely determine the external potential. Furthermore, this result indicates that a measurement of the wavefunction is a functional of n,

$$E = \langle \Psi[n] | \hat{H} | \Psi[n] \rangle \equiv E[n]. \tag{3.24}$$

The second part of the Hohenberg-Kohn paper shows that, by using the variational principle, a functional for the energy of a system can be minimised with respect to $n(\vec{r})$. The global minimum of this functional is the ground state energy, and the corresponding electron density that minimises the functional is the ground state functional. Therefore, the ground state energy can be found from the ground state density [131].

The functional that describes the energy for a system in an external potential, ν_{ext} is given below,

$$E[n] = F[n] + \int \nu_{\text{ext}} n(\vec{r}) d\vec{r} + E_{II}. \tag{3.25}$$

In this equation E_{II} describes the interaction between the ions and F_{HK} is the Hohenberg-Kohn functional that contains information of the kinetic energy, T, and potential energy, U, of the interacting electron system,

$$F_{HK}[n] = T[n] + U[n]. \tag{3.26}$$

Unfortunately, the explicit form of F_{HK} is unknown, therefore the functional for the energy of the system is not known. The Kohn-Sham scheme shows that it is possible to find the ground state density even if an analytic description of the many-body interactions is not known.

3.4.2 Kohn-Sham scheme

The functional for the energy of a system in a potential v_{ext} was described earlier in eq. 3.25. Kohn et al. showed that this functional can be rewritten with the non-interacting and interacting terms separated

$$E_{KS}[n] = T[n] + \int \nu_{\text{ext}} n(\vec{r}) d\vec{r} + E_{\text{Hartree}}[n] + E_{II} + E_{xc}[n], \tag{3.27}$$

where E_{Hartree} is the Hartree energy that describes the electron density $n(\vec{r})$ interacting with itself,

$$E_{\text{Hartree}}[n] = \frac{1}{2} \int d\vec{r} d\vec{r}' \frac{n(\vec{r}) n(\vec{r}')}{|\vec{r} - \vec{r}'|}. \tag{3.28}$$

The term E_{xc} is the exchange-correlation functional and is where the many-body effects are grouped

$$E_{xc}[n] = F_{HK}[n] - (T[n] + E_{\text{Hartree}}[n]). \tag{3.29}$$

If the explicit form of the exchange-correlation term was known then the exact ground state of a system can be found [132]. However, this is not the case and so assumptions must be made to describe this term. These assumptions are described in Sec 3.4.4.

At the start of this introduction to DFT, it was stated that it is not feasible to solve the Schrödinger equation for N electrons. Kohn et al. proposed instead an effective single particle Schrödinger equation that has solutions that can describe the behaviour of interacting particles,

$$-\frac{1}{2} \nabla^2 \Psi_i(\vec{r}) + \nu_{\text{eff}} \Psi_i(\vec{r}) = \epsilon_i(\vec{r}) \Psi_i(\vec{r}). \tag{3.30}$$

In this equation ν_{eff} is the static effective potential that is felt by the electrons in an interacting system,

$$\nu_{\text{eff}} = \nu_{\text{ext}} + \nu_H + \nu_{xc}. \tag{3.31}$$

ν_H and ν_{xc} are potentials corresponding to the Hartree and exchange-correlation terms in eq. 3.27 and both are dependent on the electron density. The solutions of eq. 3.30 can be used

to find the electron density.

To derive eq. 3.30 Kohn et al. made an assumption that the ground state density of a system of interacting electrons is equal to the ground state density for an interactionless system. The following section will describe the origin of the effective potential, ν_{eff}, in eq. 3.30. In this derivation the Born-Oppenheimer approximation will be used. As a result of the nuclei being much heavier than the electrons in a crystal, they move more slowly. In the Born-Oppenheimer approximation it is assumed the nuclei do not move. The term corresponding to the kinetic energy of the ions, E_{II}, in the functional of eq. 3.27 can be neglected as a result of this approximation,

$$E_{KS}[n] = T[n] + \int \nu_{\text{ext}} n(\vec{r}) d\vec{r} + E_{\text{Hartree}}[n] + E_{xc}[n]. \tag{3.32}$$

The Hohenberg-Kohn theorem states that the ground state density can be found by minimising the functional for the energy of a system. To find the ground state density of an interacting system eq. 3.32 is minimised with the constraint that particle number remains constant. This led to the Euler-Lagrange equation,

$$\frac{\delta T}{\delta n(\vec{r})} + \frac{\delta E_{\text{Hartree}}}{\delta n(\vec{r})} + \frac{\delta E_{xc}}{\delta n(\vec{r})} + \nu_{\text{ext}}(\vec{r}) - \mu = 0, \tag{3.33}$$

where μ is the Lagrange multiplier. Kohn et al. also determined a Euler-Lagrange equation for finding the ground state density of a non-interacting system by minimising the following functional,

$$E_{\nu_{\text{eff}}}[n] = T[n] + \int \nu_{\text{eff}} n(\vec{r}) d\vec{r}, \tag{3.34}$$

which gives,

$$\frac{\delta T}{\delta n(\vec{r})} + \nu_{\text{eff}}(\vec{r}) - \mu = 0. \tag{3.35}$$

Assuming the interacting and non-interacting ground state densities are equal is the same

as equating eq. 3.33 and eq. 3.35. These equations are equivalent if,

$$\nu_{\text{eff}} = \nu_{\text{ext}} + \frac{\delta E_{\text{Hartree}}}{\delta n(\vec{r})} + \frac{\delta E_{xc}}{\delta n(\vec{r})}. \tag{3.36}$$

The second and third terms of eq. 3.36 are ν_H and ν_{xc} respectively, which were introduced in eq. 3.31.

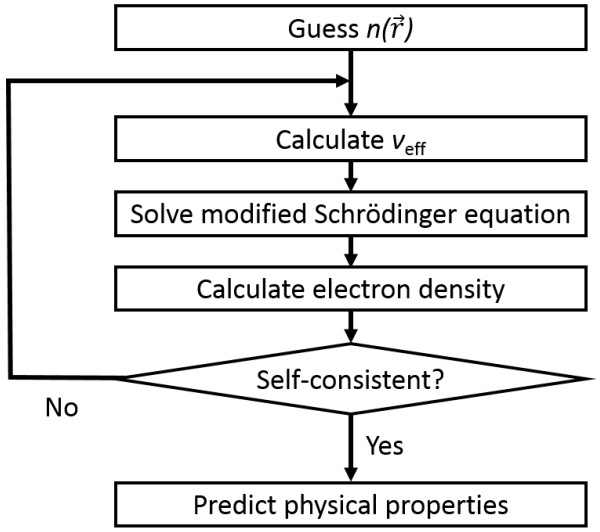

Figure 3.6: Self-consistent routine to calculate physical properties of an interacting system using DFT.

The procedure for predicting the physical properties of a material using DFT is as follows. Firstly, a guess based on atomic orbitals is made for the electron density. This electron density is used to calculate ν_{eff}. The modified Schrödinger is solved for this ν_{eff}. The solutions of this equation, $\Psi_i(\vec{r})$, can be used to calculate a new electron density. If this new density is the same as the density used as the input then this is the correct ground state density of the system and this result is said to be self-consistent. From the ground state electron density the properties of the system can be found. This procedure is illustrated in Fig. 3.6 [133].

3.4.3 Plane wave methods

From DFT it is known that the ground state properties of a system can be identified using the electron density. However, DFT does not describe how to find the electron density. To obtain the ground state properties of a material it is first necessary to identify a trial wavefunction, $\Psi(\vec{r})$, that can describe the system. This wavefunction can be expanded and the expansion coefficients can be found. The expanded wavefunction should give a good representation of how electrons behave within a solid. This wavefunction can be used when solving the modified Schrödinger equation, eq. 3.30.

There are two wavefunctions that are commonly used to describe electrons in a solid. The first is an atom centred basis function,

$$\Psi(\vec{r}) = \sum_{\vec{R},\mu} a_{\vec{R},\mu}\phi_{\mu}(\vec{r} - \vec{R}). \tag{3.37}$$

In this equation ϕ_{μ} are the atomic-like orbitals with μ the orbital index and R is the position of the atom. This function describes the behaviour of an electron in the vicinity of an atom.

The other wavefunction commonly used in DFT calculation is a plane wave,

$$\Psi_{\vec{k}}(\vec{r}) = \sum_{\vec{G}} a_{\vec{G}}(\vec{k})e^{i(\vec{k}+\vec{G})\cdot\vec{r}}, \tag{3.38}$$

where $\vec{k}$ is the wave vector and $\vec{G}$ is the reciprocal lattice vector. Quantum Espresso, a suite of plane wave codes, is used in this thesis for all DFT calculations [134].

A plane wave can be expanded using Fourier analysis. To represent a smooth function this expansion only needs a few terms. However, for a rapidly oscillating function the number of terms can be very large. This is a problem for the plane wave method because the wavefunction, that represents electrons located close to the nucleus, does indeed rapidly oscillate. These oscillations are as a consequence that eigenstates, such as the 1s and 2s orbitals, have to be orthogonal and most of the eigenstates are bound close to a nucleus.

The rapid oscillations in the wavefunction is due to the core electrons, the electrons that are strongly bound to an atom. These electrons are not involved in bonds, nor are they responsible for electronic transport in a crystal and so are not usually of interest. Therefore, an accurate way of calculating these states is not necessary.

A trick to remove the oscillations from the core states is to replace the potential due to the nuclei with a less rapidly varying pseudopotential. A consequence of this weak pseudopotential is, the core states are no longer strongly bound to the nuclei and the orthogonality oscillations are removed. This pseudopotential is chosen such that beyond a certain radius it is equivalent to the actual potential. Therefore, beyond this radius the wavefunction still gives an accurate description of the system.

3.4.4 Pseudopotentials

The pseudopotential has to contain information of the many-body interactions. These interactions are contained within the exchange-correlation functional,

$$E_{xc}[n(\vec{r})] = \int n(\vec{r})\epsilon_{xc}[n(\vec{r})]d\vec{r}, \tag{3.39}$$

where $\epsilon_{xc}[n(\vec{r})]$ is the exchange-correlation energy density and describes the energy per electron. The two most common ways of incorporating many-body interactions is through the local density approximation (LDA) and the generalised gradient approximation (GGA).

In the local density approximation the value of the exchange-correlation energy density, $\epsilon_{xc}[n(\vec{r})]$, at $\vec{r}$ is assumed to be the same as a homogeneous electron gas $\epsilon_{xc}^{hom}[n(\vec{r})]$ at $\vec{r}$,

$$E_{xc}^{\mathrm{LDA}}[n(\vec{r})] = \int n(\vec{r})\epsilon_{xc}^{\mathrm{hom}}[n(\vec{r})]d\vec{r}. \tag{3.40}$$

The homogeneous electron gas has been studied extensively and so $\epsilon_{xc}^{hom}[n(\vec{r})]$ is well known.

Like the local density approximation, the generalised gradient approximation uses a homogeneous electron gas to describe the exchange-correlation energy density. However unlike

the LDA, the correlation energy does not depend solely on the density at each point but also on the gradient of the density [133],

$$E_{xc}^{\mathrm{GGA}}[n(\vec{r})] = \int n(\vec{r})\epsilon_{xc}^{\mathrm{hom}}[n(\vec{r}), \vec{\nabla} n(\vec{r})]d\vec{r}. \tag{3.41}$$

3.5 Atomic force microscopy

Atomic force microscopy (AFM) is an experimental technique that probes the surface topology of a material. This measurement tool was designed by Gerd Binnig, who alongside Heinrich Rohrer, was awarded the Nobel prize for inventing the scanning tunnelling microscope (STM) [135].

In an AFM experiment a cantilever with a sharp tip is scanned over the surface of a sample. Forces from the material will cause the cantilever to be perturbed. These forces can be magnetic or electrostatic. The cantilever is required to have a weak spring constant, less than $10\,\mathrm{Nm}^{-1}$, such that the weak forces from the sample can result in a deflection of this apparatus [136].

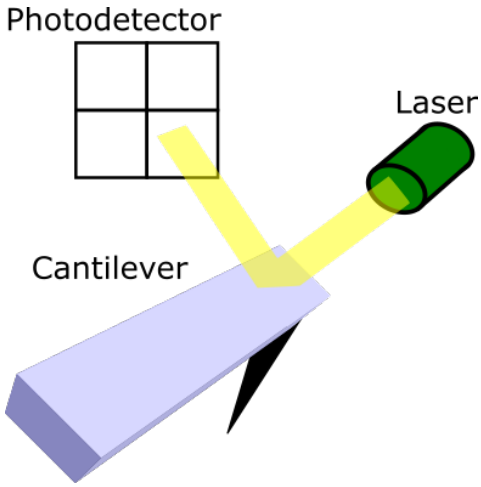

Figure 3.7: A schematic picture of the operation of an AFM.

The perturbation of the cantilever can be measured by optical techniques such as beam deflection. A laser is reflected from a mirror-like surface on the back of the cantilever. The

direction of the reflected laser light is measured by a position sensitive photodetector. A change in the position of the cantilever will result in the laser light being detected in a different place on the photodetector, as shown in Fig. 3.7. This technique can measure the deflection of a cantilever to a precision on the order of 0.1 Å [137].

An AFM can work in two different modes, contact and non-contact. In contact mode the cantilever is deflected by the short-range interatomic forces. In non-contact mode the tip on the cantilever is scanned over the surface of an object at a distance of 10 nm to 100 nm from the surface. The cantilever is driven to oscillate near to its resonant frequency. The spring constant is perturbed when in the presence of the gradient of a force,

$$C = C_0 + \frac{\partial F_z}{\partial z}, \tag{3.42}$$

where C_0 is the spring constant when no force is exerted on the cantilever and F_z is the force. The resonant frequency of the cantilever will be altered as the spring constant changes, which results in a different vibrational amplitude of the cantilever. The phase and frequency of the oscillation will also change [136].

AFM is a particularly useful tool for researching 2D materials. By scanning over an edge of a flake the thickness of the crystal can be determined [1]. The thickness of a monolayer TMD is approximately 6 Å, much larger than the resolution of an AFM. It is important to place the flake onto a substrate which is not rough so that the flake can lie flat. AFM is used in this thesis to measure the thickness of the rhenium dichalcogenide flakes.

Chapter 4

Rhenium dichalcogenides: Layered semiconductors with two vertical orientations

4.1 Preamble

The rhenium dichalcogenides are unique amongst the transition metal dichalcogenides in that they are only stable in a low symmetry structure, with the space group $P\bar{1}$. As a result of this low symmetry these materials exhibit in-plane anisotropy. Raman spectroscopy has been shown to be a useful tool to explore this anisotropy and can be used to identify the orientation of a flake. The act of flipping a flake, which is equivalent to applying a C_2 rotation about the in-plane axis, is not a symmetry that belongs to these crystals. This means that the rhenium dichalcogenides have two vertical orientations that are non-equivalent. In this paper Raman spectroscopy is demonstrated as an ideal tool to identify the vertical orientation of a flake.

The results contained in this chapter follow on from the work by Wolverson et al. where the in-plane anisotropy in $ReSe_2$ was explored using Raman spectroscopy. In the publication by Wolverson et al. the intensities of the Raman modes are measured as a function of polarisation

angle. It was shown that there is a relationship between these two quantities that can be used to determine the in-plane orientation of a flake [59].

In this paper the b crystal axis is defined to be along the direction of the rhenium chains. This is in line with other work on Raman spectroscopy of the rhenium dichalcogenides [59].

The candidate designed the experiment, prepared the samples and took the measurements. The candidate was also involved in the analysis of the results and the writing of the manuscript. Dr Wolverson realised that Raman spectroscopy would be able to identify the vertical orientations of the rhenium dichalcogenide flakes, and performed all the DFT calculations. Miss Hoye carried out some preliminary studies. Dr Dale and Dr Webb helped with the sample preparation.

4.2 Statement of authorship and copyright information

<table>
<tr><td colspan="5">This declaration concerns the article entitled:</td></tr>
<tr><td colspan="5">Rhenium dichalcogenides: Layered semiconductors with two vertical orientations</td></tr>
<tr><td colspan="5">Publication status (tick one)</td></tr>
<tr><td>Draft manuscript</td><td>Submitted</td><td>In review</td><td>Accepted</td><td>Published</td></tr>
<tr><td></td><td></td><td></td><td></td><td>✓</td></tr>
<tr><td>Publication details (reference)</td><td colspan="4">L. Hart, S. Dale, S. Hoye, J. L. Webb, and D. Wolverson, "Rhenium dichalcogenides: Layered semiconductors with two vertical orientations," Nano Letters, vol. 16, no. 2, pp. 1381–1386, 2016.</td></tr>
<tr><td>Candidate's contribution to the paper (detailed, and also given as a percentage)</td><td colspan="4">The candidate predominantly executed the experimental measurements within this publication.
Formulation of ideas: 10%
Design of methodology: 50%
Experimental work: 90%
Computational work: 0%
Presentation of data in journal format: 10%</td></tr>
<tr><td>Statement from Candidate</td><td colspan="4">This paper reports on original research I conducted during the period of my Higher Degree by Research candidature.</td></tr>
<tr><td>Signature</td><td colspan="2"></td><td>Date</td><td>29/05/2018</td></tr>
</table>

Publication title: Rhenium dichalcogenides: Layered semiconductors with two vertical orientations

The pages of this thesis this paper spans are from 61 to 76.

NANO LETTERS

Letter

pubs.acs.org/NanoLett

Rhenium Dichalcogenides: Layered Semiconductors with Two Vertical Orientations

Lewis Hart, Sara Dale, Sarah Hoye, James L. Webb, and Daniel Wolverson*

Department of Physics, University of Bath, Bath BA2 7AY, United Kingdom

Supporting Information

ABSTRACT: The rhenium and technetium diselenides and disulfides are van der Waals layered semiconductors in some respects similar to more well-known transition metal dichalcogenides (TMD) such as molybdenum sulfide. However, their symmetry is lower, consisting only of an inversion center, so that turning a layer upside-down (that is, applying a C_2 rotation about an in-plane axis) is not a symmetry operation, but reverses the sign of the angle between the two nonequivalent in-plane crystallographic axes. A given layer thus can be placed on a substrate in two symmetrically nonequivalent (but energetically similar) ways. This has consequences for the exploitation of the anisotropic properties of these materials in TMD heterostructures and is expected to lead to a new source of domain structure in large-area layer growth. We produced few-layer ReS_2 and $ReSe_2$ samples with controlled "up" or "down" orientations by micromechanical cleavage and we show how polarized Raman microscopy can be used to distinguish these two orientations, thus establishing Raman as an essential tool for the characterization of large-area layers.

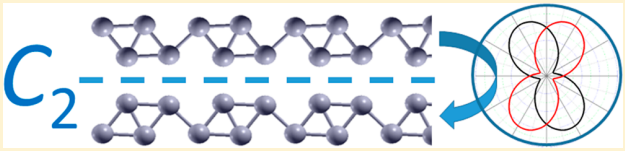

KEYWORDS: *rhenium diselenide, rhenium disulfide, $ReSe_2$, ReS_2, MoS_2, transition metal dichalcogenide, phonon, Raman spectroscopy, asymmetry*

The transition metal dichalcogenide (TMD) family has been well known since the 1960s and, particularly, since the seminal work of Wilson and Yoffe.[1] Rhenium diselenide and rhenium disulfide (and their technetium analogues) are special among the 40 or so TMDs that were identified then since, in many respects, they do not behave as expected of typical TMDs. We focus on one important aspect of this, the lack of rotational symmetry in Re-based TMDs about any in-plane axis, and the use of Raman spectroscopy to identify the resulting orientation.

The TMD family has come to attention recently with the isolation of single layers of van der Waals bonded layered materials (graphene, h-BN, MoS_2, WS_2 and several others[2]). The isolation of single TMD layers leads to the well-known indirect to direct gap transition of MoS_2,[3] and also to dramatic changes in dielectric properties,[4] because the reduction of the effective dielectric constant for an isolated layer increases exciton binding energies, sometimes to the point that neutral and even charged exciton signals can be observed in optical spectroscopy at room temperature.[5] In general, phonon frequencies are also modified in few- and monolayers.[6] Finally, it is well established that gated electrical transport at high mobility can be achieved in single layers and heterojunctions, so that field effect transistor (FET) structures can be realized.[7] Much interest is currently focused on heterostructures in which devices are built, layer by layer, from mixed graphene, h-BN and TMD layers to engineer new functionalities or improve existing material properties such as the electron mobility or the superconducting transition.[2]

In this context, the Re-TMDs will introduce features in a heterostructure that h-BN and the more well-known TMDs cannot. Their unusual nature arises from a Peierls distortion which moves the Re atoms away from the metal sites of the octahedral 1T structure into lozenges of four atoms, defined by Re−Re as well as Rechalcogen bonds.[8] These groups of Re atoms form zigzag chains running along one crystallographic axis (usually defined as the *b* axis) in the layer plane, so that material properties are highly anisotropic in the layer plane[9−12] (these Re chains are illustrated in our table-of-contents graphic with the chalcogen atoms omitted, showing how rotation about an in-plane 2-fold axis reverses the orientation of the lozenges). More details of this and of the Re-TMD structures are shown in the Supporting Information, Figure S1. The in-plane anisotropy is clear in optical absorption and reflectance near the band gap[13−21] and in Raman spectroscopy,[22] but is also observed in electrical transport.[17,19,23−26] It has been shown recently that transport measurements may be used to determine layer orientation[26,27] as, of course, could transmission electron microscopy (TEM), and, though this is certainly true, we shall show that Raman spectroscopy provides this information nondestructively and without the need for any device fabrication steps.

From all optical experiments to date, it is clear that the interlayer interaction is particularly weak even for a van der Waals-bonded material, as shown by the rather small shifts in the frequencies of the vibrational modes observed in Raman

Received: November 26, 2015
Published: January 22, 2016

DOI: 10.1021/acs.nanolett.5b04838
Nano Lett. 2016, 16, 1381−1386

spectroscopy on going from bulk to monolayer samples.[8,22,28,29] This is unfortunate, because the shifts in the Raman spectra of similar materials (graphene and MoS_2, for example) allow useful measurements of layer thickness in the crucial region of mono-, bi-, and trilayers.

By contrast, the in-plane anisotropy of Re TMDs is very easily investigated via Raman spectroscopy and the results can be analyzed in terms of the fundamental Raman tensors R_{ij} for each vibrational mode. A detailed understanding of the angle-dependence of the Raman spectra leads to strategies for mapping variations in layer orientation independent of the effects of varying layer thickness. For a material of C_i point group symmetry, the Raman tensors have no nonzero elements (examples are given in the Supporting Information, Table S1 and Figure S6). Therefore, all Raman-active modes are predicted to be observable to some degree for any crystal orientation, and to have intensities that depend on the orientation of the layer axes with respect to the incident and scattered light polarizations. We note that, often, the zone center phonons of the Re TMDs are referred to by the symmetry labels A_g-like and E_{1g}-like which are appropriate for hexagonal structures such as MoS_2. This labeling is based on similarities in the atomic displacement patterns. However, because formally all Raman-active modes belong to the A_g species, we prefer here a recently introduced labeling system in which the Raman-active modes are numbered (in Roman numerals) in order of increasing frequency.[27,30] The ReS_2 modes of relevance here are labeled in this way on Figure 1.

Representative experimental Raman spectra of ReS_2 are shown in Figure 1; a low-resolution Raman spectrum of ReS_2 was apparently reported first in the RRUFF database,[31] because ReS_2 occurs as a rare but naturally occurring mineral rheniite;[32−34] the Raman spectra of $ReSe_2$ have also been presented earlier.[22,35] The Re and Tc TMDs based on S and Se all have similar structures, though ReS_2 has been proposed to have a unit cell which is doubled along the normal to the layers and thus contains 24 instead of 12 atoms.[12] This doubling results in an increase in the predicted number of Γ-point Raman-active modes, but (as confirmed by first-principles calculations) the modes of a monolayer have frequencies close to those of a thick layer;[8,22,27,28] this appears to be true also for $ReSe_2$.[22] Here, we are not concerned with interlayer coupling and so we do not focus on few-layer flakes in this study; however, we used micromechanical cleavage to select single-crystal flakes of well-defined morphology. In all cases, these were of thickness greater than 100 nm, as was confirmed by AFM and by the absence of the silicon Raman peak at 520 cm^{-1} in the Raman spectra excited with 532 nm light. Figure 1a shows the Raman spectrum of a small bulk crystal of ReS_2 at low temperature using an excitation wavelength of 785 nm and with an experimental resolution sufficient to resolve completely all the detectable Raman signals (here, we see 16 out of the expected total of 18 A_g modes). Figure 1b shows the Raman spectrum of an exfoliated flake from the same bulk ReS_2 sample using 532 nm excitation in a Raman microscope at room temperature. The ReS_2 spectrum is now dominated by the 150, 160, and 211 cm^{-1} modes (III−V), as noted previously,[8,27,30,36] and these modes will suffice here to demonstrate the in-plane anisotropy. Figure 1a shows that the signals at low Raman shifts arise from a group of four modes (I−IV), and we note that it is necessary to take all four into account in fitting spectra even where the modes are not completely resolved. In the case of $ReSe_2$, suitable modes to consider are the 126, 160, and 172

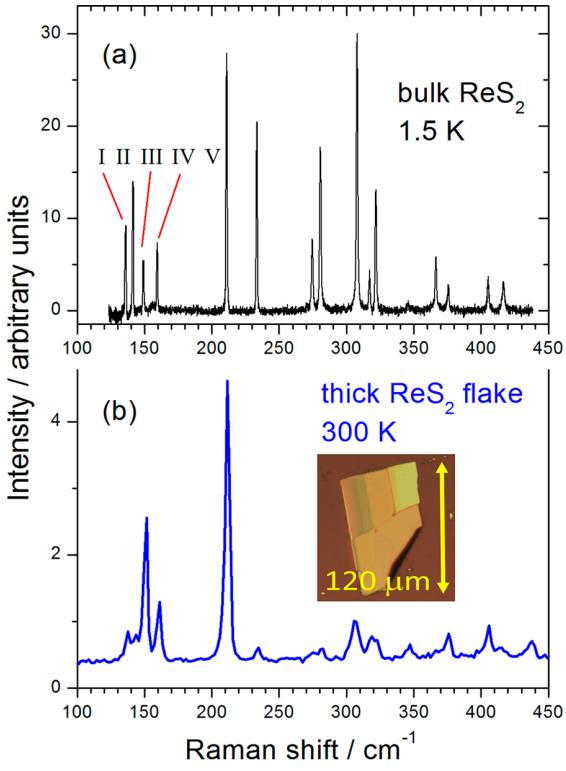

Figure 1. Raman spectra of (a) a bulk ReS_2 crystal at low temperature with an excitation wavelength of 785 nm, with macroscopic sampling showing the labeling used for the lowest frequency modes, and (b) a cleaved thick ReS_2 flake (the region used had thickness >100 nm) on a 300 nm SiO_2 layer on a silicon substrate at room temperature, with an excitation wavelength of 532 nm in a Raman microscope (data were obtained from the lower, thickest part). The difference in peak widths between (a) and (b) is accounted for by the different instrumental resolutions, and the small peak shifts between the two spectra are attributed to the difference in temperature.

cm^{-1} modes,[28] as is shown in the Supporting Information (Figure S2).

To analyze the effects of anisotropy, we define the Raman tensor for the scattering process due to a given mode as R. If we consider only the in-plane components of the electric field, we can write R as

$$R = \begin{pmatrix} u & v \\ v & w \end{pmatrix} \quad (1)$$

When the polarization of the excitation is rotated by θ with respect to the in-plane crystal axes, as already shown for $ReSe_2$,[22] the intensity $I_S(\theta)$ of a given Raman band varies with θ as

$$I_S(\theta) \propto u^2\cos^2\theta + w^2\sin^2\theta + v^2 + 2v(u+w)\sin\theta\cos\theta \quad (2)$$

for detection of both scattered polarizations with equal sensitivity, or as

$$I_{\parallel}(\theta) \propto (u\cos^2\theta + 2v\sin\theta\cos\theta + w\sin^2\theta)^2$$

given parallel detection and excitation polarizations or, finally, as

$$I_{\perp}(\theta) \propto (v[\cos^2\theta - \sin^2\theta] + [w-u]\sin\theta\cos\theta)^2$$

DOI: 10.1021/acs.nanolett.5b04838
Nano Lett. 2016, 16, 1381−1386

for perpendicular excitation and detection polarizations. We showed elsewhere that $I_S(\theta)$ is a useful experimental quantity to consider because it has a simple mathematical form, and because it always carries information about all three nonequivalent (and, generally, nonzero) components of the 2D Raman tensor.[22] In a Raman mapping experiment aimed at highlighting areas of different orientation approximately independent of variations in thickness, for example, the ratio of $I_S(\theta)$ for two different peaks in the same spectrum can be plotted to obtain a false-color contrast that is dependent principally on θ and requires only one spectrum per pixel[22] (the extent to which layer thickness affects the polarization direction of modes III and V is addressed in the Supporting Information, Figure S7).

However, because Re-TMDs do not possess rotation axes in the layer plane, turning a layer upside-down is not a symmetry operation (see the Supporting Information, Figures S1 and S3 and Table S1) and, at least in principle, should affect the observed Raman intensities. In terms of the above expressions, for example, $u \rightarrow u$, $v \rightarrow -v$, and $w \rightarrow w$ under rotation by π about the in-plane laboratory x axis, so that the measurement of $I_S(\theta)$ will now yield a result in which the sign of the final term in eq 2 is reversed (the derivation is given in the Supporting Information)

$$I_S(\theta) \propto u^2\cos^2\theta + w^2\sin^2\theta + v^2 - 2v(u + w)\sin\theta\cos\theta \quad (3)$$

This result can alternatively be viewed as the result of replacing θ by $-\theta$ and is quite general because rotation by π about any other in-plane axis is equivalent to this in-plane rotation combined with an appropriate rotation around the plane normal. The expressions for $I_\perp(\theta)$ and $I_\parallel(\theta)$ are modified by this transformation in similar ways. The appearance of the intensities predicted by eqs 2 and 3 is given in the Supporting Information, Figure S3.

We test these predictions as follows. If the bulk starting material for micromechanical cleavage has the ideal crystal structure, it should be straightforward to produce layers facing either way up by careful manipulation of the adhesive tape; fragments of the same crystal on opposite sides of the tape will deposit layers facing opposite ways up when transferred to the silicon substrate. Of course, this approach might fail if the starting crystals are twinned vertically, or if the cleavage or deposition process is disruptive enough that layers are overturned. We used thin cleaved layers because we could then identify flakes whose morphology gave an indication of the orientation of the crystal b axis. This is, however, not always unambiguous, as shown in the Supporting Information, Figure S4. We therefore confirmed the orientation of the b axis of the flakes used for the Raman measurements in each case by measurement of their optical reflectance under white light illumination in a polarizing microscope (see Supporting Information, Figure S5). Two band-to-band transitions are seen which are known from experiments[37] and first-principles modeling[38] to be orthogonally polarized along the Γ−M and Γ−K directions and to differ in energy by about 150 meV. The polarization direction giving the minimum energy is then unambiguously the direction of the b axis[38] and this can be related to the cleavage edges of the flake imaged in the same microscope. The optical absorption or reflectance, however, does not discriminate between the two possible vertical orientations of a flake.

As the excitation polarization is rotated with respect to the laboratory and crystal axes, we expect to observe a variation in intensity of the Raman modes of a given single crystal flake; typical results are shown in Figure 2a, here for ReS_2 (equivalent

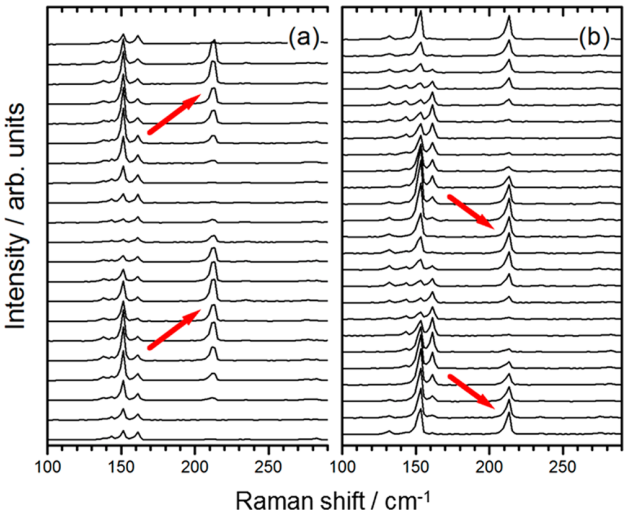

Figure 2. Raman spectra of ReS_2 flakes (both of thickness >100 nm) cleaved from the same starting crystal but placed facing (a) upward and (b) downward on the substrate. Spectra were recorded with unpolarized detection; the excitation polarization was rotated in 15° steps from 0° to 360° (bottom to top) in the same rotational direction in both cases. The red arrows highlight the sequence in which the Raman peaks at 150 and 211 cm^{-1} (modes III and V) reach their respective maxima as the excitation polarization is rotated.

data for $ReSe_2$ are shown in the Supporting Information, Figure S2). From the angle at which a given mode reaches its maximum, one can easily compare the relative orientation of different flakes produced in the same micromechanical cleavage process, whether or not their morphology is recognizable. This ability will be particularly useful when large area Re-based TMDs are grown by CVD or related techniques. In fact, the *absolute* orientation of a single flake with respect to the laboratory axes can also be determined.[27] We discuss this further by reference to data for ReS_2; in Figure 3, we plot only the peak intensity as a function of angle for the selected peaks specified above. Peak intensities were determined by fitting the spectra using mixed Lorentzian−Gaussian line shapes after careful background subtraction, taking into account also any overlapping peaks not in the required set.

Results are shown in Figure 3a and b for two large flakes of ReS_2 obtained from the same starting bulk crystal by micromechanical cleavage and deposition onto a standard silicon wafer with a 290 nm oxide layer. The bright yellow-white color over most of the area of the flakes indicates regions that are effectively bulk material. The direction of the crystallographic b axis, which frequently (but not always) forms the longer edge of cleaved crystals,[26] is indicated on images of the samples in Figure 3c and d. First, it is clear that, as expected, the data are well described by fits according to eq 1 in all cases. Second, there is an approximate correspondence between the principal axis of the Raman tensor for the 211 cm^{-1} mode V and the direction of the crystallographic b axis, as noted elsewhere.[27,30] This correspondence appears not to be exact and depends on layer thickness (see Supporting Information, Figures S6 and S7). More importantly here, we

DOI: 10.1021/acs.nanolett.5b04838
Nano Lett. 2016, 16, 1381−1386

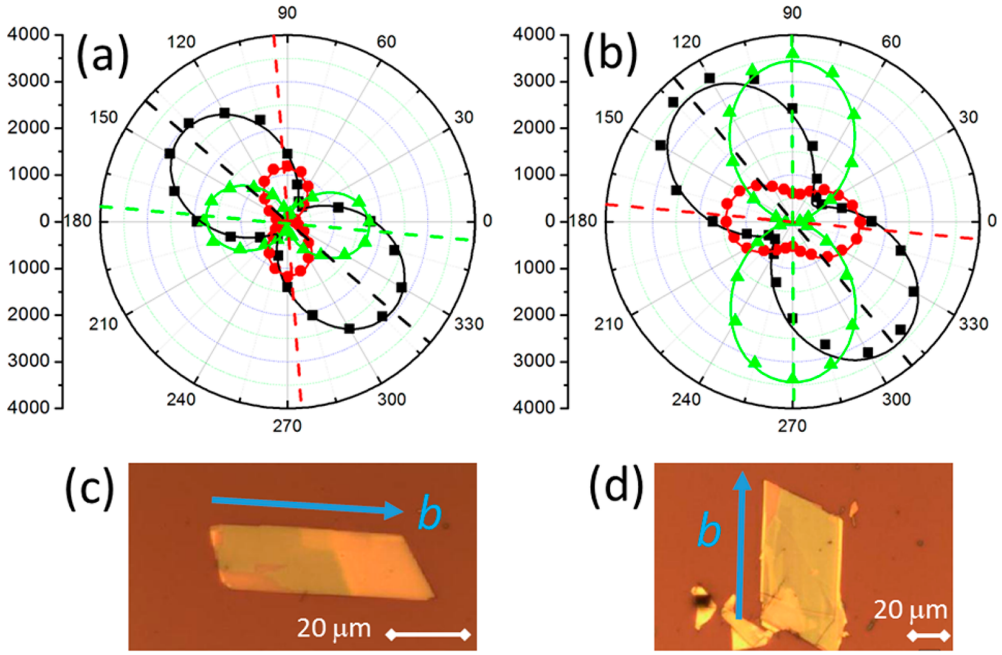

Figure 3. Intensities as a function of angle with respect to the laboratory x axis of three peaks in the Raman spectra of large ReS_2 flakes (both of thickness >100 nm) which were cleaved from the same starting crystal but were facing (a) "upward" and (b) "downward". Images of the corresponding flakes are shown in (c) and (d) respectively with a 20 μm scale bar (white) in each case; the inferred directions of the crystallographic b axes are indicated by the blue arrows. Spectra were recorded with unpolarized detection and the excitation polarization was rotated in 15° steps from 0° to 360° (bottom to top) in the same rotational direction in both cases. The peaks chosen are the 150, 160, and 211 cm^{-1} modes III–V (black squares, red circles, and green triangles, respectively). The corresponding solid lines in each case show fits to the experimental data using the expression of eq 1 and the dashed lines show the orientation of the principal axis obtained from each fit.

see that no *in-plane* rotation exists that can map the curves of Figure 3a into those of Figure 3b, as is clear also from the morphology of the chosen pair of flakes. The angles between the principal axes of the 150 cm^{-1} mode III and the modes at 160 (IV) and 211 cm^{-1} (V) are −45° and +39°, respectively in Figure 3a and are +45° and −36°, respectively in Figure 3b, with an estimated error of ±2°; the sequence of the peak maxima in angle is thus reversed in angle between Figure 3a and b, as already demonstrated by Figure 2 for the case of $ReSe_2$. This shows that Raman spectroscopy is able to distinguish the two possible orientations of Re-TMD layers and that there is no possible ambiguity between the effects of in-plane and vertical orientations in the angle-dependence of the Raman spectra.

This will be of great significance for large-area growth of materials of this low-symmetry family. In a CVD or similar growth technique, it is highly likely that different domains will be produced facing different ways up as well as having different in-plane orientations. Indeed, the in-plane orientation (that is, the direction of the b axis) will probably be more easily influenced by a suitable choice of substrate surface reconstruction or template than whether a layer faces "up" or "down". However, this remains to be tested. Certainly, the fundamental chemical nature of the upper and lower chalcogen planes is the same since they are related by a center of inversion symmetry. This implies that the energy of interaction with the substrate of a particular domain within a growing layer will not depend strongly on whether its orientation is "up" or "down". Although the vertical orientation may not influence the energetics of the layer significantly and may not be of importance for chemical processes at the surface (such as catalytic or sensing applications, for example), the coexistence of both types of domain within a growing monolayer introduces the new possibility of grain boundaries between "up" and "down" layers as well as between layers with different alignments of the b axis and, thus, may have a considerable impact on charge transport; recently, it has been shown that monolayers may be locally converted between "up" and "down" orientations under electron beam irradiation.[39] First-principles calculations and high-resolution transmission electron microscopy are now needed to explore the possible configurations that result following growth on a typical hexagonal substrate.[40] This combination of techniques has already proved powerful in analyzing the tilt and twin boundaries of, for example, CVD-grown MoS_2, where a variety of ring structures at the boundaries are found to form and which give gap states responsible for marked changes in the luminescence intensity and electrical conductance.[41,42]

In summary, it has been shown that low symmetry of the distorted-1T transition metal dichalcogenides leads to two possible vertical layer orientations and that these can be produced in a controlled fashion by micromechanical cleavage. The vertical orientation of these layers can be identified easily by Raman spectroscopy. It was already shown in earlier studies that the in-plane orientation can be determined; here, it is shown that both vertical and in-plane orientation can be found simultaneously and unambiguously from the same spectra, though several polarization-dependent spectra per point on the sample surface must be measured in order to achieve this. This work paves the way for the investigation and characterization of few-layer samples grown by vapor-phase methods on supporting substrates.

DOI: 10.1021/acs.nanolett.5b04838
Nano Lett. 2016, 16, 1381−1386

■ ASSOCIATED CONTENT

Supporting Information

The Supporting Information is available free of charge on the ACS Publications website at DOI: 10.1021/acs.nanolett.5b04838.

ReS_2 and $ReSe_2$ crystal structures; character table for the C_i point group; derivation of eq 3; Raman spectra of $ReSe_2$ as a function of orientation; schematic diagrams of flake orientation and the ambiguity of morphology; reflectivity as a function of angle for independent confirmation of orientation; selected Raman tensor elements and their calculation details; dependence of Raman polarization on flake thickness. (PDF)

■ AUTHOR INFORMATION

Corresponding Author

*E-mail d.wolverson@bath.ac.uk.

Author Contributions

The manuscript was written through contributions of all authors and all authors have given approval to the final version of the manuscript. S.H. carried out preliminary studies, D.W. conceived the investigation, S.D. and J.L.W. contributed to preparation and characterization of the samples, L.H. and D.W. carried out more extended studies, and D.W. and L.H. analyzed and interpreted the data.

Notes

The authors declare no competing financial interest.

■ ACKNOWLEDGMENTS

This work was supported by the Centre for Graphene Science of the Universities of Bath and Exeter, funded by the EPSRC (U.K.) under grant EP/G036101 and support was also provided by EPSRC grant EP/M022188. Computational work was performed on the University of Bath's High Performance Computing Facility. Data supporting this study are available from the University of Bath data archive free of charge; see DOI:10.15125/BATH-00105.

■ ABBREVIATIONS

TMD:transition metal dichalcogenide; CVD:chemical vapor deposition

■ REFERENCES

(1) Wilson, J. A.; Yoffe, A. D. The Transition Metal Dichalcogenides: Discussion and Interpretation of the Observed Optical, Electrical and Structural Properties. *Adv. Phys.* **1969**, *18*, 193−335.

(2) Geim, A. K.; Grigorieva, I. V. Van Der Waals Heterostructures. *Nature* **2013**, *499*, 419−425.

(3) Splendiani, A.; Sun, L.; Zhang, Y.; Li, T.; Kim, J.; Chim, C.-Y.; Galli, G.; Wang, F. Emerging Photoluminescence in Monolayer MoS_2. *Nano Lett.* **2010**, *10*, 1271−1275.

(4) Andersen, K.; Latini, S.; Thygesen, K. S. Dielectric Genome of Van Der Waals Heterostructures. *Nano Lett.* **2015**, *15*, 4616.

(5) Berkelbach, T. C.; Hybertsen, M. S.; Reichman, D. R. Theory of Neutral and Charged Excitons in Monolayer Transition Metal Dichalcogenides. *Phys. Rev. B: Condens. Matter Mater. Phys.* **2013**, *88*, 045318.

(6) Molina-Sánchez, A.; Wirtz, L. Phonons in Single-Layer and Few-Layer MoS_2 and WS_2. *Phys. Rev. B: Condens. Matter Mater. Phys.* **2011**, *84*, 155413.

(7) Wang, Q. H.; Kalantar-Zadeh, K.; Kis, A.; Coleman, J. N.; Strano, M. S. Electronics and Optoelectronics of Two-Dimensional Transition Metal Dichalcogenides. *Nat. Nanotechnol.* **2012**, *7*, 699−712.

(8) Tongay, S.; Sahin, H.; Ko, C.; Luce, A.; Fan, W.; Liu, K.; Zhou, J.; Huang, Y.-S.; Ho, C.-H.; Yan, J.; et al. Monolayer Behaviour in Bulk ReS_2 Due to Electronic and Vibrational Decoupling. *Nat. Commun.* **2014**, *5*, 3252.

(9) Alcock, N. W.; Kjekshus, A. Crystal Structure of $ReSe_2$. *Acta Chem. Scand.* **1965**, *19*, 79.

(10) Wildervanck, J. C.; Jellinek. The Dichalcogenides of Technetium and Rhenium. *J. Less-Common Met.* **1971**, *24*, 73−81.

(11) Murray, H. H.; Kelty, S. P.; Chianelli, R. R.; Day, C. S. Structure of Rhenium Disulfide. *Inorg. Chem.* **1994**, *33*, 4418−4420.

(12) Lamfers, H. J.; Meetsma, A.; Wiegers, G. A.; deBoer, J. L. The Crystal Structure of Some Rhenium and Technetium Dichalcogenides. *J. Alloys Compd.* **1996**, *241*, 34−39.

(13) Huang, Y. S.; Ho, C. H.; Liao, P. C.; Tiong, K. K. Temperature Dependent Study of the Band Edge Excitons of ReS_2 and $ReSe_2$. *J. Alloys Compd.* **1997**, *262*, 92−96.

(14) Ho, C. H.; Liao, P. C.; Huang, Y. S.; Yang, T. R.; Tiong, K. K. Optical Absorption of ReS_2 and $ReSe_2$ Single Crystals. *J. Appl. Phys.* **1997**, *81*, 6380−6383.

(15) Ho, C. H.; Liao, P. C.; Huang, Y. S.; Tiong, K. K. Piezoreflectance Study of the Band-Edge Excitons of Res2. *Solid State Commun.* **1997**, *103*, 19−23.

(16) Ho, C. H.; Huang, Y. S.; Liao, P. C.; Tiong, K. K. Piezoreflectance Study of Band-Edge Excitons of $ReS_{2-X}Se_x$ Single Crystals. *Phys. Rev. B: Condens. Matter Mater. Phys.* **1998**, *58*, 12575−12578.

(17) Ho, C. H.; Huang, Y. S.; Chen, J. L.; Dann, T. E.; Tiong, K. K. Electronic Structure of ReS_2 and $ReSe_2$ from First-Principles Calculations, Photoelectron Spectroscopy, and Electrolyte Electroreflectance. *Phys. Rev. B: Condens. Matter Mater. Phys.* **1999**, *60*, 15766−15771.

(18) Ho, C. H.; Huang, Y. S.; Liao, P. C.; Tiong, K. K. Crystal Structure and Band-Edge Transitions of $ReS_{2-X}Se_x$ Layered Compounds. *J. Phys. Chem. Solids* **1999**, *60*, 1797−1804.

(19) Ho, C. H.; Huang, Y. S.; Tiong, K. K. An Electrolyte Electroreflectance Study of ReS_2. *Solid State Commun.* **1998**, *109*, 19−22.

(20) Ho, C. H.; Yen, P. C.; Huang, Y. S.; Tiong, K. K. Polarized Electrolyte-Electroreflectance Study of ReS_2 and $ReSe_2$ Layered Semiconductors. *J. Phys.: Condens. Matter* **2001**, *13*, 8145−8152.

(21) Ho, C. H.; Huang, Y. S.; Tiong, K. K. In-Plane Anisotropy of the Optical and Electrical Properties of ReS_2 and $ReSe_2$ Layered Crystals. *J. Alloys Compd.* **2001**, *317*, 222−226.

(22) Wolverson, D.; Crampin, S.; Kazemi, A. S.; Ilie, A.; Bending, S. J. Raman Spectra of Monolayer, Few-Layer, and Bulk $ReSe_2$: An Anisotropic Layered Semiconductor. *ACS Nano* **2014**, *8*, 11154−11164.

(23) Tiong, K. K.; Ho, C. H.; Huang, Y. S. The Electrical Transport Properties of ReS_2 and $ReSe_2$ Layered Crystals. *Solid State Commun.* **1999**, *111*, 635−640.

(24) Ho, C. H.; Hsieh, M. H.; Wu, C. C.; Huang, Y. S.; Tiong, K. K. Dichroic Optical and Electrical Properties of Rhenium Dichalcogenides Layer Compounds. *J. Alloys Compd.* **2007**, *442*, 245−248.

(25) Liang, C. H.; Tiong, K. K.; Huang, Y. S.; Dumcenco, D.; Ho, C. H. In-Plane Anisotropic Electrical and Optical Properties of Gold-Doped Rhenium Disulphide. *J. Mater. Sci.: Mater. Electron.* **2009**, *20*, 476−479.

(26) Liu, E.; Fu, Y.; Wang, Y.; Feng, Y.; Liu, H.; Wan, X.; Zhou, W.; Wang, B.; Shao, L.; Ho, C.-H.; et al. Integrated Digital Inverters Based on Two-Dimensional Anisotropic ReS_2 Field-Effect Transistors. *Nat. Commun.* **2015**, *6*, 6991.

(27) Chenet, D. A.; Aslan, O. B.; Huang, P. Y.; Fan, C.; van der Zande, A. M.; Heinz, T. F.; Hone, J. C. In-Plane Anisotropy in Mono- and Few-Layer ReS_2 Probed by Raman Spectroscopy and Scanning Transmission Electron Microscopy. *Nano Lett.* **2015**, *15*, 5667−5672.

(28) Zhao, H.; Wu, J.; Zhong, H.; Guo, Q.; Wang, X.; Xia, F.; Yang, L.; Tan, P.-H.; Wang, H. Interlayer Interactions in Anisotropic Atomically-Thin Rhenium Diselenide. 2015, *arXiv:1504.07664*.

DOI: 10.1021/acs.nanolett.5b04838
Nano Lett. 2016, 16, 1381−1386

arXiv.org e-Print archive. http://arxiv.org/abs/1504.07664 (accessed December 2015).
(29) Chenet, D. A.; Aslan, O. B.; Huang, P. Y.; Fan, C.; van der Zande, A. M.; Heinz, T. F.; Hone, J. C. In-Plane Anisotropy in Mono- and Few-Layer ReS_2 Probed by Raman Spectroscopy and Scanning Transmission Electron Microscopy. *Nano Lett.* **2015**, *15*, 5667−5672.
(30) Nagler, P.; Plechinger, G.; Schüller, C.; Korn, T. Observation of Anisotropic Interlayer Raman Modes in Few-Layer ReS_2. 2015, *arXiv:1511.02645*. arXiv.org e-Print archive. http://arxiv.org/abs/1511.02645 (accessed December 2015).
(31) Downs, R. T. The RRUFF Project: An Integrated Study of the Chemistry, Crystallography, Raman and Infrared Spectroscopy of Minerals. *19th General Meeting of the International Mineralogical Association (Proceedings)*; I. M. A. annd Mineralogical Society: Washington, DC, 2006; pp O03−13.
(32) Korzhinsky, M. A.; Tkachenko, S. I.; Shmulovich, K. I.; Taran, Y. A.; Steinberg, G. S. Discovery of a Pure Rhenium Mineral at Kudriavy Volcano. *Nature* **1994**, *369*, 51−52.
(33) Taran, Y. A.; Hedenquist, J. W.; Korzhinsky, M. A.; Tkachenko, S. I.; Shmulovich, K. I. Geochemistry of Magmatic Gases from Kudryavy Volcano, Iturup, Kuril Islands. *Geochim. Cosmochim. Acta* **1995**, *59*, 1749−1761.
(34) Samotoin, N. D.; Magazina, L. O.; Znamenskii, V. S. Structure and Morphology Characteristics of Natural Rhenium Sulphild from Kudryavyi Volcano Fumaroles, Intrup Island, Kuriles. *Doklady Akademii nauk. Rossijskaâ akademiâ nauk* **1995**, *345*, 518−522.
(35) Yang, S. X.; Tongay, S.; Yue, Q.; Li, Y. T.; Li, B.; Lu, F. Y. High-Performance Few-Layer Mo-Doped $ReSe_2$ Nanosheet Photodetectors. *Sci. Rep.* **2014**, *4*, 6.
(36) Feng, Y.; Zhou, W.; Wang, Y.; Zhou, J.; Liu, E.; Fu, Y.; Ni, Z.; Wu, X.; Yuan, H.; Miao, F. Raman Vibrational Spectra of Bulk to Monolayer ReS_2 with Lower Symmetry. 2015, *arXiv:1502.02835*. arXiv.org e-Print archive. http://arxiv.org/abs/1502.02835 (accessed December 2015).
(37) Ho, C. H.; Huang, Y. S.; Tiong, K. K.; Liao, P. C. Absorption-Edge Anisotropy in ReS_2 and $ReSe_2$ Layered Semiconductors. *Phys. Rev. B: Condens. Matter Mater. Phys.* **1998**, *58*, 16130−16135.
(38) Zhong, H.-X.; Gao, S.; Shi, J.-J.; Yang, L. Quasiparticle Band Gaps, Excitonic Effects, and Anisotropic Optical Properties of the Monolayer Distorted 1 T Diamond-Chain Structures ReS_2 and $ReSe_2$. *Phys. Rev. B: Condens. Matter Mater. Phys.* **2015**, *92*, 115438.
(39) Lin, Y.-C.; Komsa, H.-P.; Yeh, C.-H.; Björkman, T. r.; Liang, Z.-Y.; Ho, C.-H.; Huang, Y.-S.; Chiu, P.-W.; Krasheninnikov, A. V.; Suenaga, K. Single-Layer ReS_2: Two-Dimensional Semiconductor with Tunable in-Plane Anisotropy. *ACS Nano* **2015**, *9*, 11249.
(40) Ji, Q. Q.; Zhang, Y.; Zhang, Y. F.; Liu, Z. F. Chemical Vapour Deposition of Group-Vib Metal Dichalcogenide Monolayers: Engineered Substrates from Amorphous to Single Crystalline. *Chem. Soc. Rev.* **2015**, *44*, 2587−2602.
(41) van der Zande, A. M.; Huang, P. Y.; Chenet, D. A.; Berkelbach, T. C.; You, Y.; Lee, G.-H.; Heinz, T. F.; Reichman, D. R.; Muller, D. A.; Hone, J. C. Grains and Grain Boundaries in Highly Crystalline Monolayer Molybdenum Disulphide. *Nat. Mater.* **2013**, *12*, 554−561.
(42) Najmaei, S.; Liu, Z.; Zhou, W.; Zou, X.; Shi, G.; Lei, S.; Yakobson, B. I.; Idrobo, J.-C.; Ajayan, P. M.; Lou, J. Vapour Phase Growth and Grain Boundary Structure of Molybdenum Disulphide Atomic Layers. *Nat. Mater.* **2013**, *12*, 754−759.

DOI: 10.1021/acs.nanolett.5b04838
Nano Lett. 2016, 16, 1381−1386

Rhenium dichalcogenides: layered semiconductors with two vertical orientations

Lewis Hart, Sara Dale, Sarah Hoye, James L. Webb and Daniel Wolverson.

Department of Physics, University of Bath, Bath BA2 7AY, United Kingdom.

Supporting information

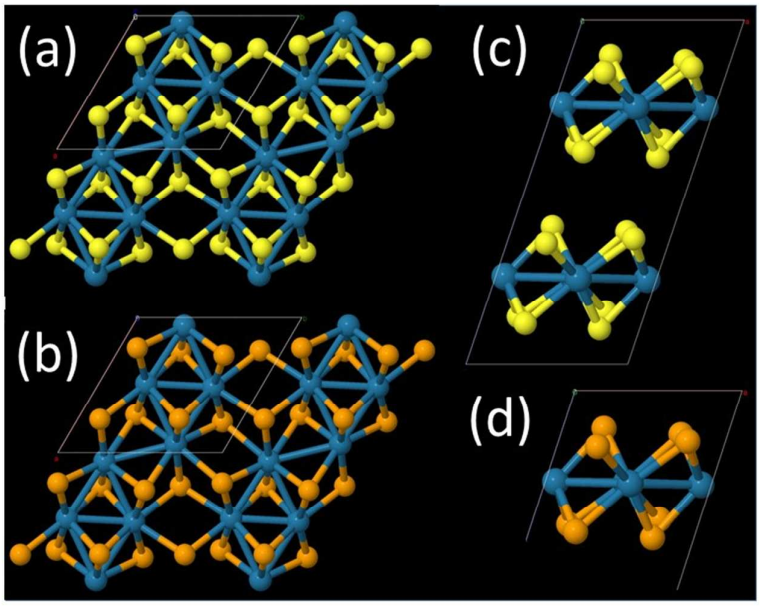

Figure S1. (a) and (b): ReS_2 and $ReSe_2$ structures respectively, viewed along the *c* axis, which is approximately normal to the layer plane. Four unit cells are shown in order to illustrate the Re chains (yellow: S; orange: Se; blue: Re atoms). (c) and (d): single ReS_2 and $ReSe_2$ unit cells respectively, now viewed along the conventional *a* axis, showing the doubling of the ReS_2 unit cell along the *c* axis proposed by Lamfers *et al.*[1].

C_i	E	i	*order* = 2	
A_g	1	1	x^2,y^2,z^2, R_x,R_y,R_z	Raman-active only
A_u	1	-1	x, y, z	Infra-red active only

Table S1 Character table for the C_i point group of the unit cells of ReS_2 and $ReSe_2$.

Derivation of equation (3) in the main text.

The Raman-active modes all transform as x^2, etc., and thus belong to symmetry species A_g. The general three-dimensional Raman tensor R_n for the nth mode of type A_g has no non-zero elements but is symmetric and may be written:

$$R_n = \begin{pmatrix} u & v & a \\ v & w & b \\ a & b & c \end{pmatrix}.$$

Below (figure S6), we list values of the Raman tensors calculated by first-principles density functional theory for the Raman-active modes of bulk ReS_2; we have already presented calculated Raman tensors for $ReSe_2$ elsewhere[2].

The operator T representing a rotation of π about the laboratory in-plane x axis is

$$T = \begin{pmatrix} 1 & 0 & 0 \\ 0 & -1 & 0 \\ 0 & 0 & -1 \end{pmatrix}.$$

Under the rotation T, the Raman tensor transforms to $R' = T^{-1}RT$. The operator T is clearly self-inverse, so that

$$T^{-1}RT = \begin{pmatrix} 1 & 0 & 0 \\ 0 & -1 & 0 \\ 0 & 0 & -1 \end{pmatrix}\begin{pmatrix} u & v & a \\ v & w & b \\ a & b & c \end{pmatrix}\begin{pmatrix} 1 & 0 & 0 \\ 0 & -1 & 0 \\ 0 & 0 & -1 \end{pmatrix} = \begin{pmatrix} u & -v & -a \\ -v & w & b \\ -a & b & c \end{pmatrix}.$$

The two-dimensional block of R' relevant to the scattering of light with an in-plane polarization is therefore

$$R' = \begin{pmatrix} u & -v \\ -v & w \end{pmatrix}.$$

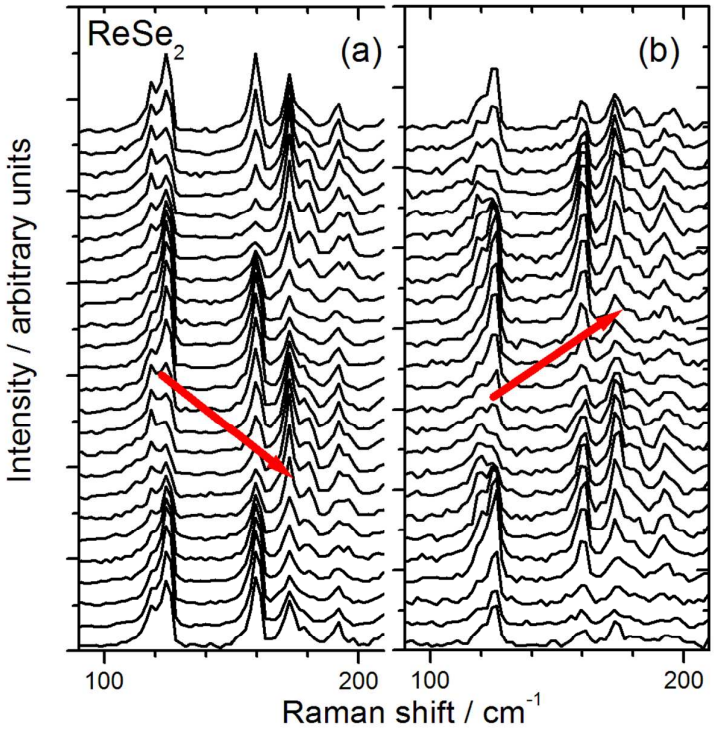

Figure S2. Raman spectra of $ReSe_2$ flakes cleaved from the same starting crystal but placed facing (a) upwards and (b) downwards on the substrate. Spectra were recorded with unpolarized detection; the excitation polarization was rotated in 15° steps from 0° to 360° (bottom to top) in the same rotational direction in both cases. The red arrows highlight the sequence in which the Raman peaks at 126, 160 and 172 cm^{-1} reach their respective maxima as the excitation polarization is rotated.

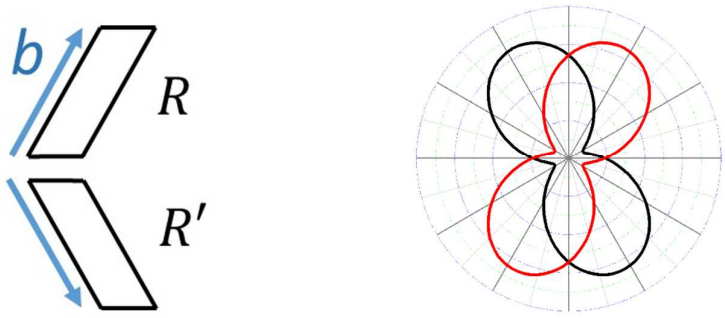

Figure S3. Left: the relationship between flakes that transform to one another under T and therefore have Raman tensors R and R' respectively. Right: demonstration of the predicted angle dependences of one particular Raman mode for R (black) and R' (red) given hypothetical values of (u, v, w) and using Equations (2) and (3) of the main text.

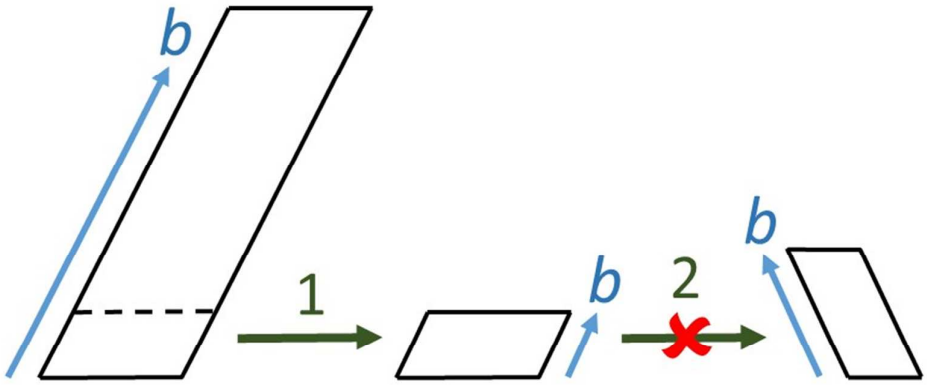

Figure S4. Left: the orientation of the *b*-axis of a typical large flake with a clearly recognizable long edge and ~60° and ~120° angles between edges can easily be identified. Centre: step 1 represents a fracture along the horizontal *a* axis which yields fragments with a misleading morphology (such flakes are less common but are sometimes found following exfoliation; one such region is visible, for example, in Figure 3a of Ref. 25 of the main text). Right: upside-down flakes with the typical morphology are visually *identical* to the flakes produced by step 1 but differ from them because only rotation about an in-plane axis can generate upside-down flakes. There is no cleavage process or rotation about the normal to the plane (i.e, no step 2) that can transform one into the other.

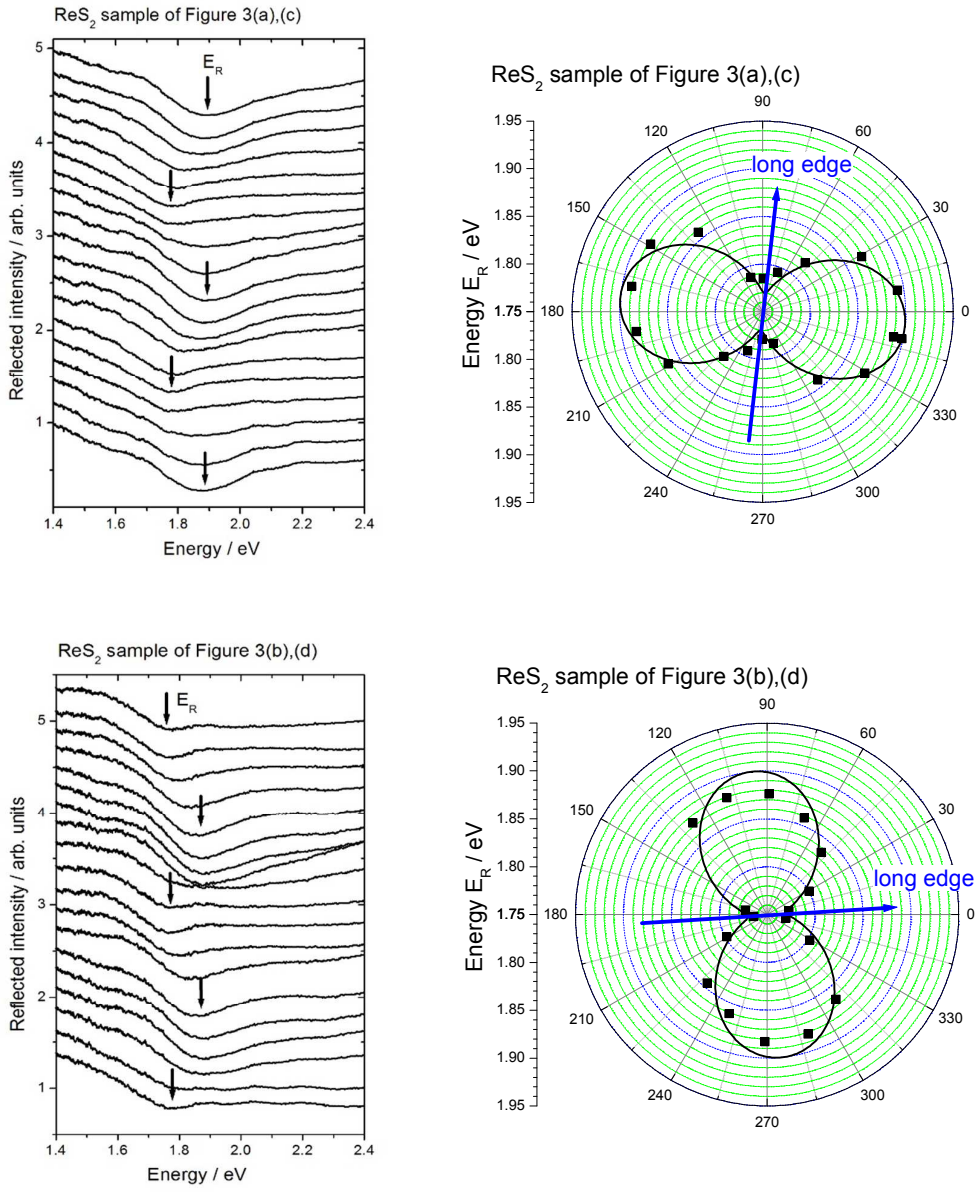

Figure S5. Top left: reflectance under illumination by linearly polarized white light of the sample of figure 3(a) as a function of angle (successive spectra were taken at 20° intervals and are displaced vertically for clarity). Spectra were normalized at each angle to the reflectivity of a mirror placed at the sample position. Top right: the energy of the reflectance minimum indicated by arrows as a function of polarization angle (the blue arrow indicates the direction of the long cleavage edge of the sample). The solid line is a guide to the eye based on the calculated transition energies of Zhong *et al.* [3]. Bottom left and right: as the top, but for the sample of Figure 3(b).

mode III	**154.23 cm^{-1}**	
0.0253	0.10964	0.08818
0.10964	0.10664	0.00642
0.08818	0.00642	0.03399
mode IV	**164.02 cm^{-1}**	
0.00397	0.04068	0.00427
0.04068	0.07046	0.01687
0.00427	0.01687	0.03186
mode V	**218.79 cm^{-1}**	
0.05927	0.02795	0.04505
0.02795	0.03923	0.02655
0.04505	0.02655	0.01348

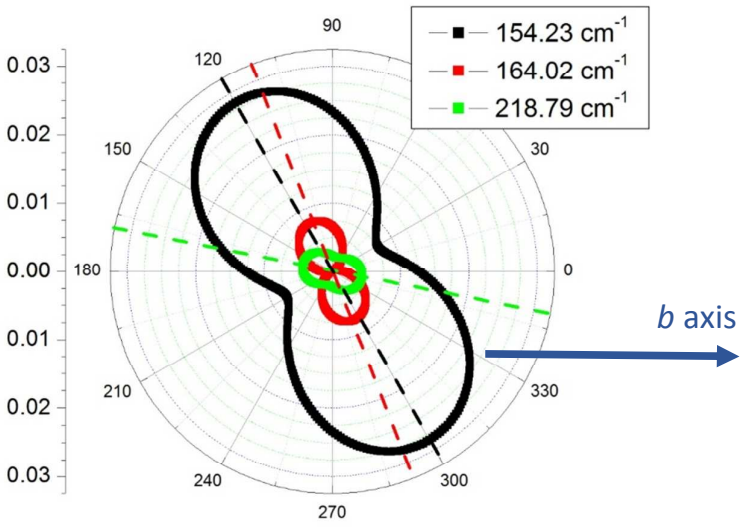

Figure S6. Top: table of specimen predicted values of the Raman tensors R_n of modes III, IV and V calculated via density functional perturbation theory. Bottom: angle-dependence of the three modes III (black), IV (red) and V (green) for linearly polarized excitation and unpolarized detection. The direction of the crystallographic *b* axis is taken as the zero of angle as indicated by the blue arrow. This figure should be compared to Figures 3(a) and 3(b) of the main text; although agreement is not precise, it is clear that mode V is predicted to be aligned close to the *b* axis and that the other two modes lie either side of it.

Calculation details of Figure S6:

The Quantum Espresso code[4, 5] was used to perform the calculations of Figure S6, first relaxing the atomic positions and unit cell parameters from the coordinates of Lamfers *et al.*[1] and then calculating the Γ-point phonon frequencies, atomic displacements and Raman tensors. Perdew-Wang[6] pseudopotentials were used in the local density approximation with a plane wave kinetic energy cutoff of 50 Rydberg. An 8×8×8 Monkhorst-Pack[7] grid of k-points was used for integration over the Brillouin zone of a bulk-like ReS_2 structure containing one layer per unit cell. It is not our aim here to present a definitive calculation of the Raman tensors of ReS_2, since that is a major task which is ongoing and is beyond the scope of this paper, but these results show good qualitative agreement with experiment, in that (i) mode V lies close to the *b* axis; (ii) modes III and IV lie either side of mode V and exchange sides if the crystal axes are inverted. The agreement with experimentally observed Raman frequencies (within 3%) is typical of this level of calculation[8].

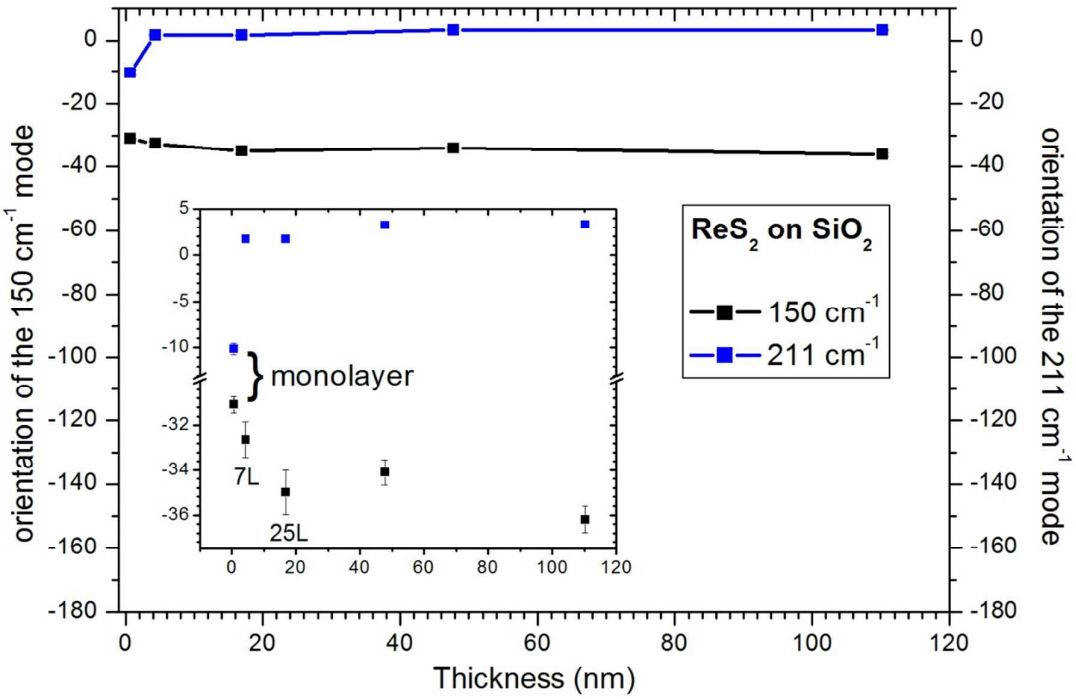

Figure S7. Dependence of the polarization of the ReS_2 150 cm^{-1} (III) and 211 cm^{-1} (V) Raman peaks on the ReS_2 flake thickness. Solid squares: the angles (referred to the laboratory axes) at which the maxima of the Raman peaks appear as the excitation polarization is rotated. Lines: guides to the eye. The inset shows the same data on an expanded vertical scale. These data were obtained using a single exfoliated flake which had several regions of different thickness all with accurately aligned long cleavage edges. The thickness of each region was determined by AFM. For the thickest sample here (~110 nm), the attenuation of the 532 nm laser beam in the flake was strong enough that no silicon Raman peak at 520 cm^{-1} could be observed in the spectrum; we take this as a practical definition of a thick layer throughout the present work.

References

1. Lamfers, H. J.; Meetsma, A.; Wiegers, G. A.; deBoer, J. L., The Crystal Structure of Some Rhenium and Technetium Dichalcogenides. *J. Alloys Compd.* **1996**, *241*, 34-39.
2. Wolverson, D.; Crampin, S.; Kazemi, A. S.; Ilie, A.; Bending, S. J., Raman Spectra of Monolayer, Few-Layer, and Bulk Rese2: An Anisotropic Layered Semiconductor. *ACS Nano* **2014**, *8*, 11154-11164.
3. Zhong, H.-X.; Gao, S.; Shi, J.-J.; Yang, L., Quasiparticle Band Gaps, Excitonic Effects, and Anisotropic Optical Properties of the Monolayer Distorted 1 T Diamond-Chain Structures Res 2 and Rese 2. *Phys. Rev. B* **2015**, *92*, 115438.
4. Baroni, S.; de Gironcoli, A.; Dal, C., Phonons and Related Crystal Properties from Density-Functional Perturbation Theory. *Rev. Mod. Phys.* **2001**, *73*, 515-562.
5. Paolo, G.; Stefano, B.; Nicola, B.; Matteo, C.; Roberto, C.; Carlo, C.; Davide, C.; Guido, L. C.; Matteo, C.; Ismaila, D.*, et al.*, Quantum Espresso: A Modular and Open-Source Software Project for Quantum Simulations of Materials. *J. Phys.: Condens. Matter* **2009**, *21*, 395502.
6. Perdew, J. P.; Wang, Y., Accurate and Simple Analytic Representation of the Electron-Gas Correlation Energy. *Phys. Rev. B* **1992**, *45*, 13244.
7. Monkhorst, H. J.; Pack, J. D., Special Points for Brillouin-Zone Integrations. *Phys. Rev. B* **1976**, *13*, 5188-5192.
8. Feng, Y.; Zhou, W.; Wang, Y.; Zhou, J.; Liu, E.; Fu, Y.; Ni, Z.; Wu, X.; Yuan, H.; Miao, F., Raman Vibrational Spectra of Bulk to Monolayer Res2 with Lower Symmetry. *arXiv preprint arXiv:1502.02835* **2015**.

4.4 Discussions

The focus of this paper was to show that there are two vertical orientations of the rhenium dichalcogenides and to demonstrate that Raman spectroscopy can be used to determine whether a flake is facing "up" or "down".

There is currently a lot of interest in producing monolayer transition metal dichalcogenides from CVD. In principle, both vertical orientations of the rhenium dichalcogenides are expected to grow. Since this paper was published there has been an investigation into growth of the rhenium dichalcogenides that utilises the angle-resolved polarised Raman spectroscopy methodology described in this chapter. Wu et al. produced ReS_2 by CVD and noticed flakes with multiple in-plane orientations grew [47].

There are a few interesting results in the supporting information which are only mentioned briefly in the main paper. These results are described in more detail here. Firstly, Fig. S7 shows the polarisation angle corresponding to the maximum intensity for a Raman mode as a function of thickness. This figure demonstrates that this polarisation angle does not vary with thickness for flakes that are bulk-like. All of the flakes that are used in the main paper are bulk crystals. Therefore, the thickness dependences do not need to be considered when determining the validity of the results. Secondly, an alternative method for finding the in-plane crystal orientation of the rhenium dichalcogenides is presented in the supporting information, Fig. S5. The excitons in the rhenium dichalcogenides have anisotropic properties. From photoreflectivity measurements an excitonic transition is observed. The energy of this transition changes periodically with the angle of linear polarisation. Using these photoreflectivity results it was possible to confirm the orientation of the flakes used in the main paper.

There are a number of ways to identify the in-plane orientation of a rhenium dichalcogenide flake including electronic transport and piezoreflectivity measurements. However, none of these techniques can identify the vertical orientation of ReS_2 or $ReSe_2$. Raman spectroscopy can determine whether a flake is facing "up" or "down" as well as the in-plane orientation. Moreover, Raman spectroscopy is non-invasive and quick, therefore it is hoped that the results

in this paper are easily reproducible.

Chapter 5

Lattice dynamics of the rhenium and technetium dichalcogenides

5.1 Preamble

In the previous chapter a way of identifying the vertical orientation of the rhenium dichalcogenides was discovered. Raman spectra of both ReS_2 and $ReSe_2$ were obtained in the process. Whilst looking at the vibrational modes of these materials a relationship was noticed: the frequency of the phonon modes of $ReSe_2$ are related to those of ReS_2 by a scaling factor. This chapter looks at this relationship by modelling the vibrations using a simple ball and spring model.

The aims of this paper are: (i) to give a detailed description of the lattice dynamics; (ii) to show there is a relationship between the frequencies of the Raman modes of the rhenium dichalcogenides; and (iii) to use this relationship to predict the frequency of the Raman modes of the technetium dichalcogenides.

The technetium dichalcogenides are relatively unexplored materials. Given that technetium is radioactive this is not surprising. These crystals could have applications in the medical industry and in disposal of nuclear waste [138]. It is hoped that the results in this

paper will aid future work on these materials.

The candidate was involved with the experimental measurements and interpretation of the results. Dr Wolverson conceived the idea for the paper and performed all the DFT calculations.

5.2 Statement of authorship and copyright information

<table>
<tr><td colspan="5">This declaration concerns the article entitled:</td></tr>
<tr><td colspan="5">Lattice dynamics of the rhenium and technetium dichalcogenides</td></tr>
<tr><td colspan="5">Publication status (tick one)</td></tr>
<tr><td>Draft manuscript</td><td>Submitted</td><td>In review</td><td>Accepted</td><td>Published</td></tr>
<tr><td></td><td></td><td></td><td></td><td>✓</td></tr>
<tr><td>Publication details (reference)</td><td colspan="4">D. Wolverson and L. S. Hart, “Lattice dynamics of the rhenium and technetium dichalcogenides,” Nanoscale Research Letters, vol. 11, no. 1, p. 250, 2016.</td></tr>
<tr><td>Candidate’s contribution to the paper (detailed, and also given as a percentage)</td><td colspan="4">The candidate contributed to the experimental measurements in this publication.
Formulation of ideas: 30%
Design of methodology: 0%
Experimental work: 50%
Computational work: 0%
Presentation of data in journal format: 0%</td></tr>
<tr><td>Statement from Candidate</td><td colspan="4">This paper reports on original research I conducted during the period of my Higher Degree by Research candidature.</td></tr>
<tr><td>Signature</td><td colspan="2"></td><td>Date</td><td>29/05/2018</td></tr>
</table>

Publication title: Lattice dynamics of the rhenium and technetium dichalcogenides

The pages of this thesis this paper spans are from 83 to 88.

Wolverson and Hart *Nanoscale Research Letters* (2016) 11:250
DOI 10.1186/s11671-016-1459-9

Nanoscale Research Letters

NANO EXPRESS Open Access

Lattice Dynamics of the Rhenium and Technetium Dichalcogenides

Daniel Wolverson* and Lewis S. Hart

Abstract

The rhenium and technetium dichalcogenides are layered van der Waals semiconductors which show a large number of Raman-active zone-centre phonon modes as a result of their unusually large unit cells and deviation from hexagonal symmetry. They thus offer the possibility of introducing in-plane anisotropy into composite heterostructures based on van der Waals materials, and Raman spectroscopy is generally used to determine their in-plane orientation. We show that first-principles calculations give a good description of the lattice dynamics of this family of materials and thus predict the zone-centre phonon frequencies and Raman activities of TcS_2. We consider the distribution of the phonon modes in frequency and their atomic displacements and give a unified understanding of the phonon frequencies and Raman spectra of ReS_2, TcS_2 and $ReSe_2$ in terms of the scaling of Raman frequency with the chalcogen mass.

Keywords: Rhenium sulphide, Technetium sulphide, Rhenium selenide, Transition metal dichalcogenide, Raman spectroscopy

Background

The transition metal dichalcogenides (TMD) have been known for a considerable time; the basic properties of about 40 members of the family were reviewed in 1969 [1]. However, the enormous fundamental scientific interest generated by the isolation of graphene, and the potentially disruptive technologies based on it, has stimulated interest in the wider family of two-dimensional layered van der Waals materials, to which the TMDs belong, with some 2500 publications on the archetypal family member MoS_2 alone in 2015. This level of activity is likely to be sustained as researchers develop the concept of devices based on multi-layered structures [2] in which dissimilar materials are stacked to achieve new functionalities, for instance, as light emitters [3, 4]. The key to this approach is the wide variety of behaviors that the TMDs exhibit, with metallic, semiconducting and superconducting phases, with properties that can be tuned by doping, and with novel types of coupling between spin and valley physics [5]. Here, we consider some of the less well-studied TMDs, based on Re and Tc, which are also attracting growing interest.

The rhenium and technetium dichalcogenides are layered van der Waals semiconductors with large unit cells due to their deviation from hexagonal symmetry towards a distorted 1T′ structure with space group $P\bar{1}$ in which the metal atoms group into parallelograms of four atoms [6–8]. They thus offer the unusual possibility of introducing a built-in planar anisotropy into composite heterostructures. Clearly, if their anisotropy is to be useful, one must be able to determine their in-plane orientation, and one promising method for this is Raman spectroscopy [9] since the large unit cell and lack of symmetry-related degeneracies leads to a large number (18) of Raman-active zone-centre phonon modes [9, 10].

It has already been shown that first-principles calculations can give a good description of the lattice dynamics of this family of materials [9, 10]; here, we compare predictions of the phonon frequencies of ReS_2, TcS_2 and $ReSe_2$. The zone-centre phonon modes show a common distribution in frequency, and we give a simple interpretation of this in terms of the atomic displacements, which leads to a unified understanding of the Raman spectra of ReS_2, TcS_2 and $ReSe_2$.

Little is known directly about crystalline TcS_2 though its structure is known [6, 8] and its electronic band structure has been predicted via density functional theory [11–13]. Technetium is not found naturally on Earth but only occurs as a by-product of nuclear fission of uranium-235; all its isotopes are unstable. The most readily available

*Correspondence: d.wolverson@bath.ac.uk
Department of Physics, University of Bath, Claverton Down, Bath, UK

isotope, ^{99m}Tc, is used in nuclear medicine as a radiopharmaceutical for labeling applications and is highly radioactive with a half-life of ∼6 h. In that context, it is sometimes produced in the form of a colloid with rhenium sulphide [14]. A longer-lived isotope is ^{99}Tc (half-life 2.13×10^5 years), and the planning of long-term control and storage for this radionuclide in a water-insoluble form is a priority. One proposed strategy involves sequestration of ^{99}Tc by the formation of its sulphides [15]. For both these applications, a knowledge of the Raman spectrum of TcS_2 should provide a useful analytic and diagnostic tool. We therefore also present a prediction of the Raman-active modes of TcS_2 and show how these relate to those of the analogous rhenium compounds.

Methods

Raman spectra in a backscattering geometry were obtained for the rhenium dichalcogenides using a Renishaw InVia Raman microscope with a ×50 objective lens giving a laser spot size of around 1 μm with, typically, 100 μW of 532-nm excitation; this microscope also provided the images of the samples in Fig. 1. The preparation (by micro-mechanical cleavage) and characterization of the $ReSe_2$ samples is described elsewhere [9], and the ReS_2 sample was prepared similarly. The $ReSe_2$ sample was a few unit cells in thickness whereas the ReS_2 sample was thicker; the differences between monolayer, few-layer and bulk Raman spectra of these materials are small [9, 10], being much less significant than in the case of MoS_2, for example, but have recently been shown to vary systematically with thickness, as do the interlayer modes [16–19].

Calculations of phonon frequencies were carried out using density functional perturbation theory [20] (DFPT) as implemented in the Quantum Espresso code [21]. Initial atomic coordinates were taken from earlier X-ray diffraction studies [7, 8] and were relaxed to reduce the atomic forces below 10^{-3} eV/Å. We have explored the use of norm-conserving pseudopotentials (NCPP) and also the projector augmented wave (PAW) method within both the local density (LDA) and generalized gradient (GGA) approximations; the resulting phonon frequencies given by these methods vary by less than ±2 % and are in good agreement with experiment, as found by other authors [10, 22]. The criteria for the convergence of the total energy with respect to kinetic energy cutoffs (here typically 680 eV) and k-point grid size (typically $6 \times 6 \times 6$ for 3D or $6 \times 6 \times 1$ for 2D) were discussed earlier [9]. Since the bulk unit cell of ReS_2 may be doubled along the out-of-plane axis [8] (that is, the unit cell may contain two layers), we calculated the phonon modes for an isolated monolayer with a single layer per supercell, so as to obtain the same number of modes and thus facilitate comparison. Since the differences between the phonon modes of monolayers and multiple layers are small for a transition metal dichalcogenide [10, 23], this procedure is justified. We note also that this question is not resolved, and one group saw no evidence of doubling of the unit cell for ReS_2 [24].

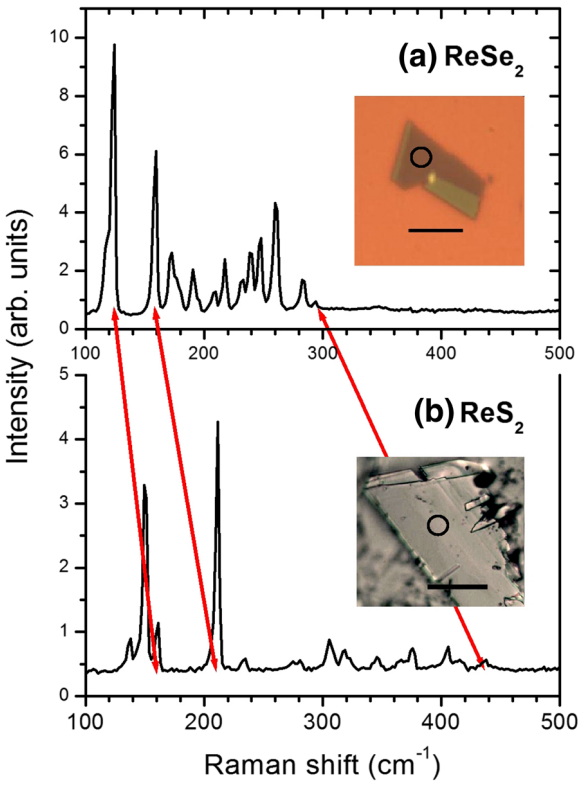

Fig. 1 The Raman spectra of thick **a** $ReSe_2$ and **b** ReS_2 flakes on a SiO_2/silicon substrate at room temperature; the *red arrows* link the peaks in the two materials corresponding to three phonon modes of significance for the present discussion. The *insets* show the the sample flakes used; the *circles* show the areas sampled and the *bars* indicate a scale of 20 μm

Results and Discussion

Figure 1 shows representative spectra of $ReSe_2$ and ReS_2; most of the 18 expected Raman-active A_g modes can be seen and, as has been described in detail before, the peak intensities are a function of the angle of orientation between the excitation laser polarization and the in-plane crystal axes [9, 18]. For these low-symmetry materials, all components of the Raman tensors for each A_g mode are non-zero, so that all Raman-active modes have a finite intensity at any angle, but the maximum intensities of different modes occur at different angles. The modes are densely spaced in frequency, but for both materials there is a noticeable "gap" in the spectrum between the 9th and 10th modes as indicated by the red

arrows in Fig. 1 (the higher red arrow links the positions of the highest-frequency Raman-active modes). This makes the two modes in either side of this gap easy to recognize even when weak; they are also found to be amongst the strongest modes in the Raman spectrum [25–28], and so have been a focus of other studies, where they are sometimes labelled as E_{2g}-like and A_{1g}-like by analogy with MoS_2 [10]; the E_{2g}-like modes are identified because they have significant in-plane displacements, which would twofold degenerate in hexagonal symmetry, and the modes that have displacements with components predominantly normal to the plane would be non-degenerate and are A_{1g}-like.

We focus on the two modes either side of the gap in the following. In Table 1, we give the frequencies of the Raman-active A_g modes nearest to the gap limits (these are the 8th or 9th and 10th or 11th modes), and the highest frequency Raman-active mode (35th or 36th), and compare to our experimental values. The indices at which A_u (IR) and A_g (Raman) modes occur are not exactly the same for the set of materials or even for the same material with different choices of (for example) pseudopotential, because close-lying A_u and A_g modes can sometimes exchange positions in the sequence. Note that calculations of the phonon dispersion of ReS_2 show that the gap is not a bandgap, in that it does not extend over the whole Brillouin zone [10], but it is an important and reproducible feature at the zone center. A recent calculation of the phonon dispersion of TcS_2 used a $2\times2\times1$ supercell, which yields a somewhat better accuracy in the phonon frequencies than the present approach but folds several modes into the range of the gap and so masks its existence in the zone-centre Raman modes [13].

To summarize the DFPT predictions, we plot in Fig. 2 the calculated frequencies of the 33 zone-centre vibrational modes (18 A_g and 15 A_u) in order of increasing frequency. The gap occurs in all three materials at the same position, between the 9th and 10th modes, emphasizing the strong similarity between these three compounds. The modes of the sulphides however cover a larger frequency range than those of the selenide, as one would expect based on the lower mass of sulphur (32.065) compared to selenium (78.96), and the frequencies of the Tc and Re sulphides are closely similar well above the gap but different

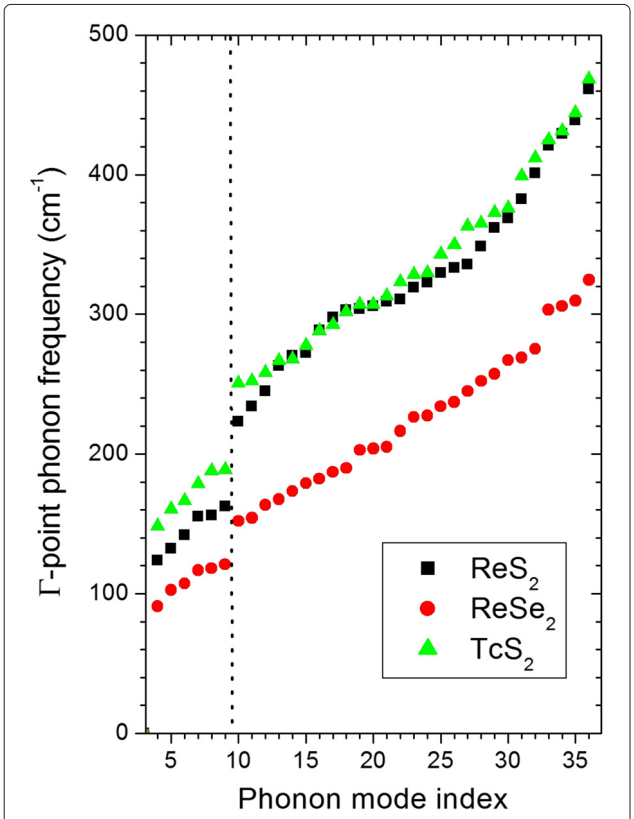

Fig. 2 The calculated zone-centre phonon modes of ReS_2 (*black squares*), $ReSe_2$ (*red circles*) and TcS_2 (*green triangles*) plotted in order of increasing frequency. All modes are either IR- or Raman-active. The *vertical dotted line* indicates the position in frequency of the gap in the phonon spectrum between modes 9 and 10. Note, modes 1–3 are zero-frequency rigid displacements of the unit cell and are not plotted

Table 1 Calculated zone-centre phonon frequencies of gap-edge and highest Raman-active modes (cm^{-1})

Mode	TcS_2 calc.	ReS_2 calc.	ReS_2 expt.	$ReSe_2$ calc.	$ReSe_2$ expt.
8 or 9	187.9	162.0	161.3	120.9	123.8
10 or 11	252.3	218.2	211.4	152.0	158.2
highest A_g	444.27	440.7	438.5	309.6	293.9

near and below it. This suggests a simple classification of the modes into those in which the displacements of the metal atoms are significant (mainly below the gap) and those where it is predominantly the chalcogens that are moving (mainly above the gap). By considering the predicted atomic displacements for all modes, we can see that this classification is justified, though there are too many modes to show an exhaustive set of displacements here. As an example, we show in Fig. 3 one view of the predicted displacements for the two gap-edge modes (top and bottom rows, respectively). The displacements of the metal atoms are approximately in-plane and are significant for the lower-frequency mode (8 or 9) but smaller for the higher mode; however, for the higher mode (10 or 11), there are significant out-of-plane displacements of the chalcogen atoms. Similar patterns of phonon displacements were presented earlier for ReS_2 [10] and, as Fig. 3 shows, the displacement patterns are broadly similar for all three compounds. Concentrating on the displacements of the chalcogen atoms, we can also see the in-plane character of mode 9 (E_{2g}-like) and the out-of-plane character

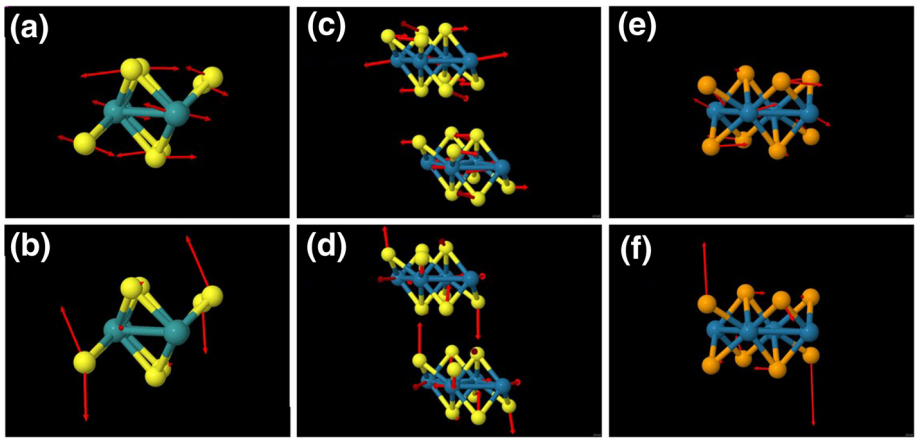

Fig. 3 The unit cell and phonon displacement vectors (*red*) for TcS_2 (**a**, **b**), ReS_2 (**c**, **d**) and $ReSe_2$ (**e**, **f**). *Top row*: displacements for the highest frequency mode (mode 9) below the gap and *bottom row*: displacements for the lowest frequency mode above the gap (mode 10). S, *yellow*; Se, *orange*; Tc, *turquoise*; Re, *blue*

of mode 10 (A_{1g}-like), in agreement with earlier work [10], and that this is valid also for TcS_2.

The similarity of the calculated displacements suggests that the interpretation above is reasonable. To test this further, we make the very simple assumption that, if interatomic "force constants" k are comparable, the frequencies of corresponding displacement patterns will scale with the square root of the mass m of the displaced atoms ($\omega \propto \sqrt{k/m}$). For the modes above the gap, this is the chalcogen mass, and therefore, we replot the calculated phonon frequencies in Fig. 4 (top panel) multiplied by $\sqrt{32.065} = 5.66$ (sulphides) and by $\sqrt{78.96} = 8.89$ (selenide). The effect of this scaling is dramatic; all three sets of phonon modes now almost coincide above the gap. We can also test the idea that the modes below the gap should scale with the square root of the reduced mass taking into account the metal ions (Fig. 4, bottom panel); the displacement patterns of Fig. 3 suggest that this will not be so successful, because both metal and chalcogen atoms are displaced significantly in the below gap modes. However, by comparison of Fig. 4 with Fig. 2, it is clear that the ReS_2 and TcS_2 modes 4–9 now lie closer together.

Finally, in Table 2, the calculated zone-centre phonon frequencies of TcS_2 are given, since these have not been presented elsewhere. We also give the predicted infrared and Raman activities of these modes, principally to identify the Raman-active modes of the set; it should be noted that the Raman activity given here is the one computed in Quantum Espresso and other packages and represents a specific experimental geometry and an average over all possible sample orientations, as given in Eq. (6) of Porezag et al. [29]. So it does not correspond to the experimental configuration for a cleaved flake supported on a substrate;

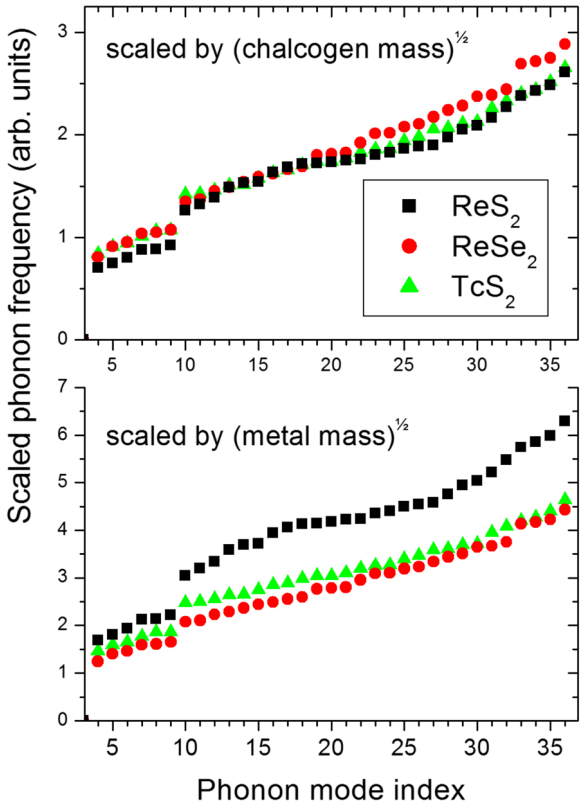

Fig. 4 The calculated zone-centre phonon modes of ReS_2 (*black squares*), $ReSe_2$ (*red circles*) and TcS_2 (*green triangles*) plotted in order of increasing frequency and scaled as discussed. *Top*: scaled by the square root of the chlacogen mass; *bottom*: scaled by the square root of the transition metal mass

Table 2 Calculated zone-centre phonon frequencies of TcS_2

Index	Frequency (cm^{-1})	IR Activity	Raman Activity
4	148.14	0.0000	428
5	160.38	0.0000	1016
6	166.40	0.0484	0
7	178.54	0.0000	3964
8	187.93	0.0000	900
9	188.51	0.1416	0
10	250.77	0.3533	0
11	252.28	0.0000	3967
12	258.18	0.3939	0
13	266.53	0.0000	505
14	267.82	1.2843	0
15	277.76	0.0000	806
16	287.93	0.3621	0
17	292.34	0.0000	4655
18	301.69	0.0000	2999
19	306.90	0.1785	0
20	307.26	0.0000	3179
21	312.84	0.0000	2761
22	323.05	1.6289	0
23	328.50	0.0000	1318
24	329.73	4.2948	0
25	343.13	2.9997	0
26	349.84	0.0000	4650
27	362.87	0.1476	0
28	365.12	0.0000	961
29	372.55	0.2031	0
30	375.97	0.0000	5592
31	399.18	0.3195	0
32	411.93	0.0000	6409
33	424.81	0.0000	19,660
35	444.27	0.0000	9908
36	468.57	3.9835	0

however, it would be relevant to the measurements on a polycrystalline or colloidal sample, the forms in which TcS_2 is likely to be available.

Conclusions

We have shown that a simple argument based on scaling by chalcogen mass allows one to understand the zone centre phonon modes of the rhenium and technetium dichalcogenides in a unified way and to understand qualitatively the distribution of the modes in frequency. This emphasizes the strong similarity between the members of this family of materials. The good agreement between the predicted and experimental frequencies of the Raman bands of the rhenium dichalcogenides gives us confidence in the behavior predicted for the technetium dichalcogenides, and this may be of use in monitoring the chemical composition of technetium-containing suspensions and colloids.

Competing Interests
The authors declare that they have no competing interests.

Authors' Contributions
DW conceived the project and carried out the computational work; both authors carried out the experimental work. Both authors read and approved the final manuscript.

Acknowledgements
This work was supported by the Centre for Graphene Science of the Universities of Bath and Exeter, funded by the EPSRC (UK) under grants EP/G036101 and EP/M0022188; LH is supported by the Bath/Bristol Centre for Doctoral Training in Condensed Matter Physics, grant EP/L015544. Computational work was performed on the University of Bath's High Performance Computing Facility. Data created during this research are freely available from the University of Bath data archive at DOI:10.15125/BATH-00130.

Received: 24 March 2016 Accepted: 2 May 2016
Published online: 13 May 2016

References

1. Wilson JA, Yoffe AD (1969) The transition metal dichalcogenides: discussion and interpretation of the observed optical, electrical and structural properties. Adv Phys 18(73):193–335
2. Geim AK, Grigorieva IV (2013) van der Waals heterostructures. Nature 499(7459):419–425
3. Wang X, Xia F (2015) van der Waals heterostructures: stacked 2D materials shed light. Nat Mater 14(3):264–265
4. Withers F, Del Pozo-Zamudio O, Schwarz S, Dufferwiel S, Walker PM, Godde T, Rooney AP, Gholinia A, Woods CR, Blake P, Haigh SJ, Watanabe K, Taniguchi T, Aleiner IL, Geim AK, Fal'ko VI, Tartakovskii AI, Novoselov KS (2015) WSe2 light-emitting tunneling transistors with enhanced brightness at room temperature. Nano Lett 15(12):8223–8228
5. Xiao D, Liu GB, Feng WX, Xu XD, Yao W (2012) Coupled spin and valley physics in monolayers of MoS_2 and other group-VI dichalcogenides. Phys Rev Lett 108(19):196802
6. Wildervanck JC, Jellinek F (1971) The dichalcogenides of technetium and rhenium. J Less-Common Metals 24(1):73–81
7. Murray HH, Kelty SP, Chianelli RR, Day CS (1994) Structure of rhenium disulfide. Inorg Chem 33(19):4418–4420
8. Lamfers HJ, Meetsma A, Wiegers GA, deBoer JL (1996) The crystal structure of some rhenium and technetium dichalcogenides. J Alloys Compounds 241(1-2):34–39
9. Wolverson D, Crampin S, Kazemi AS, Ilie A, Bending SJ (2014) Raman spectra of monolayer, few-layer, and bulk $ReSe_2$: an anisotropic layered semiconductor. Acs Nano 8(11):11154–11164
10. Tongay S, Sahin H, Ko C, Luce A, Fan W, Liu K, Zhou J, Huang YS, Ho CH, Yan J, Ogletree DF, Aloni S, Ji J, Li S, Li J, Peeters FM, Wu J (2014) Monolayer behaviour in bulk ReS_2 due to electronic and vibrational decoupling. Nat Commun 5:3252
11. Fang CM, Wiegers GA, Haas C, deGroot RA (1997) Electronic structures of ReS_2, $ReSe_2$ and Tcs_2 in the real and the hypothetical undistorted structures. J Phys Condensed Matter 9(21):4411–4424
12. Weck PF, Kim E, Czerwinski KR (2013) Semiconducting layered technetium dichalcogenides: insights from first-principles. Dalton Trans 42(43):15288–15295
13. Jiao Y, Zhou L, Ma F, Gao G, Kou L, Bell JM, Sanvito S, Du A (2016) Predicting single-layer technetium dichalcogenides (TcX_2, X= S, Se) with promising applications in photovoltaics and photocatalysis. ACS Appl Mater Interfaces 8(8):5385–5392
14. Koizumi M, Nomura E, Yamada Y, Takiguchil T, Tanaka K, Yoshimoto M, Makita M, Sakamoto G, Kasumi F, Ogata E (2003) Sentinel node detection

using 99mTc-rhenium sulphide colloid in breast cancer patients: evaluation of 1 day and 2 day protocols, and a dose-finding study. Nuclear Med Commun 24(6):663–670
15. Fan D, Anitori RP, Tebo BM, Tratnyek PG, Lezama Pacheco JS, Kukkadapu RK, Engelhard MH, Bowden ME, Kovarik L, Arey BW (2013) Reductive sequestration of pertechnetate by nano zerovalent iron transformed by abiotic sulfide. Environ Sci Technol 47(10):5302–5310
16. Nagler P, Plechinger G, Schüller C, Korn T (2016) Observation of anisotropic interlayer raman modes in few-layer ReS_2. physica status solidi (RRL)-Rapid Research Letters 10(2):185–189
17. Lorchat E, Froehlicher G, Berciaud S (2016) Splitting of interlayer shear modes and photon energy dependent anisotropic raman response in n-layer $ReSe_2$ and ReS_2. ACS Nano 10(2):2752–2760
18. Chenet DA, Aslan OB, Huang PY, Fan C, van der Zande AM, Heinz TF, Hone JC (2015) In-plane anisotropy in mono- and few-layer ReS_2 probed by Raman spectroscopy and scanning transmission electron microscopy. Nano Lett 15(9):5667–5672
19. He R, Yan JA, Yin Z, Ye Z, Ye G, Cheng J, Li J, Lui CH (2016) Coupling and stacking order of ReS_2 atomic layers revealed by ultralow-frequency raman spectroscopy. Nano Lett 16:1404–1409
20. Baroni S, de Gironcoli S, Dal Corso A, Giannozzi P (2001) Phonons and related crystal properties from density-functional perturbation theory. Rev Mod Phys 73:515–562
21. Giannozzi P, Baroni S, Bonini N, Calandra M, Car R, Cavazzoni C, Ceresoli D, Chiarotti GL, Cococcioni M, Dabo I, Corso AD, de Gironcoli S, Fabris S, Fratesi G, Gebauer R, Gerstmann U, Gougoussis C, Kokalj A, Lazzeri M, Martin-Samos L, Marzari N, Mauri F, Mazzarello R, Paolini S, Pasquarello A, Paulatto L, Sbraccia C, Scandolo S, Sclauzero G, Seitsonen AP, Smogunov A, Umari P, Wentzcovitch RM (2009) Quantum espresso: a modular and open-source software project for quantum simulations of materials. J Phys Condens Matter 21(39):395502
22. Feng Y, Zhou W, Wang Y, Zhou J, Liu E, Fu Y, Ni Z, Wu X, Yuan H, Miao F (2015) Raman vibrational spectra of bulk to monolayer ReS_2 with lower symmetry]. Phys Rev B 92:054110
23. Zhao H, Wu J, Zhong H, Guo Q, Wang X, Xia F, Yang L, Tan PH, Wang H (2015) Interlayer interactions in anisotropic atomically-thin rhenium diselenide. Nano Research 8(11):3651–3661
24. Ho CH, Huang YS, Liao PC, Tiong KK (1999) Crystal structure and band-edge transitions of ReS_2-xSex layered compounds. J Phys Chem Solids 60(11):1797–1804
25. Yang S, Tongay S, Yue Q, Li Y, Li B, Lu F (2014) High-performance few-layer mo-doped $ReSe_2$ nanosheet photodetectors. Sci Rep 4:5442
26. Taube A, Lapinska A, Judek J, Zdrojek M (2015) Temperature dependence of raman shifts in layered $ReSe_2$ and $SnSe_2$ semiconductor nanosheets. Appl Phys Lett 107(1):13105–13105
27. Yang S, Wang C, Sahin H, Chen H, Li Y, Li SS, Suslu A, Peeters FM, Liu Q, Li J, Tongay S (2015) Tuning the optical, magnetic, and electrical properties of $ReSe_2$ by nanoscale strain engineering. Nano Lett 15(3):1660–1666
28. Keyshar K, Gong Y, Ye G, Brunetto G, Zhou W, Cole DP, Hackenberg K, He Y, Machado L, Kabbani M, et al. (2015) Chemical vapor deposition of monolayer rhenium disulfide (ReS_2). Adv Mater 31:4640–4648
29. Porezag D, Pederson MR (1996) Infrared intensities and Raman-scattering activities within density-functional theory. Phys Rev B 54:7830–7836

5.4 Discussions

This paper shows that the frequencies of the ReS_2 Raman modes are related to the $ReSe_2$ modes by a scale factor. By using a simple ball and spring model it is shown that this scale factor depends only on the chalcogen mass. The rhenium dichalcogenides have a large number of Raman-active zone-centre phonon modes. There is therefore the possibility of testing the ball and spring model over a large dataset. This model works well for all 18 of the DFT calculated Raman modes.

We can have confidence in our DFT predictions of the phonon modes of the rhenium dichalcogenides because the calculated frequencies agree well with the peaks in the experimentally measured Raman spectra. However, there are no Raman spectra to compare to the calculated Raman modes of the technetium dichalcogenides. Using this simple ball and spring model an estimate of the frequencies of the phonon modes of technetium disulphide can be made and then used to compare to DFT calculations.

To make this model an assumption was made that the strength of the chemical bonds in $ReSe_2$ and ReS_2 are equivalent. Given the success of the model there is reason to believe this is a reasonable assumption and can be applied to the alloys of these materials, $ReSe_{2-x}S_x$. The frequency of the Raman modes are expected to increase linearly with sulphur dopant concentration, x, in this alloy. The reason for this is, by introducing the sulphur dopant the crystal is made lighter.

Research on the properties of the technetium dichalcogenides is currently active and recently a review on these materials was published citing the paper in this chapter [138].

Chapter 6

Identifying light impurities in transition metal dichalcogenides: the local vibrational modes of S and O in $ReSe_2$ and $MoSe_2$

6.1 Preamble

In the last two chapters a detailed description of the lattice dynamics of the rhenium dichalcogenides was given. These materials may have applications when doped. It therefore will be useful to have an understanding of the vibrational properties of the alloys of these crystals. This chapter investigates how the Raman modes of $ReSe_2$ are perturbed when impurities are introduced.

One of the applications for the rhenium dichalcogenides is as photodetectors [80]. The band gap of these materials can be tuned by introducing dopants, which is a desirable feature for the aforementioned application. The concentration of dopants within a crystal can be determined using Raman spectroscopy [115]. This paper will look at introducing low mass

impurities, such as sulphur, into $ReSe_2$. A sulphur atom can replace a selenium in one of four inequivalent positions of the unit cell of $ReSe_2$, as illustrated in Fig. 2 of the main paper. From Raman spectroscopy of $ReSe_{1.875}S_{0.125}$, four different Raman modes are observed that correspond to the local vibrational modes of sulphur impurities that are located in each of these four inequivalent positions. This paper also investigates low mass impurities in $MoSe_2$.

Wen et al. had previously looked at the Raman spectra of $ReSe_{2-x}S_x$ monolayers, for $0< x <2$. When looking at an alloy that corresponded to $ReSe_2$ that was lightly doped with sulphur, $ReSe_{1.8}S_{0.2}$, they were able to observe most of the phonon modes. However, the local sulphur vibrational modes in $ReSe_{1.8}S_{0.2}$ were not observed by this group [115]. It is these modes which are the focus of this chapter.

Furthermore, this paper shows how to make the signal from out-of-plane Raman modes more intense using an "edge-on" geometry. This technique is applicable to all 2D materials and it is hoped that it will be used on other crystals in the future.

The strength of the paper in this chapter is: (i) the frequencies of the local sulphur vibrational modes are predicted using DFT; (ii) these modes are observed at the frequencies expected; and (iii) the relationship of the intensities of the modes with the polarisation angle of light is derived.

In this publication the crystal axis a is defined to be along the rhenium chain.

The candidate designed the experiment, prepared the samples, undertook the measurements and analysed the results. The candidate was also involved with the writing of the manuscript. The DFT calculations were made by Mr Murkin, Dr Webb and Dr Wolverson, and the crystals were grown by Dr Lin.

6.2 Statement of authorship and copyright information

This declaration concerns the article entitled:				
Identifying light impurities in transition metal dichalcogenides: the local vibrational modes of S and O in $ReSe_2$ and $MoSe_2$				
Publication status (tick one)				
Draft manuscript	Submitted	In review	Accepted	Published
				✓
Publication details (reference)	L. S. Hart, J. L. Webb, S. Murkin, D. Wolverson, and D.-Y. Lin, "Identifying light impurities in transition metal dichalcogenides: the local vibrational modes of S and O in $ReSe_2$ and $MoSe_2$," *npj 2D Materials and Applications*, vol. 1, no. 1, p. 41, 2017.			
Candidate's contribution to the paper (detailed, and also given as a percentage)	The candidate predominantly executed the measurements and contributed considerably to the design of the experiment. Formulation of ideas: 70% Design of methodology: 70% Experimental work: 100% Computational work: 0% Presentation of data in journal format: 70%			
Statement from Candidate	This paper reports on original research I conducted during the period of my Higher Degree by Research candidature.			
Signature			Date	29/05/2018

Publication title: Identifying light impurities in transition metal dichalcogenides: the local vibrational modes of S and O in $ReSe_2$ and $MoSe_2$

The pages of this thesis this paper spans are from 94 to 117.

npj | 2D Materials and Applications

www.nature.com/npj2dmaterials

ARTICLE OPEN

Identifying light impurities in transition metal dichalcogenides: the local vibrational modes of S and O in $ReSe_2$ and $MoSe_2$

Lewis S. Hart[1], James L. Webb[1], Stephen Murkin[1], Daniel Wolverson[1] and Der-Yuh Lin[2]

The transition metal dichalcogenides provide a rich field for the study of two-dimensional materials, with metals, semiconductors, superconductors and charge density wave materials being known. Members of this family are typically hexagonal, but those based on rhenium ($ReSe_2$ and ReS_2) and their ternary alloys are attracting attention due to their triclinic structure and their resulting, strong in-plane anisotropy. Here, Raman spectra of dilute $ReSe_{2-x}S_x$ alloys containing low levels of sulfur ($x \leq 0.25$) were obtained in order to investigate the distribution of substitutional sulfur atoms over the non-equivalent chalcogen sites of the $ReSe_2$ unit cell. Four different Raman bands arising from the local vibrational modes of sulfur atoms were observed, corresponding to these four sites. One local vibrational mode has a substantially in-plane displacement of the sulfur atom, two are partially out-of-plane and one is completely out-of-plane. The interpretation of the experimental data is based on calculations of the lattice dynamics and non-resonant Raman tensors of a model alloy via density functional theory. For comparison, polarization-dependent Raman spectra of pure ReS_2 are also presented; a dramatic increase in the Raman cross-section is found for the out-of-plane modes when the excitation polarization is normal to the layers and the light propagates in the layer plane. A similar increase in cross-section is found experimentally for the local vibrational modes of sulfur in dilute $ReSe_{2-x}S_x$ alloys and is predicted for dilute sulfur-containing alloys based on $MoSe_2$. The analogous local vibrational modes of substitutional oxygen impurities in $ReSe_2$ were also investigated computationally.

npj 2D Materials and Applications (2017)1:41 ; doi:10.1038/s41699-017-0043-1

INTRODUCTION

Rhenium disulfide (ReS_2) and rhenium diselenide ($ReSe_2$) have attracted considerable recent attention because of their unusual structure. They belong to the transition metal dichalcogenide (TMD) family reported by Wilson and Yoffe[1] but, unlike more well-known TMDs, their structure is highly anisotropic in the layer plane and this is reflected in all their physical properties.[2–4] The class of van der Waals layered semiconductors with in-plane anisotropy is a topic of great current interest and, besides ReS_2 and $ReSe_2$, it includes black phosphorus,[5–7] GeS,[8] transition metal trichalcogenides[9] and Sb_2Se_3.[10] Proposed applications of ReX_2 (X = S, Se) include plasmonic materials,[11] polarization-sensitive photodetectors with high sensitivity,[12–15] inverters,[16] catalytic devices,[17,18] and few-layer field effect[19,20] or heterojunction[21] transistor structures.

The anisotropy of the ReX_2 compounds arises because, instead of adopting the octahedral (2H) or trigonal (1T) polymorphs typical of TMDs, they undergo a distortion to form a trigonal 1T′ polymorph.[22] The rhenium atoms are bonded to each other to form diamond-like chains, with the direction of the chains defined here as the *a* direction[23] (Supplementary Fig. S1). The inter-layer coupling is unusually weak compared to other TMDs,[24–26] though recent angle-resolved photoemission spectroscopy (ARPES) studies show that the band structure of the bulk ReX_2 family still has a three-dimensional character.[27–30] $ReSe_2$ is an indirect band gap semiconductor for all numbers of layers[31–34] with a band gap of 1.36 eV[34] whilst there is disagreement as to the nature of the band gap for bulk ReS_2, with some groups reporting an indirect band gap of 1.41 eV and others claiming a direct band gap of 1.5 eV.[31–36]

In this paper, we focus on the alloys of composition $ReSe_{2-x}S_x$. These alloys are of interest for two major reasons. Firstly, by changing the composition of sulfur within these alloys it is possible to tune the band gap,[32,37] as found for other TMD alloys[38] and alloys can be produced over the whole composition range, with the anisotropic trigonal structure being preserved throughout. Secondly, the more well-known TMDs exhibit strong spin-orbit splittings (SOS) in the valence band, with the magnitude of this SOS being 180 meV at the *K* and *K*′ points of the Brillouin zone for bulk MoS_2.[39] $ReSe_2$ has space group $p\bar{1}$, with inversion symmetry even for monolayers and thus its spin-orbit splitting is expected to be zero throughout the Brillouin zone. However, DFT calculations with and without the inclusion of spin-orbit coupling (SOC) show that the SOC of the rhenium *d* bands still perturbs the band structure of $ReSe_2$ significantly.[40] By introducing a sulfur impurity, the center of inversion is removed; as a result of this symmetry breaking, the host crystal field acts as an asymmetric potential and will lift the spin degeneracy at least locally.[41] Rhenium has a high atomic number (higher than molybdenum and tungsten) and thus the spin-orbit splitting is expected to develop rapidly with this symmetry breaking. However, a random distribution of impurity atoms may effectively restore inversion symmetry if the crystal field averages to zero. It is therefore essential to understand whether particular chalcogen sites are preferred and whether non-equilibrium growth techniques or

[1]Centre for Nanoscience and Nanotechnology, Department of Physics, University of Bath, Bath BA2 7AY, United Kingdom and [2]Department of Electronics Engineering, National Changhua University of Education, Changhua 50007, Taiwan
Correspondence: Lewis S. Hart (l.s.hart@bath.ac.uk) or Daniel Wolverson (d.wolverson@bath.ac.uk)

Received: 1 August 2017 Revised: 23 October 2017 Accepted: 31 October 2017
Published online: 22 November 2017

post-growth methods can be used to influence the distribution of sulfur over the possible sites.

Here, we address the key question of how to identify sulfur impurities on the different chalcogen sites in $ReSe_{2-x}S_x$ (Supplementary Fig. S1) and we show that this is possible via Raman spectroscopy. In addition, we consider whether substitutional oxygen impurities on chalcogen sites may be detected by the same method. Because all ternary alloys in the TMD family are of considerable potential interest, we consider also the case of sulfur impurities in a more representative and conventional TMD, $MoSe_2$, for which experimental Raman data already exist, identifying similarities in the structure of the Raman tensors for the impurity local vibrational modes (LVMs) in each case.

$ReSe_2$ has 4 formula units per unit cell (12 atoms) and 36 vibrational normal modes are therefore expected of which 33 have non-zero frequencies at the Brillouin zone center and 18 are Raman-active A_g species. Once the center of inversion is eliminated in a random alloy, all 33 modes become Raman-active in principle. There have been very few Raman studies of sulfur-doped $ReSe_2$[32,42] though Liu et al. reported the Raman spectrum of the ReSeS ternary alloy. However, with 33 modes spread over a range of 100–500 cm^{-1}, the analysis of this spectrum is not trivial.[25] Wen et al. reported Raman spectroscopy of $ReSe_{2-x}S_x$ alloy monolayers suggesting, for low sulfur compositions, that the higher frequency modes disappear.[43] It is shown here that these modes can be observed clearly in dilute alloy samples, and appropriate experimental geometries for this are identified.

RESULTS

Raman scattering of high-frequency vibrational modes of ReS_2

Before considering the alloys, we discuss a useful but uncommon experimental geometry in which the laser excitation propagates in the layer plane. Such “edge-on” spectroscopic experiments have identified out-of-plane vibrational modes in the Raman spectra of other 2D materials[44,45] and the technique can give a better understanding of photoluminescence selection rules.[46] This geometry is particularly valuable for identifying the highest-frequency vibrational mode of $ReSe_{2-x}S_x$; to show this, we consider first the case of pure ReS_2. The Brillouin zone-center phonon modes of ReS_2 include 18 Raman-active modes,[24,47] several of which can be seen in the experimental data of Fig. 1a. Their intensities I are determined by Raman tensors R according to

$$I \propto |e_i.R.e_s|^2, \quad (1)$$

where e_i and e_s are the incident and scattered light polarization vectors respectively. As in the case of $ReSe_2$, all Raman-active modes in ReS_2 belong to the non-degenerate symmetry species A_g with a Raman tensor R which has only non-zero elements and is given in Cartesian axes in the laboratory frame by

$$R = \begin{pmatrix} u & v & r \\ v & w & s \\ r & s & t \end{pmatrix}. \quad (2)$$

We used a polarization-insensitive spectrometer with no analyzer before the detector.[48] Then, with propagation of light along the normal to the layer plane (i.e, along z in the coordinate system of equation 2), the Raman scattering of intensity/a given mode is

$$I = u^2 \cos^2\theta + w^2 \sin^2\theta + v^2 + 2v(u+w)\sin\theta\cos\theta; \quad (3)$$

θ is the polarization angle of the excitation with respect to the in-plane x direction, here parallel to the rhenium chains and the crystallographic direction a as shown in Fig. 1b. The use of equation 3 to model the angle-dependent Raman scattering of bulk $ReSe_2$ and ReS_2 was tested previously.[48,49]

For ReS_2, the highest-frequency predicted mode (438 cm^{-1}) has a relatively large component t of the Raman tensor R as defined in equation 2 (atomic displacement patterns and numerical values of R are given in Supplementary Fig. S3). Therefore, when the incident light is polarized perpendicular to the layer plane, the 438 cm^{-1} Raman mode will be significantly more intense than for polarization in the layer plane. To test this, we use the "edge-on" geometry with the propagation of light along the crystallographic a direction, Fig. 1c. Analogous to equation 3, the intensity of each Raman band with unpolarized detection now follows the relationship

$$I = t^2 \cos^2\varphi + w^2 \sin^2\varphi + s^2 + 2s(w+t)\sin\varphi\cos\varphi \quad (4)$$

for excitation polarized parallel and perpendicular to the layer normal ($\varphi = 0°$ and $\varphi = 90°$ respectively). Figure 1a shows the resulting Raman spectra of ReS_2. The intensities of the lower-frequency modes (from 100 to 400 cm^{-1}) change by less than a factor of two between these two polarizations; however, the intensity of the 438 cm^{-1} mode increases very strikingly at $\varphi = 0°$ and fitting the experimental data gives an enhancement of

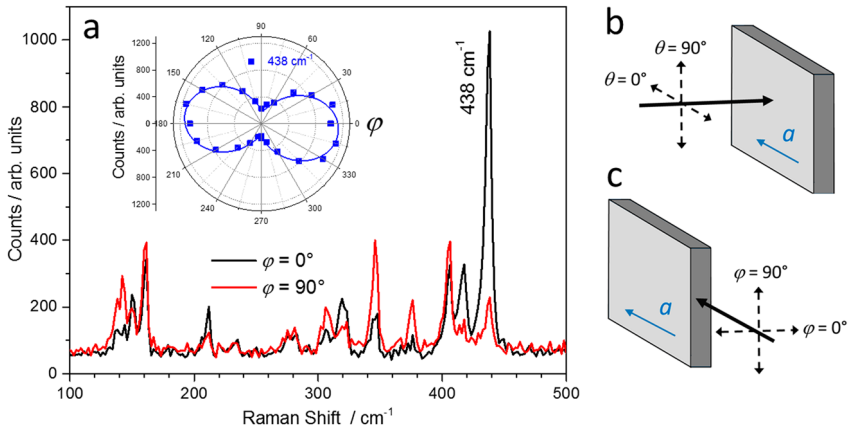

Fig. 1 Enhancement of the Raman signals of ReS_2 in the "edge-on" geometry. **a** Raman spectra of ReS_2 for light polarized parallel ($\varphi = 0°$, black line) and perpendicular ($\varphi = 90°$, red line) to the normal to the layers z with the direction of propagation along the crystallographic a direction (the direction of the rhenium chains). Inset: experimentally-determined (points) and fitted (solid line) dependence of the intensity of the 438 cm^{-1} Raman mode of ReS_2 on the angle φ in this geometry. **b** and **c** Schematic diagrams of the conventional and "edge-on" Raman experiments respectively; the solid black arrows represent the direction of the incident laser beam (back scattered light is detected in both cases) and the dashed arrows define the angles used to specify the laser polarization

$I_{para}/I_{perp} \sim 6$. The true enhancement in this geometry may be even larger, given that the thickness of the flake is comparable to the laser spot size, so that the effective volume of sample is lower in the "edge-on" geometry. The inset to Fig. 1a shows the measured dependence of the intensity of the 438 cm^{-1} Raman signal on the incident polarization angle φ. A fit using equation 4 has been added, showing the predicted two-fold symmetry. Supplementary Fig. S3 shows the simulated angle dependence based on the Raman tensor obtained from DFT calculations, which give a predicted value of $I_{para}/I_{perp} \sim 14$, in reasonable agreement with experiment. Finally, the inset of Fig. 1 shows that the polarization direction at maximum signal is inclined at $6 \pm 1°$ to the normal to the layers; this is also reproduced in the simulated angle-dependence (Supplementary Fig. S3).

These results demonstrate, firstly, that the calculated Raman tensors for the ReS_2 system (and the atomic displacements on which they depend) are reliable and, secondly, that the highest-frequency Raman active phonon of ReS_2 involves the out-of-plane motion of the sulfur atoms, with a strong Raman cross-section for excitation polarized normal to the layers. $ReSe_2$ shows very similar polarization-dependence for its highest frequency Raman-active mode with predicted and measured $I_{para}/I_{perp} \sim 12$ and 4, respectively (Supplementary Fig. S4).

Lattice dynamics of $ReSe_{1.75}S_{0.25}$: computational results

We now turn to alloys dilute enough to display a sulfur LVM in a $ReSe_2$ lattice; this facilitates experimental recognition of this mode, and provides an input for modified random element isodisplacement (MREI) models,[50,51] as applied recently to a range of TMDs.[52–55]

Figure 2 (inset) shows the eight chalcogen sites that substitutional sulfur may occupy in the $ReSe_2$ unit cell. The number of arrangements of r sulfur atoms on the n chalcogen sites of the primitive unit cell (considered as non-equivalent) is given by ${}^nC_r$ with $n = 8$. This number should be halved since each configuration has an experimentally-equivalent one related by inversion (Fig. 2, inset). Therefore, for one sulfur atom per unit cell, composition $ReSe_{1.75}S_{0.25}$, the sulfur atom can occupy one of only four distinct chalcogen positions; for two sulfur atoms per unit cell, there are 14 non-equivalent arrangements and for three there are 28. It is feasible but computationally expensive to calculate the phonon modes for all these configurations but at low sulfur concentrations this is unnecessary, as follows. Ho et al. concluded from X-ray studies that sulfur in bulk crystals grown by vapor transport is distributed homogenously. If we assume sulfur is randomly distributed with a constant occupation probability of $x/2$ for any chalcogen site, then by the binomial theorem, the probability of r sulfur atoms being within a single unit cell is $P(r) = {}^8C_r\ (1 - x/2)^{8-r}\ (x/2)^r$. Thus, for our experimental concentration of one sulfur per eight formula units, $x = 0.125$, $P(0) = 0.60$, $P(1) = 0.32$, $P(2) = 0.07$, and $P(m) < 0.01$ for all $m > 2$. Thus, the most probable unit cell configuration is pure $ReSe_2$ and only ~8% of unit cells contain more than one sulfur atom.

The lattice modes of $ReSe_{1.75}S_{0.25}$ were calculated via density functional perturbation theory (DFPT) and Fig. 2 summarizes the results: the frequencies up to the 29th mode are similar to those of $ReSe_2$[49] and are insensitive to the site occupied by sulfur (changes in frequencies vary by less than typical DFPT accuracy, ~2–3%). From the 30th mode upwards, the frequencies diverge from those of $ReSe_2$. The most dramatic change is seen at mode 36, which occurs at four remarkably different frequencies: 350, 390, 410 and 433 cm^{-1}, depending on the site occupied by the sulfur (Fig. 2, right). These frequencies cover a large enough range that Raman spectroscopy should be capable of identifying sulfur in all four sites, in contrast to the case of the binary compound ReSeS, where there are many possible unit cell configurations, so that its Raman bands overlap strongly. The Raman tensors associated with these modes are given in Supplementary Fig. S5, and we compare these to experiment later

Importantly, our LVM calculations are not significantly affected by the use of a small unit cell. We have calculated the frequencies of the phonon modes for a $2 \times 1 \times 1$ and a $2 \times 2 \times 1$ supercell, each containing one sulfur atom (compositions $ReSe_{1.825}S_{0.125}$ and $ReSe_{1.9375}S_{0.0625}$) and find the spread of high-frequency modes is similar to those calculated for $ReSe_{1.75}S_{0.25}$ (frequencies are tabulated in Supplementary Fig. S5, and compared graphically, Fig. S9). We do see small systematic differences in the frequencies of the spatially-extended phonons as the unit cell size changes (Supplementary Fig. S9) as expected since the net chalcogen mass in the supercell is changing.

An important observation is that the predicted frequency of the sulfur LVM at site D (433 cm^{-1}) is extremely close to the highest-

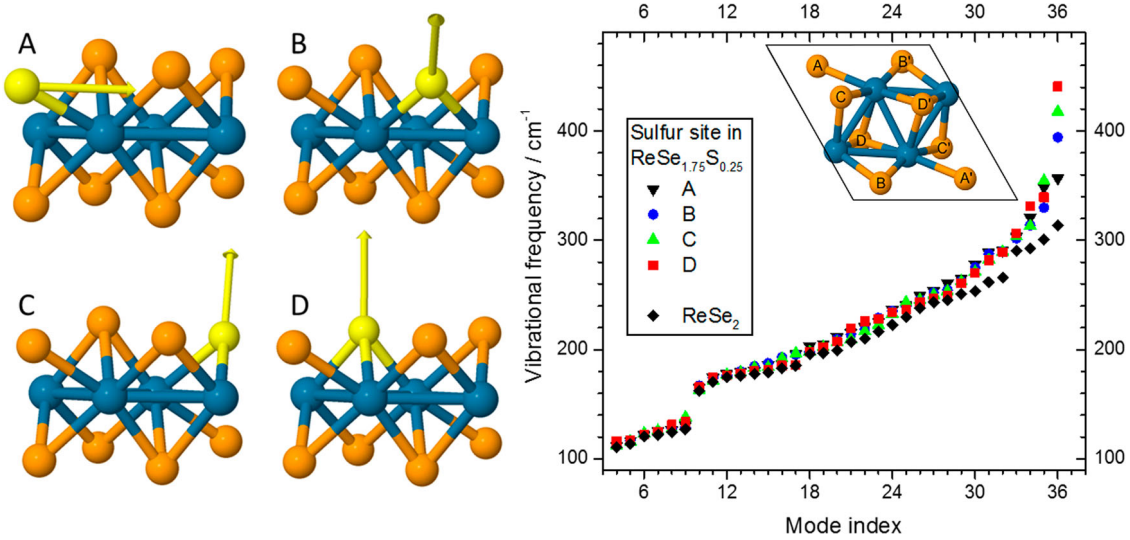

Fig. 2 Local vibrational modes of substitutional S in $ReSe_2$. Left: primitive unit cells of $ReSe_{1.75}S_{0.25}$ with a sulfur impurity placed in each of the non-equivalent positions A–D in turn. Yellow arrows show calculated displacements of the atoms in the highest-frequency LVM; those for A and D lie in the plane of the page. Right: calculated frequencies of the zone-center phonon modes (in order of increasing frequency) for a $ReSe_{1.75}S_{0.25}$ unit cell with a sulfur atom in each of the sites A–D; the phonon frequencies of $ReSe_2$ are plotted in the same way for comparison. The inset unit cell shows sites A–D viewed normal to the layer and inversion-related sites A′–D′ are also shown

frequency phonon mode of ReS_2 observed in the previous section (438 cm^{-1}). This is not a coincidence; the atomic displacements are related for both modes and predominantly involve the same chalcogen site D (compare Fig. 2 and Fig S1). This phonon branch in ReS_2 is essentially dispersionless; the calculated phonon dispersion for ReS_2[24] shows that the motions of sulfur atoms in neighboring unit cells are not strongly correlated, so that a large supercell is not required. Another way of demonstrating this is that the displacements of neighboring atoms tend to zero rapidly with distance from the sulfur atom, particularly for the D site (Supplementary Fig. S8) so that the high-frequency sulfur vibrational modes are localized and independent of concentration.

We conclude that the highest-frequency LVM of sulfur in $ReSe_2$ is related to the highest-frequency phonon mode of ReS_2 and its predicted frequency is the same to within the typical accuracy of DFPT calculations. Thus, the appearance of this mode in the Raman spectra of $ReSe_{2-x}S_x$ alloys is not evidence of ReS_2 phase segregation, but does indicate the presence of substitutional sulfur. Similar behavior is expected for light substitutional S (and O) impurities in other TMDs, as exemplified next by the case of $MoSe_2$.

Lattice dynamics of $MoSe_{2-x}S_x$: computational results

We now consider the related question of the LVM arising from sulfur as a light impurity in a more conventional, hexagonal TMD, choosing 2H-MoS_xSe_{2-x}, for which experimental Raman studies have been reported.[38,52] Here, only one chalcogen site exists in the primitive unit cell, and localized modes can be of both A or B (out-of-plane, non-degenerate) and E (in-plane, two-fold degenerate) symmetry types.[56] Our findings are summarized in Fig. 3; as in the case of $ReSe_2$, the highest-frequency mode involves an out-of-plane motion of the S impurity whilst other atomic displacements are small. Again, the largest deviation in frequency from the bulk modes of $MoSe_2$ is seen for the highest-frequency modes, though there are now four modes that are strongly distinguished from the host phonons. The highest-frequency sulfur-related mode is non-degenerate (type A), there is a nearly-degenerate pair of in-plane modes, and there is one lower-frequency non-degenerate mode. The highest-frequency sulfur mode is once more above the top of the $MoSe_2$ phonon dispersion, forming an out-of-plane LVM.

Experimental studies of 2H-MoS_xSe_{2-x} showed that the observed phonon frequencies can be described well by an MREI model from which the impurity (local) modes of sulfur in $MoSe_2$

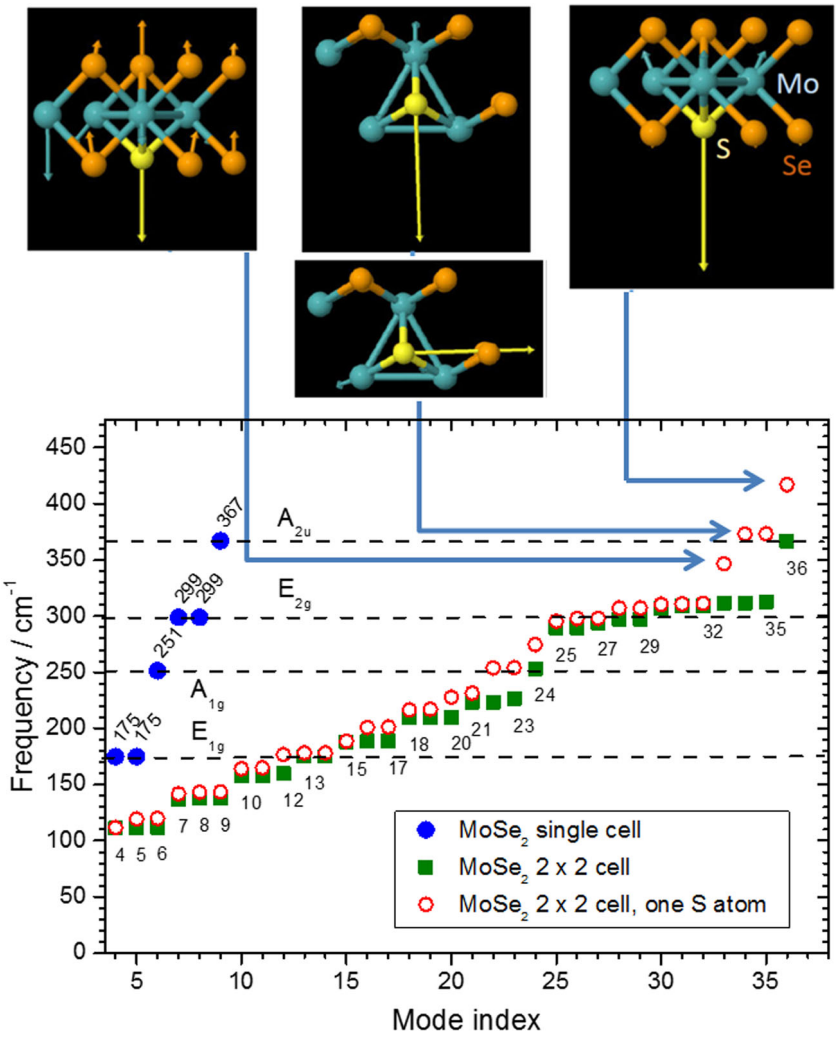

Fig. 3 Local vibrational modes of substitutional S in $MoSe_2$.Top: atomic displacements of the four highest-frequency vibrational modes of monolayer $MoSe_2$ containing one S impurity atom per 12-atom $2\times2\times1$ supercell ($MoSe_{1.75}S_{0.25}$), calculated via DFPT (vectors are scaled proportionately to the atomic displacement and are drawn for all atoms but some are too small to be seen). Bottom: vibrational frequencies calculated by DFPT for a single $MoSe_2$ unit cell, a $2\times2\times1$ $MoSe_2$ supercell, and a $2\times2\times1$ supercell with one Se atom replaced by S. The horizontal dashed lines indicate the symmetry species and the frequencies of the bulk $MoSe_2$ zone-center modes

(adjustable parameters in MREI) were inferred to have frequencies of 343 cm-1 (for the in-plane E_{2g} mode) and 391 cm-1 (A_{1g} mode). These values are in good agreement with those we obtain from DFPT as shown on Fig. 3, which are 367 and 417 cm^{-1} for the E-type modes (34,35) and A-type mode (36), respectively. The agreement is particularly good if we take into account the fact that our calculations for $MoSe_2$ systematically overestimate the phonon frequencies by about 5%, or ~16 cm^{-1} in this frequency range.

These modes were not observed unambiguously at low concentrations in the previous study, although there is some weak structure in the experimental spectra for $x = 0.2$ at around 350–360 cm^{-1} which strengthens and evolves towards the MoS_2 E_{2g} mode with increasing sulfur content.[52] A difficulty in backscattering experiments is that numerous overtone modes fall within the frequency range of the sulfur LVM, for example $E_{1g} + A_{1g}$ and E_{2g} + LA(M).[52] An experiment in the "edge-on" geometry may be able to resolve this. The calculated Raman tensors for modes 33–36 are given in Supplementary Fig. S14 and, for the highest-frequency LVM, *t* is ~17 times larger than the next largest component of the Raman tensor, so that its "edge-on" signal should be enhanced by up to $\sim 17^2 = 270$. This agrees qualitatively with data on vertically-aligned MoS_2 layers (for which the backscattering geometry is now "edge-on"), where the intensity of the A_{1g} mode at 408 cm^{-1} increased relative to that of the E_{2g} mode (383 cm^{-1}) in the "edge-on" geometry.[45]

Experimental Raman spectra of $ReSe_{1.875}S_{0.125}$

We now test the above predictions experimentally for a dilute alloy and compare to the pure binary materials, taking $ReSe_{1.875}S_{0.125}$ as a composition that is dilute enough for a true LVM to exist but concentrated enough that signals are easily detected. Measured Raman spectra of $ReSe_2$, $ReSe_{1.875}S_{0.125}$ and ReS_2 are shown in Fig. 4. We note first that we observe bands in the $ReSe_2$ spectrum which have not previously been reported (seen on the left of Fig. 4b). These lie between 320 and 360 cm^{-1} and do not correspond to first-order Raman-active modes of $ReSe_2$.[48] These bands are most probably due to overtones or combinations of phonons, as are known to be observed in some TMDs[57–59] though, owing to the large number of bands (36) in the phonon dispersion of $ReSe_2$, it is difficult to identify the exact branches giving rise to these overtones.

By comparing the alloy spectra to that of $ReSe_2$, we observe four peaks which can be attributed to the substitutional sulfur LVM, which we label A–D; the frequencies of these are shown in Table 1. Peak A is predicted from our DFPT calculations to be at 350 cm^{-1} and there is indeed a peak in the Raman spectra of the alloy near this position (345 cm^{-1}); however, this overlaps with a broad band in the $ReSe_2$ spectrum, and so it is not possible to attribute this peak unambiguously to a LVM. The other three Raman bands of the alloy, B–D, are expected from calculations of their Raman tensors (Supplementary Fig. S5) to be more intense than band A, and are observed in a region of the Raman spectra where there are no modes of the pure material (Fig. 4a, b), so their

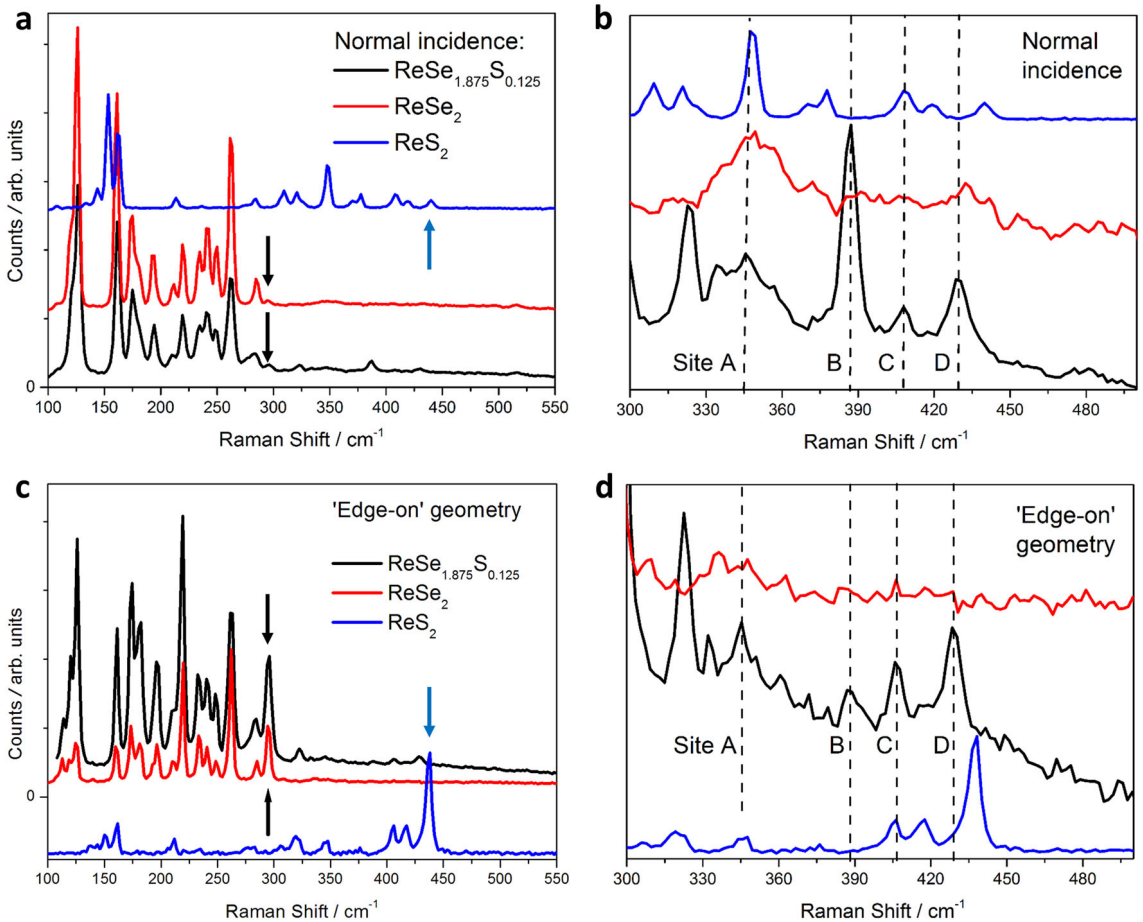

Fig. 4 Experimental Raman spectra of ReS_2, $ReSe_2$, and $ReSe_{1.875}S_{0.125}$. **a** Raman spectra for excitation normal to the layers and the incident polarization in-plane and perpendicular to the *a* direction; **b** Raman spectra as in **a** but showing the high frequency region on an expanded scale; **c** Raman spectra recorded using the "edge-on" geometry with the incident polarisation normal to the layers; **d** Raman spectra in the "edge-on" geometry as in **c** in the frequency region of the LVMs. Spectra are displaced vertically for clarity. Vertical arrows in **a** and **c** indicate the highest-frequency phonon modes of pure $ReSe_2$ (296 cm^{-1}) and ReS_2 (438 cm^{-1})

Table 1. Calculated and experimental frequencies for the highest-frequency Raman mode of substitutional sulfur impurities on the four non-equivalent sites A–D in $ReSe_2$ (Supplementary Fig. S1)

Sulfur site	Frequency (cm^{-1})			
	DFT, single cell (12 atoms) $ReSe_{1.75}S_{0.25}$	DFT, supercell doubled along *a* $ReSe_{1.875}S_{0.125}$	DFT, supercell doubled along *a, b* $ReSe_{1.9375}S_{0.0625}$	Experiment $ReSe_{1.875}S_{0.125}$
A	350	356	347	345*
B	390	396	386	386
C	410	416	417	408
D	433	438	437	429

The experimental band marked * coincides with an overtone Raman band of $ReSe_2$

identification is clear. There is also a strong peak at 322 cm^{-1}, close to the frequencies of the 34th and 35th alloy modes, which is particularly strong in this geometry. This mode almost certainly arises from the incorporation of sulfur since it is not seen in $ReSe_2$ but, because the 34th and 35th modes are so close-lying for the different sulfur sites A–D, it is difficult to assign this peak to a specific site or mode with certainty (Fig. 2 shows that these modes are closely grouped between 310 to 350 cm^{-1}). However, the agreement of these observations with DFPT results (shown in Table 1) to well within the limits of error (here, a ~3% overestimate) gives us confidence in the assignment of at least three of the four highest-frequency Raman bands to sulfur LVMs. Table 1 includes calculated results with three supercells, giving sulfur concentrations above, below and equal to the experimental concentration; the results do not vary significantly, as expected of an LVM. Supplementary Fig. S9 gives further comparison of the results for different supercells.

The highest-frequency vibration was predicted above to have a large out-of-plane displacement and a large element *t* in its Raman tensor (Eq. 2). Therefore this mode should give a strong signal for incident light polarized perpendicular to the layer. To test this, Raman spectra were obtained in the "edge-on" geometry as for ReS_2 above; results are shown in Fig. 4c, d). Using this geometry, these modes are clearly identifiable, demonstrating that this experimental technique allows for the identification of the highest vibrational mode of lightly sulfur doped $ReSe_2$. The Raman tensors, normal incidence θ-dependence and "edge-on" φ-dependence of bands A–D are presented in Supplementary Figs. S5, S6 and S7 and, as found experimentally, our calculations predict that the near in-plane mode B is stronger than band D for polarization in the layer plane and normal to *a* (see Fig. 4b, S7) whilst D is stronger than B for polarization normal to the layers (see Fig. 4d, S5).

One comment concerns the frequencies of the spatially extended phonon modes (below 300 cm^{-1}) for the alloy, Fig. 4a, c. Fitting of these spectra reveals that all bands shift to higher frequency by about 1% with respect to the corresponding modes of $ReSe_2$, confirming the incorporation of sulfur. This shift is known[43] and, over the whole composition range, is approximately linear. It is reproduced in our calculations and is principally accounted for by the mass difference of the chalcogen atoms[47] though, interestingly, the sulfur site plays a role; the calculated shifts of representative lattice modes (Supplementary Fig. S10) are dependent on the location of sulfur atom (Supplementary Figs. S11 and S12). We chose modes #9 and #10 (124.8 and 159.7 cm^{-1} in $ReSe_2$) for this, and we used their calculated atomic displacement patterns to identify the analogous modes in the alloy (Supplementary Fig. S10). Thus, interpolation between the binary compounds can only be used to infer composition from alloy mode frequencies if some assumption is made about the distribution of sulfur over sites A-D, such as the random distribution normally assumed in MREI.[52,55]

Oxygen impurities in $ReSe_2$: computational results

It is interesting to ask whether oxygen can form a similar substitutional impurity to sulfur, either via contamination during bulk crystal growth in silica or via atmospheric oxidation. Previous computational studies have investigated oxygen incorporated into ReX_2, either as substitutional atomic O[60] or molecular O_2, and have studied the resulting electronic band structure. Here, we investigate what vibrational modes would be expected from substitutional oxygen impurities; this is important for our understanding of the dilute alloys with sulfur in order to establish that the LVMs we observe are not due, for example, to native oxide at the surface. Figure 5 shows that the highest vibrational mode again has four frequencies corresponding to oxygen occupying sites A–D and these lie in a different range to those of sulfur. The displacement patterns are, however, similar to those of sulfur and the Raman tensors again have large components for polarization normal to the layers.

We annealed $ReSe_2$ in air with times and temperatures following a previous work,[61] where X-ray photoelectron spectroscopy (XPS) revealed surface oxidation. However, we did not observe any oxygen-related modes, presumably because Raman is not as surface-sensitive as XPS and the total quantity of oxide is small. There are reports of the Raman spectra of Re oxides, including partially oxidized ReS_2 containing ReO_3,[62] pure ReO_3[63,64] and Re_2O_7,[50,65,66] but neither of these oxides possesses a configuration analogous to the O atom bridging three Re atoms (site D) that provides the highest frequency LVM here, and neither shows strong Raman bands in the region of 450 to 650 cm^{-1}. It is not our aim here to investigate all configurations of oxygen in $ReSe_2$ and, certainly, more substantial structural modifications and also the role of chalcogen vacancies[67,68] should be considered.

In summary, the LVMs observed in dilute sulfur alloys cannot be attributed to oxygen, and we do not detect significant oxidation of micron-scale flakes even after annealing. However, our results provide a means of identifying the specific configuration of a substitutional oxygen atom on a $ReSe_2$ chalcogen site.

DISCUSSION

The frequencies of the LVMs of substitutional oxygen and sulfur atoms on the four non-equivalent chalcogen sites A–D of $ReSe_2$ have been identified computationally and those of sulfur have been verified experimentally. The four LVMs of sulfur have remarkably different frequencies, providing a means of monitoring the occupation of these sites in $ReSe_{2-x}S_x$ alloys. Analogous behavior has been predicted for the cases of oxygen impurities in $ReSe_2$ and sulfur impurities in $MoSe_2$. The relationship between the $ReSe_{2-x}S_x$ LVMs and the highest-frequency phonon mode of ReS_2 has also been demonstrated. The agreement between experimental and computational results extends also to the enhanced Raman scattering cross-sections when the experimental geometry is chosen so that the light propagates in the layer plane,

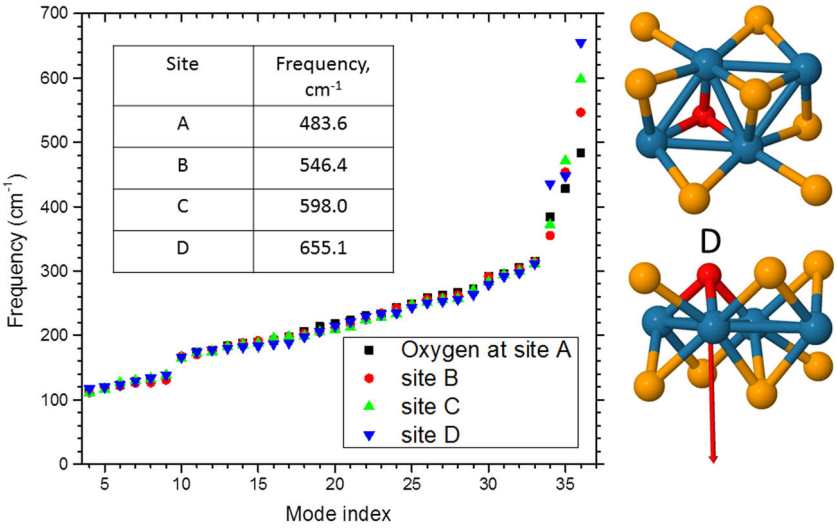

Fig. 5 Local vibrational modes of substitutional O in $ReSe_2$. Left: calculated phonon frequencies of the zone center modes for ReSe2 with one substitutional oxygen atom per unit cell, placed on each of the sites A–D. Right: The unit cell with oxygen at site D, viewed normal (top) and edge-on (bottom) to the layer; the red arrow indicates the displacement of the oxygen atom in the 655.1 cm^{-1} mode (index 36)

which is predicted from the non-resonant Raman tensors. This effect has been demonstrated in Raman spectroscopic studies of both ReS_2 and a dilute $ReSe_{2-x}S_x$ alloy and is predicted for $MoSe_{2-x}S_x$. In a dilute alloy sample, all four LVMs were observed, though the identification of the band arising from site A was tentative since it overlaps an overtone band of $ReSe_2$. The observation of all four predicted bands suggests a random distribution of substitutional sulfur impurities in bulk alloys grown by vapor transport.

METHODS

The ReS_2 crystals were supplied by 2D Semiconductors, CA, and have a purity of 99.9995% characterized by secondary ion mass spectroscopy. $ReSe_2$ samples were supplied by HQgraphene, Netherlands. A sulfur-containing $ReSe_2$ sample with a nominal composition of $ReSe_{1.9}S_{0.1}$ was grown via chemical vapor transport following the technique described by Huang et al.[69] and energy-dispersive X-ray analysis (EDX) indicated a sulfur concentration of ~1 sulfur atom per 8 formula units ($ReSe_{1.875}S_{0.125}$), consistent with the nominal composition. EDX results also suggested a small chalcogen deficiency in this sample, as found by Ho et al.[42] From EDX in imaging mode, a uniform distribution of sulfur was found on a macroscopic scale (Supplementary Fig. S13). Synchrotron-based ARPES studies of the binary compounds and associated XPS measurements[28,29] revealed no significant impurities except for native surface oxide for samples cleaved in air. Samples cleaved in UHV did not show the presence of oxygen. Thick (micron-scale) flakes of the rhenium dichalcogenides were exfoliated using blue Nitto tape and placed onto Gel-Film® WF 6.0 mil in order to perform out-of-plane Raman measurements. To explore the effects of oxygen incorporation, samples were annealed in air following the procedure reported for ReS_2,[61] but no changes were observed in the Raman spectra. Small changes in the lower-frequency ReS_2 phonons were reported after exposure to O_2 plasma,[62] but this was coupled with the appearance of ReO_3 in XPS spectra, rather than substitutional oxygen.

Raman spectra were recorded using a Renishaw inVia Raman microscope with a 50× lens with a spatial resolution of ~1 µm. A 532 nm laser was used for all the results presented here and the intensity was kept below 300 µW. No polarization analyzer was used; the detector was previously demonstrated to be polarization insensitive for Raman shifts below 500 cm^{-1}.[48] For "edge-on" measurements, thick flakes were exfoliated onto Gel-Pak film using micromechanical exfoliation. A single crystal flake partially suspended from the edge of the film was then identified (Supplementary Fig. S2) and the sample was placed upon a support to orient it easily. It would be challenging to observe the signals we discuss below in few-layer structures but suitable structures could be prepared by exfoliation onto graphite, supporting the resulting heterostructure in the same way as above.

Data presented here were obtained with a photon energy of 2.33 eV, above the excitonic band gaps of $ReSe_2$ and ReS_2 (1.3–1.6 eV, discussed above), so we do not expect strong resonant or optical interference effects in the Raman scattering. Spectra obtained using 1.58 eV excitation (above the band gap of $ReSe_2$ but close to that of ReS_2) did not show significant changes at room temperature though we observe clear resonant effects in the Raman scattering of bulk ReS_2 at low temperatures in the energy range of its excitonic transitions (results will be presented elsewhere).

Phonon modes of all materials were calculated using DFPT using a plane wave basis as implemented in the Quantum Espresso code.[70,71] Calculation of the non-resonant Raman tensors necessitated the use of norm-conserving pseudopotentials; the valence of Re was taken as 7 with atomic configuration $5d^5\ 6\ s^2$ and a local density approximation exchange-correlation functional was used of the PZ form.[72] Convergence of the total energy was checked with respect to the kinetic energy cutoff (60 Rydberg) and the Monkhorst-Pack *k*-point grid[73] for a 12-atom unit cell of (8 × 8 × 8). Bulk, three-dimensional material was simulated with three different cell sizes; 12-atoms, 24-atoms and 48-atoms, corresponding to the primitive unit cell and cells doubled along one or both in-plane dimensions. In each case, one S atom was introduced, with separate calculations being made for each of the four non-equivalent chalcogen positions. This gave effective concentrations of twice, equal to, and half of the experimental concentration of S. Initial unit cell parameters and atomic coordinates were taken from Lamfers et al.[23] or Ho et al.[32] with similar results; these were relaxed to obtain atomic forces less than 10^{-3} eV/Å. Similar criteria gave good agreement for the phonons of other TMDs.[74,75] The atomic configuration in the vicinity of the S impurity undergoes significant relaxation in order to shorten the Re-S bond distance (e.g, to 2.33 Å compared to a distance of 2.45 Å for a Se atom on the same site). The resulting structure is stable, with no imaginary phonon frequencies. Calculated frequencies were overestimated by up to 2–3% compared to experiment, typical of the above methodology, and confirmed by our experimental results for ReS_2 and $ReSe_2$. The crystal structures were drawn using the Jmol or XCrysden packages.[76]

It is beyond our present scope to consider the dependence of the phonons on layer thickness, but studies of ReS_2[77,78] and $ReSe_2$[48,79] as well as $Re(S,Se)_2$[43] show that the phonons shift only weakly in frequency with thickness down to the monolayer level. For the LVMs that are our focus, we find no significant dependence on unit cell size.

Data availability

Data that supports the findings of this study is available from the University of Bath archive (DOI: 10.15125/BATH-00373)

ACKNOWLEDGEMENTS

L.S.H. acknowledges the EPSRC Centre for Doctoral Training in Condensed Matter Physics (CDT-CMP, grant EP/L015544/1). J.L.W. was supported under EPSRC grant EP/M022188. DYL acknowledges support by the Ministry of Science and Technology Grant no. MOST 105-2112-M-018-006. Computational work was performed on the University of Bath's High Performance Computing Facility.

AUTHOR CONTRIBUTIONS

L.S.H. carried out the experimental Raman studies and was first author of the paper; S. M., J.L.W. and D.W. carried out the computational modeling and L.S.H., J.L.W., and D. W. analyzed the data. D.Y.L. grew and characterized the alloy crystals used and all authors discussed the results and contributed to the final version of the paper.

ADDITIONAL INFORMATION

Supplementary information accompanies the paper on the *npj 2D Materials and Applications* website (https://doi.org/10.1038/s41699-017-0043-1).

Competing interests: The authors declare that they have no competing financial interests.

Publisher's note: Springer Nature remains neutral with regard to jurisdictional claims in published maps and institutional affiliations.

REFERENCES

1. Wilson, J. A. & Yoffe, A. D. Transition metal dichalcogenides discussion and interpretation of observed optical, electrical and structural properties. *Adv. Phys.* **18**, 193–335 (1969).
2. Rahman, M., Davey, K. & Qiao, S. Z. Advent of 2D rhenium disulfide (ReS2): fundamentals to applications. *Adv. Funct. Mater.* **27**, 1606129 (2017).
3. Hafeez, M., Gan, L., Saleem Bhatti, A. & Zhai, T. Rhenium dichalcogenides (ReX_2, X = S or Se): an emerging class of TMDs family. *Mater. Chem. Front.* **1**, 1917–1932 (2017).
4. Ho, C. H., Huang, Y. S. & Tiong, K. K. In-plane anisotropy of the optical and electrical properties of ReS_2 and $ReSe_2$ layered crystals. *J. Alloys Compd.* **317**, 222–226 (2001).
5. Wang, Y. et al. Remarkable anisotropic phonon response in uniaxially strained few-layer black phosphorus. *Nano Research* **8**, 3944–3953 (2015).
6. Ribeiro, H. B. et al. Unusual angular dependence of the Raman response in black phosphorus. *ACS Nano* **9**, 4270–4276 (2015).
7. Qiao, J., Kong, X., Hu, Z.-X., Yang, F. & Ji, W. High-mobility transport anisotropy and linear dichroism in few-layer black phosphorus. *Nat. Commun.* **5**, 4475 (2014).
8. Tan, D. et al. Anisotropic optical and electronic properties of two-dimensional layered germanium sulfide. *Nano Research* **10**, 546–555 (2017).
9. Kong, W. et al. Angle resolved vibrational properties of anisotropic transition metal trichalcogenide nanosheets. *Nanoscale* **9**, 4175–4182 (2017).
10. Song, H. et al. Highly anisotropic Sb_2Se_3 nanosheets: gentle exfoliation from the bulk precursors possessing 1D crystal structure. *Adv. Mater.* **29**, 1700441 (2017).
11. Nemilentsau, A., Low, T. & Hanson, G. Anisotropic 2D materials for tunable hyperbolic plasmonics. *Phys. Rev. Lett.* **116**, 066804 (2016).
12. Yang, S. X. et al. High-performance few-layer Mo-doped $ReSe_2$ nanosheet photodetectors. *Sci. Rep.* **4**, 6 (2014).
13. Yang, S. X. et al. Layer-dependent electrical and optoelectronic responses of $ReSe_2$ nanosheet transistors. *Nanoscale* **6**, 7226–7231 (2014).
14. Liu, F. et al. Highly sensitive detection of polarized light using anisotropic 2D ReS_2. *Adv. Funct. Mater.* **26**, 1169–1177 (2016).
15. Liu, E. et al. High responsivity phototransistors based on few-layer ReS_2 for weak signal detection. *Adv. Funct. Mater.* **26**, 1938–1944 (2016).
16. Liu, E. et al. Integrated digital inverters based on two-dimensional anisotropic ReS_2 field-effect transistors. *Nat. Commun.* **6**, 6991 (2015).
17. Wang, L. et al. Layered rhenium sulfide on free-standing three-dimensional electrodes is highly catalytic for the hydrogen evolution reaction: Experimental and theoretical study. *Electrochem. Commun.* **63**, 39–43 (2016).
18. Qi, F. et al. Self-assembled chrysanthemum-like microspheres constructed by few-layer $ReSe_2$ nanosheets as a highly efficient and stable electrocatalyst for hydrogen evolution reaction. *Electrochim. Acta* **224**, 593–599 (2017).
19. Byunggil, K., Youngchan, K., Jeong Ho, C. & Changgu, L. Ambipolar transport based on CVD-synthesized $ReSe_2$. *2D Mater.* **4**, 025014 (2017).
20. Xu, K. et al. Sulfur vacancy activated field effect transistors based on ReS2 nanosheets. *Nanoscale* **7**, 15757–15762 (2015).
21. Wang, X. et al. Enhanced rectification, transport property and photocurrent generation of multilayer $ReSe_2/MoS_2$ p–n heterojunctions. *Nano Res.* **9**, 507–516 (2016).
22. Kertesz, M. & Hoffmann, R. Octahedral vs trigonal-prismatic coordination and clustering in transition-metal dichalcogenides. *J. Am. Chem. Soc.* **106**, 3453–3460 (1984).
23. Lamfers, H. J., Meetsma, A., Wiegers, G. A. & deBoer, J. L. The crystal structure of some rhenium and technetium dichalcogenides. *J. Alloys Compd.* **241**, 34–39 (1996).
24. Tongay, S. et al. Monolayer behaviour in bulk ReS_2 due to electronic and vibrational decoupling. *Nat. Commun.* **5**, 3252 (2014).
25. Liu, F. C. et al. Optoelectronic properties of atomically thin ReSSe with weak interlayer coupling. *Nanoscale* **8**, 5826–5834 (2016).
26. Zhao, H. et al. Interlayer interactions in anisotropic atomically thin rhenium diselenide. *Nano Res.* **8**, 3651–3661 (2015).
27. Biswas, D. et al. Narrow-band anisotropic electronic structure of ReS_2. *Phys. Rev. B* **96**, 085205 (2017).
28. Webb, J. L. et al. Electronic band structure of ReS_2 by high-resolution angle-resolved photoemission spectroscopy. *Phys. Rev. B* **96**, 115205 (2017).
29. Hart, L. S. et al. Electronic bandstructure and van der Waals coupling of $ReSe_2$ revealed by high-resolution angle-resolved photoemission spectroscopy. *Sci Rep* **7**, 5145 (2017).
30. Gehlmann, M. et al. Direct observation of the band gap transition in atomically thin ReS_2. *Nano Lett.* **17**, 5187–5192 (2017).
31. Tongay, S. et al. Monolayer behaviour in bulk ReS_2 due to electronic and vibrational decoupling. *Nat. Commun.* **5**, 3252 (2014).
32. Ho, C. H., Huang, Y. S., Liao, P. C. & Tiong, K. K. Crystal structure and band-edge transitions of $ReS_{2-x}Se_x$ layered compounds. *J. Phys. Chem. Solids* **60**, 1797–1804 (1999).
33. Huang, Y. S., Ho, C. H., Liao, P. C. & Tiong, K. K. Temperature dependent study of the band edge excitons of ReS_2 and $ReSe_2$. *J. Alloys Compd.* **262**, 92–96 (1997).
34. Ho, C. H., Huang, Y. S., Tiong, K. K. & Liao, P. C. Absorption-edge anisotropy in ReS_2 and $ReSe_2$ layered semiconductors. *Phys. Rev. B* **58**, 16130–16135 (1998).
35. Gutierrez-Lezama, I., Reddy, B. A., Ubrig, N. & Morpurgo, A. F. Electroluminescence from indirect band gap semiconductor ReS_2. *2d Mater.* **3**, 045016 (2016).
36. Aslan, O. B., Chenet, D. A., van der Zande, A. M., Hone, J. C. & Heinz, T. F. Linearly polarized excitons in single- and few-layer ReS_2 crystals. *ACS Photonics* **3**, 96–101 (2016).
37. Ho, C.-H., Liu, Z.-Z. & Lin, M.-H. Direct and indirect light emissions from layered $ReS_{2-x}Se_x$ ($0 \le x \le 2$). *Nanotechnology* **28**, 235203 (2017).
38. Mann, J. et al. 2-Dimensional transition metal dichalcogenides with tunable direct band gaps: $MoS_{2(1-x)}Se2_x$ monolayers. *Adv. Mater.* **26**, 1399–1404 (2014).
39. Yuan, H. T. et al. Evolution of the valley position in bulk transition-metal chalcogenides and their monolayer limit. *Nano. Lett.* **16**, 4738–4745 (2016).
40. Ho, C. H., Huang, Y. S., Chen, J. L., Dann, T. E. & Tiong, K. K. Electronic structure of ReS_2 and $ReSe_2$ from first-principles calculations, photoelectron spectroscopy, and electrolyte electroreflectance. *Phys. Rev. B* **60**, 15766–15771 (1999).
41. Dresselhaus, G. Spin-orbit coupling effects in zinc blende structures. *Phys. Rev.* **100**, 580–586 (1955).
42. Ho, C. H., Huang, Y. S., Liao, P. C. & Tiong, K. K. Piezoreflectance study of band-edge excitons of ReS2-xSex single crystals. *Phys. Rev. B* **58**, 12575–12578 (1998).
43. Wen, W. et al. Anisotropic spectroscopy and electrical properties of 2D $ReS_{2(1-x)}Se_{2x}$ alloys with distorted 1T structure. *Small.* **13**, 1603788 (2017).
44. Kawashima, Y. & Katagiri, G. Observation of the out-of-plane mode in the Raman scattering from the graphite edge plane. *Phys. Rev. B* **59**, 62–64 (1999).
45. Kong, D. S. et al. Synthesis of MoS_2 and $MoSe_2$ films with vertically aligned layers. *Nano. Lett.* **13**, 1341–1347 (2013).
46. Wang, G. et al. In-plane propagation of light in transition metal dichalcogenide monolayers: optical selection rules. *Phys. Rev. Lett.* **119**, 047401 (2017).
47. Wolverson, D. & Hart, L. S. Lattice dynamics of the rhenium and technetium dichalcogenides. *Nanoscale Res. Lett.* **11**, 1–6 (2016).
48. Wolverson, D., Crampin, S., Kazemi, A. S., Ilie, A. & Bending, S. J. Raman spectra of monolayer, few-layer, and bulk $ReSe_2$: An anisotropic layered semiconductor. *ACS Nano* **8**, 11154–11164 (2014).
49. Hart, L., Dale, S., Hoye, S., Webb, J. L. & Wolverson, D. Rhenium dichalcogenides: layered semiconductors with two vertical orientations. *Nano Lett.* **16**, 1381–1386 (2016).
50. Mitra, B., Gao, X., Wachs, I. E., Hirt, A. & Deo, G. Characterization of supported rhenium oxide catalysts: effect of loading, support and additives. *Phys. Chem. Chem. Phys.* **3**, 1144–1152 (2001).
51. Peterson, D., Petrou, A., Giriat, W., Ramdas, A. & Rodriguez, S. Raman scattering from the vibrational modes in $Zn_{1-x}Mn_xTe$. *Phys. Rev. B* **33**, 1160 (1986).
52. Jadczak, J. et al. Composition dependent lattice dynamics in $MoS_xSe_{(2-x)}$ alloys. *J. Appl. Phys.* **116**, 193505 (2014).
53. Dumcenco, D. O., Kobayashi, H., Liu, Z., Huang, Y. S. & Suenaga, K. Visualization and quantification of transition metal atomic mixing in $Mo_{1-x}W_xS_2$ single layers. *Nat. Commun.* **4**, 1351 (2013).

54. Chanchal & Garg, A. K. MREI-model calculations for layered mixed crystals of the series $HfS_{2-x}Te_x$ (0 < = x < = 2). *Indian J. Pure Appl. Phys.* **46**, 330–333 (2008).
55. Chanchal & Garg, A. K. MREI-model calculations of Raman-active modes in layered mixed crystals TiS2-xSex (0 < = x < = 2). *J. Raman Spectrosc.* **39**, 115–118 (2008).
56. Sekine, T., Izumi, M., Nakashizu, T., Uchinokura, K. & Matsuura, E. Raman scattering and infrared reflectance in 2H-MoSe2. *J. Phys. Soc. Jpn.* **49**, 1069–1077 (1980).
57. Mitioglu, A. et al. Second-order resonant Raman scattering in single-layer tungsten disulfide WS 2. *Phys. Rev. B* **89**, 245442 (2014).
58. Pimenta, M. A., del Corro, E., Carvalho, B. R., Fantini, C. & Malard, L. M. Comparative study of Raman spectroscopy in graphene and MoS_2-type transition metal dichalcogenides. *Acc. Chem. Res.* **48**, 41–47 (2014).
59. Lee, J.-U., Park, J., Son, Y.-W. & Cheong, H. Anomalous excitonic resonance Raman effects in few-layered MoS_2. *Nanoscale* **7**, 3229–3236 (2015).
60. Cakir, D., Sahin, H. & Peeters, F. M. Doping of rhenium disulfide monolayers: a systematic first principles study. *Phys. Chem. Chem. Phys.* **16**, 16771–16779 (2014).
61. Davis, S. Photoemission studies of rhenium disulfide oxidation: Altered core-level structure and reactivity of defect sites. *Catal. Lett.* **2**, 1–7 (1989).
62. Shim, J. et al. High-performance 2D rhenium disulfide (ReS_2) transistors and photodetectors by oxygen plasma treatment. *Adv. Mater.* **28**, 6985–6992 (2016).
63. Stachiotti, M., Corà, F., Catlow, C. & Rodriguez, C. First-principles investigation of ReO_3 and related oxides. *Phys. Rev. B* **55**, 7508 (1997).
64. Purans, J., Purans, A., Kuzmin, E., Cazzanelli, G. & Mariotto Disorder-induced Raman scattering in rhenium trioxide (ReO_3). *J. Phys. Condens. Matter.* **19**, 226206 (2007).
65. Beattie, I. R. & Ozin, G. A. Vibrational spectrum of gaseous, liquid, and solid Re_2O_7. *J. Chem. Soc. A*, 2615–2619, (1969).
66. Lacheen, H. S., Cordeiro, P. J. & Iglesia, E. Isolation of rhenium and ReOx species within ZSM5 channels and their catalytic function in the activation of alkanes and alkanols. *Chem. Eur. J.* **13**, 3048–3057 (2007).
67. Davis, S. & Carver, J. Oxygen chemisorption at defect sites in MoS_2 and ReS_2 basal plane surfaces. *Appl. Surf. Sci.* **20**, 193–198 (1984).
68. KC, S., Longo, R. C., Wallace, R. M. & Cho, K. Surface oxidation energetics and kinetics on MoS_2 monolayer. *J. Appl. Phys.* **117**, 135301 (2015).
69. Huang, T. P., Lin, D. Y., Kao, Y. C., Wu, J. D. & Huang, Y. S. Polarized thermoreflectance and reflectance study of ReS_2 and ReS_2:Au single crystals. *Jpn. J. Appl. Phys.* **50**, 04DH17 (2011).
70. Giannozzi, P. et al. QUANTUM ESPRESSO: a modular and open-source software project for quantum simulations of materials. *J. Phys. Condens. Matter* **21**, 395502 (2009).
71. Lazzeri, M. & Mauri, F. First-principles calculation of vibrational raman spectra in large systems: signature of small rings in crystalline SiO_2. *Phys. Rev. Lett.* **90**, 036401 (2003).
72. Perdew, J. P. & Zunger, A. Self-interaction correction to density-functional approximations for many-electron systems. *Phys. Rev. B* **23**, 5048–5079 (1981).
73. Monkhorst, H. J. & Pack, J. D. Special points for Brillouin-zone integrations. *Phys. Rev. B* **13**, 5188–5192 (1976).
74. Rice, C. et al. Raman-scattering measurements and first-principles calculations of strain-induced phonon shifts in monolayer MoS_2. *Phys. Rev. B* **87**, 081307 (2013).
75. Wang, F. et al. Strain-induced phonon shifts in tungsten disulfide nanoplatelets and nanotubes. *2D Mater.* **4**, 015007 (2016).
76. Kokalj, A. Computer graphics and graphical user interfaces as tools in simulations of matter at the atomic scale. *Comput. Mater. Sci.* **28**, 155–168 (2003).
77. Chenet, D. A. et al. In-plane anisotropy in mono- and few-layer ReS_2 probed by raman spectroscopy and scanning transmission electron microscopy. *Nano. Lett.* **15**, 5667–5672 (2015).
78. McCreary, A. et al. Intricate resonant raman response in anisotropic ReS_2. *Nano Lett.* **17**, 5897 (2017).
79. Lorchat, E., Froehlicher, G. & Berciaud, S. Splitting of interlayer shear modes and photon energy dependent anisotropic raman response in n-layer $ReSe_2$ and ReS_2. *ACS Nano* **10**, 2752–2760 (2016).

Identifying light impurities in transition metal dichalcogenides: the local vibrational modes of S and O in $ReSe_2$ and $MoSe_2$.

Supplementary material

Lewis S. Hart[1], James L. Webb[1], Stephen Murkin[1], Daniel Wolverson[1] and Der-Yuh Lin[2]

[1] Centre for Nanoscience and Nanotechnology, Department of Physics, University of Bath, Bath BA2 7AY, United Kingdom.

[2] Department of Electronics Engineering, National Changhua University of Education, Changhua 50007, Taiwan

Email: l.s.hart@bath.ac.uk

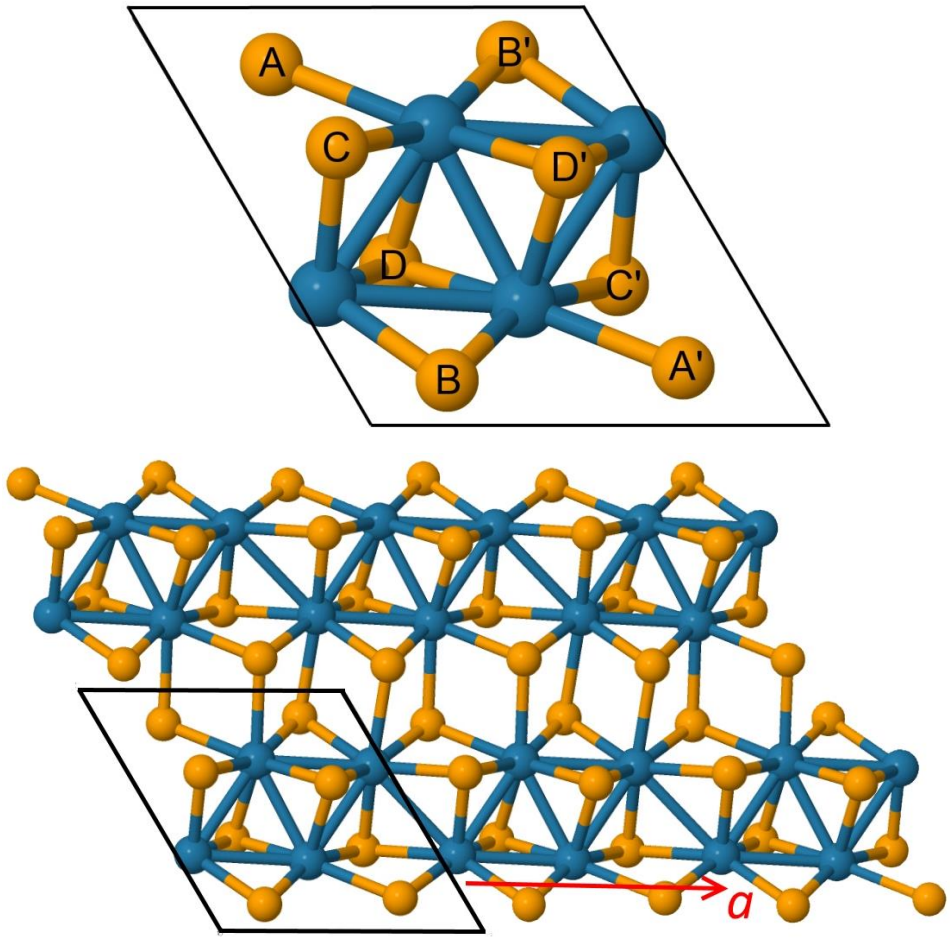

Figure S1 Top: Guide to the labelling of the non-equivalent chalcogen sites (orange) in $ReSe_2$: this appears also in the main text, Figure 2, and is reproduced here for convenience. Rhenium atoms are blue here. Bottom: View of a single layer from above (along the normal to the layer) showing the 2D unit cell defined by the in-plane *a* and *b* axes and the definition of the *a* axis along the Re chains.

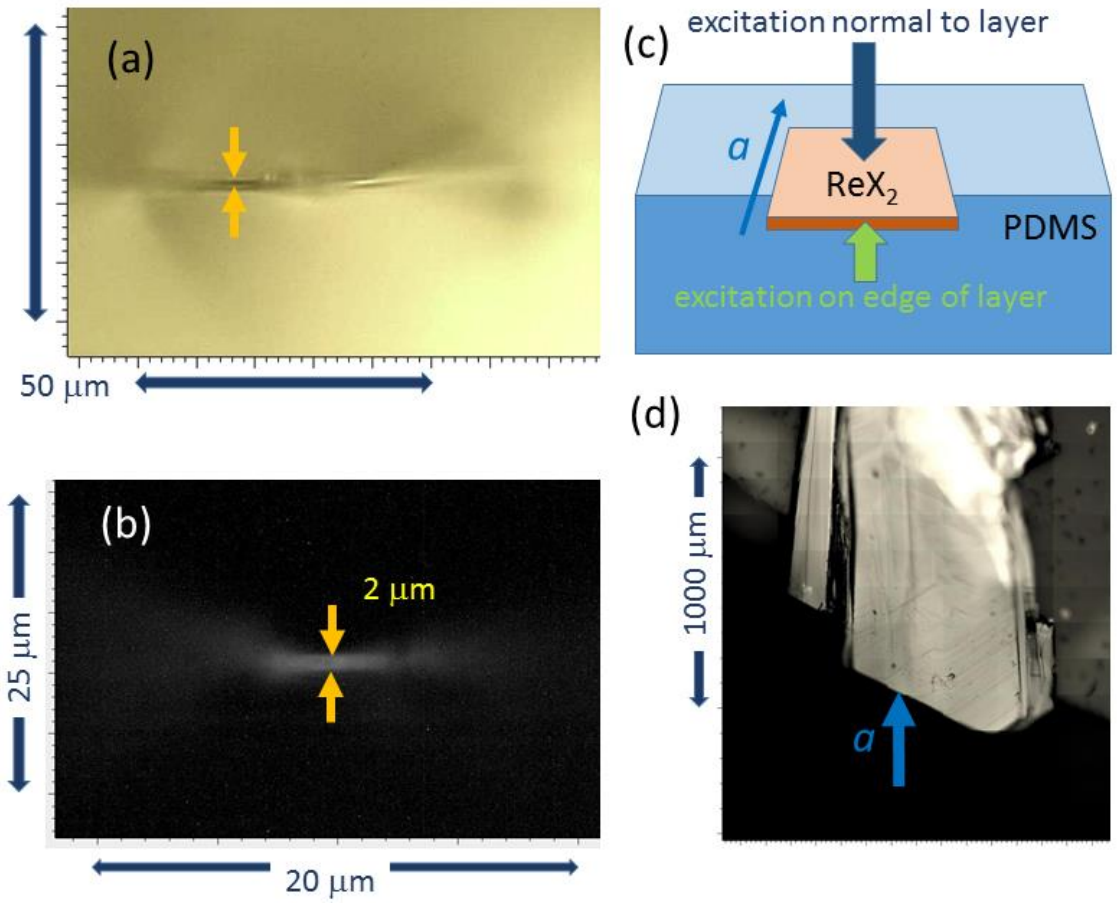

Figure S2 (a) and (b) Views of the edge of a typical flake, recorded with the camera of the Raman microscope with 50× and 100× objectives respectively, showing (yellow arrows) the flake thicknesses, which were typically 0.5 to 2 µm. The flake projects far enough forward of the supporting PDMS that the substrate and most of the flake are out of focus in these images.

(c) Schematic perspective view of the assembly for the edge-on measurements, showing how the ReX_2 flake is transferred to the edge of a PDMS block and projects from the face of the block.

(d) View of an actual flake looking down on the flake and substrate, showing the dominant cleavage along the crystallographic *a* and *b* directions. The blue arrow points in the direction of the *a* axis and also the direction of the excitation in the 'edge-on' experiment. This orientation was confirmed by polarised Raman measurements using normal incidence, the procedure for which has been discussed in several recent publications cited in the main text.

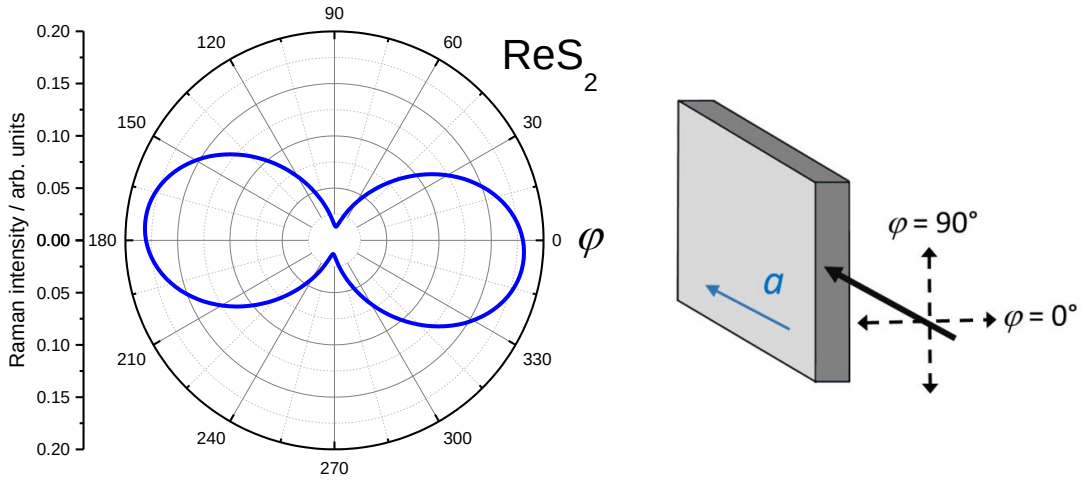

Figure S3. Simulated dependence of the intensity of the highest-frequency Raman-active A_g mode of ReS_2 (experimental Raman shift 438 cm^{-1}) on polarization angle φ defined in the schematic diagram on the right and in the main text, using equation 4 and the Raman tensor for mode 35 below. The assumed geometry is the 'edge-on' configuration in which the light propagates in the layer plane along the crystallographic *a* axis and $\varphi = 0^{\circ}$ corresponds to polarization perpendicular to the plane. The calculated atomic displacement patterns below show that the two inversion-related sulfur atoms bridging a closely-bonded triangle of rhenium atoms (we refer to these positions as site D) have the largest displacements in these modes; the two modes form a pair which are even and odd with respect to inversion symmetry and are Raman- and IR-active respectively.

ReS_2 A_g mode #35, 451 cm^{-1}: Raman tensor (arb. units)		
-0.21602	-0.00148	-0.01018
-0.00148	-0.11774	+0.03043
-0.01018	+0.03043	-0.42344
ReS_2 A_u mode #36, 463 cm^{-1}: Raman tensor (arb. units)		
0.0	0.0	0.0
0.0	0.0	0.0
0.0	0.0	0.0

A_g mode, #35:

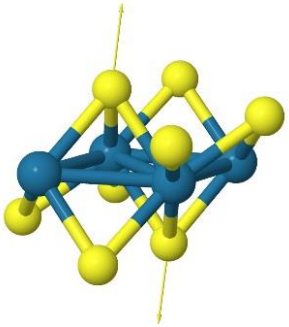

A_u mode, #36:

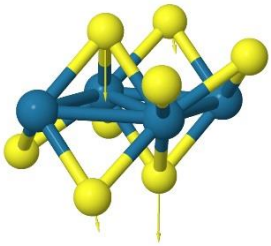

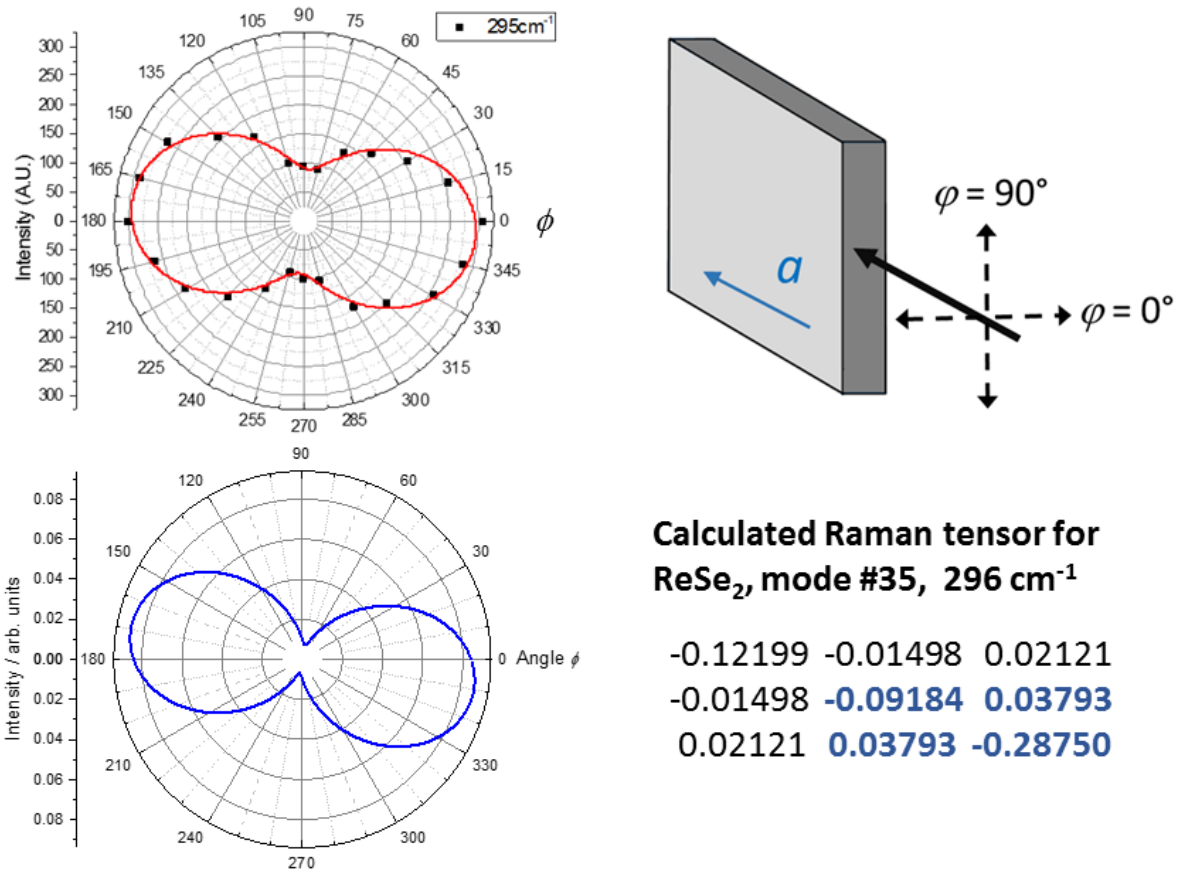

Figure S4. Dependence of the intensity of the highest-frequency Raman-active A_g mode of $ReSe_2$ (number #35, experimental Raman shift 295 cm^{-1}) on the polarization angle φ defined in the schematic diagram, top right. The polar plot, top left, shows experimental data (points) and a fit to them using equation 4 of the main text (red solid line).

The polar plot (bottom left) shows a simulation of the angle-dependence of the same mode using the calculated Raman tensor for this more (table, bottom right; the relevant components *w*, *s*, and *t* of the Raman tensor are in bold, blue). The simulated angle-dependence shows a good agreement with the experimental data, in particular reproducing the polarization direction of maximum intensity to within ~7°, confirming that $ReSe_2$ shows similar behavior to that observed in ReS_2 (Figure 1 of the main text).

$ReSe_{1.75}S_{0.25}$, local vibrational mode #36, sites A-D, edge-on

$ReSe_2$:S calculated Raman tensors and frequencies for mode #36					
Site A	**350 cm^{-1} (356, 347)**		**Site C**	**410 cm^{-1} (416, 417)**	
0.06618	-0.06114	-0.01547	-0.10243	0.06700	0.04700
-0.06114	0.03348	0.02275	0.06700	-0.09500	-0.02737
-0.01547	0.02377	**-0.00579**	0.04700	-0.02737	**-0.11485**
Site B	**390 cm^{-1} (396, 386)**		**Site D**	**433 cm^{-1} (438, 437)**	
0.04199	0.01875	-0.01749	0.11419	0.06931	0.05725
0.01875	0.21094	-0.12298	0.06931	-0.02943	-0.02794
-0.01749	-0.12298	**0.08982**	0.05725	-0.02794	**-0.21023**

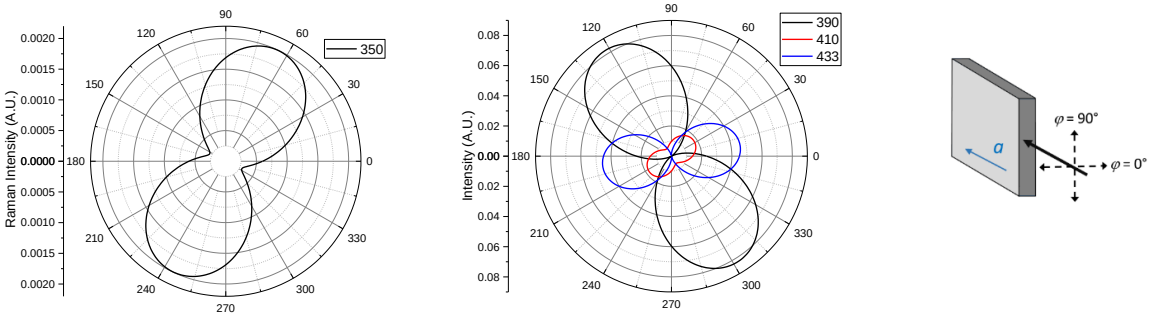

Figure S5. Top: Raman tensors (calculated using density functional theory) of the highest-frequency local vibrational modes (LVM) of $ReSe_{1.75}S_{0.25}$ with sulfur placed at each of the four inequivalent sites in the unit cell, A-D. The calculations of the Raman tensors used a single unit cell. For comparison, the pairs of frequency values in brackets (in blue) were obtained using firstly a 2×1×1 and secondly a 2×2×1 supercell with one S atom per supercell.

Bottom: angle-dependent polar plots based on these Raman tensors using equation 4 of the main text for these four modes, with $\varphi = 0^\circ$ corresponding to polarization perpendicular to the layer plane and the light propagation in the *a* direction, (the direction of the rhenium chains). The lowest-frequency LVM (for sulfur on site A, left panel) is plotted on separate axes since it is very weak; it was not observed experimentally. As discussed in the text, the out-of-plane mode due to sulfur on site D (blue) gives strongest Raman scattering for light polarized normal to the layer, $\varphi = 0^\circ$.

$ReSe_{1.875}S_{0.125}$, experimental local vibrational modes, edge-on

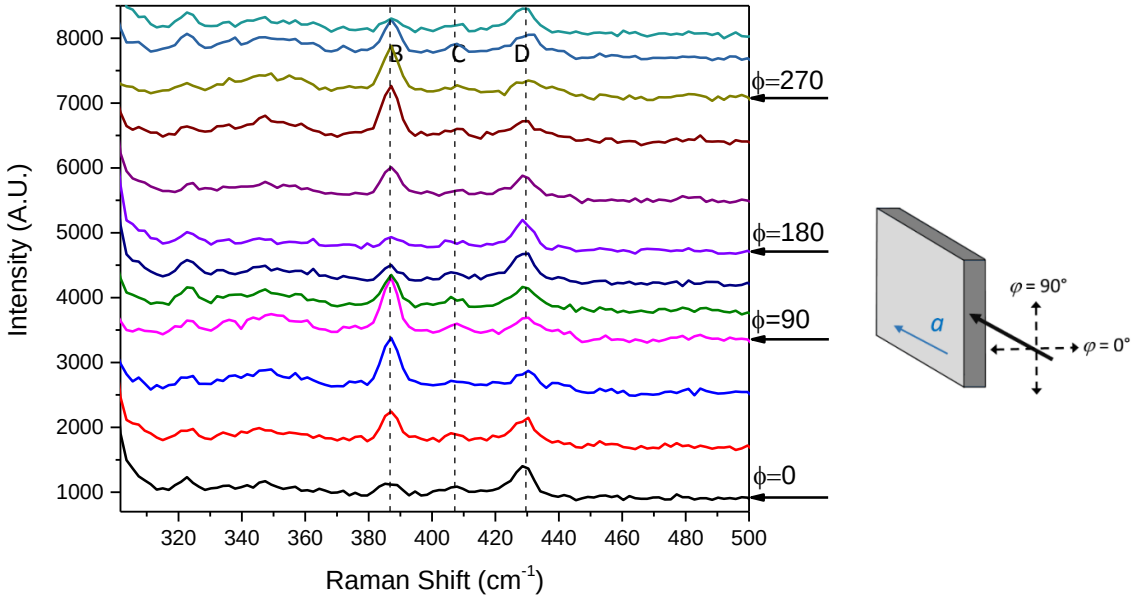

Figure S6. Experimental dependence on angle ϕ of the local vibrational modes of sulfur in $ReSe_{1.875}S_{0.125}$. The spectra measured at a set of angles ϕ in coarse (30°) steps clearly show that the intensity of mode D is greatest near $\phi = 0$, and mode B dominates when the excitation has a component polarized in the plane of the layers. Also as expected, modes A and C are weaker. In practice, two measurements in the two polarizations shown in the schematic diagram on the right would be sufficient to confirm the exchange of relative strengths between modes B and D.

Note that mode B is strongest when the excitation is in-plane and, given the crystal orientation shown in the schematic diagram on the right, the excitation is then also normal to the crystallographic direction *a*. The following results for normal incidence show that this is also the in-plane direction in which mode B is strongest.

$ReSe_{1.75}S_{0.25}$, local vibrational mode #36, normal incidence

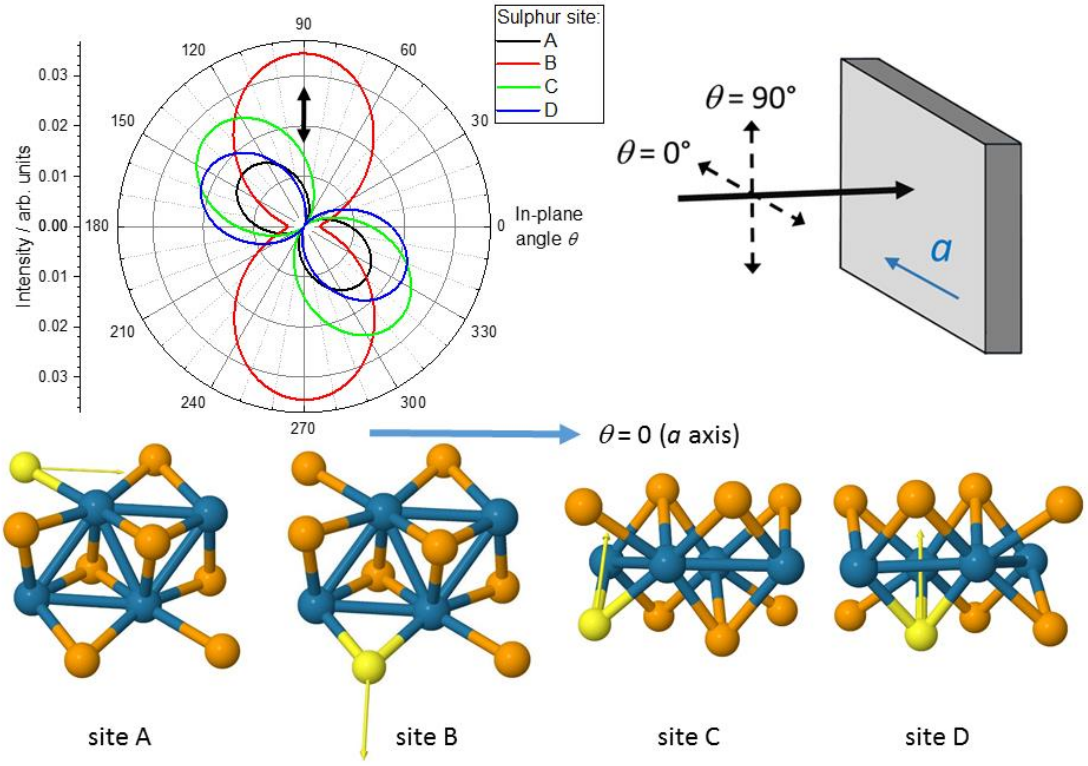

Figure S7. Top: angle-dependent polar plots of the predicted Raman scattering intensity of the highest-frequency vibrational modes of $ReSe_{1.75}S_{0.25}$ with sulfur placed at each of the four inequivalent sites in the unit cell, A-D. The calculated curves are based on the Raman tensors given in Figure S3 above using equation 3 of the main text, with $\theta = 0^{\circ}$ corresponding to polarization along the *a* direction, (the direction of the rhenium chains).

Bottom: the atomic displacements of these four modes, showing the predominantly in-plane displacement of the sulfur atom on site B. The Raman scattering of the mode associated with site B is strongly polarized along the in-plane direction normal to the rhenium chains, marked by the black arrow on the polar plot, and is the dominant mode of the four for this polarization, as can be seen in Figure 4(b) of the main text.

$ReSe_{1.75}S_{0.25}$, sulfur LVM: displacements of neighboring atoms

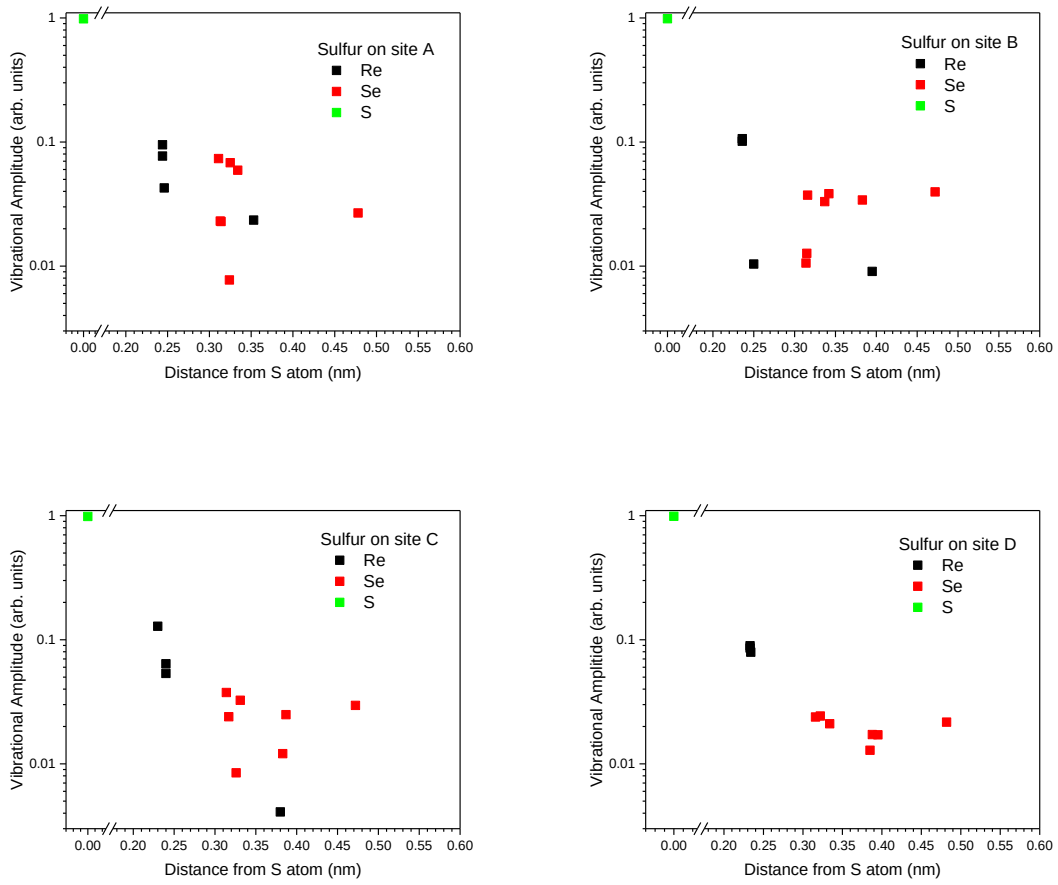

Figure S8. Amplitudes of vibration of the atoms neighboring a sulfur impurity as a function of distance from it, calculated via DFPT for the highest-frequency vibrational mode of $ReSe_{1.75}S_{0.25}$. The sulfur atom is placed at each of the four non-equivalent sites A-D and taken as the origin in each case. This demonstrates the rapid decrease in vibrational amplitude away from the S atom, justifying the description of these modes as local vibrational modes and showing why the predicted vibrational frequencies of these modes are in good agreement with experiment even for calculations based on a single unit cell.

$ReSe_{1.75}S_{0.25}$, calculated LVMs for different compositions

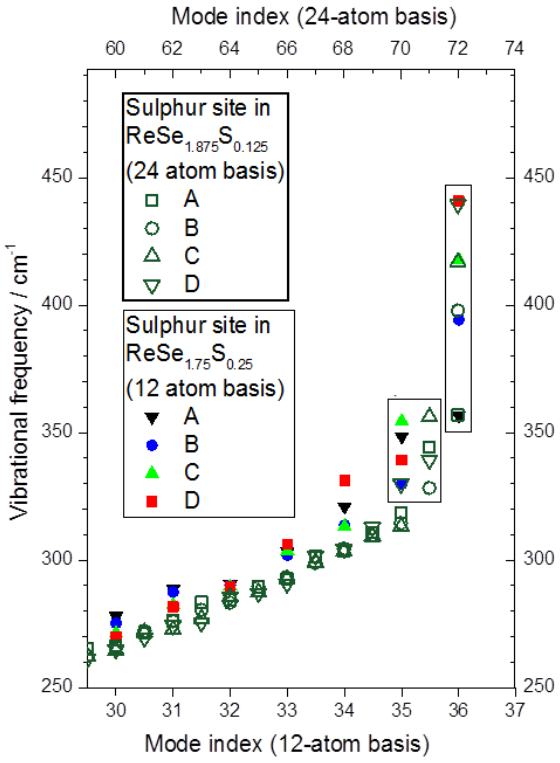

Figure S9. Calculated frequencies of the vibrational modes of $ReSe_{1.875}S_{0.125}$ (hollow symbols) and $ReSe_{1.75}S_{0.25}$ (filled symbols) plotted in order of increasing frequency. The former composition corresponds best to the experimental sample while the latter composition is the one used in the calculations presented in the main text.

For each composition, the four symbols correspond to one S atom being placed at each of the inequivalent chalcogen sites A-D in turn. The highest-frequency mode (enclosed in a box on the figure) has indices #36 (for the 12-atom unit cell) and #72 (24-atom unit supercell) and corresponds to the four local vibrational modes of the four possible S atom configurations. The results demonstrate that the calculated frequency of this mode is the same within typical limits of error for DFT for both unit cells and, hence, both effective compositions. This is true also of the next-highest mode in frequency (#35, #71). A systematic difference between the calculated frequencies for the lower-frequency modes can be seen and arises because the spatially-extended phonon modes are more sensitive to the supercell dimensions.

$Re(Se,S)_2$ alloys, lattice modes as function of composition

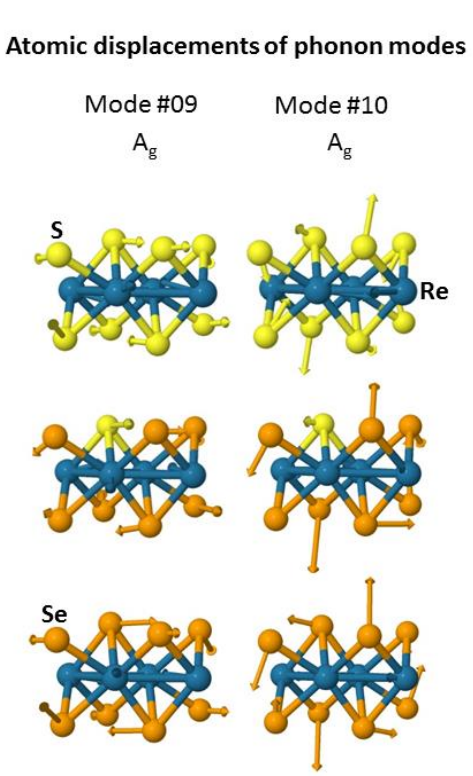

Material	Mode #09	Mode #10
ReS_2 calculated:	161.6 cm^{-1}	218.3 cm^{-1}
experiment:	160.5 cm^{-1}	212.7 cm^{-1}
$ReSe_{1.75}S_{0.25}$ mean calc. over sites A-D:	132.8 cm^{-1}	165.3 cm^{-1}
$ReSe_{1.875}S_{0.125}$ experiment:	126.2 cm^{-1}	161.1 cm^{-1}
$ReSe_2$ calculated:	123.6 cm^{-1}	159.8 cm^{-1}
experiment:	124.8 cm^{-1}	159.7 cm^{-1}

Figure S10. Calculated vibrational frequencies of two dominant Raman-active lattice (phonon) modes #9 and #10 for pure $ReSe_2$, ReS_2, and an alloy $ReSe_{1.75}S_{0.25}$. For each composition, the atomic displacements are shown on the left, in order to check that the atomic displacement patterns are similar, and thereby to justify the comparison of the frequencies. Use of the atomic displacements to identify comparable modes is essential here because the phonon modes lie close in frequency and because, for any alloy, all 33 vibrational modes are in principle Raman-active. This means that the order in frequency of the modes is not necessarily preserved across the composition range, especially for supercell calculations.

The alloy composition used in this calculation corresponds to one S atom per unit cell, placed at each of the inequivalent chalcogen sites A-D in turn. For the alloy, the given frequencies of modes #9 and #10 in the table are averages over the calculated frequencies for sites A-D (the separate frequencies are given in the next two tables) as a guide to the recognition of these modes in the experimental data. The frequencies of the experimental modes thus identified as #9 and #10 are also given. The discrepancy between experimental and calculated frequencies arises since the exact composition does affect the spatially-extended phonon modes.

$Re(Se,S)_2$ alloys, estimate of composition from lattice modes

Material	Mode #9 frequency calculated via LDA DFT, units of cm^{-1}	Sulphur content *x* deduced by linear interpolation
ReS_2	161.6	
$ReSe_{1.75}S_{0.25}$ site A	133.9	0.27
$ReSe_{1.75}S_{0.25}$ site B	129.0	0.14
$ReSe_{1.75}S_{0.25}$ site C	138.0	0.38
$ReSe_{1.75}S_{0.25}$ site D	133.9	0.18
$ReSe_2$	123.6	
Exact sulfur content $x = 0.25$		Mean deduced $x = 0.24$

Figure S11. Calculated vibrational frequencies of the prominent Raman-active lattice (phonon) mode #9 of $ReSe_{1.75}S_{0.25}$ with one sulfur atom located at each of the four non-equivalent chalcogen sites A-D in turn. Assuming a linear interpolation between binary compounds ReS_2 and $ReSe_2$, one can use these calculated frequencies to extract an estimate of the sulfur composition of the unit cell and compare this estimate to the exact figure of 0.25 (i.e, one in eight chalcogens is S in ReX_2). The right-hand column shows that this interpolation is only approximate; mode #9 (and most others) would show a small dependence on which site the S occupies in a perfectly ordered alloy. In a more realistic sample with S located randomly on all four sites, however, interpolation should be more reliable; taking an unweighted mean of the frequencies over sites A-D gives an estimated sulfur content of 0.24. Similar results are obtained using, for example, mode #10.

$Re(Se,S)_2$ alloys, lattice modes as function of S site

Calculated mode frequencies (cm^{-1})	Single cell ($a \times b \times c$)	Double along a ($2a \times b \times c$)
	12 atoms (one S) $ReSe_{1.75}S_{0.25}$	24 atoms (one S) $ReSe_{1.875}S_{0.125}$
Mode #9 S on site A	133.9	133.9
Mode #9 S on site B	129.0	133.9
Mode #9 S on site C	138.0	132.6
Mode #9 S on site D	130.3	134.8
Mode #10 S on site A	165.2	163.8
Mode #10 S on site B	167.0	164.1
Mode #10 S on site C	163.3	163.3
Mode #10 S on site D	165.6	164.3

Figure S12. Calculated vibrational frequencies of two dominant Raman-active lattice (phonon) modes #9 and #10 of ReX_2 with one sulfur atom located at each of the four non-equivalent sites A-D. Calculations were performed for a 12-atom primitive unit cell and for 24-atom ordered alloy supercells, doubled in one or both of the in-plane directions (since this 2D material has much weaker interactions between the layers, we do not consider supercells doubled along the out-of-plane lattice vector). The results demonstrate that the variation in calculated frequency of the modes is not systematic (for example, the sulfur site giving the highest or lowest frequency is not the same as the cell changes) but the variation is small (at most 2%) and well within the intrinsic limits of the DFT calculation. The variation in frequency for the larger unit cell arises because the equivalent S concentration is less than for the smaller cell, and the frequencies converge as they approach the binary limits of 123.6 and 159.8 cm^{-1} calculated for $ReSe_2$ (Fig. S4C).

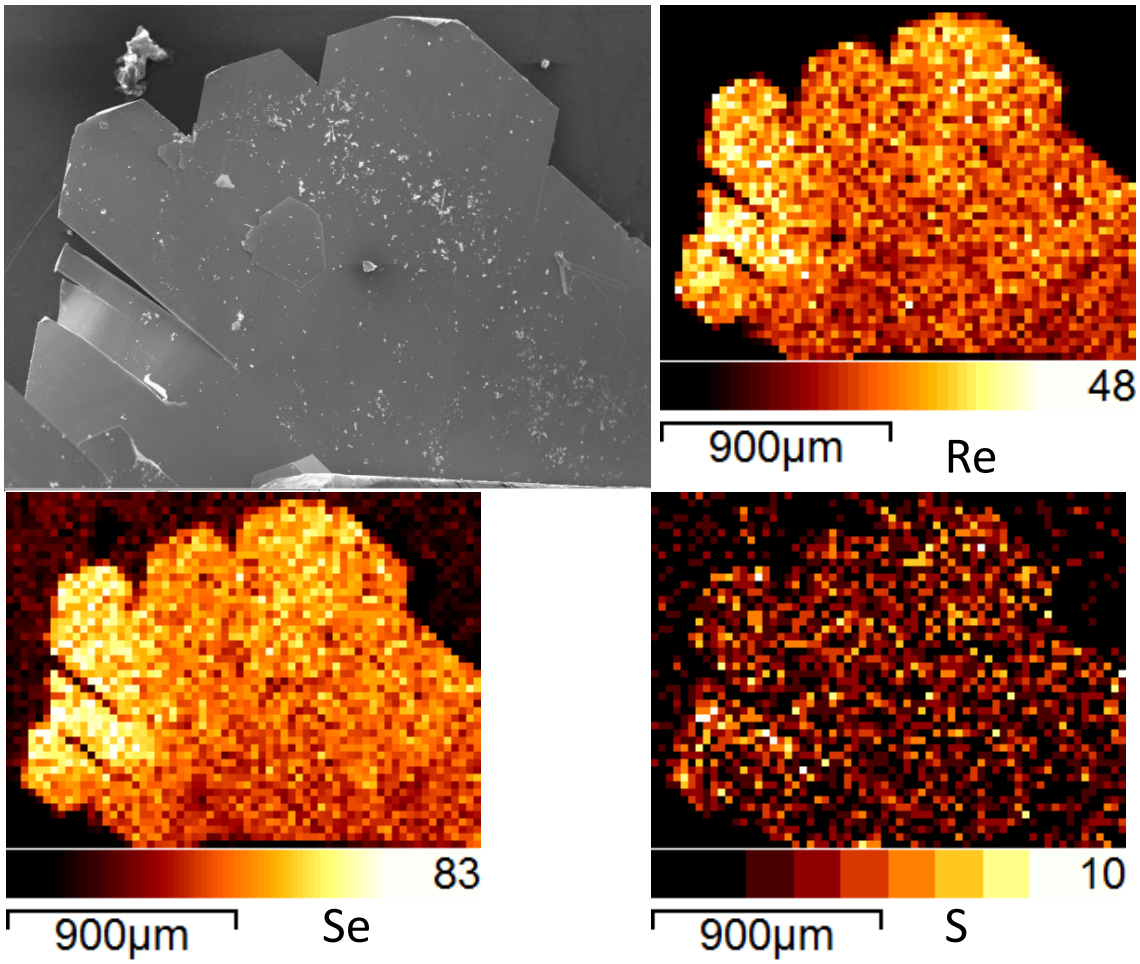

Figure S13. EDX maps of $ReSe_2$ doped with sulfur, with color bars showing counts. The average stoichiometry of this sample, deduced from this data, is $ReSe_{1.875}S_{0.125}$. This is in agreement with the nominal composition of the bulk alloy samples.

$MoSe_2$ Raman tensors

$$R = \begin{pmatrix} u & v & r \\ v & w & s \\ r & s & t \end{pmatrix}$$

$$I = t\cos^2\varphi + w\sin^2\varphi + s^2 + 2s(w+t)\sin\varphi\cos\varphi$$

Mode 33 Freq. = 347 cm^{-1}
0.05782 -0.02597 -0.00006
-0.02597 0.05427 0.00011
-0.00006 0.00011 0.03219

Mode 34 Freq. = 373 cm^{-1}
0.00286 -0.08077 -0.00695
-0.08077 0.08262 0.00327
-0.00695 0.00327 -0.00002

Mode 35 Freq. = 373 cm^{-1}
0.08313 -0.07803 -0.00267
-0.07803 -0.00315 0.00685
-0.00267 0.00685 0.00197

Mode 36 Freq. = 417 cm^{-1}
-0.00059 0.00327 0.00008
0.00327 0.00147 -0.00021
0.00008 -0.00021 0.05356

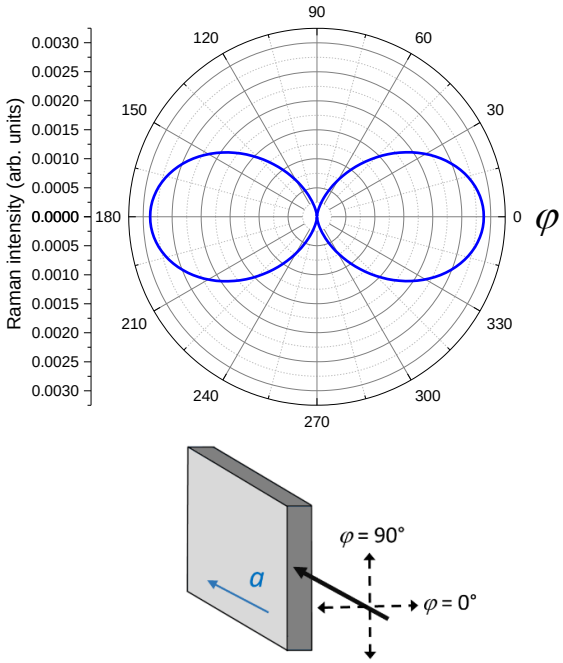

Figure S14. Left: Raman tensors predicted for each local vibrational mode of dilute substitutional S in $MoSe_2$ with the largest components in each case highlighted in red (calculated by DFPT for a 2×2×1 supercell with one Se atom replaced by S). The high symmetry of $MoSe_2$ implies that all chalcogen sites in the supercell are equivalent, so only one impurity configuration need be considered. As in the case of $ReSe_2$, the highest-frequency mode, #36, involves an out-of-plane motion of the S impurity whilst other atomic displacements are very small, and its Raman tensor *R* has a large component *t* (as defined here and in the main text) so that the 'edge-on' geometry will be appropriate for detection of this mode in $MoSe_2$. Right: dependence on polarization angle of the Raman scattering arising from mode #36, calculated using Eq. 4 of the main text, reproduced above. Excitation polarized parallel ($\varphi = 0^\circ$) to the normal to the layers gives a stronger cross-section by a factor of ~200 compared to excitation polarized in the layer plane.

6.4 Discussions

This paper looks at the material, $ReSe_{1.875}S_{0.125}$, which has four vibrational modes from sulphur in four inequivalent positions of the unit cell. These modes are found at four different wavenumbers which are spread over a large enough frequency range that each mode should be observable. However, these modes are all very weak. Therefore, one of the major challenges involved with this project was to obtain these modes with a significant signal-to-noise ratio. Two different approaches to improve the signal-to-noise ratio are invoked in this paper. The first involves a long exposure time. A measurement time of 30 minutes was chosen because this was the longest exposure time that could be made before the detector was saturated. The Renishaw Raman spectrometer offers software that allows the averaging of multiple measurements. This means a measurement of an hour could in principle be made by having an exposure time of 30 minutes and taking an average of two spectra. Unfortunately, there is readout noise involved in taking averages, so no averaging was done to make any of the figures in the paper of this chapter. The second method involved taking a Raman spectroscopy measurement utilising the "edge-on" geometry. From DFT calculations it was realised that one of the local vibrational sulphur modes oscillates in the out-of-plane direction. The "edge-on" geometry, as explained in the main paper, is the geometry which gives the maximum intensity for out-of-plane vibrations.

The rhenium dichalcogenides have a centre of inversion within the unit cell. This means unlike the group VI TMDs spin-orbit splitting is absent for flakes of any number of layers. Introducing impurities into the unit cell of the rhenium dichalcogenides will break inversion symmetry locally, leading to spin-orbit splitting. Although this work does not investigate spin-orbit splitting, it may be of use for future projects which utilise doping to introduce spin-orbit splitting.

Chapter 7

Electronic bandstructure and van der Waals coupling of $ReSe_2$ revealed by high-resolution angle-resolved photoemission spectroscopy

7.1 Preamble

The anisotropy in the rhenium dichalcogenides manifests itself in the vibrations of the atoms and in the electronic band dispersions. The lattice dynamics of these materials have been described in detail in the last three chapters. The next four chapters will investigate the anisotropy in the band structures of these crystals.

This chapter looks at ARPES measurements of $ReSe_2$. The anisotropy is demonstrated by taking cuts of the band structure along different directions in the Brillouin zone. This anisotropy is quantified by measuring the effective mass of the charge carriers along and

perpendicular to the rhenium chains. This paper also investigates the electronic coupling between the layers of this crystal. The locations of the valence band maxima are found which is used to shed light on whether $ReSe_2$ is a direct or an indirect band gap semiconductor. There have been a large number of theoretical predictions of the band structure of $ReSe_2$ (see Sec 2.2.3). These papers come to conflicting conclusions about the nature of the band gap and the strength of the interlayer coupling. Therefore, it was considered timely for ARPES measurements of $ReSe_2$.

Atomic coordinates taken from Lamfers et al. are used to produce the DFT calculated band structures [30]. To be consistent with this work, the crystal lattice vector a is defined to be along the directions of the rhenium chains.

Note: There is a mistake in the caption of Fig. 4 in the sentence "(a) Measured and calculated dispersions along the b^*_{2D} direction and (b) normal to it". The bands in (a) are perpendicular to b^*_{2D} and the bands in (b) are parallel to the b^*_{2D} direction. There is one further mistake in the paper, on page 5, in the bottom paragraph in the sentence, "effective masses of $0.4m_e$ and $1.2m_e$ have been directly determined along the direction of the Re-atomic chains and orthogonal to them, respectively". The effective mass of the charge carries measured in this work are $0.7m_e$ and $1.2m_e$.

The candidate was involved with the sample preparation, ARPES measurements and interpretation of the results. This work was all done at the ANTARES beamline at the Synchrotron Soleil with the help of Dr Webb, Dr Wolverson and the beamline scientists. The electronic transport data in the supporting information was obtained by Dr Dale and Dr Bending, and Dr Wolverson performed the DFT calculations.

7.2 Statement of authorship and copyright information

<table>
<tr><td colspan="5">This declaration concerns the article entitled:</td></tr>
<tr><td colspan="5">Electronic bandstructure and van der Waals coupling of $ReSe_2$ revealed by high-resolution angle-resolved photoemission spectroscopy</td></tr>
<tr><td colspan="5">Publication status (tick one)</td></tr>
<tr><td>Draft manuscript</td><td>Submitted</td><td>In review</td><td>Accepted</td><td>Published</td></tr>
<tr><td></td><td></td><td></td><td></td><td>✓</td></tr>
<tr><td>Publication details (reference)</td><td colspan="4">L. S. Hart, J. L. Webb, S. Dale, S. J. Bending, M. Mucha-Kruczynski, D. Wolverson, C. Chen, J. Avila, and M. C. Asensio, “Electronic bandstructure and van der Waals coupling of $ReSe_2$ revealed by high-resolution angle-resolved photoemission spectroscopy,” Scientific Reports, vol. 7, no. 1, p. 5145, 2017.</td></tr>
<tr><td>Candidate’s contribution to the paper (detailed, and also given as a percentage)</td><td colspan="4">The candidate contributed to the experimental measurements in this publication.
Formulation of ideas: 60%
Design of methodology: 50%
Experimental work: 50%
All the ARPES measurements were done with the help of the beamline scientists
Computational work: 0%
Presentation of data in journal format: 20%</td></tr>
<tr><td>Statement from Candidate</td><td colspan="4">This paper reports on original research I conducted during the period of my Higher Degree by Research candidature.</td></tr>
<tr><td>Signature</td><td colspan="2"></td><td>Date</td><td>29/05/2018</td></tr>
</table>

Publication title: Electronic bandstructure and van der Waals coupling of $ReSe_2$ revealed by high-resolution angle-resolved photoemission spectroscopy

The pages of this thesis this paper spans are from 123 to 141.

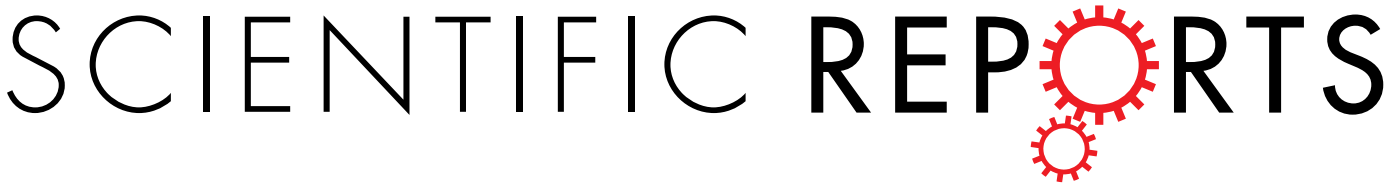

OPEN

Electronic bandstructure and van der Waals coupling of $ReSe_2$ revealed by high-resolution angle-resolved photoemission spectroscopy

Received: 15 March 2017
Accepted: 26 May 2017
Published online: 11 July 2017

Lewis S. Hart[1], James L. Webb[1], Sara Dale[1], Simon J. Bending[1], Marcin Mucha-Kruczynski[1], Daniel Wolverson[1], Chaoyu Chen[2], José Avila[2] & Maria C. Asensio[2]

$ReSe_2$ and ReS_2 are unusual compounds amongst the layered transition metal dichalcogenides as a result of their low symmetry, with a characteristic in-plane anisotropy due to in-plane rhenium 'chains'. They preserve inversion symmetry independent of the number of layers and, in contrast to more well-known transition metal dichalcogenides, bulk and few-monolayer Re-TMD compounds have been proposed to behave as electronically and vibrational decoupled layers. Here, we probe for the first time the electronic band structure of bulk $ReSe_2$ by direct nanoscale angle-resolved photoemission spectroscopy. We find a highly anisotropic in- and out-of-plane electronic structure, with the valence band maxima located away from any particular high-symmetry direction. The effective mass doubles its value perpendicular to the Re chains and the interlayer van der Waals coupling generates significant electronic dispersion normal to the layers. Our density functional theory calculations, including spin-orbit effects, are in excellent agreement with these experimental findings.

The layered TMD family includes a rich palette of superconductors, metals[1] and semiconductors with direct and indirect gaps, and offers fascinating possibilities for the realisation of nanoscale electronic, optoelectronic and photonic devices through the assembly of heterostructures[2]. These may include dissimilar TMDs, but also graphene and boron nitride[3,4]. Typical semiconducting TMDs (MoS_2, WS_2, WSe_2) are hexagonal, with inversion symmetry in the bulk which is absent for the monolayer; the profound changes in the band structure in monolayer TMDs and their implications for device applications have been reviewed recently[5,6]. This symmetry-breaking in hexagonal monolayers leads to a finite SO splitting and to the non-equivalence of the K^+ and K^- valleys[7]. The exciton binding energies and SO splittings are typically large[7,8], giving optical access to well-defined spin-valley states even at room temperature. At the same time, the direct gap of monolayers appears at the K points, so that circularly polarised excitation can address selectively either K^+ or K^- valleys. By alloying, for example, $MoSe_2$ with WSe_2, the magnitude of the SO splitting may be varied, and this allows tuning of the above effects[9].

However, the TMD family also includes materials which do not conform to the typical expectations above[1], and this much less well-known group of TMDs expands the range of possible heterostructures. One such material is $ReSe_2$ (and the closely-related ReS_2), as discussed in a recent review[6], in which the only symmetry operation is inversion[10–13]. In contrast to typical TMDs, an inversion centre in Re-TMDs is preserved *even in monolayers*, so that few-layer Re-TMDs are expected to have zero SO splitting independent of layer number[14]. Nevertheless, spin-orbit effects still modify the band structure of $ReSe_2$, shifting the transition metal (Re) *d*-orbitals that make up its band edges[15]. Consequently, perturbations that break inversion symmetry, such as alloying[16] or external electric fields[17], may allow one to manipulate the valence band SO splitting in $ReSe_2$ or ReS_2, and this splitting will grow *from zero* rapidly on applying a given perturbation.

[1]Centre for Nanoscience and Nanotechnology, Department of Physics, University of Bath, Bath, BA2 7AY, United Kingdom. [2]Synchrotron SOLEIL, Saint Aubin, and Université Paris-Saclay, BP 48 91192, Gif-sur-Yvette, France. Correspondence and requests for materials should be addressed to D.W. (email: d.wolverson@bath.ac.uk) or M.C.A. (email: maria-carmen.asensio@synchrotron-soleil.fr)

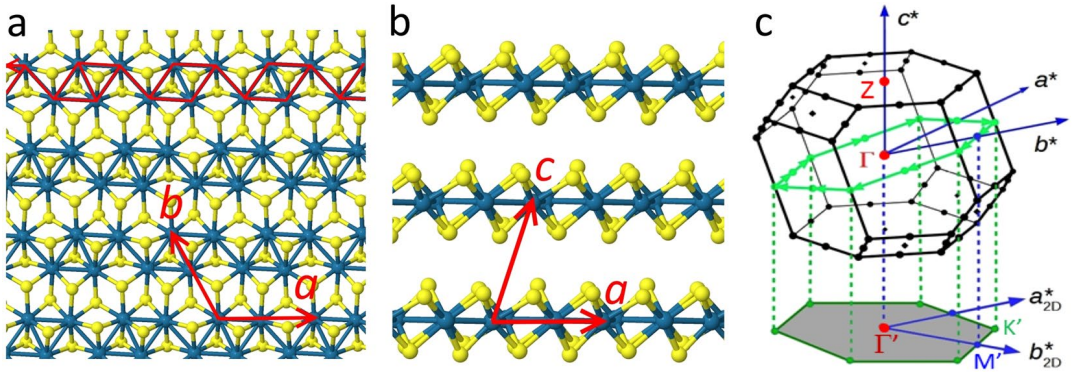

Figure 1. Crystal structure and first Brillouin zone of triclinic $ReSe_2$. (**a**) View of a single layer seen from above and (**b**) from the side. Re atoms are coloured blue and Se atoms are yellow. The directions of the lattice vectors ***a***, ***b*** and ***c*** are indicated; ***a*** is defined here as the direction of the rhenium chains, highlighted in red in (**a**). (**c**) First Brillouin zone of $ReSe_2$ indicating the reciprocal lattice vectors ***a****, ***b**** and ***c**** and the conventional points Γ (0, 0, 0) and Z (0, 0, ±½). The tilted green hexagon indicates a path in reciprocal space around points of the type (±½, 0, 0); the lower gray hexagon shows the pseudo-Brillouin zone defined by the projections of these points onto the real space layer plane, with basis vectors labelled $\boldsymbol{a}^*_{2D}$ and $\boldsymbol{b}^*_{2D}$ and centre Γ'.

Thus, the Re-TMDs promise a new means to control SO effects in few-layer semiconductor heterostructures. Being highly anisotropic 2D materials, they also offer new possibilities as hyperbolic plasmonic materials[18] or polarisation-sensitive photodetectors[14,19,20]. Interest in anisotropic 2D materials is growing rapidly, with the isolation of few-layer black phosphorus and analogues such as GeS; relative to these materials, however, we find ReS_2 and $ReSe_2$ are more promising because they are stable in air[21]. In particular, the van der Waals coupling between layers has been estimated as very weak and consequently quasi-monolayer behaviour in bulk Re-TDMs has been reported based on recent micro-Raman and photoluminescence results[19]. However, recent angle-resolved Raman studies conclude that exciton-phonon coupling and more exotic interactions can be present in Re-TMD compounds[22]. Nevertheless, to predict what might be achieved using the Re-TMDs, a precise understanding of their band structure is essential. There have only been a few attempts to model either bulk or monolayer Re-TMDs[14,23,24] and calculations have not explored the full Brillouin zone. Furthermore, no direct band structure determination has been reported to date, though indirect data on optical absorption[25–28] and transport properties[29–34] are available. The present work addresses this lack of information for the case of bulk $ReSe_2$.

We present here the first measurements of the valence band structure of bulk $ReSe_2$, using angle-resolved photoemission (ARPES) with nanoscale spatial resolution (nano-ARPES). Our results are modelled via density functional theory (DFT) including spin-orbit (SO) effects. We find a remarkable band structure, with two valence band maxima within the first Brillouin zone and related by inversion symmetry, but not located on any special high-symmetry points or paths and, therefore, predicted to be subject to strong SO splitting if an external perturbation is applied[17] (though the present data show no SO splitting, consistent with the presence of inversion symmetry). The ARPES data reflect the strong in-plane asymmetry peculiar to the transition metal dichalcogenides (TMDs) based on Re[10–13], with very different valence band dispersions parallel or perpendicular to the Re chains that run along the crystallographic *a* direction (see Fig. 1a and b). As a result, the effective mass along the Re chains is almost twice that orthogonal to them. Even more interestingly, the excitation energy dependence of the nano-ARPES data shows a striking out-of-plane dispersion, indicating that the interlayer van der Waals coupling in $ReSe_2$ is appreciable and therefore, the electronic properties on monolayer $ReSe_2$ compounds could be dramatically different to the bulk material. Finally, even if a full understanding of the momentum-resolved electronic structure of $ReSe_2$ is particularly complex due to its triclinic crystal structure, the two-fold theoretical and experimental approach taken here allows us to identify the electronic hallmark of this compound as well as how the bulk band structure relates to that of Re-TMD monolayers.

Results

ARPES Fermi surface and constant energy mapping. One of the most illuminating modes of angle-resolved photoemission (ARPES) measurement nowadays is to monitor with high energy and angular resolution the photoemission signal from states in a given energy window near the Fermi level as a function of electron wavevector parallel to the crystal surface, since it is this wavevector component that is conserved in photoemission[35]. For a three-dimensional material, this yields a section through reciprocal space, which is nearly planar, that is, having a nearly constant wavevector component normal to the sample surface. However, the deviation of this section from planarity can become important, as will be discussed below.

To interpret our nano-ARPES data for bulk $ReSe_2$, we first need to discuss its crystal structure and reciprocal lattice. Figure 1a and b show how the Re atoms within a layer form groups of four in linked chains of rhombuses, driven by a distortion of the unstable metallic hexagonal structure into the semiconducting 1 T' phase[23,36]. These layers stack along the crystallographic ***c*** axis which, note, is *not* normal to the layers (Fig. 1b). Figure 1c shows the resulting Brillouin zone for the bulk material; the reciprocal lattice vectors ***a**** and ***b**** do not lie in the real space layer plane so that, unlike the cases of hexagonal MoS_2 or WS_2, the plane probed in ARPES does not contain these basis vectors. Instead, ARPES will (to a first approximation) map a plane normal to ***c**** with a 2D quasi-unit cell

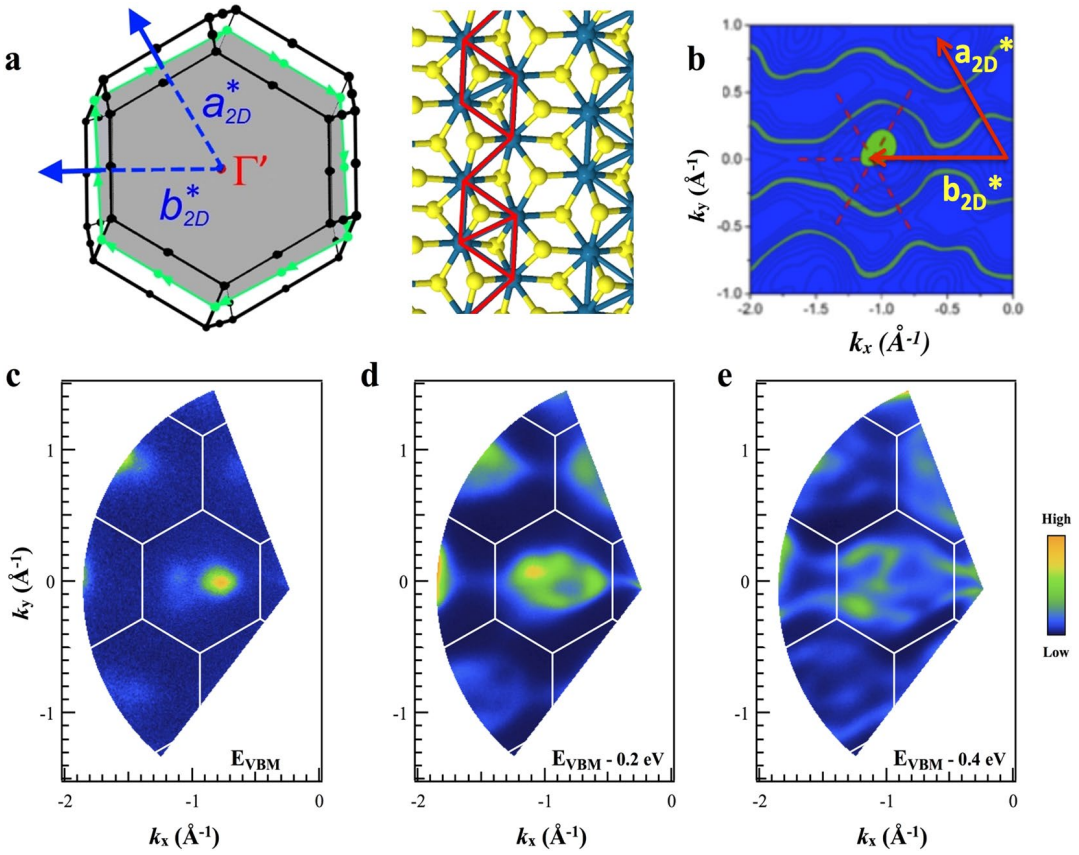

Figure 2. ARPES maps of photoemission intensity as a function of in-plane wavevector (**a**) View along the c^* axis of the first Brillouin zone, showing the irregular hexagon (gray) defined by a^*_{2D} a and b^*_{2D}, and top view of a single $ReSe_2$ layer indicating the orientation of the chains with respect to the Brillouin zone. (**b**) A theoretical contour plot at 0.4 eV below the valence band maximum. The dotted cross indicates the position of a Γ' point. For comparison, in Figure S1 of the supplementary information all experimental contour plots are compared with the corresponding theoretical ones. (**c–e**) Experimental maps (**c**) near the valence band maximum (VBM); (**d**) 0.2 eV below the VBM and (**e**) 0.4 eV below the VBM.

consisting of the shaded irregular hexagon which is defined by the projections of a^* and b^*. Figure 1c shows that this hexagon is a projection of the tilted hexagon that contains some of the special points of the Brillouin zone (BZ). The 2D quasi-Brillouin zone itself does not contain any special points and, consequently, the conventional labels for the high-symmetry points of a regular hexagon (K and M) are not strictly applicable. For convenience, however, we will keep these labels and number these points $K_1..K_3$ and $M_1..M_3$ later, when it is necessary to distinguish between the non-equivalent K and M directions. Likewise, the centre of the 2D quasi-unit cell, Γ', is a point on the line joining Γ and Zpoints (Fig. 1c), and is not necessarily the true 3D Brillouin zone centre. For a monolayer, the gray hexagon becomes the true 2D reciprocal space unit cell, so that labels Γ, K and M become strictly correct[14].

We now turn to the nano-ARPES maps shown in Fig. 2. The 2D images show photoemission intensity as a function of in-plane wavevector (k_x, k_y) for states at a series of three energies near and just below the valence band maximum (VBM), using a fixed excitation photon energy of 100 eV; we discuss the implications of the choice of excitation energy below. Using a gold sample as reference *in situ*, the energy difference between the Fermi level and the valence band maximum located in Fig. 2c has been precisely determined to be 1.4 ± 0.025 eV, close to the direct excitonic optical band gaps of $ReSe_2$ at low temperatures (1.386 and 1.409 eV[37,38] at 15 K). This is consistent with the fact that the present $ReSe_2$ samples are highly *n*-type as indicated by the transport characteristics of FET structures made from the same batch of material (see Supplementary Information Figs S2 and S3) so that the Fermi level is close to the conduction band. More usually, $ReSe_2$ is found to be p-type[31,39] though this is not universally the case[40]. Given this information, we can label the constant energy surfaces of Fig. 2c–e with the binding energies (1.4 eV, 1.6 eV and 1.8 eV) or (0 eV, 0.2 eV and 0.4 eV), depending on whether the Fermi energy or the valence band maximum respectively is taken as a reference (see Fig. 2).

The 2D quasi-Brillouin zone (Figs 1c and 2a) is clear in the distribution of the maxima in Fig. 2(c–e) and is in excellent agreement with lattice vectors calculated from the crystal axes determined by X-ray diffraction[10]. Even more striking is the anisotropy these maps show between k_x and k_y directions. This is seen most clearly in Fig. 2(e) where the contours of photoemission intensity form wavy 'ribbons' running along the k_x direction parallel to b^*_{2D}; this is the direction perpendicular to the Re chains, which we define to be along the real space vector a (Fig. 1). This result reveals a much flatter valence band dispersion for carriers moving perpendicular to the chains

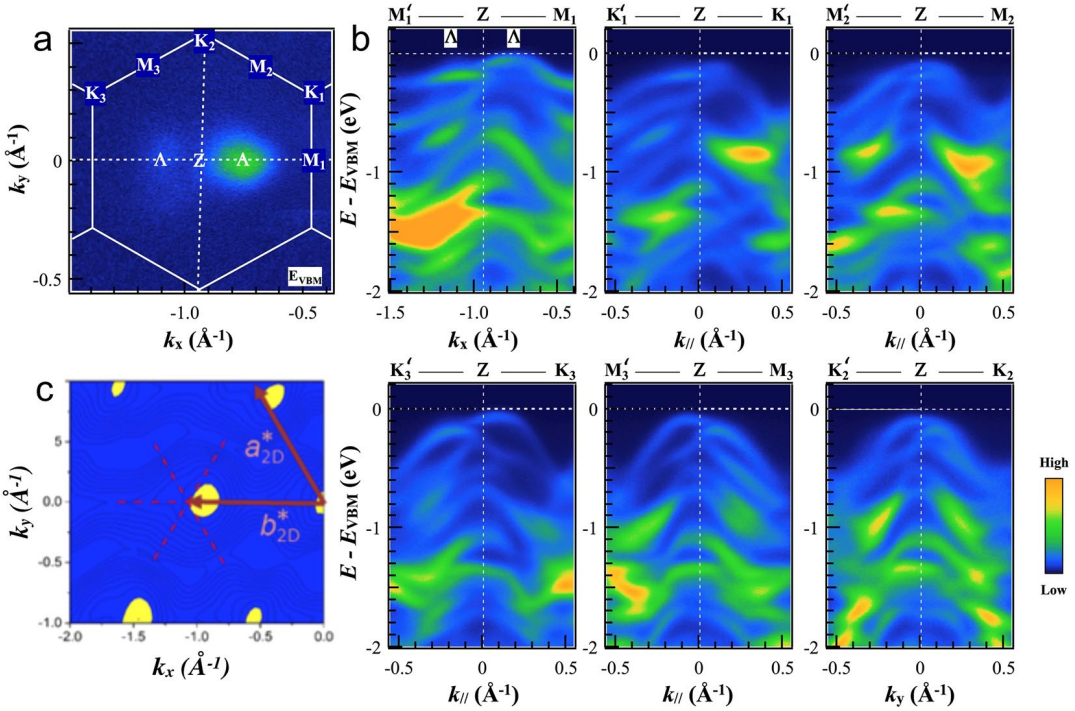

Figure 3. Electronic band structure of $ReSe_2$ (**a**) ARPES constant energy plots measured with 100 eV photon energy throughout the reciprocal unit $ReSe_2$ cell. Experimental photoemission signal as a function of in-plane momentum at an energy close to the VBM for a section through the Brillouin zone passing through the Z point, showing the special points of the quasi-Brillouin zone including the position of the local VBM (labelled Λ) (**b**) ARPES data along the M'ZM and K'ZK directions in the reciprocal space. (**c**) DFT calculations of the density of states at the top of the valence band in the plane containing the Z point, in good agreement with experimental results shown in panel (**a**).

compared to those moving along the chains (we return to this point below). For comparison, Fig. S1 of the Supplementary Information shows the contours of constant energy calculated via DFT for a section through the Brillouin zone, probing the uppermost VB state. The energies of the contours are the same energies at which the experimental contours have been measured.

The experimental and calculated constant energy maps throughout the reciprocal space unit cell reflect the characteristic signatures of the density of states at a given energy and momentum. Note that the calculated images are not simulations of the ARPES signals, as the latter depend also on the photoemission matrix elements. Nevertheless, both sets of patterns show a remarkable agreement. Firstly, it is clearly noticeable that the highest–energy states do not appear centred on a Γ' point, but are displaced to either side. Secondly, for photoelectrons of higher binding energies, both the nano-ARPES and the theoretical results show the development of the one-dimensional ('wavy') structure over exactly the same energy and momentum ranges (see Figs 2b and e and S1 of the Supplementary Information). Finally, we note that this good agreement between experimental and theoretical results extends to lower-energy VB states, not just those of the uppermost band; in Fig. 2b, for example, we have to include a contribution from the next band down in energy, which appears in the experimental energy range.

The in-plane anisotropy of the electronic structure of $ReSe_2$ can be investigated more deeply by recording high energy- and angular-resolution photoemission scans along selected high symmetry directions. Figure 3 shows such scans through the 2D quasi-Brillouin zone for a plane passing through the Z point in reciprocal space (see Fig. 1c). For completeness, we show equivalent sections of the Brillouin zone and valence band dispersions passing through the Γ point of the three-dimensional Brillouin zone in the Supporting Information (Figs S9 and S10). Figure 3a shows the Fermi surface map recorded in this plane, and also shows how we define the labels for the non-equivalent points K_1..K_3 and M_1..M_3. Here, we use a prime (e.g, M') to represent the projection through Z of a given point (e.g, M) to its equivalent in the next Brillouin zone. In Fig. 3b, the nano-ARPES scans are shown for the six directions of type M'-Z-M and K'-Z-K'. Figure 3b shows the effects of anisotropy in several distinct ways.

Firstly, it shows unmistakably the inequivalent character of the K_2-Z and M_1-Z directions which are parallel and perpendicular respectively to the Re chains. Secondly, the dispersions are similar in the K_1-Z and K_3-Z directions, which make approximately the same angle to K_2 (and thus to the Re chains), and the dispersions in the M_2-Z and M_3-Z directions are similar to each other for the same reason. Finally, there is a clear asymmetry between the dispersions along M'-Z and M-Z, that is, either side of the Z point in the same direction. This is due to the shape of the three-dimensional Brillouin zone shown in Fig. 1c; there are no true reciprocal lattice vectors in the plane being probed, so M' is not equivalent to M. The fact that the Brillouin zone has to be considered as three-dimensional indicates the existence of significant inter-layer coupling (we return to this point later).

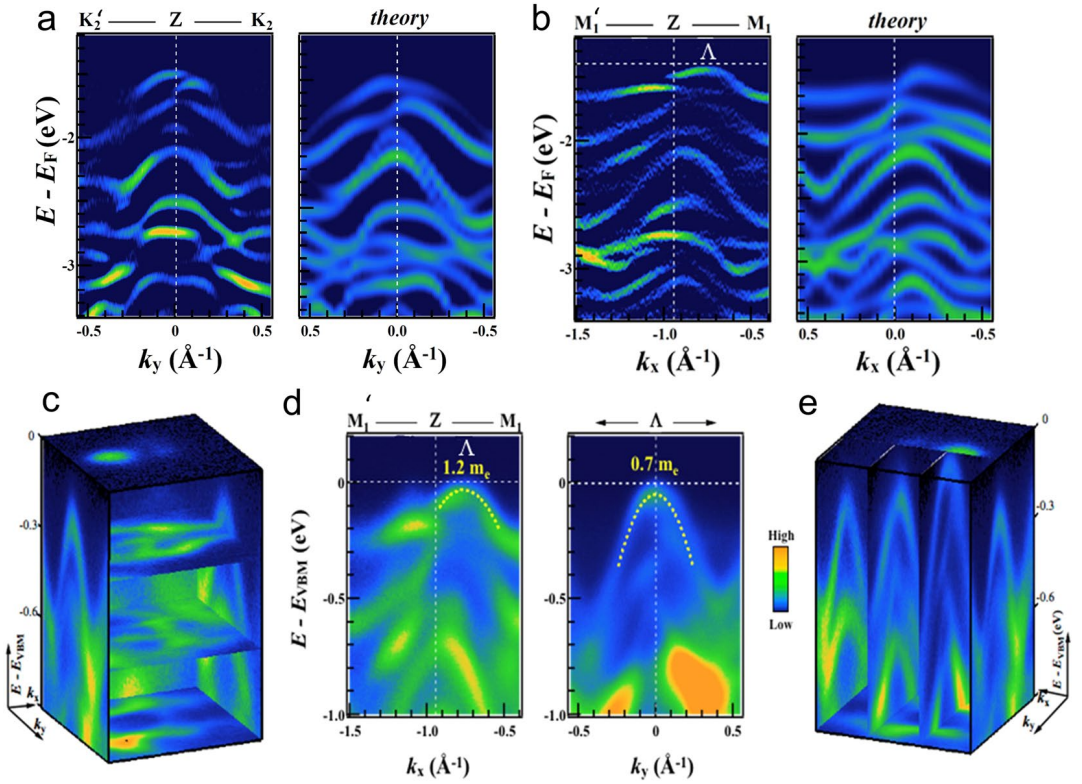

Figure 4. Valence band dispersion. (**a**) Measured and calculated dispersions along the b^*_{2D} direction and (**b**) normal to it. In (**a**) and (**b**), the colour scale of the calculated data is arbitrary but in the same sense as the experimental data and indicates the projection of the VB states onto the Re *d* orbitals. (**c**) and (**e**) panels show the same data of panels (**a**) and (**b**) in 3D plots. (**d**) Dispersion measured by ARPES along the b^*_{2D} direction (left) and normal to it (right) passing through the point Λ. Fitted dispersions are shown as dashed lines, giving the effective masses at Λ in these two directions.

To test the agreement of our experimental and theoretical results more closely, Fig. 4 shows the measured and calculated band dispersions along the key orthogonal directions (a) Z-K_2 and (b) Z-M_1 over a large energy range (to binding energies of more than 3 eV below the Fermi level). For clarity, the experimental dispersions are second derivatives of the raw photoemission data where the colour scale represents signal strength whilst, in the calculated dispersions, the colour scale represents the projection of the VB states onto the Re *d* orbitals, for which a broadening in energy of $\Delta E = 68$ meV and an energy grid step of 20 meV were used. In the theoretical curves of Fig. 4a,b the occasional periodic structure is an artefact of these grid choices. The non-conservation of the initial electron momentum expressed by Eq. 1 (see below) has been taken into account in the simulated dispersions using an inner potential of 19.1 eV. The number and structure of bands within the ~2 eV energy range of this data is clear in Fig. 4a,b, and the asymmetry of the bands is once more very striking. We conclude that the present level of DFT approximation (see Methods) is adequate to describe the band structure well, but that account must be taken of the three-dimensional nature of the band structure that gives rise to the structure of Fig. 4a.

The comprehensive ARPES datasets represented in Fig. 4c,e that give the sections through the Brillouin zone of Fig. 4a,b also allow us to obtain the electronic dispersions exactly at the local valence band maximum near Z (labelled as the point Λ) both along the 1D Re chains and orthogonal to them. Measured dispersions passing through Λ are shown in Fig. 4(d) along the b^*_{2D} direction (left) towards M_1, and normal to b^*_{2D} (right). Fitted parabolas (Fig. 4d, dotted white lines) allow a precise estimation of the degree of in-plane anisotropy. Effective masses of 0.4 m_e and 1.2 m_e have been directly determined along the direction of the Re-atomic chains and orthogonal to them, respectively. Clearly, the effective mass is lowest in the direction normal to b^*_{2D} or, equivalently, the direction parallel to the Re chains in real space. In a 2D TMD, the phonon-limited mobility depends on the inverse square of the effective mass[34,41,42] so that we expect a higher mobility along the Re chains. The ARPES results thus provide a direct experimental explanation for the higher mobility in the Re chain direction found very recently for top-gate field effect transistors (FETs) based on few-layer $ReSe_2$. From their measured mobility values, Zhang *et al.* deduced effective masses of 1.88 m_e parallel to the Re chains and 6.02 m_e along the other in-plane crystallographic direction for *monolayer* $ReSe_2$ FET structure prepared on h-BN[40]; this shows a somewhat larger ratio of maximum to minimum effective masses (3.2) than we observe (1.2/0.7 = 1.71). There only a few reported measurements of the effective masses in 3D bulk material but Hu *et al.*[43] report perpendicular and parallel mobilities of 6.8 and 20.8 $cm^2 V^{-1} s^{-1}$ respectively in bulk W-doped $ReSe_2$, giving an estimate of the ratio of perpendicular to parallel effective masses as $(20.8/6.8)^{0.5} = 1.75$, very close to what we observe. Likewise, Tiong *et al.*[30] found a ratio of resistivities of ~4, giving an estimate of the ratio of perpendicular to parallel effective masses of ~2.

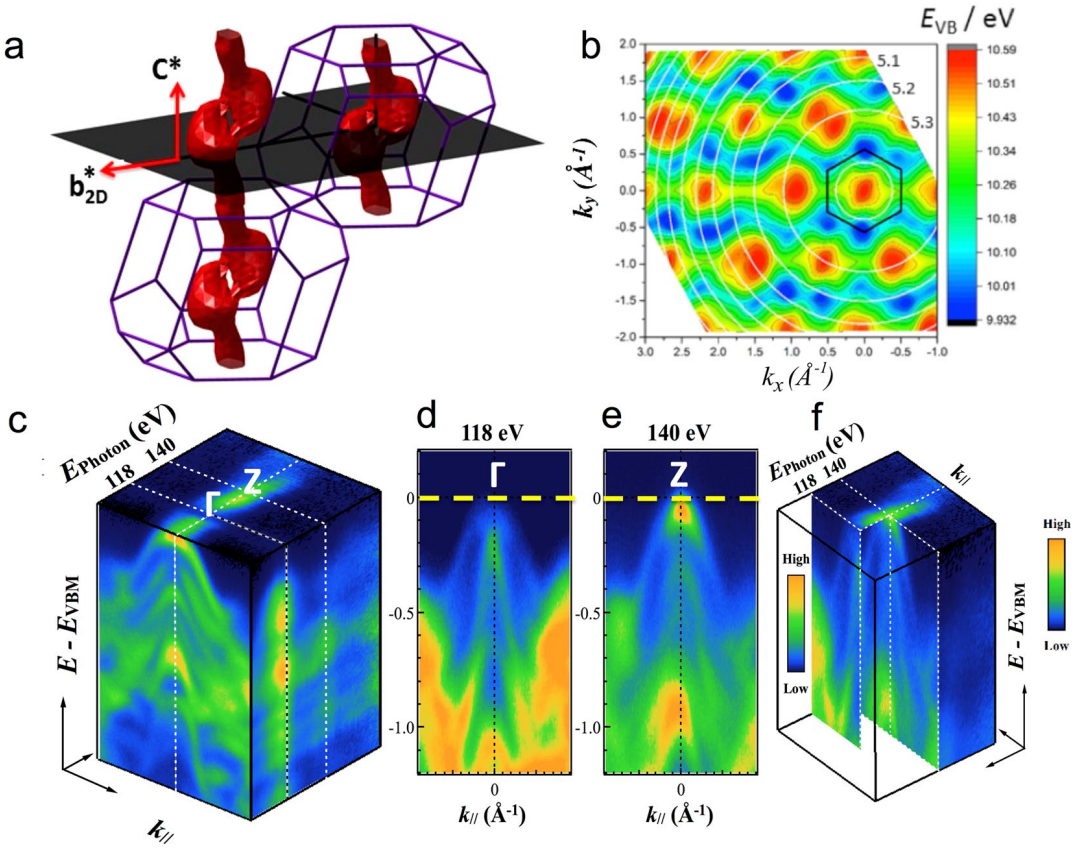

Figure 5. Three-dimensional electronic band structure of the $ReSe_2$ (**a**) Perspective view of the Brillouin zone: red surface: the constant energy surface for the valence band states at 80 meV below the valence band maximum. The shaded plane shows a plane parallel to the crystal layers; this is the plane sampled in an ARPES experiment at a given excitation phonon energy (neglecting the curvature due to momentum conservation discussed in the text). (**b**) Energy E_{VB} of the highest-lying valence band state as a function of in-plane momenta $\boldsymbol{k_x}$ and $\boldsymbol{k_y}$, calculated taking into account the variation of the momentum k_z normal to the layer expressed by equation 1. White circles indicate contours of constant k_z (three are labelled, top right, by their values in units of $2\pi/\boldsymbol{c^*}$) and the black hexagon shows the in-plane quasi-unit cell of Fig. 1(c) and (f) nano-ARPES signal (blue = low to orange = high) as a function of energy below the Fermi energy (vertical axis) and in-plane momentum $\boldsymbol{k_{xy}}$, for excitation energies of 118 and 140 eV (left and right respectively). **(d)** and **(e)** panels show the nano-ARPES electronic dispersion of the valence bands at the Γ and Z points of the 3D Brillouin unit cell.

However, more experimental data as a function of carrier concentration is needed since hole, electron and ambipolar transport have all been reported in $ReSe_2$.

The simulations showed in Figs 2, 3 and 4 account for the non-conservation of the initial electron momentum k_z perpendicular to the crystal surface in photoemission[35]. This is particularly important here, since there is significant dispersion of the energy bands in the k_z ($\boldsymbol{c^*}$) direction, as shown by the calculated constant-energy surfaces plotted in Fig. 5a. We proceed as follows: assuming the final state is a free electron with kinetic energy E_{kin} and a parabolic dispersion starting at the inner potential V_0, then k_z in the initial state is

$$|k_z| = \frac{\sqrt{2m}}{\hbar}\sqrt{(E_{kin}\cos^2\theta) + V_0} \quad (1)$$

where m is the free electron mass, θ is the polar emission angle, and $E_{kin} = E_{photon} - \phi - E_B$ where E_{photon} is the excitation photon energy, ϕ is the work function of the material and E_B is the binding energy of the initial state[44]. For $ReSe_2$, the inner potential V_0 is unknown and so its value was estimated as part of this work.

To determine V_0, the excitation photon energy has been varied whilst monitoring the photoemission perpendicular to the crystal surface ($\theta = 0$); we look for those photon energies for which k_z in the above equation is an integer or half-integer multiple of the reciprocal lattice vector $\boldsymbol{c^*}$ (the Γ and Z points respectively) Experimental data are shown in Fig. 5c. The ARPES dispersion as a function of the incident photon energy for 95 eV $< E_{photon} <$ 180 eV shows clear photoemission minima and maxima at 118 and 141 eV respectively, (Figs 5c–f and S4 of the Supplementary Information). This, together with the magnitude of $\boldsymbol{c^*}$ (0.984 $Å^{-1}$) gives $V_0 = 19.1 \pm 0.1$ eV (see SI, Fig. S4 for further discussion of the analysis). This value is typical for similar TMDs (e.g, $V_0 = 13$ eV for WSe_2)[45].

For finite in-plane momentum ($\theta \neq 0$), as in the maps of Fig. 2 and equation 1 shows that the value of k_z in the initial state will vary as θ is varied at a given binding energy and photon energy. Therefore, the experimental section through the 3D band structure is not strictly planar, as drawn in Fig. 5a, but is curved. A view of a calculated Fermi surface map over a very wide in-plane momentum range is shown in Fig. 5b, where the circular contours of constant k_z centred on ($k_x = 0$, $k_y = 0$) are also plotted (labelled by their respective multiples of $\boldsymbol{c}^*$) and two examples of how this map changes with excitation energy are shown in Fig. S5 of the Supplementary Information. Remarkably, we see that the local VB maxima are sometimes situated in the centre of the pseudo-Brillouin zone at Γ' (for instance, this is the case for the ($k_x = 0$, $k_y = 0$) VBM which is at the centre of the hexagonal quasi-unit cell indicated on Fig. 5b) and sometimes they lie either side of the Γ' point. This reveals again the significant degree of dispersion of the VB in the $\boldsymbol{c}^*$ direction normal to the layers. The surfaces of constant energy are not simple cylinders oriented along $\boldsymbol{c}^*$, but bifurcate periodically as shown in Fig. 5a, so that transverse sections through them will show one or two maxima depending on the height of the section in the $\boldsymbol{c}^*$ direction and, thus, the choice of excitation photon energy.

To visualise this bifurcation better, we have also plotted constant energy surfaces at about 0.2 eV below the VBM for the full 3D Brillouin zone (the red surface in Fig. 5a). Where the constant energy surfaces split into two, constant energy surfaces closer to the Fermi level show that there are two global VB maxima located close to the plane of c^* and b^*_{2D} in the volume of the BZ, but not at its surface, and not at any special k-points; they are centred in the lobes of the surface shown in Fig. 5a. These maxima are missed in previous calculations of the band structure which have usually focussed on the dispersion along paths between high-symmetry points in the BZ[24]. In Fig. S6 of the Supplementary Information, we show calculated valence and conduction band dispersions along the path in the Brillouin zone passing through these two maxima, to confirm that the gap at this point is indirect.

Discussion

In studies of the rhenium chalcogenides, much attention has focused on the question of whether $ReSe_2$ and ReS_2 possess indirect or direct bandgaps in bulk and monolayer forms. This discussion was based initially on optical studies of few-micron sized bulk samples and was extended to the monolayers as these became available; a consensus is gradually emerging that $ReSe_2$ has an indirect band gap with a valence band maximum located away from the Brillouin zone centre, and that it remains indirect down to one monolayer, whilst ReS_2 was claimed until recently to have a direct gap at all thicknesses. First-principles calculations at various levels of approximation have been used to support the experimental studies and it is clear that the positions of the band extrema in such calculations are sensitive to the details of the calculation (in particular, whether or not SOC is included, and what rhenium valence is assumed in DFT) so that previous reports are not entirely consistent.

The present work has tested these ideas and we find that the valence band maxima are indeed located away from the zone centre, as suspected, but that they do not sit precisely on a high symmetry direction and so are easily missed in calculations following conventional paths around special k points in the Brillouin zone[24,46]. Nevertheless, the dispersion in the directions analogous to the two-dimensional hexagonal M and K points is of importance because it shows directly the anisotropy found in experimental studies of optical and transport properties. The key directions are b^*_{2D} (which lies in the real space layer plane, is perpendicular to the Re chains and is a vector in direction Γ-M_1) and the vector in direction Γ-K_2 which also lies in the plane and is normal to b^*_{2D}. Figure 2 showed already that these two directions will display the basic crystal anisotropy very clearly. The measured and calculated valence band dispersions for bulk $ReSe_2$ in these two directions are shown in Fig. 4; the colour map in the calculated results indicates the projection of the state onto the Re d orbitals, which are the major constituent of the valence band edge. It is clear that the valence band maximum lies off-centre and that there is good quantitative agreement between the band structures in both Γ-M_1 and Γ-K_2 directions down to a binding energy $E - E_F$ of at least −2 eV. We emphasize that no fitting has been carried out here; the momentum scale for the simulations is adjusted only by the ratio between the experimental and calculated lattice parameters, so as to scale the Brillouin zones to the same size. This agreement gives confidence in the calculations over the whole Brillouin zone summarised in Figs 3, 4 and 5. In the Supplementary information, Fig. S7, we show predictions for a ReSe2 monolayer based on the same level of approximation; we find it also to be a highly anisotropic material with an indirect gap; the VBM is located either side of Γ, as the projection of Fig. 5a onto the k_x-k_y plane would suggest, and the conduction band minimum is located at Γ.

Methods

ARPES experiments. Photoemission studies were carried out using the ARPES k-microscope of the ANTARES beamline of the SOLEIL synchrotron, equipped with two Fresnel zone plates for focusing of the synchrotron radiation to a beam size of ~100 nm (or 140 μm in micro-ARPES mode) and an order selection aperture to eliminate higher diffraction orders. The nanoscale resolution ensured that monocrystalline regions were probed. The bulk polycrystalline sample was mounted on a nano-positioning stage which allowed both angle-resolved and mapping measurements (the latter were used to identify homogeneous single-crystal regions of the sample, which was cleaved in UHV prior to measurement). Experiments were performed at photon energies from 95 to 180 eV with an energy resolution of ~10 meV and angular resolution of ~0.2° corresponding, for electron energies around 100 eV, to an in-plane momentum resolution of ~0.02 $Å^{-1}$. ARPES measurements were carried out with the sample rear-cooled to 100 K in a vacuum of better than 10^{-10} mbar on a surface cleaved under vacuum.

Density functional theory calculations. DFT simulations used the Quantum Espresso[47] (QE) suite of plane-wave codes for total energy and band structure calculations and for post-processing to obtain electronic wavefunctions projected onto atomic bases. XCrysden[48] was used for real and reciprocal space visualisation, including the generation of Fig. 1. Fully relativistic pseudopotentials and projector augmented wave (PAW) datasets were generated using QE and PSLibrary[49] for both PBESOL[50] (generalized gradient approximation, GGA) and PZ[51] (local density approximation, LDA) exchange-correlation functionals; the valence of Re was taken as

15 ($5s^2$ $5p^6$ $5d^5$ $6s^2$). No dispersion corrections (representing van der Waals forces) were included, though the PBESOL functional has been shown[52] to be capable of yielding results for vdW systems that are as good as those obtained from semi-empirical approaches aimed at treating dispersive interactions such as DFT-D2[53,54]. Atomic coordinates were taken from Lamfers *et al.*[10] and were relaxed to obtain forces less than 10^{-3} eV Å^{-1}. Kinetic energy cutoffs were typically 60 Ry (816 eV) and Monkhorst-Pack[55] *k*-point meshes of $6 \times 6 \times 6$ were used; meshes up to $10 \times 10 \times 10$ produced no significant changes in the band structures obtained. Results obtained using LDA and GGA are qualitatively similar; for instance, the VB anisotropy and the bifurcation of the VBM appear in both and the main difference, as expected, is in the size of the band gap.

Sample characterisation. Polycrystalline bulk samples were obtained from hqgraphene.com and secondary ion mass spectrometry was used by the manufacturers to confirm 99.9995% purity with respect to common impurities including the halogen transport agents used in crystal growth. Samples were studied extensively by Raman spectroscopy[24], confirming their 1 T' phase and good crystal quality. Single-crystal domains varied in size from a few hundred to tens of μm (see Fig. S8 of the Supporting Information).

Data availability. Data supporting this study are available from the University of Bath data archive (DOI: 10.15125/BATH-00332.

References

1. Wilson, J. A. & Yoffe, A. D. The transition metal dichalcogenides: discussion and interpretation of the observed optical, electrical and structural properties. *Adv. Phys.* **18**, 193–335, doi:10.1080/00018736900101307 (1969).
2. Rahman, M., Davey, K. & Qiao, S. Z. Advent of 2D Rhenium Disulfide (ReS_2): Fundamentals to Applications. *Adv. Funct. Mater.* **27**, 1606129, doi:10.1002/adfm.201606129 (2017).
3. Geim, A. K. & Grigorieva, I. V. Van der Waals heterostructures. *Nature* **499**, 419–425, doi:10.1038/nature12385 (2013).
4. Wang, X. & Xia, F. Van der Waals heterostructures: Stacked 2D materials shed light. *Nat Mater* **14**, 264–265, doi:10.1038/nmat4218 (2015).
5. Wang, Q. H., Kalantar-Zadeh, K., Kis, A., Coleman, J. N. & Strano, M. S. Electronics and optoelectronics of two-dimensional transition metal dichalcogenides. *Nat. Nanotechnol* **7**, 699–712, doi:10.1038/nnano.2012.193 (2012).
6. Duan, X., Wang, C., Pan, A., Yu, R. & Duan, X. Two-dimensional transition metal dichalcogenides as atomically thin semiconductors: opportunities and challenges. *Chem. Soc. Rev.* **44**, 8859–8876, doi:10.1039/C5CS00507H (2015).
7. Zhu, Z. Y., Cheng, Y. C. & Schwingenschlögl, U. Giant spin-orbit-induced spin splitting in two-dimensional transition-metal dichalcogenide semiconductors. *Phys. Rev. B* **84**, 153402, doi:10.1103/PhysRevB.84.153402 (2011).
8. He, K. *et al.* Tightly Bound Excitons in Monolayer WSe_2. *Phys. Rev. Lett.* **113**, 026803, doi:10.1103/PhysRevLett.113.026803 (2014).
9. Wang, G. *et al.* Spin-orbit engineering in transition metal dichalcogenide alloy monolayers. *Nat Commun* **6**, doi:10.1038/ncomms10110 (2015).
10. Lamfers, H. J., Meetsma, A., Wiegers, G. A. & deBoer, J. L. The crystal structure of some rhenium and technetium dichalcogenides. *J. Alloys Compd.* **241**, 34–39, doi:10.1016/0925-8388(96)02313-4 (1996).
11. Wildervanck, J. C. & Wildervanck, F. & Jellinek. The dichalcogenides of technetium and rhenium. *J. Less-Common Met.* **24**, 73–81 (1971).
12. Murray, H. H., Kelty, S. P., Chianelli, R. R. & Day, C. S. Structure of rhenium disulphide. *Inorg. Chem.* **33**, 4418–4420, doi:10.1021/ic00097a037 (1994).
13. Alcock, N. W. & Kjekshus, A. Crystal structure of $ReSe_2$. *Acta Chem. Scand.* **19**, 79, doi:10.3891/acta.chem.scand.19-0079 (1965).
14. Zhong, H.-X., Gao, S., Shi, J.-J. & Yang, L. Quasiparticle band gaps, excitonic effects, and anisotropic optical properties of the monolayer distorted 1T diamond-chain structures ReS_2 and $ReSe_2$. *Phys. Rev. B* **92**, doi:10.1103/PhysRevB.92.115438 (2015).
15. Ho, C. H., Huang, Y. S., Chen, J. L., Dann, T. E. & Tiong, K. K. Electronic structure of ReS_2 and $ReSe_2$ from first-principles calculations, photoelectron spectroscopy, and electrolyte electroreflectance. *Phys. Rev. B* **60**, 15766–15771, doi:10.1103/PhysRevB.60.15766 (1999).
16. Ho, C. H., Huang, Y. S., Liao, P. C. & Tiong, K. K. Piezoreflectance study of band-edge excitons of $ReS_{2-x}Se_x$ single crystals. *Phys. Rev. B* **58**, 12575–12578, doi:10.1103/PhysRevB.58.12575 (1998).
17. Zibouche, N., Philipsen, P., Kuc, A. & Heine, T. Transition-metal dichalcogenide bilayers: Switching materials for spintronic and valleytronic applications. *Phys. Rev. B* **90**, 125440, doi:10.1103/PhysRevB.90.125440 (2014).
18. Nemilentsau, A., Low, T. & Hanson, G. Anisotropic 2D Materials for Tunable Hyperbolic Plasmonics. *Phys. Rev. Lett.* **116**, doi:10.1103/PhysRevLett.116.066804 (2016).
19. Yang, S. X. *et al.* High-Performance Few-layer Mo-doped $ReSe_2$ Nanosheet Photodetectors. *Sci Rep* **4**, 6, doi:10.1038/srep05442 (2014).
20. Liu, E. *et al.* High Responsivity Phototransistors Based on Few-Layer ReS_2 for Weak Signal Detection. *Adv. Funct. Mater.* **26**, 1938–1944, doi:10.1002/adfm.201504408 (2016).
21. Joshua, O. I., Gary, A. S., Herre, S. JvdZ. & Andres, C.-G. Environmental instability of few-layer black phosphorus. *2D Materials* **2**, 011002, doi:10.1088/2053-1583/2/1/011002 (2015).
22. Lorchat, E., Froehlicher, G. & Berciaud, S. Splitting of interlayer shear modes and photon energy dependent anisotropic Raman response in n-layer $ReSe_2$ and ReS_2. *ACS Nano* **10**, 2752–2760, doi:10.1021/acsnano.5b07844 (2016).
23. Tongay, S. *et al.* Monolayer behaviour in bulk ReS2 due to electronic and vibrational decoupling. *Nature Communications* **5**, doi:10.1038/ncomms4252 (2014).
24. Wolverson, D., Crampin, S., Kazemi, A. S., Ilie, A. & Bending, S. J. Raman Spectra of Monolayer, Few-Layer, and Bulk $ReSe_2$: An Anisotropic Layered Semiconductor. *ACS Nano* **8**, 11154–11164, doi:10.1021/nn5053926 (2014).
25. Huang, Y. S., Ho, C. H., Liao, P. C. & Tiong, K. K. Temperature dependent study of the band edge excitons of ReS_2 and $ReSe_2$. *J. Alloys Compd.* **262**, 92–96, doi:10.1016/s0925-8388(97)00335-6 (1997).
26. Ho, C. H., Liao, P. C., Huang, Y. S. & Tiong, K. K. Piezoreflectance study of the band-edge excitons of ReS_2. *Solid State Commun.* **103**, 19–23, doi:10.1016/s0038-1098(97)00135-x (1997).
27. Ho, C. H., Liao, P. C., Huang, Y. S. & Tiong, K. K. Temperature dependence of energies and broadening parameters of the band-edge excitons of ReS_2 and $ReSe_2$. *Phys. Rev. B* **55**, 15608–15613, doi:10.1103/PhysRevB.55.15608 (1997).
28. Ho, C. H., Liao, P. C., Huang, Y. S., Yang, T. R. & Tiong, K. K. Optical absorption of ReS_2 and $ReSe_2$ single crystals. *J. Appl. Phys.* **81**, 6380–6383, doi:10.1063/1.365357 (1997).
29. Liang, C. H., Tiong, K. K., Huang, Y. S., Dumcenco, D. & Ho, C. H. In-plane anisotropic electrical and optical properties of gold-doped rhenium disulphide. *Journal of Materials Science-Materials in Electronics* **20**, 476–479, doi:10.1007/s10854-008-9685-2 (2009).
30. Tiong, K. K., Ho, C. H. & Huang, Y. S. The electrical transport properties of ReS_2 and $ReSe_2$ layered crystals. *Solid State Commun.* **111**, 635–640, doi:10.1016/s0038-1098(99)00240-9 (1999).
31. Yang, S. X. *et al.* Layer-dependent electrical and optoelectronic responses of $ReSe_2$ nanosheet transistors. *Nanoscale* **6**, 7226–7231, doi:10.1039/c4nr01741b (2014).
32. Ho, C. H., Hsieh, M. H., Wu, C. C., Huang, Y. S. & Tiong, K. K. Dichroic optical and electrical properties of rhenium dichalcogenides layer compounds. *J. Alloys Compd.* **442**, 245–248, doi:10.1016/j.jallcom.2006.08.359 (2007).

33. Jariwala, B. *et al.* Synthesis and Characterization of ReS_2 and $ReSe_2$ Layered Chalcogenide Single Crystals. *Chem. Mater.* **28**, 3352–3359, doi:10.1021/acs.chemmater.6b00364 (2016).
34. Liu, E. *et al.* Integrated digital inverters based on two-dimensional anisotropic ReS_2 field-effect transistors. *Nat Commun* **6**, doi:10.1038/ncomms7991 (2015).
35. Huefner, S. *Photoelectron Spectroscopy* (Springer, 1996).
36. Fang, C. M., Wiegers, G. A., Haas, C. & deGroot, R. A. Electronic structures of ReS_2, $ReSe_2$ and TcS_2 in the real and the hypothetical undistorted structures. *J. Phys.: Condens. Matter* **9**, 4411–4424, doi:10.1088/0953-8984/9/21/008 (1997).
37. Dumcenco, D., Huang, Y. S., Liang, C. H. & Tiong, K. K. Optical characterization of Au-doped rhenium diselenide single crystals. *J. Appl. Phys.* **104**, doi:10.1063/1.2977682 (2008).
38. Jian, Y.-C., Lin, D.-Y., Wu, J.-S. & Huang, Y.-S. Optical and Electrical Properties of Au- and Ag-Doped $ReSe_2$. *Japanese Journal of Applied Physics* **52**, doi:10.7567/JJAP.52.04CH06 (2013).
39. Wang, X. *et al.* Enhanced rectification, transport property and photocurrent generation of multilayer $ReSe_2/MoS_2$ p–n heterojunctions. *Nano Research* **9**, 507–516, doi:10.1007/s12274-015-0932-6 (2016).
40. Zhang, E. *et al.* Tunable Ambipolar Polarization-Sensitive Photodetectors Based on High-Anisotropy $ReSe_2$ Nanosheets. *ACS Nano* **10**, 8067–8077, doi:10.1021/acsnano.6b04165 (2016).
41. Price, P. Two-dimensional electron transport in semiconductor layers. I. Phonon scattering. *Annals of Physics* **133**, 217–239 (1981).
42. Xi, J., Long, M., Tang, L., Wang, D. & Shuai, Z. First-principles prediction of charge mobility in carbon and organic nanomaterials. *Nanoscale* **4**, 4348–4369, doi:10.1039/C2NR30585B (2012).
43. Hu, S. Y., Liang, C. H., Tiong, K. K., Huang, Y. S. & Lee, Y. C. Electrical anisotropy of W-doped $ReSe_2$ crystals. *J. Electrochem. Soc.* **153**, J100–J102, doi:10.1149/1.2209589 (2006).
44. Damascelli, A. Probing the electronic structure of complex systems by ARPES. *Phys. Scr.* **2004**, 61, doi:10.1238/Physica.Topical.109a00061 (2004).
45. Riley, J. M. *et al.* Direct observation of spin-polarized bulk bands in an inversion-symmetric semiconductor. *Nature Physics* **10**, 835–839 (2014).
46. Zhao, H. *et al.* Interlayer Interactions in Anisotropic Atomically-thin Rhenium Diselenide. *Nano Res.* **8**, 3651, doi:10.1007/s12274-015-0865-0 (2015).
47. Giannozzi, P. *et al.* QUANTUM ESPRESSO: a modular and open-source software project for quantum simulations of materials. *J. Phys.: Condens. Matter* **21**, 395502, doi:10.1088/0953-8984/21/39/395502 (2009).
48. Kokalj, A. Computer graphics and graphical user interfaces as tools in simulations of matter at the atomic scale. *Comput. Mater. Sci.* **28**, 155–168, doi:10.1016/S0927-0256(03)00104-6 (2003).
49. Dal Corso, A. Pseudopotentials periodic table: From H to Pu. *Comput. Mater. Sci.* **95**, 337–350, doi:10.1016/j.commatsci.2014.07.043 (2014).
50. Perdew, J. P. *et al.* Restoring the Density-Gradient Expansion for Exchange in Solids and Surfaces. *Phys. Rev. Lett.* **100**, 136406, doi:10.1103/PhysRevLett.100.136406 (2008).
51. Perdew, J. P. & Zunger, A. Self-interaction correction to density-functional approximations for many-electron systems. *Phys. Rev. B* **23**, 5048–5079, doi:10.1103/PhysRevB.23.5048 (1981).
52. Tunega, D., Bučko, T. & Zaoui, A. Assessment of ten DFT methods in predicting structures of sheet silicates: Importance of dispersion corrections. *The Journal of Chemical Physics* **137**, 114105, doi:10.1063/1.4752196 (2012).
53. Grimme, S. Semiempirical GGA-type density functional constructed with a long-range dispersion correction. *J. Comput. Chem.* **27**, 1787–1799 (2006).
54. Bucko, T., Hafner, J. r., Lebegue, S. & Angyán, J. G. Improved description of the structure of molecular and layered crystals: ab initio DFT calculations with van der Waals corrections. *The Journal of Physical Chemistry A* **114**, 11814–11824, doi:10.102/jp106469x (2010).
55. Monkhorst, H. J. & Pack, J. D. Special points for Brillouin-zone integrations. *Phys. Rev. B* **13**, 5188–5192, doi:10.1103/PhysRevB.13.5188 (1976).

Acknowledgements

Work was supported by the Engineering and Physical Sciences Research Council of the UK under grant EP/P004830/1 and LSH received a studentship under grant EP/L014544/1. JLW was supported under grant EP/M022188. ARPES measurements were provided at the ANTARES beamline of the SOLEIL synchrotron under project 20151237. Computational work was performed on the University of Bath's High Performance Computing Facility.

Author Contributions

L.S.H. and J.L.W. prepared and characterised the samples and L.S.H., J.L.W., C.C. and J.A. carried out the ARPES measurements. D.W., M.C.A. and J.A. conceived the measurements and D.W. carried out the computational work. S.D. and S.J.B. created the device structures and carried out the transport measurements. M.M.K. created Figure 5a and all authors contributed to the interpretation of the data. All authors read and approved the manuscript.

Additional Information

Supplementary information accompanies this paper at doi:10.1038/s41598-017-05361-6

Competing Interests: The authors declare that they have no competing interests.

Publisher's note: Springer Nature remains neutral with regard to jurisdictional claims in published maps and institutional affiliations.

Electronic bandstructure and van der Waals coupling of $ReSe_2$ revealed by high-resolution angle-resolved photoemission spectroscopy

Lewis S Hart[1], James L Webb[1], Sara Dale[1], Simon J. Bending[1], Marcin Mucha-Kruczynski[1], Daniel Wolverson[1*], Chaoyu Chen[2], José Avila[2], Maria C. Asensio[2]

[1]Centre for Nanoscience and Nanotechnology, Department of Physics, University of Bath, Bath BA2 7AY, United Kingdom
[2]Synchrotron SOLEIL, Saint Aubin, and Université Paris-Saclay, BP 48 91192 Gif-sur-Yvette, France

Supplementary information

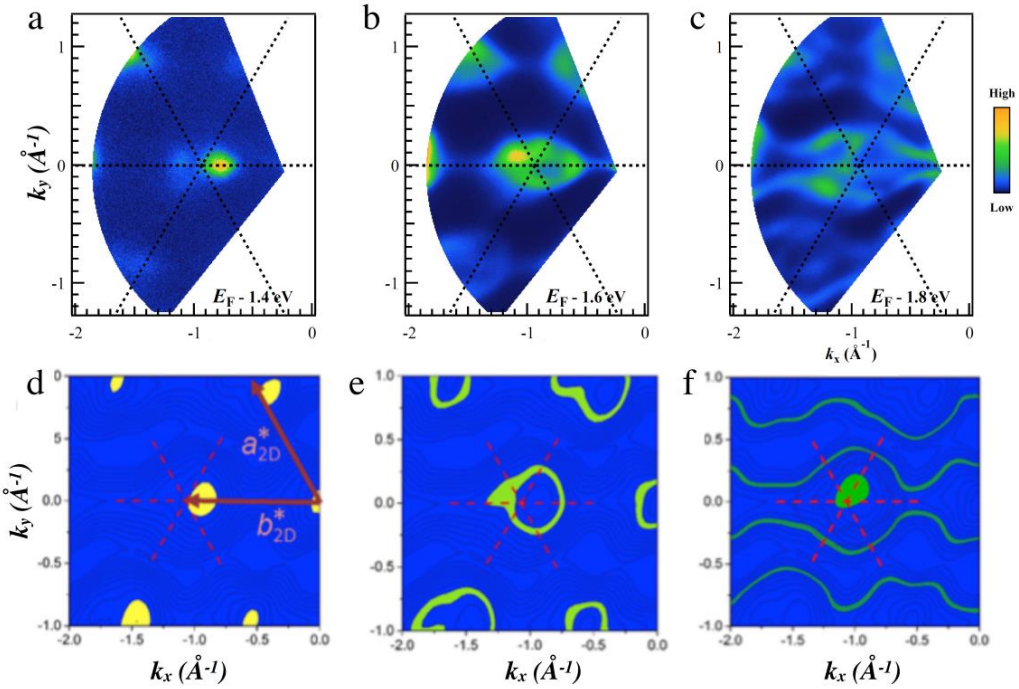

Figure S1. **ARPES maps of photoemission intensity as a function of in-plane wavevector** (**a**) near the valence band maximum (VBM); (**b**) 0.2 eV below the VBM and (**c**) 0.4 eV below the VBM. In each case, the dotted cross indicates the position of a Γ' point. For comparison, panels (**d**)-(**f**) show calculated constant energy contours of the highest energy valence band (**d**) near the VBM; (**e**) 0.2 eV below the VBM and (**f**) 0.4 eV below the VBM. In (**f**), the top of the next valence band contributes the near-central solid spot. The red arrows in (**d**) indicate the 2D projected reciprocal lattice vectors defined in Figure 1 and the dashed red lines again mark a Γ' point. The bar on the right indicates the arbitrary colour scale representing photoemission intensity (a-c), and valence band energy (d-f) respectively.

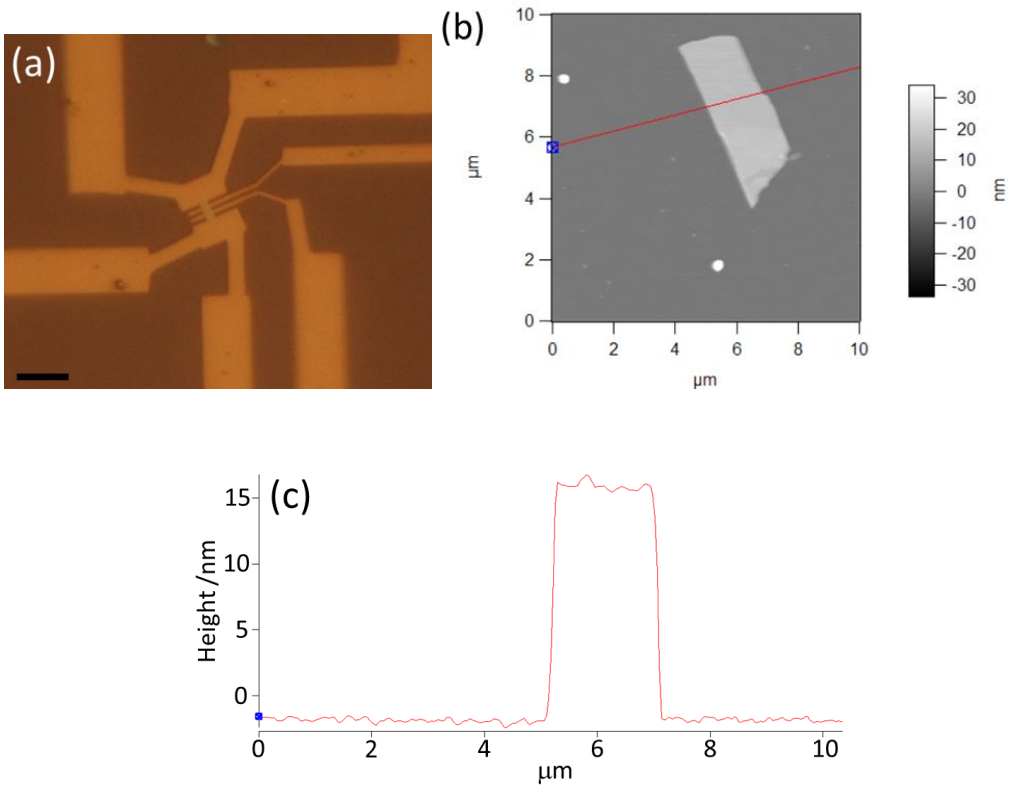

Figure S2. (a) Optical microscopy image of a field effect transistor structure fabricated from a $ReSe_2$ flake fabricated on an n^+-Si/SiO_2 (300 nm) substrate. The scale bar in bottom left hand corner represents 10 µm; (b) AFM image of the same $ReSe_2$ flake before electrical contacts were fabricated on top of the flake, with the red line showing the path of a line scan to determine the flake thickness; (c) An AFM line scan taken from image (b) to determine the height of the flake. The height was measured to be 18.3 nm and corresponds to a thickness of 26 monolayers (ref. 1 of main text).

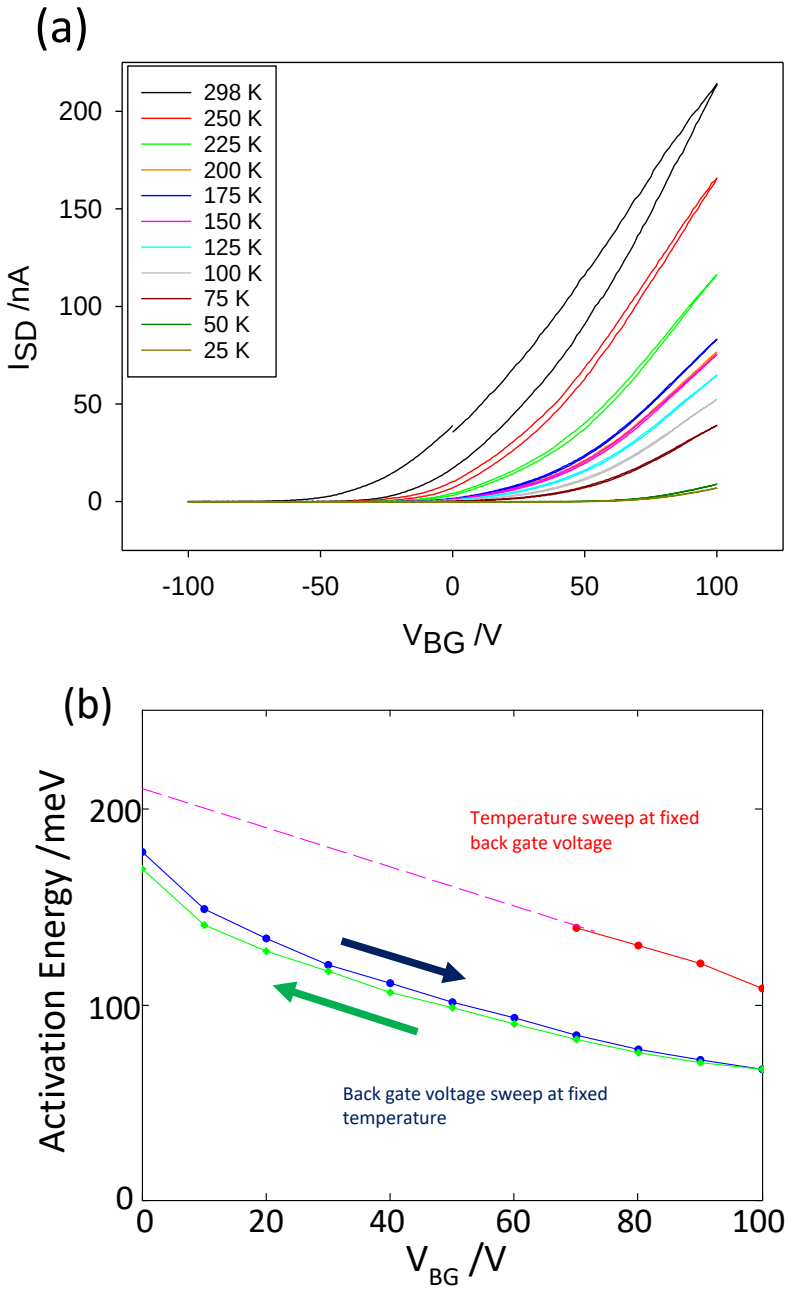

Figure S3. (a) Measurements of the $ReSe_2$ field effect transistor shown in figure S1 carried out at different temperatures with a back gate voltage V_{bg} applied to the n^+-Si substrate. The asymmetry of the source-drain current can be seen as a function of V_{bg} and clearly indicates n-type doping; (b) estimated activation energies deduced from fixed temperature back gate voltage sweeps (green and blue curves) and temperature sweep at fixed back gate voltage (red curve). A hysteresis can clearly be seen; however, both indicate an activation energy of 190 ± 20 meV, much smaller than half the band gap of $ReSe_2$.

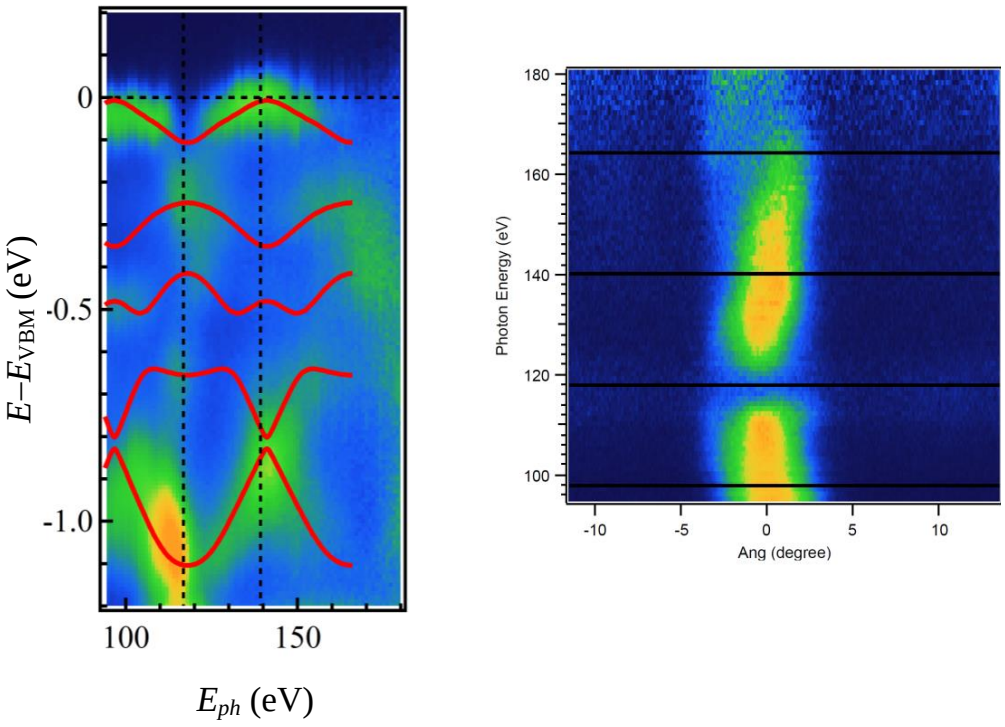

Figure S4. Left: photoemission signal for electrons with zero in-plane momentum and energies below the valence band maximum E_{VBM} as a function of excitation photon energy E_{ph}. Red lines: calculated valence band dispersion as a function of momentum in the c^* direction normal to the sample surface. Right: excerpt from the same dataset for $E\text{-}E_{VBM} = 0$, viewed as a function of emission angle to the sample normal, showing the photoemission signal for zero in-plane momentum as a function of excitation energy.

Estimate of the inner potential (V_0)

From the above data, there are minima and maxima in $E\text{-}E_{VBM}$ for the top valence band at excitation energies of 118 and 141 eV. Taking equation 1 of the main text,

$$|k_z| = \frac{\sqrt{2m}}{\hbar}\sqrt{(E_{kin}\, cos^2\theta) + V_0}$$

and recognizing that k_z is only determined to within an integer multiple n of the reciprocal lattice vector in the c^* (z) direction, then we require that, for $\theta = 0$ ($k_x = k_y = 0$),

$$n|c^*| = \frac{\sqrt{2m}}{\hbar}\sqrt{E_{kin} + V_0}, \quad E_{kin} = 118 \text{ eV}$$

and

$$\left(n + \frac{1}{2}\right)|c^*| = \frac{\sqrt{2m}}{\hbar}\sqrt{E_{kin} + V_0}, \qquad E_{kin} = 141 \text{ eV}$$

These conditions are satisfied with $c^* = 0.984$ Å^{-1} and $V_0 = 19.1$ eV if $n = 6$. Adjacent integers (or half-integers) yield negative or implausibly large values of V_0.

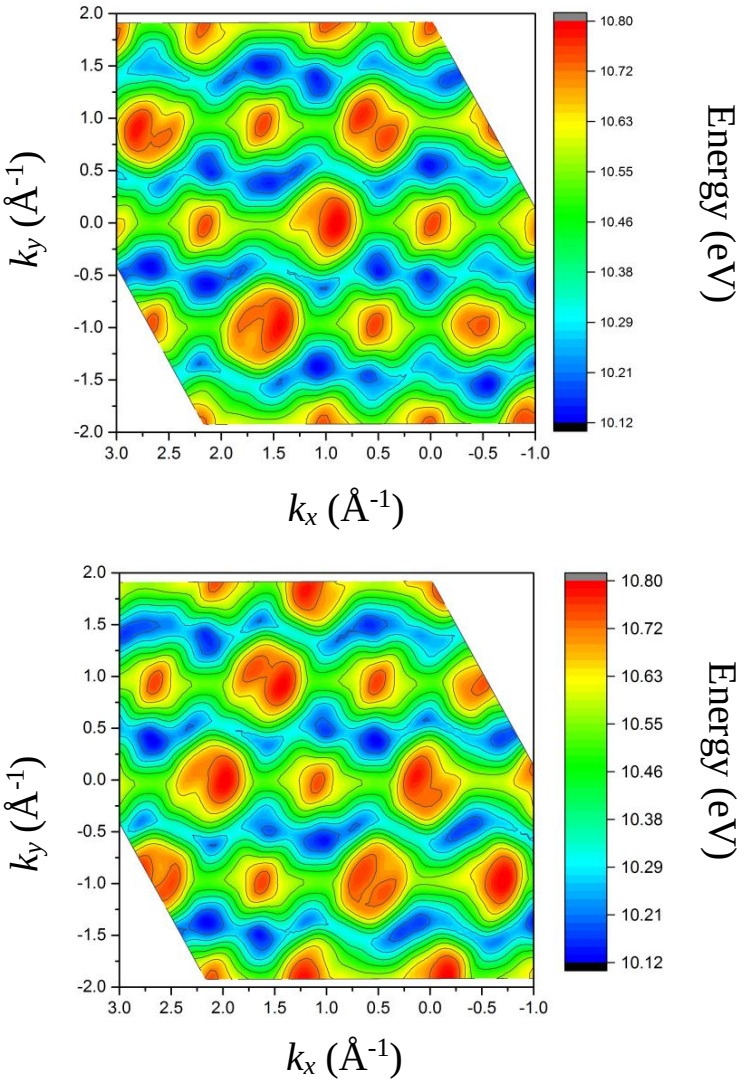

Figure S5.
Calculated ARPES sections through the highest valence band as a function of in-plane momentum k_x and k_y, taking into account the effects of the inner potential. Top: excitation energy 97 eV (which places the Z point at $k_x = k_y = 0$); bottom: excitation energy 118 eV (with the Γ point at $k_x = k_y = 0$). This demonstrates how the choice of excitation energy (and therefore c^* component) affects the measured section through the valence band constant-energy surfaces.

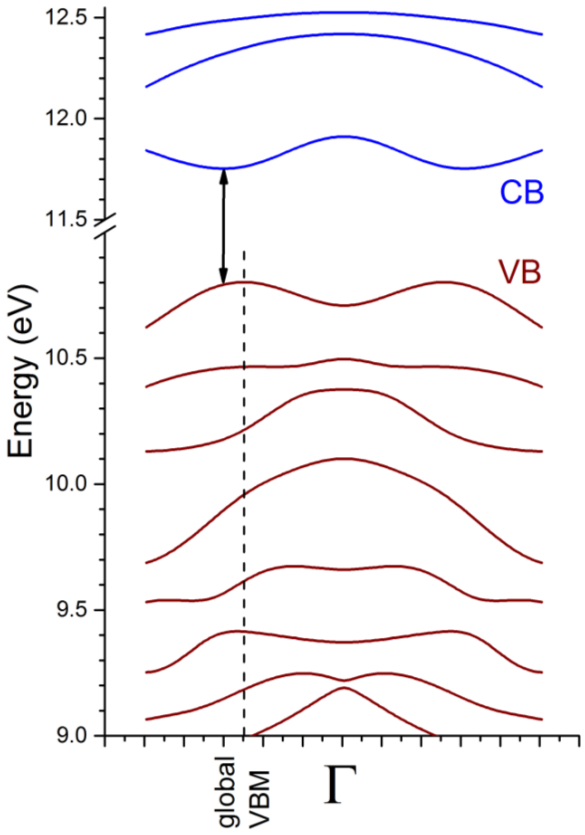

Figure S6
Calculated conduction band (top) and valence band (bottom) dispersion (energy versus momentum) for a path along the line passing through the two global valence band maxima within the first Brillouin zone (these are related by inversion through Γ). The vertical arrow through the conduction band minimum demonstrates that, at the VBM, the valence to conduction band transition is indirect though the band extrema lie quite close.

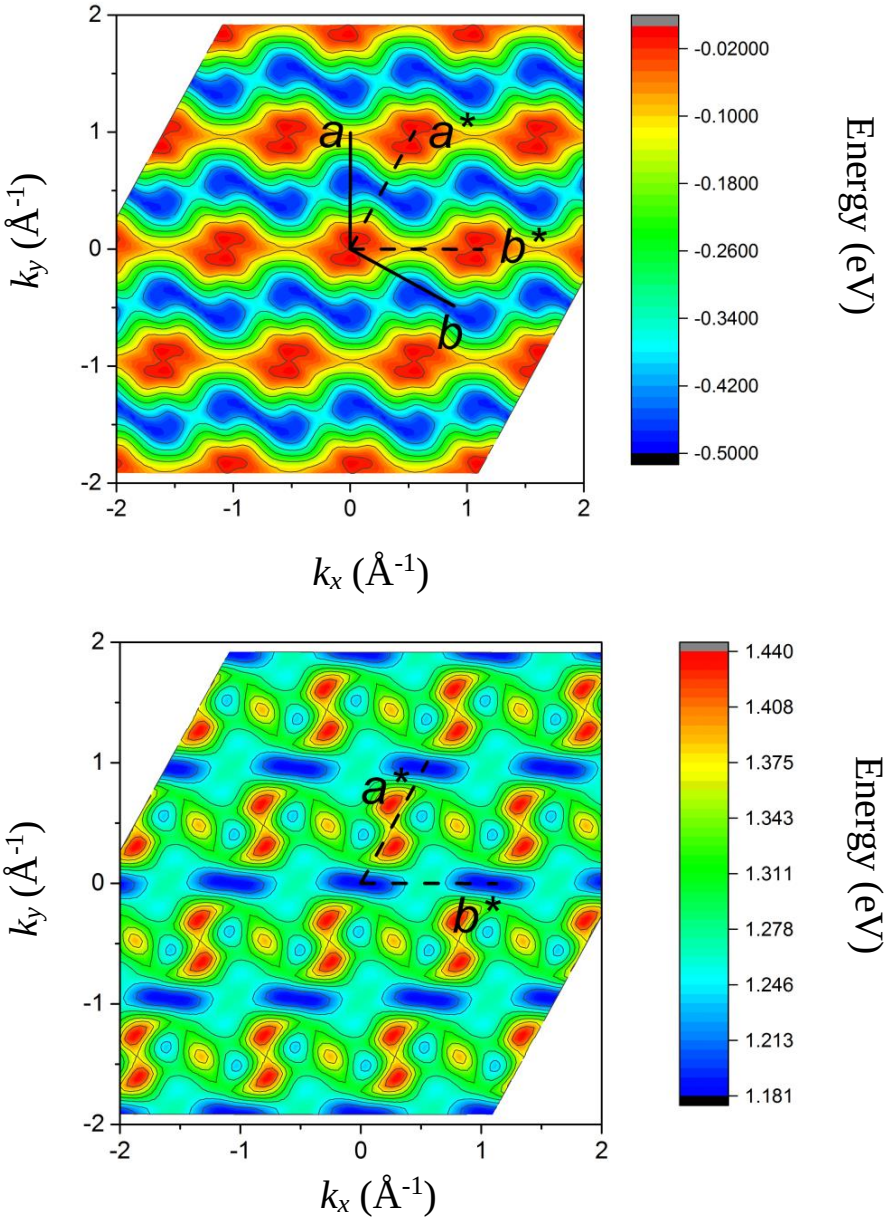

Figure S7

Calculated energies of the highest-lying valence band (top) and lowest conduction band (bottom) as a function of in-plane momenta k_x and k_y for a $ReSe_2$ **monolayer**. The reciprocal and real space lattice vectors are indicated. The local valence band maxima are highest in energy (red) and the conduction band minima are low in energy (blue), showing that the optical transition for monolayers is again indirect within the approximations of the fully relativistic DFT used (spin-orbit coupling included).

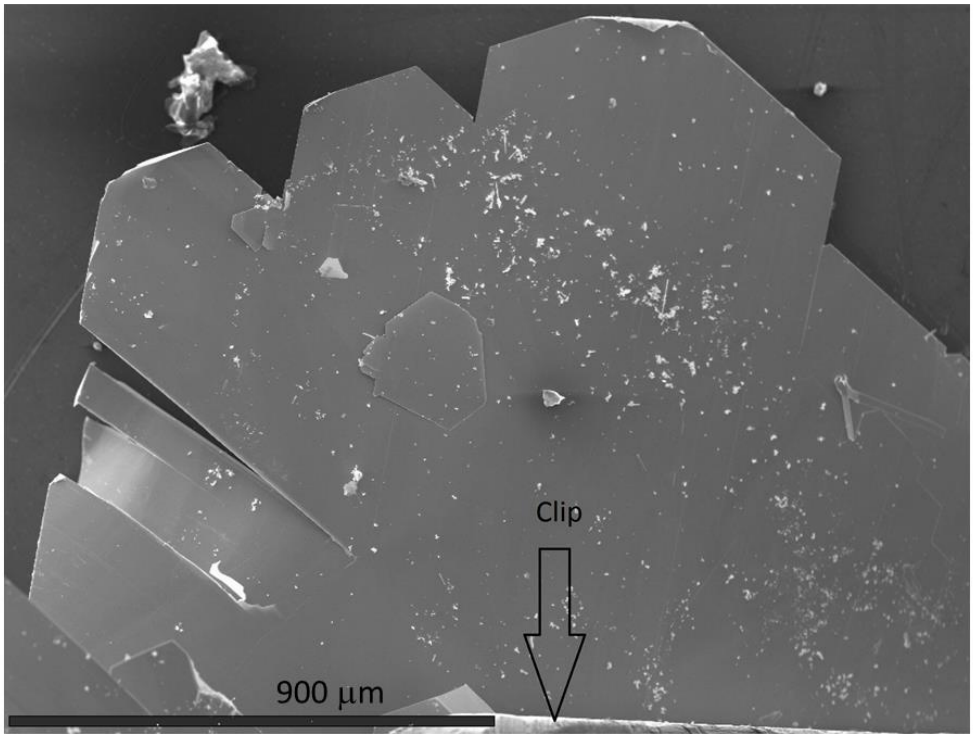

Figure S8
Scanning electron microscope image of a typical bulk crystal (which is the starting material before cleaving in UHV) showing large crystalline domains but with some misoriented detached flakes and few-micron-scale debris on the surface (scale bar is bottom left). Freshly cleaved surfaces will have less debris but a high spatial resolution was advantageous in finding regions (after cleaving in UHV) that gave well-resolved ARPES spectra associated with a single crystal domain.

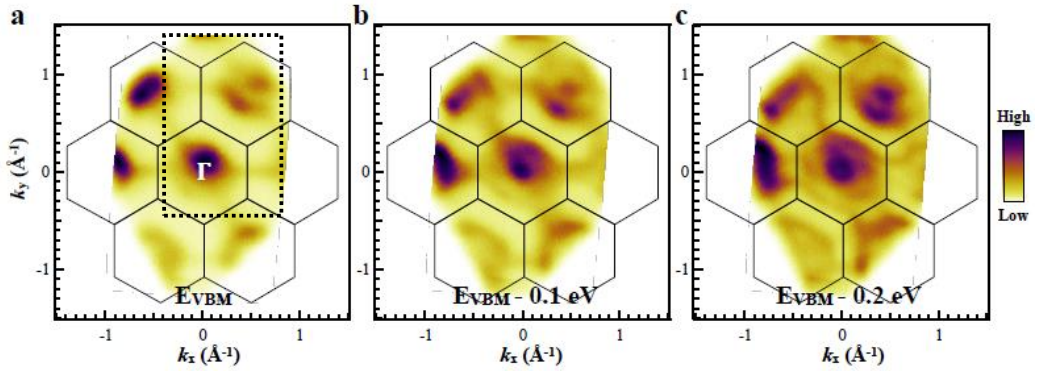

Figure S9

ARPES maps of photoemission intensity as a function of in-plane wavevector (a) near the valence band maximum (VBM); (**b**) 0.1 eV below the VBM and (**c**) 0.2 eV below the VBM. The excitation energy was 118 eV corresponding, according to the calculation of Fig. S4, to placing the three-dimensional Γ point at $k_x = k_y = 0$ in the ARPES maps. The above data can be compared to the simulation of Fig. S5, lower panel, which is reproduced again below for convenience; the dotted box in the experimental data highlights the Γ point and one neighbouring Γ' point which has a clear double structure due to the bifurcation of the constant energy surfaces shown in the main text, Fig. 5. Similar "double" Γ' points appear also in the simulated data below, and the Γ point at $k_x = k_y = 0$ shows a similar off-centre shape.

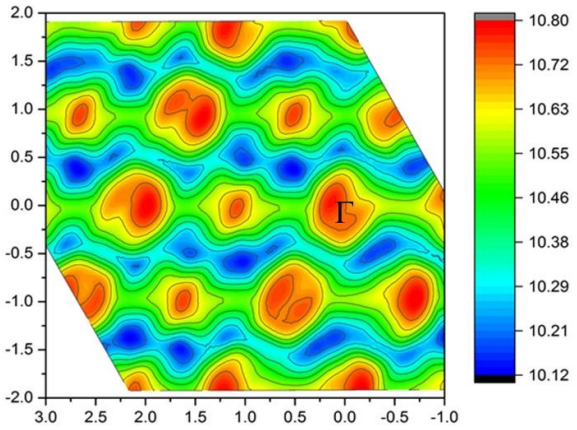

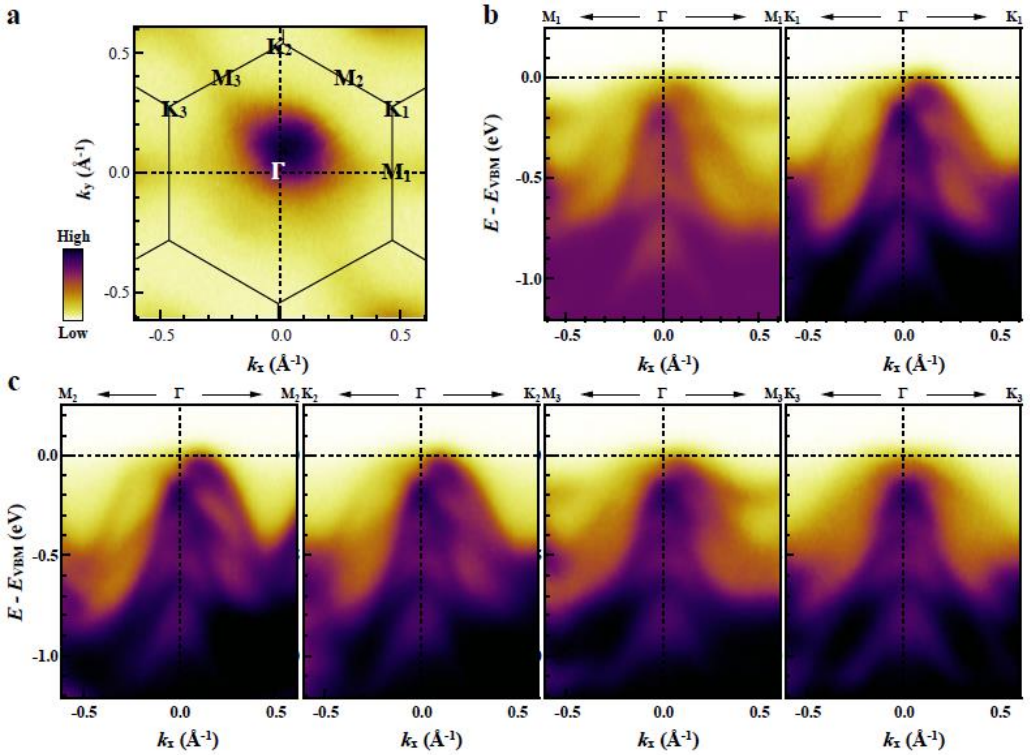

Figure S10

(a) Experimental photoemission signal as a function of in-plane momentum at an energy close to the VBM for a section through the Brillouin zone, showing the special points of the 2D quasi-Brillouin zone. This data can be compared to that of Fig. 3 of the main text but, as for Fig. S9, was now recorded with an excitation photon energy of 118 eV corresponding, according to the calculation of Fig. S4, to placing the three-dimensional Γ point at $k_x = k_y = 0$ in the ARPES maps. (**b**) ARPES data along the M'ΓM and K'ΓK directions in the reciprocal space (in each panel, k_x represents the in-plane momentum in the particular direction shown at the top of the panel). As analysed in detail for the Z point, the dispersion is flatter in the M1 direction and is more pronounced in the other directions.

7.4 Discussions

The results in this chapter show that: (i) the electronic band structure is anisotropic; (ii) the valence band maxima are not located along any of the high symmetry directions; and (iii) the band gap of bulk $ReSe_2$ is indirect.

The ARPES measurements in this paper are complemented by DFT calculations of the band structure. By using LDA and GGA pseudopotentials an excellent agreement can be found between the calculated and measured bands. This agreement is good for both the higher and lower lying valence bands, giving confidence in the results.

A limitation of this work is that only the valence bands of $ReSe_2$ are measured; to determine the nature of the band gap, it would be ideal to measure the conduction bands. It is possible to observe the conduction bands in an ARPES experiment by in situ electron doping the crystal using alkali materials. The facilities for in situ doping were not available at the ANTARES beamline. Nevertheless, this paper does predict the band gap of $ReSe_2$ by calculating the conduction bands using the same pseudopotential that gave valence bands which agreed with the ARPES measurements.

The ARPES measurements contained in this paper were all made using the nano-ARPES facility at the ANTARES beamline. A review into the progress of nano-ARPES has recently been published with some of the figures from the paper in this chapter reproduced [128].

It was previously thought that bulk $ReSe_2$ behaves like a stack of electrically decoupled monolayers. The results in this paper show that this is not the case and that the bulk crystal is a 3D material. By 3D material, it is meant that the band structure depends on k_z as well as k_x and k_y. The interlayer interactions are absent in a monolayer. Therefore the band structure of a monolayer is expected to be different to that of the bulk. In the next chapter ARPES and complementary DFT calculations are presented for monolayer $ReSe_2$.

Chapter 8

Angle-resolved photoemission measurements of monolayer $ReSe_2$

$ReSe_2$ has attracted interest in recent years because it is a layered material and so can be exfoliated down to a few atomic layers. This chapter will look at the properties of the few layer forms of this material.

There have been a large number of theoretical investigations that predict the band structure of monolayer $ReSe_2$. DFT calculations using LDA or GGA pseudopotentials find an indirect band gap, with the VBM near Γ [59]; however, GW self-energy corrected DFT calculations predict a direct band gap, with the VBM directly at Γ [57]. In principle ARPES measurements can identify the VBM, and this will be helpful in determining the nature of the band gap of monolayer $ReSe_2$.

Thanks to the technological advancements in the field of ARPES it is now possible to focus the spot size of the incident beam to less than a micron in diameter. This spatial resolution is essential for the measurement of thin flakes of TMDs. A monolayer of $ReSe_2$ usually exfoliates at best as a parallelogram with the long edge $\sim$10μm in length but with a width $\sim$2-5μm.

ARPES has been successfully utilised to measure the electronic band structures of many different monolayers including $MoSe_2$, WSe_2 and graphene [139]. A monolayer and a bilayer

of ReS_2 have also been measured [56]. In this chapter ARPES results of monolayer $ReSe_2$ will be presented.

8.1 Sample preparation

The preparation of a monolayer sample for ARPES can be more challenging than preparing a bulk crystal. The bulk sample can be cleaved in the preparation chamber in UHV conditions, exposing a fresh, clean surface. In contrast, there are many steps required to prepare an exfoliated monolayer, most of which cannot be done in UHV.

To achieve intense, well-defined bands there a few requirements of the sample. Firstly, the monolayer has to be flat. As described in Sec 3.2, if translational invariance is conserved the in-plane crystal momentum can be determined by measuring the emission angles of the photoelectrons. Any curvature in the flake will result in a change of these emission angles which will in turn cause error in determining the crystal momentum. For the monolayer to be flat the substrate must too be flat. Secondly, the surface of the monolayer has to be clean. If there are any contaminants upon the monolayer then they could impede the journey of the photoelectron from the sample to the photodetector. The sample has to be placed upon a conductive substrate to prevent charging. In an ARPES experiment electrons are liberated from a crystal, and if these electrons are not replenished the sample will become charged. The charge will result in an electric field that will perturb the energies of the emitted photoelectrons.

To fulfil all of the above requirements the monolayer was placed upon a graphite flake that is attached to a highly doped silicon substrate. Both the graphite and the silicon are conductive so no charging is expected. The graphite flake was prepared by micromechanical exfoliation, leaving a freshly cleaved, flat surface on which to place the $ReSe_2$ monolayer. To obtain a monolayer of $ReSe_2$, a bulk crystal was exfoliated onto a thin PDMS film. The monolayer of $ReSe_2$ was located using an optical microscope. Finally, the $ReSe_2$ monolayer was deterministically transferred from the PDMS to the graphite flake using the dry transfer

technique described in Sec 3.3 [130]. The van der Waals forces between the $ReSe_2$ monolayer and graphite flake will pull the two crystals together. Therefore, the monolayer will adopt the flat shape of the graphite beneath it [100]. The graphite and $ReSe_2$ crystals were grown by HQ Graphene.

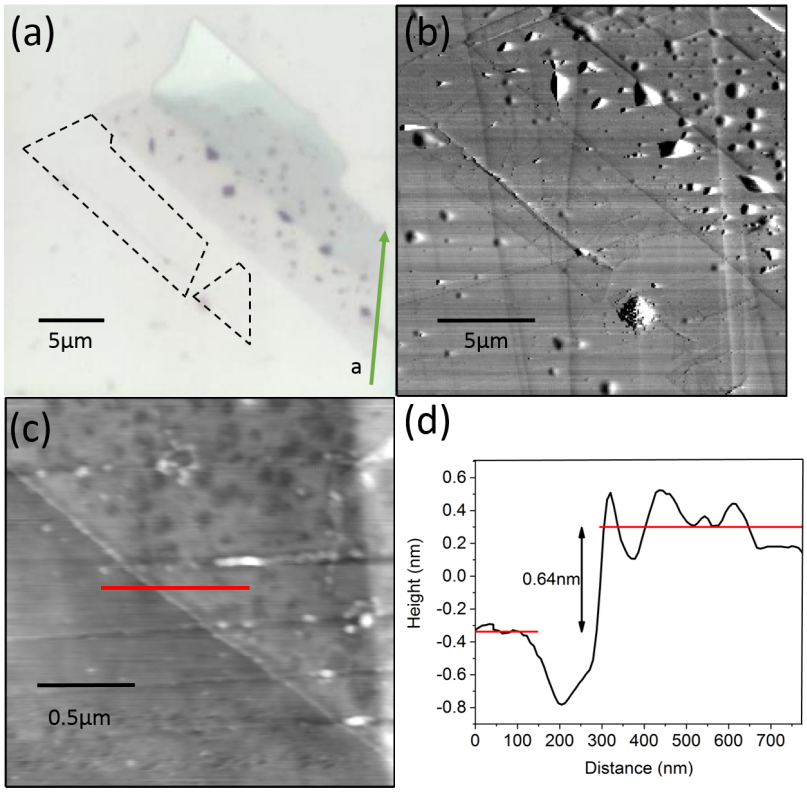

Figure 8.1: (a) Optical image of a $ReSe_2$ monolayer and (b) an AFM phase image of the same monolayer. (c) An AFM image of the edge of a flake which was used to make the thickness measurement in (d).

Figure 8.1a shows an optical image of the $ReSe_2$ monolayer flake that is on a piece of graphite. The direction of the rhenium chains is defined as the a direction so that the results in this chapter can be directly compared to the bulk ARPES data in Chapter 7. A point worth noting is the long edge of the $ReSe_2$ flake is not along the a direction.

The sample was cleaned using a solvent wash of acetone and isopropanol. The monolayer was then annealed at 400°C in an inert atmosphere of argon for 5 hours. The sample was annealed for two reasons. The first is annealing can be used to remove any contaminants from

the top of the monolayer. The second is to improve the flatness of the sample. When a flake is stamped using the dry transfer technique there are usually some bubbles and wrinkles left in the monolayer, which originate from the stress involved with the transfer. Annealing the sample will result in these bubbles combining into fewer, larger bubbles. The total surface energy of the material is reduced as a consequence of combining the bubbles and this process is known as Ostwald ripening [140]. Figure 8.1b shows an AFM image of the $ReSe_2$ flake after annealing, where large bubbles are visible, particularly on the bulk-like material. Figure 8.1d is an AFM measurement showing the thickness of the $ReSe_2$ is 0.64 nm, which confirms this flake is a monolayer. The flake was also annealed at 400°C, for over 12 hours, in ultra-high vacuum (UHV) prior to measurement.

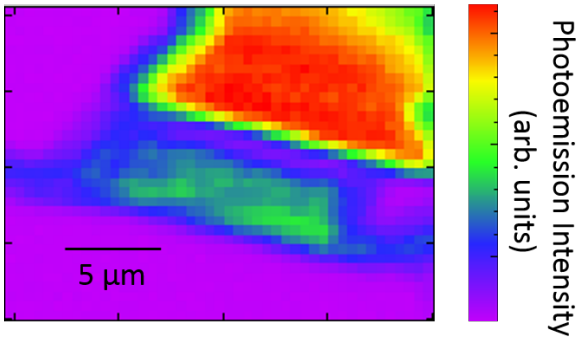

Figure 8.2: Map of photoemission intensity as a function of the spatial coordinates x and y.

Once the sample has been prepared, it can be transported into the measurement chamber. The sample can be moved into the position of the X-ray beam by translating the sample holder. Unfortunately, it is not possible to see the flake using any optical technique when it is in the measurement chamber. Instead a map of photoemission intensity is used to locate the flake. This involves making a photoemission measurement at an energy corresponding to a valence band of the desired flake, then translating the sample stage and taking another measurement. This is repeated such that the photoemission intensity can be measured as function of the spatial coordinates, x and y. There will be more signal when the X-ray beam is on the flake. Figure 8.2 shows the map of photoemission intensity used to locate the $ReSe_2$

monolayer. It is noteworthy that the intensity of photoemission from the monolayer differs to that of the bulk flake. The ARPES measurements made in this chapter were done using a photon energy of 100 eV and the samples were cooled to approximately 100 K.

The samples used in this body of work were prepared using mechanical exfoliation. An alternative way of producing a monolayer is through epitaxial growth; this can be done in a vacuum [11]. If the sample can be transported to the measurement chamber in vacuum, then the surface should be clean and acquisition of high quality ARPES spectra becomes possible.

8.2 Electronic anisotropy

The electronic band structure of bulk $ReSe_2$ is highly anisotropic. This section explores whether this anisotropy is modified in the monolayer. The Brillouin zone of this material is displayed in Fig. 8.3e. Like the bulk there are three inequivalent K and M points. However, unlike the bulk the reciprocal lattice plane that is measured in an ARPES experiment is the plane containing the high symmetry directions. This is explained in detail in Chapter 7.

Figure 8.3a and b show the electronic band structure of monolayer $ReSe_2$ along two orthogonal directions. As well as the electronic dispersion curves of $ReSe_2$ there are graphite bands visible. The monolayer is much larger than the spot size of the X-ray and the measurement was taken in the middle of the monolayer, therefore it can be deduced that the graphite bands were measured through the monolayer. To make it clear which bands are from graphite they are superimposed with yellow curves from DFT calculations, which were produced by Dr Wolverson. The band structure of graphite has been studied extensively. The high symmetry point Γ was located by comparing the ARPES measurements with the DFT calculated bands. Importantly, there is very little overlap of the graphite bands with the $ReSe_2$ bands since the Brillouin zone of graphite is much larger than that of $ReSe_2$.

Figure 8.3c and d are second derivatives of the band structures in Fig. 8.3a and b. This section will first take a look at the electronic dispersion curves of $ReSe_2$ along Γ-M_1, the direction perpendicular to the rhenium chains. Perhaps, the most interesting feature in Fig. 8.3c

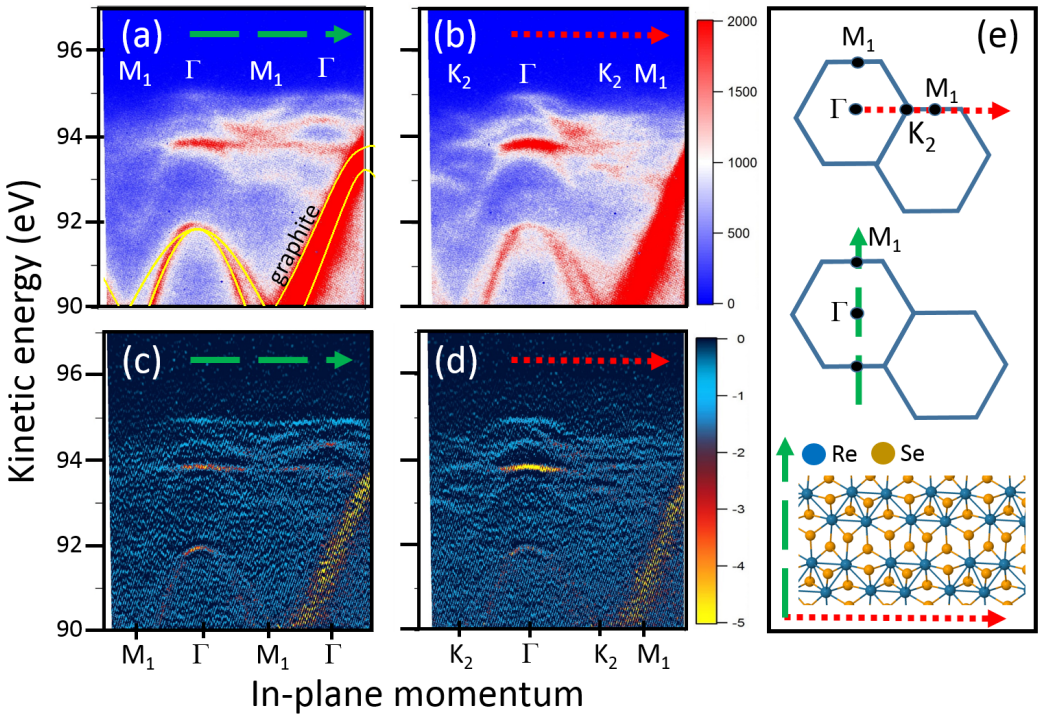

Figure 8.3: The electronic band structure of monolayer $ReSe_2$. Valence band dispersions along the Γ-M_1 direction (a) and the Γ-K_2 direction (b). (c) and (d) are the second derivatives of (a) and (b) respectively. (e) The Brillouin zone and crystal lattice of $ReSe_2$.

is the uppermost valence band. It is very flat, such that the difference between the maximum and minimum of the band is approximately 100 meV. The band structure along the Γ-K_2 direction, parallel to rhenium chains, is presented in Fig. 8.3d. The band structure is very different to the Γ-M_1 direction, therefore there is anisotropy in the electronic dispersions of monolayer $ReSe_2$. The uppermost valence band is much more dispersive in the Γ-K_2 direction than along Γ-M_1. The same phenomenon was observed in Chapter 7 for the the bulk, where it was stated that the phonon-limited mobility in a 2D TMD depends on the inverse square of the mass [28], which means the more dispersive a band is, the higher the mobility of the charge carriers. Like the bulk, the mobility in a monolayer is larger along the rhenium chains than perpendicular to them.

The Brillouin zone of $ReSe_2$ is small compared to other TMDs due to the distorted struc-

ture of this material. The measurements in Fig.8.3a-d span a large enough region of k-space to contain two of these Brillouin zones. In addition to the bands along the Γ-K_2 direction, Fig. 8.3b also contains the electronic band structure along the high symmetry direction K_2-M_1. The uppermost valence band, along K_2-M_1, is found to be rather dispersive and have a local valence band maximum at M_1.

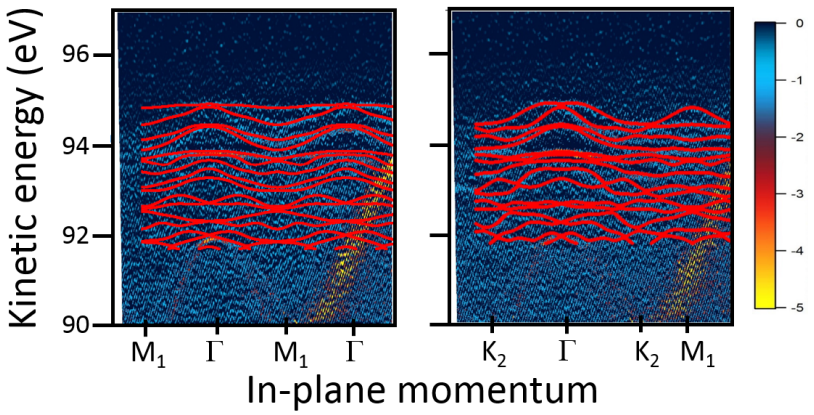

Figure 8.4: Second derivatives of the electronic band structure of monolayer $ReSe_2$, (left) perpendicular to and (right) parallel to the rhenium chains, with DFT calculated bands overlaid.

As mentioned in Chapter 7, the measurement of the k_z plane in adjacent Brillouin zones is different, due to non-conservation of perpendicular momentum. For a monolayer, the electronic dispersions do not depend on k_z. Therefore, the band structures in different Brillouin zones are equivalent. This is seen in Fig. 8.3, where the bands along the Γ-M_1 direction in two neighbouring Brillouin zones appear to be very similar.

The electronic band structure of monolayer $ReSe_2$ has been calculated using ab initio DFT with fully relativistic pseudopotentials. By using a fully relativistic LDA pseudopotential the spin-orbit coupling can be incorporated. The atomic coordinates of bulk $ReSe_2$ were taken from Lamfers et al. [30]. To model a monolayer the interlayer distance of a bulk crystal was increased to approximately 20Å, which results in the electronic coupling between the layers becoming negligible. These DFT calculations were done by Dr Wolverson and Miss Gunasekera. The second derivatives of the electronic dispersions along Γ-M_1 and Γ-K_2

are overlaid with these calculations in Fig. 8.4. The theory and experiment agree that the uppermost valence band in the Γ-M_1 direction is flat and this band is also flat in the vicinity of Γ along Γ-K_2. Furthermore, there is an excellent agreement between the DFT calculations and ARPES measurements for the lower lying bands.

8.3 Comparison of monolayer and bulk $ReSe_2$

The bulk and monolayer flakes of $ReSe_2$ displayed in Fig. 8.1 were both measured so that a comparison between multilayer and single-layer $ReSe_2$ can be made. These flakes are exfoliated from the same single crystal and so have the same orientation and purity. The bands in the bulk crystal were probed using a photon energy of 100 eV, which corresponds to a reciprocal lattice plane that is approximately at the top of the first Brillouin zone, displayed in Fig. 8.5 as a blue hexagon. As mentioned in the previous chapter, the plane measured in an ARPES experiment of bulk $ReSe_2$ does not contain the reciprocal lattice vectors, a^* and b^*. Instead the surface Brillouin zone is measured, which is a projection of the plane containing a^* and b^* onto the real space layer plane and is displayed in Fig.8.5e as a grey hexagon. This pseudo-Brillouin zone does not contain any of the high symmetry points and so to compare with the monolayer, Γ, K_2 and M_1 are projected onto this measured plane and labelled, $\bar{\Gamma}$, $\bar{K_2}$ and $\bar{M_1}$. The surface and monolayer Brillouin zones are equivalent, therefore the measured reciprocal lattice planes of bulk and monolayer $ReSe_2$ contain the same basis vectors, defined here as a^*_{2D} and b^*_{2D}. This section will first address whether the band gap of the monolayer is direct or indirect. Following this, the band structures of bulk and monolayer $ReSe_2$ will be compared along and perpendicular to b^*_{2D}, which correspond to the directions perpendicular and parallel to the rhenium chains respectively.

In Chapter 7, the conduction band minimum of monolayer $ReSe_2$ was determined to be at Γ. From the ARPES measurements in Fig. 8.5a and c it can be see that the uppermost valence band in the vicinity of the Γ point in both the Γ-M_1 and Γ-K_2 directions is very flat. The flat region of this band contains the VBM. Unfortunately, from the ARPES data presented,

it is not possible to determine whether the VBM is at Γ or at another point along this very flat band. To understand the optical spectra of a $ReSe_2$ monolayer it may not be necessary to know the exact position of the VBM. An interband transition across the direct gap at Γ is much more likely than a transition across an indirect band gap of similar size. This is because the latter relies on electron-phonon scattering to fulfil conservation of momentum.

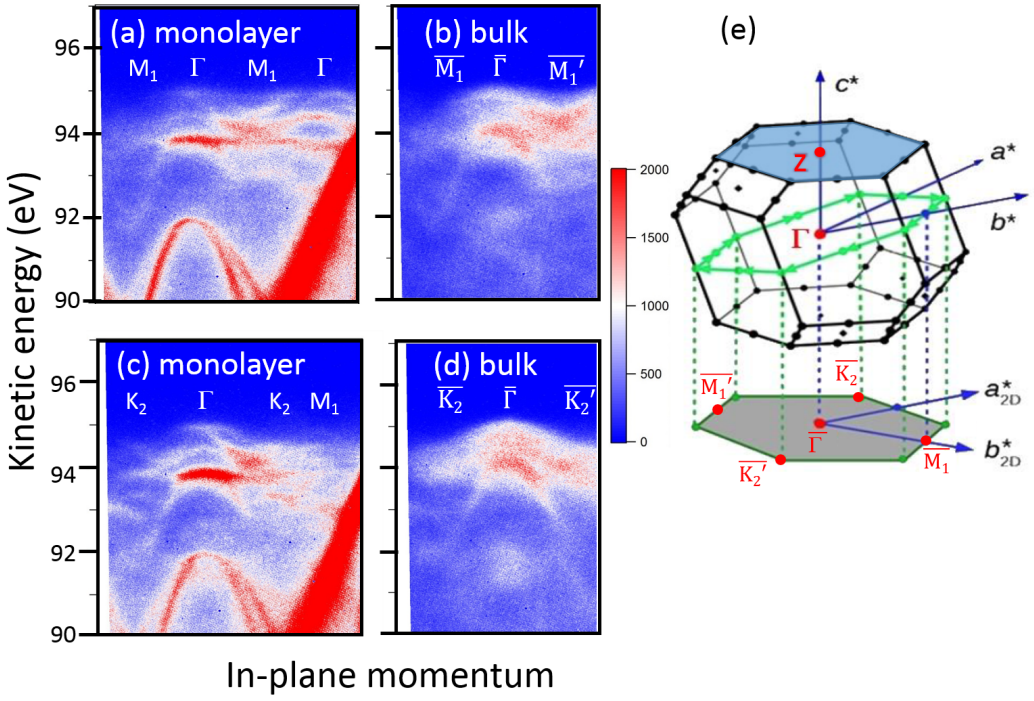

Figure 8.5: Valence band dispersions along the direction perpendicular to the rhenium chains, (a) for a monolayer and (b) for bulk $ReSe_2$. (c) Monolayer and (d) bulk electronic band structures measured along the rhenium chain direction. (e) The Brillouin zone of bulk ReS_2 with a green hexagon representing the plane that contains the reciprocal lattice vectors, a^* an b^*. The grey hexagon represents the surface Brillouin zone, which is equivalent to the Brillouin zone for a monolayer, and so the reciprocal lattice vectors within this hexagon are a^*_{2D} and b^*_{2D}. The blue hexagon represents the reciprocal plane probed in the bulk crystal. Figure e was modified from Ref. [141].

The band structures of the bulk and monolayer will now be compared along b^*_{2D}, the direction perpendicular to the rhenium chain, which are presented in Fig. 8.5a and b. In a bulk crystal the uppermost valence band is slightly parabolic. However, this is not the case for the monolayer, where the band is flat. An explanation for why the uppermost valence band

becomes flat in the monolayer is as follows. In the bulk the charge carriers can travel along the layer plane or by hopping to an adjacent layer. In a monolayer, there is no interlayer coupling, so the electrons can only move along the layer plane and this may impede the motion of the charge carriers, resulting in a large effective mass. Some of the changes to the band structure can also be attributed to quantum confinement.

A flat band is characteristic of a crystal with low mobility. The low mobility in the monolayer would make it a poor candidate for a material to be used in an FET. However, Yang et al. have performed electronic transport measurements of a monolayer and thin flakes that indicate the mobility is larger in the monolayer [83]. This group do not comment on the direction along the flakes that they measure. The direction of the measurement which will affect the mobility they obtain. There has been electronic transport measurements on monolayer ReS_2 that find the conductance in the monolayer is much smaller than the bulk [79]. The upppermost valence band in ReS_2, like $ReSe_2$, is flat in the monolayer but parabolic in the bulk [56].

The top of the uppermost valence band in the Z plane of the bulk is at a higher energy than the VBM in the monolayer. The difference of these maxima is approximately 200 meV. This indicates that the band gap could be larger in the monolayer than in the bulk. Arora et al. measure a larger optical band gap in monolayer $ReSe_2$ compared to the bulk [53]. It is an important point to note that the VBM of bulk $ReSe_2$ is at point in the Brillouin zone that is not along any of the high symmetry directions. This VBM is not measured in Fig.8.5, so it is not possible to directly compare the VBM of the bulk to the VBM of the monolayer.

The electronic band structures of monolayer and bulk $ReSe_2$ measured along the direction perpendicular to b^*_{2D}, the direction of the rhenium chain, are shown in Fig. 8.5c and d . The highest lying valence band is dispersive for both the bulk and the monolayer. However, in the vicinity of Γ the monolayer has a rather flat band.

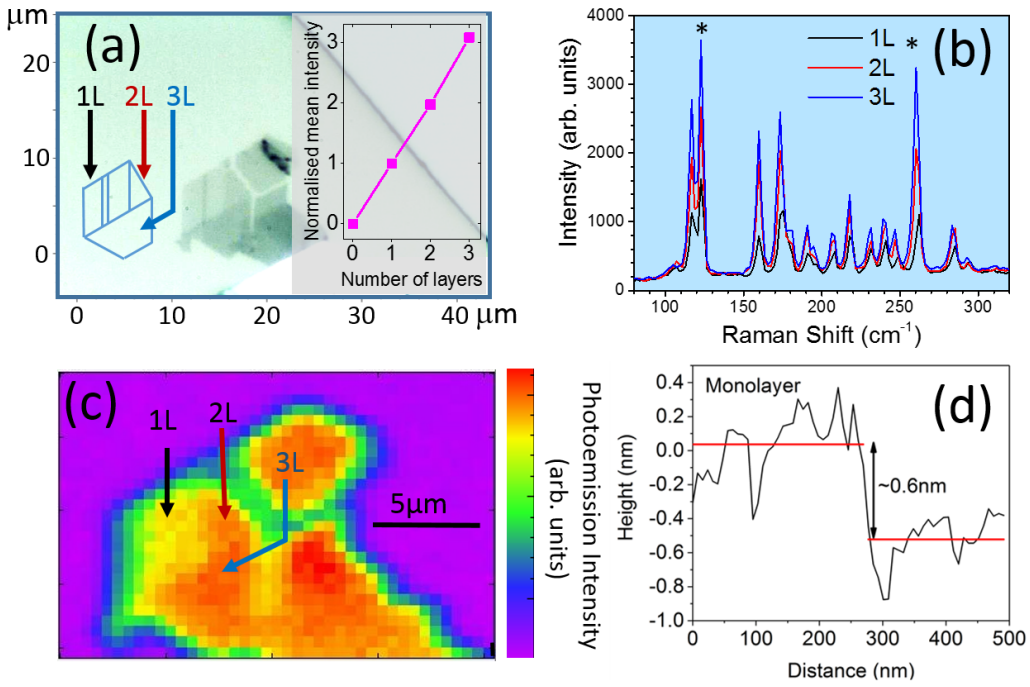

Figure 8.6: (a) An optical image of $ReSe_2$ on top of a piece of graphite. (b) Raman spectra of monolayer, bilayer and trilayer $ReSe_2$ flakes. The inset of (a) is a graph of the average normalised intensity of the two most intense Raman modes in (b), which are depicted with asterisks, as a function of layer number. (c) Map of photoemission intensity as a function of the spatial coordinates x and y for the region containing the monolayer, bilayer and trilayer flakes. (d) AFM measurement of the thickness of the monolayer.

8.4 ARPES measurements of mono-, bi- and trilayer $ReSe_2$

As well as the ARPES results of a monolayer of $ReSe_2$, this chapter presents ARPES measurements of bilayer and trilayer $ReSe_2$. A collection of $ReSe_2$ flakes were placed upon a piece of graphite using dry transfer. Figure 8.6a shows an optical image of the transferred $ReSe_2$ crystals. The Raman spectra of the three thinnest flakes are shown in Fig. 8.6b. The intensities of the Raman modes of these three samples increases linearly. The intensities are expected to increase linearly with layer number so this Raman measurement can be used as evidence that these flakes are monolayer, bilayer and trilayer. The reason for this relationship with thickness is that, the thicker the crystal, the greater the probability an inelastic scattering event can occur. The $ReSe_2$ flakes are sufficiently thin that it can be assumed they

do not absorb any of the light [142]. The graphite flake that the $ReSe_2$ is placed upon is sufficiently thick that interference effects, like those seen for flakes on SiO_2, are not expected [39]. Figure 8.6d is AFM data confirming that the thinnest flake in Fig. 8.6a is a monolayer.

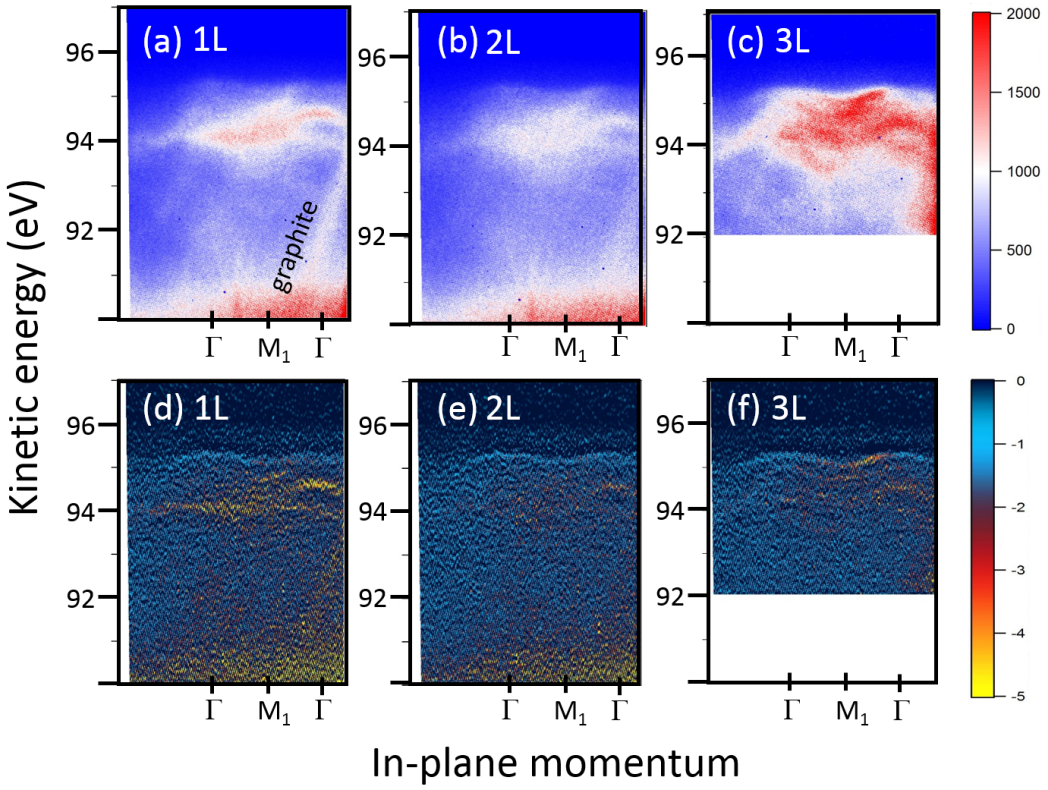

Figure 8.7: Valence band dispersions of (a) a monolayer, (b) a bilayer and (c) a trilayer of $ReSe_2$. The second derivatives of (a),(b) and (c) are presented in (d), (e) and (f).

Figure 8.6c shows a map of photoemission intensity as a function of x and y of the monolayer, bilayer and trilayer. The orientation of the flakes in this image is the same as the optical image in Fig. 8.6a. Interestingly, the photoemission intensity increases with layer number. This is to be expected because the thicker the crystal, the greater the probability of a photoemission event. For sufficiently thick flakes this relationship will not be true as the photoelectrons are only expected to be emitted from the top couple of nanometres of a sample [125].

The electronic band structures of the monolayer, bilayer and trilayer are displayed in Fig. 8.7a-c along Γ-M_1, the direction perpendicular to rhenium chains. A graphite band can be seen in the bottom right of Fig. 8.7. This band is visible in Fig. 8.7a and b but is not in Fig. 8.7c. This means it is possible to see the graphite through the monolayer and bilayer flake but not the trilayer.

Figure 8.7.c-f are the second derivatives of the valence band dispersions for the monolayer, bilayer and trilayer respectively. The first thing of note is the bands from these flakes are of poorer quality than the bands from Fig. 8.3. The most likely reason for this is that these flakes are not as clean as the monolayer used to produce Fig. 8.3. Nevertheless, the uppermost valence band can be seen clearly. This band is rather flat for the monolayer, and as the layer number increases this band becomes more parabolic. The bands in the trilayer are similar to the bands that were measured for bulk $ReSe_2$.

8.5 Discussions

Presented in this chapter are the first ARPES results of a monolayer of $ReSe_2$. Much like its bulk counterpart, a monolayer of $ReSe_2$ exhibits in-plane anisotropy in the layer plane; the the uppermost valence band is more dispersive in the Γ-K_2 direction than the Γ-M_1 direction. The highest lying valence band is more dispersive along the direction of the rhenium chain than perpendicular to this chain where the valence band is flat. A consequence of having a flat uppermost valence band is that the mobility of the material is expected to be small. Many electronic devices, such as FETs, require materials with high mobilities, therefore, the non-dispersive highest lying valence band may limit the applications of monolayer $ReSe_2$.

From the ARPES data it is not possible to determine whether the monolayer has a direct or indirect band gap. The DFT calculations in Chapter 7 predict the CBM to be at Γ. The ARPES results indicate that the VBM is in a flat band in the vicinity of Γ, which means the direct and indirect band gaps are approximately equal.

The structures of some of the bands in monolayer $ReSe_2$ differ considerably from bulk

$ReSe_2$. This difference can be explained in terms of the lack of interlayer coupling in the monolayer. It was previously thought the interlayer coupling is negligible in $ReSe_2$. This was shown to not be the case in Chapter 7. In this chapter it is stated that there needs to be interlayer coupling in the bulk to explain the shape of the bands of the monolayer.

Chapter 9

Electronic band structure of ReS_2 by high-resolution angle-resolved photoemission spectroscopy

9.1 Preamble

Much like $ReSe_2$, the electronic properties of ReS_2 are highly anisotropic. In this paper the electronic band structure of bulk ReS_2 is measured, using ARPES, along different cuts of the Brillouin zone to demonstrate this anisotropy. There has been conflicting evidence as to whether ReS_2 is a direct or indirect band gap semiconductor. Using a combination of DFT calculations and ARPES measurements the location and direct/indirect nature of this gap is explored. It was previously thought the bulk rhenium dichalcogenides behave as stacks of electronically decoupled monolayers [52]. However, the previous chapter showed that this is not the case for $ReSe_2$. The interlayer coupling is investigated in bulk ReS_2 by measuring the valence band dispersions along the k_z direction.

The DFT calculations of the electronic band structures were again made using the lattice parameters of ReS_2 found by Lamfers et al. [30]. To be consistent with their work the a

crystal axis is defined to be along the direction of the rhenium chains.

Note: There is a mistake in the caption of Fig. 7 of the main paper in the sentence, "Calculation of the VB maximum and CB minimum as a function of k_z for all k_x, k_y (solid line) and restricted to the Γ-Z direction $k_x = 0$, $k_y = 0$ (dashed line)." Where it reads "solid line" it should be "dashed line" and vice versa.

The candidate helped with the preparation of the sample, the measurements and the analysis of the results. All results presented in this paper are from work done at the ANTARES beamline at the Synchrotron Soleil with the help of the beamline scientists at this facility. Dr Webb and Dr Wolverson performed the DFT calculations.

9.2 Statement of authorship and copyright information

<table>
<tr><td colspan="5">This declaration concerns the article entitled:</td></tr>
<tr><td colspan="5">Electronic band structure of ReS_2 by high-resolution angle-resolved photoemission spectroscopy</td></tr>
<tr><td colspan="5">Publication status (tick one)</td></tr>
<tr><td>Draft manuscript</td><td>Submitted</td><td>In review</td><td>Accepted</td><td>Published</td></tr>
<tr><td></td><td></td><td></td><td></td><td>✓</td></tr>
<tr><td>Publication details (reference)</td><td colspan="4">J. L. Webb, L. S. Hart, D. Wolverson, C. Chen, J. Avila, and M. C. Asensio, “Electronic band structure of ReS_2 by high-resolution angle-resolved photoemission spectroscopy,” *Physical Review B*, vol. 96, no. 11, p. 115205, 2017.</td></tr>
<tr><td>Candidate’s contribution to the paper (detailed, and also given as a percentage)</td><td colspan="4">The candidate considerably contributed to the experimental measurements in this publication.
Formulation of ideas: 60%
Design of methodology: 50%
Experimental work: 50%
All the ARPES measurements were done with the help of the beamline scientists
Computational work: 0%
Presentation of data in journal format: 20%</td></tr>
<tr><td>Statement from Candidate</td><td colspan="4">This paper reports on original research I conducted during the period of my Higher Degree by Research candidature.</td></tr>
<tr><td>Signature</td><td colspan="2"></td><td>Date</td><td>29/05/2018</td></tr>
</table>

Publication title: Electronic band structure of ReS_2 by high-resolution angle-resolved photoemission spectroscopy

The pages of this thesis this paper spans are from 161 to 172.

Electronic band structure of ReS_2 by high-resolution angle-resolved photoemission spectroscopy

James L. Webb,* Lewis S. Hart, and Daniel Wolverson
Centre for Nanoscience and Nanotechnology, Department of Physics, University of Bath, Bath BA2 7AY, United Kingdom

Chaoyu Chen, Jose Avila, and Maria C. Asensio†
Synchrotron SOLEIL, Saint Aubin, and Université Paris-Saclay, BP 48 91192 Gif-sur-Yvette, France
(Received 20 April 2017; revised manuscript received 26 July 2017; published 18 September 2017)

The rhenium-based transition metal dichalcogenides (TMDs) are atypical of the TMD family due to their highly anisotropic crystalline structure and are recognized as promising materials for two-dimensional heterostructure devices. The nature of the band gap (direct or indirect) for bulk, few-, and single-layer forms of ReS_2 is of particular interest, due to its comparatively weak interplanar interaction. However, the degree of interlayer interaction and the question of whether a transition from indirect to direct gap is observed on reducing thickness (as in other TMDs) are controversial. We present a direct determination of the valence band structure of bulk ReS_2 using high-resolution angle-resolved photoemission spectroscopy. We find a clear in-plane anisotropy due to the presence of chains of Re atoms, with a strongly directional effective mass which is larger in the direction orthogonal to the Re chains ($2.2m_e$) than along them ($1.6m_e$). An appreciable interplane interaction results in an experimentally measured difference of $\approx$100−200 meV between the valence band maxima at the Z point $(0,0,\frac{1}{2})$ and the Γ point (0,0,0) of the three-dimensional Brillouin zone. This leads to a direct gap at Z and a close-lying but larger gap at Γ, implying that bulk ReS_2 is marginally indirect. This may account for recent conflicting transport and photoluminescence measurements and the resulting uncertainty about the nature of the band gap in this material.

DOI: 10.1103/PhysRevB.96.115205

I. INTRODUCTION

The transition metal dichalcogenides (TMDs) are a class of material that can form thin sheets down to a single monolayer, analogous to graphene but consisting of compound semiconducting materials rather than a single atomic species. These semiconducting properties are what have attracted considerable recent interest with regard to fabricating and controlling new devices from stacked two-dimensional (2D) layered materials, the van der Waals heterostructures [1]. The fundamental properties of other TMD materials such as MoS_2 and WS_2 have been intensively studied in recent years [2–4] with a view towards creating novel electro-optic devices [5].

Of these materials ReS_2 is of particular interest due to several properties. Its optical [6,7] and electrical transport properties are highly anistropic, in particular with higher mobility in certain in-plane crystallographic directions, as determined by electrical measurements using bulklike flakes [8,9], making it an interesting material for the fabrication of field-effect transistors and polarization-sensitive photodetectors [8,10,11]. In this context, ReS_2 has the advantage of being stable under ambient conditions, unlike some similar 2D materials [12]. Next, spin-orbit coupling is important in ReS_2, though the presence of inversion symmetry means that spin-orbit splitting in unperturbed layers of any thickness is zero and may be manipulated via doping or gating. Finally, unlike many other TMD materials [13,14], it has been proposed there is no transition from indirect to direct band gap with reduced thickness, meaning that the distinction between mono- and few-layer structures is not crucial for device concepts [15]. If true, this could be advantageous in terms of building efficient optical devices.

Figure 1(a) shows a schematic model of the atomic structure of ReS_2 with the lattice vector directions $\boldsymbol{a}$, $\boldsymbol{b}$, and $\boldsymbol{c}$ indicated. Here $\boldsymbol{a}$ lies in the direction of the Re chains and $\boldsymbol{b}$ at about 120° to them. This structure has been confirmed experimentally by scanning probe microscopy studies [16], indirectly by Raman spectroscopy [15,17] and by single crystal x-ray diffraction by Lamfers *et al.* [18] with a triclinic structure and in-plane lattice parameters $a = 6.352$ Å and $b = 6.446$ Å. The question of whether the unit cell contains one or two layers stacked along the out-of-plane c axis has been resolved in favor of a single layer, giving four formula units per unit cell [19], with $c = 6.403$ Å to 6.461 Å [20].

In performing the angle-resolved photoemission spectroscopy (ARPES) measurements we effectively probe the projection of the k points in the 3D Brillouin zone (BZ) of the material onto a quasi-2D flat plane (k_z = constant; the value of k_z is determined by the choice of excitation photon energy). This is exemplified in Fig. 1(b) for points in the full 3D BZ in a plane passing through the Γ point (shaded yellow), which are projected onto the measurement plane to produce a quasi-2D Brillouin zone in k_x, k_y. This quasi-BZ is shown at the bottom of Fig. 1(b) and is an irregular hexagon centered on $\overline{\Lambda}$. Here we show the projection of the lattice vectors $\boldsymbol{a}^*$ and $\boldsymbol{b}^*$ onto the measurement plane as $\boldsymbol{a}^\dagger$ and $\boldsymbol{b}^\dagger$. If the bulk material were thinned to a 2D monolayer, this quasi-BZ would ultimately represent a good approximation to the 2D BZ as used in other work, for example Tongay *et al.* [15], to calculate the properties of monolayer ReS_2. We label directions $\overline{M}$ and $\overline{K}$ following this and other work and in order to show the direction of measurement of the ARPES data. It is necessary to distinguish between directions $\overline{M}_1 \cdots \overline{M}_3$ and $\overline{K}_1 \cdots \overline{K}_3$ since, in this triclinic material, none of these are related by symmetry. The

*j.l.webb@bath.ac.uk
†maria-carmen.asensio@synchrotron-soleil.fr

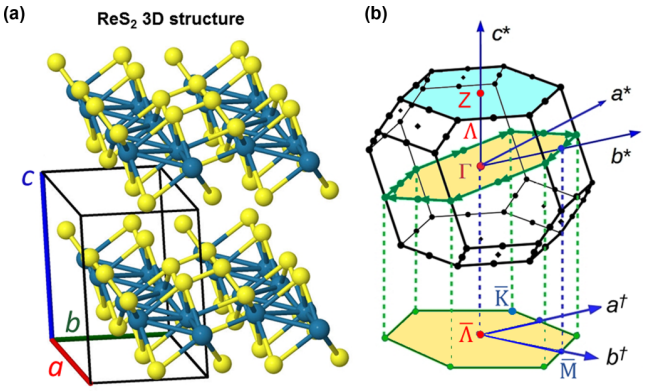

FIG. 1. The atomic structure of ReS_2. (a) Re atoms in blue and S in yellow with the unit cell shown by the vectors $\boldsymbol{a}$, $\boldsymbol{b}$, $\boldsymbol{c}$. Chains of Re atoms run along the in-plane vector taken here as $\boldsymbol{a}$, with the second in-plane vector $\boldsymbol{b}$ at about 120° to the chain direction. (b) The conventional triclinic Brillouin zone of ReS_2, showing the reciprocal lattice vectors $\boldsymbol{a}^*$, $\boldsymbol{b}^*$, and $\boldsymbol{c}^*$, with the latter passing through the labeled Γ and Z points along the direction Λ. Two planes which pass through Γ (the Γ plane) and Z (the Z plane) and other high-symmetry points are shaded; in our ARPES experiments, we effectively measure a projection of the 3D Brillouin zone onto the plane k_z = constant. This is shown schematically at the bottom of (b) by the irregular hexagon, which is the projection of the Γ plane. $\boldsymbol{a}^\dagger$ and $\boldsymbol{b}^\dagger$ represent the projections of the reciprocal lattice vectors in the k_z = constant plane, $\overline{K}$ and $\overline{M}$ are the k_z = constant projections of their respective high-symmetry points, and $\overline{\Lambda}$ is the projection of the general point Λ.

directions $\boldsymbol{b}^*$ and $\boldsymbol{b}^\dagger$ are orthogonal to the real-space vector $\boldsymbol{a}$, so that directions $\overline{M}_1$ and $\overline{K}_2$ are exactly orthogonal and approximately parallel, respectively, to the rhenium chains of ReS_2.

Although electrical transport and optical absorption measurements have given some indirect insight into the ReS_2 band structure, along with *ab initio* calculations of the material properties [15,21,22], it is evident that gap size as well as the direct or indirect character of the gap is particularly sensitive to the details of any computational model (for instance, the choice of pseudopotential and whether spin-orbit coupling is included). Consequently, the direct, accurate determination of the electronic band structure is necessary and timely. This is a task for which ARPES is ideally suited. However, two primary difficulties exist in performing these measurements: They must be performed on a clean surface, ideally a crystal cleaved under ultrahigh-vacuum conditions, and the crystal facets of the material must be larger than the spot size of the x-ray beam in order to obtain clear, monocrystalline data. Recent advances in TMD handling and advances towards micro- and nano-ARPES systems with beam sizes on the 100-nm scale mean these problems can now be overcome.

In this work we present the main results of our direct determination of the valence band structure of bulk ReS_2 using nano-ARPES, mapping the photoemission intensity in directions along and perpendicular to the Re atomic chains of the material and measuring also constant binding energy contours throughout large portions of the full 3D Brillouin zone. Our findings show the effect of the in-plane anisotropy on the electronic dispersions and the van der Waals interactions between planes, revealing the electronic dispersion perpendicular to the constitutive layers. Most importantly, we also have found significant differences between the electronic structure at the valence band maxima at the Z $(0,0,\frac{1}{2})$ and the Γ (0,0,0) points. We find there is a high-lying valence band maximum at the Z point moving to a lower-lying one at Γ, in agreement with our calculated band structure. In conjunction with our calculated conduction band minima, this implies a direct band gap at the Z point with an indirect gap at or near the Γ point. All these observations together provide an explanation for the anisotropy observed in electrical and optical measurements and the uncertainty regarding the direct or indirect nature of the ReS_2 band gap.

II. METHODS

Samples were commercially grown via Bridgman single-crystal growth by 2D Semiconductors USA and were confirmed 99.9995% pure using secondary ion mass spectrometry. We performed prior studies on the crystals using Raman spectroscopy in order to confirm their phase and high crystal quality [23].

Nano-ARPES measurements were performed using the k microscope at the ANTARES beamline at the Soleil synchrotron, Paris, with a spot size of 100 nm. At a photon energy of 100 eV, this beamline has an angular resolution of ∼0.2° and an energy resolution of ∼10 meV. The advantage of the nano-ARPES technique for the study of ReS_2 is that the x-ray beam spot size is smaller than the size of the crystallites (generally a few microns to tens of microns, as determined by optical microscopy), ensuring that the measured dispersion is obtained only from a single facet, which is important due to the high degree of direction-dependent anisotropy in the band structure. The samples were prepared by cleaving *in situ* under UHV conditions (pressure $< 1 \times 10^{-10}$ mbar). A nanopositioning system was used to locate clean and flat areas of the sample with maximum ARPES intensity with measurements performed at photon energies from 95–180 eV. The sample was rear cooled using liquid nitrogen to approximately 100 K in order to reduce thermal noise.

Density functional theory (DFT) calculations were performed using the QUANTUM ESPRESSO package [24] to perform structural relaxation and obtain total energy and band-structure simulations. We focus here on results obtained using a nonrelativistic Perdew-Burke-Ernzerhof (PBE) generalized gradient approximation (GGA) exchange-correlation functional [25], but we also explored the use of a fully relativistic Perdew-Zunger (PZ) local density approximation (LDA) functional [26] with projector augmented wave (PAW) pseudopotentials generated by QE and PSLIBRARY46. The GGA and LDA results are compared to the experimental data in the Supplemental Material, Figs. S1 and S2, respectively [27]. The valence of Re was taken as 15 (configuration $5s^2 5p^6 5d^5 6s^2$). Kinetic energy cutoffs were 70 Ry (816 eV), and Monkhorst-Pack k-point meshes of $12 \times 12 \times 12$ were used with a single 12-atom unit cell.

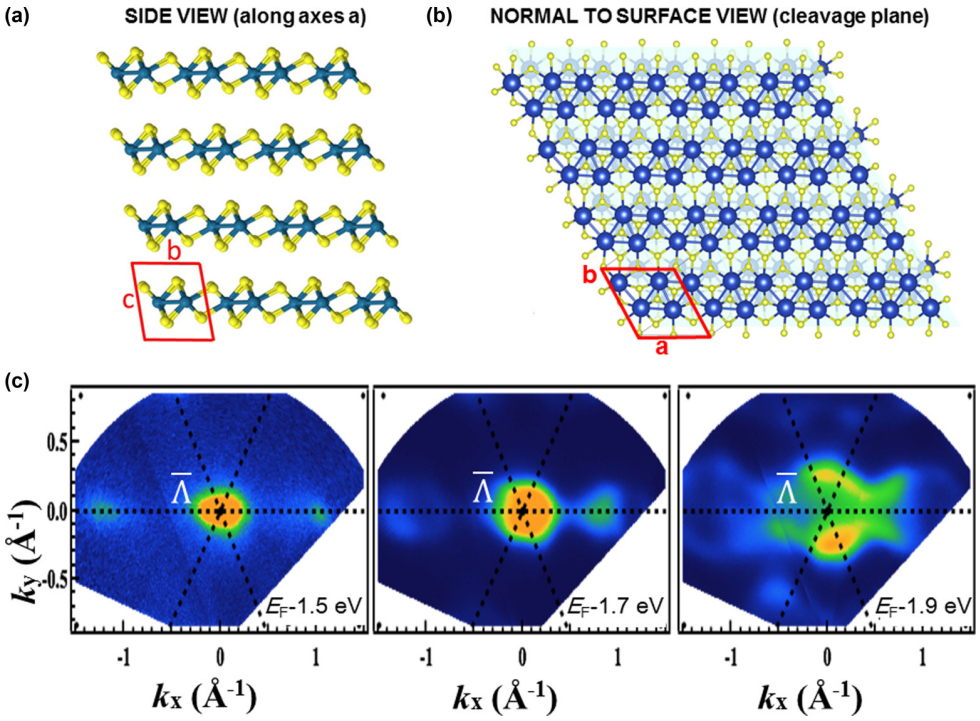

FIG. 2. Side (a) and normal (b) views of the ReS_2 structure; (c) constant energy surfaces going down in the valence band from 1.5 to 1.9 eV below the Fermi energy E_F and centered at the $\overline{\Lambda}$ point, as discussed in the text. Significant asymmetry is observed between the direction $\boldsymbol{a}$ along the chains (which are parallel to k_y) and that perpendicular to them (k_x, or $\boldsymbol{b}^{\dagger}$). The maximum of the valence band (VBM) for this value of k_z (see text) appears at $\overline{\Lambda}$.

III. RESULTS

First, we consider how the observed constant energy maps in the k_z = constant plane reflect the crystal symmetry; Fig. 2 shows views of the crystal structure looking along the $\boldsymbol{a}$ and parallel to the $\boldsymbol{c}$ directions. In Fig. 2(c), we show a constant energy surface plot of the ARPES signal intensity probing a set of binding energies E_b moving downwards in energy from the Fermi energy (E_F) and recorded by illuminating the samples with photons of energy hν = 100 eV. This excitation energy was chosen since it gives the optimum transmission of the zone plate used to focus the excitation beam. As we shall see below, this excitation energy means that the plane probed intersects the $\boldsymbol{c}^*$ axis at a point lying on the line Γ-Z. Following the notation of Fig. 1(b), we label a general point of this type as $\overline{\Lambda}$; this point is the origin ($k_x = k_y = 0$) of the 2D quasi-Brillouin zone and thus is the origin of the binding energy contour plots for a given excitation energy.

Using a gold sample *in situ* in the ARPES system, the Fermi edge of its density of states was precisely determined; this experimental Fermi energy is shared by the ReS_2 sample as they have a common ground potential. We find that the Fermi level of the semiconductor sample is 1.5 eV above the valence band maximum, putting a lower bound on the single-particle band gap of 1.5 eV (unoccupied bands are not recorded by ARPES, so the conduction band minimum was not recorded here). This value is close to the lowest-lying excitonic band gap of $E_1^{ex} = 1.55$ eV recorded at the same temperature (100 K) [28], showing the *n*-type character of our material. The doping state of ReS_2 is dependent on the details of the crystal growth, with *p*-type material also being possible depending on the vapor transport method used [6,29]. Consequently, the ARPES constant energy plots of Fig. 2(c) can be labeled at this local maximum of the valence band with binding energies of 1.5, 1.7, and 1.9 eV below the Fermi level.

The plots of Fig. 2(c) clearly indicate a "wavy" shape of the contours related to the in-plane chains of Re atoms sketched in Fig. 2(b). This implies a marked difference between the dispersion in the direction along the Re chains and that perpendicular to them, with a more abrupt drop in the valence band energy along the chains. Such anisotropy directly affects the effective mass and hence the mobility in the two perpendicular directions. This aspect will be studied in detail below, where we obtain representative effective masses in both directions from our ARPES data. However, it is important to note that this in-plane anisotropy is not exclusive to these two directions. Figure 3 indicates that the band structure along different $\overline{M'}$-$\overline{\Lambda}$-$\overline{M}$ directions is dissimilar, confirming that the in-plane anisotropy is not restricted to the directions along and perpendicular to the chains of Re atoms. The same remark can be made about the electronic dispersions along the $\overline{K'}$-$\overline{\Lambda}$-$\overline{K}$ directions, which are also not equivalent, even though the tops of the bands in all directions are centered at the surface $\overline{\Lambda}$ projection, as shown in Fig. 3(a). We distinguish in Fig. 3 between points on either side of $\overline{\Lambda}$ (e.g., $\overline{M'}$ and $\overline{M}$) because there is inversion symmetry only through the *true* Γ point and so these pairs are not related by real reciprocal lattice vectors. Indeed, it can be seen in some of the ARPES plots of Figs. 3(b) and 3(c) that the dispersion is not exactly symmetrical about $\overline{\Lambda}$ for this reason.

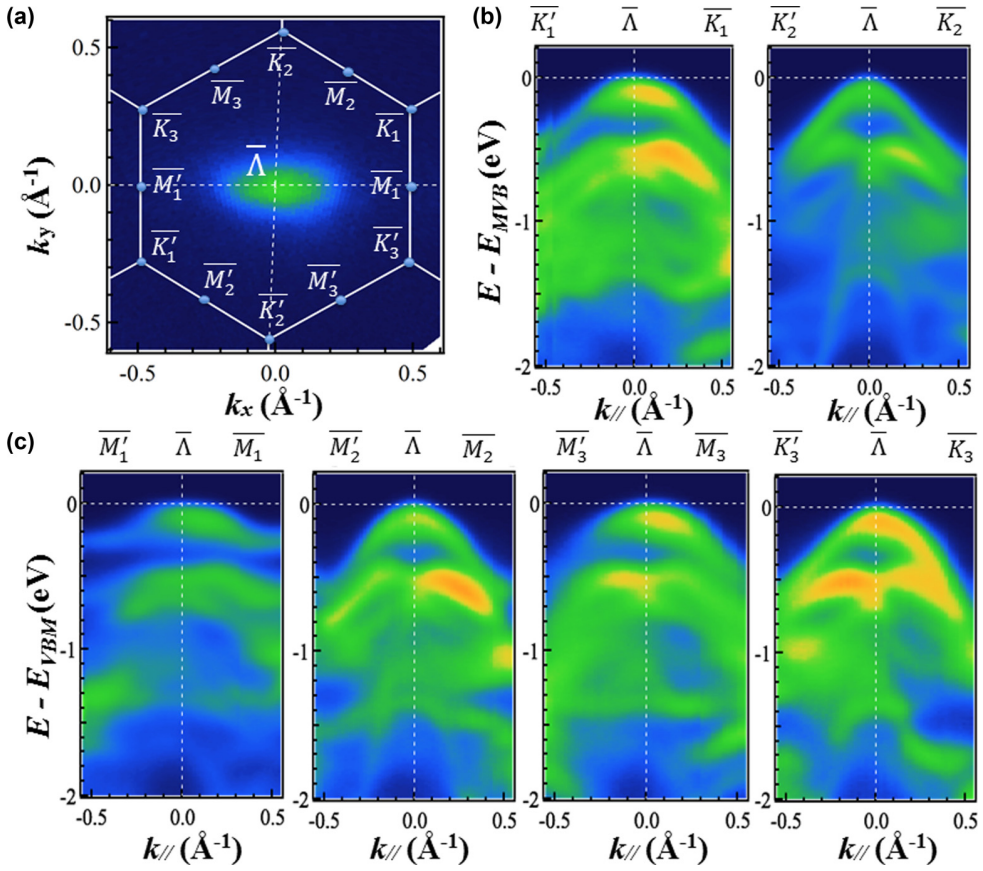

FIG. 3. Panel (a) shows the constant energy surface in the valence band at 1.5 eV below the Fermi energy E_E as shown in Fig. 2(c) with the labels of the high-symmetry points projected onto the (k_x,k_y) plane. Panels (b) and (c) show high-resolution ARPES plots recorded using an excitation photon energy of h$\nu = 100$ eV along the six inequivalent $\overline{K'}$-$\overline{\Lambda}$-$\overline{K}$ and $\overline{M'}$-$\overline{\Lambda}$-$\overline{M}$ directions.

Thus far, we have measured the bands only at an arbitrary point along $\boldsymbol{c}^*$ (corresponding to the excitation energy of 100 eV), and this limits our analysis. Consequently, it is important to probe the limits of the 3D Brillouin zone at the Γ and Z points. This can be achieved in ARPES by varying the excitation photon energy; the systematic study of the energy dependence of the ARPES signals allows the mapping of the whole ReS_2 3D BZ, and a precise analysis then provides the exact location of the planes intersecting the Γ and Z points of the ReS_2 3D Brillouin zone, defined in Fig. 1(b). In brief, in order to obtain experimentally the perpendicular dispersion of the bands, ARPES plots are recorded systematically by varying k_z, scanning through the Γ point at $k_z = 0$ and the Z point at $k_z = |c^*|/2$. Figure 4(a) depicts the out-of-plane dispersion of the bands (that is, along k_z), obtained as the incident photon energy is varied. The results plotted in Fig. 4(a) demonstrate that photon energies of 131 and 111 eV correspond to the Γ and Z points, respectively, consistent with initial electron state momenta that are integer and half-integer multiples of $|c^*| = 1.03$ Å^{-1}, if we assume a value of the inner potential for ReS_2 of $V_{in} = 16 \pm 2$ eV. This potential is conventionally used to represent the effects of the nonconservation of photoelectron momentum normal to the emitting surface [30], and the value we obtain is consistent with those of the similar TMDs WSe_2 and $ReSe_2$ [31,32].

Figure 4(b) shows plots of the the second derivative of the dispersion for the two most representative directions, along k_x and k_y ($\overline{M}_1$ and $\overline{K}_2$) with excitation energies selected from the dataset of Fig. 4(a) so that the selected planes pass through the Z and Γ symmetry points (top and bottom panels, respectively). The in-plane anisotropy of the dispersions along the k_x and k_y directions is very noticeable. Interestingly, a distinct inequivalence between the electronic band dispersion at Z and Γ points is also observed. A typical, very flat top to the valence band appears for $\overline{M'}_1$-Γ-$\overline{M}_1$, while more dispersive bands characterize the VBM at the Z point. We find that the binding energy of the VBM at the Z point is lower than at Γ with a difference of 100–200 meV. The 3D plot of the same data in k_x and k_y versus E_B shows a clear, single peak in the valence band at Z, as might be characteristic of a direct band-gap transition at this point. In previous recent indirect measurements and *ab initio* calculations, a direct band gap at Γ had been proposed [15,33], though no calculations of the valence band throughout the whole Brillouin zone have been reported.

To determine quantitatively some key details of the electronic structure of ReS_2, Fig. 5 shows the ARPES intensity recorded along $\overline{K'}_2$-Z-$\overline{K}_2$ and $\overline{M'}_1$-Z-$\overline{M}_1$ directions. Despite the low symmetry in the plane, the band dispersions are approximately symmetric about the Z point, as Figs. 5(a)–5(c) show. The fitted parabolae [dotted black lines in Fig. 5(b)]

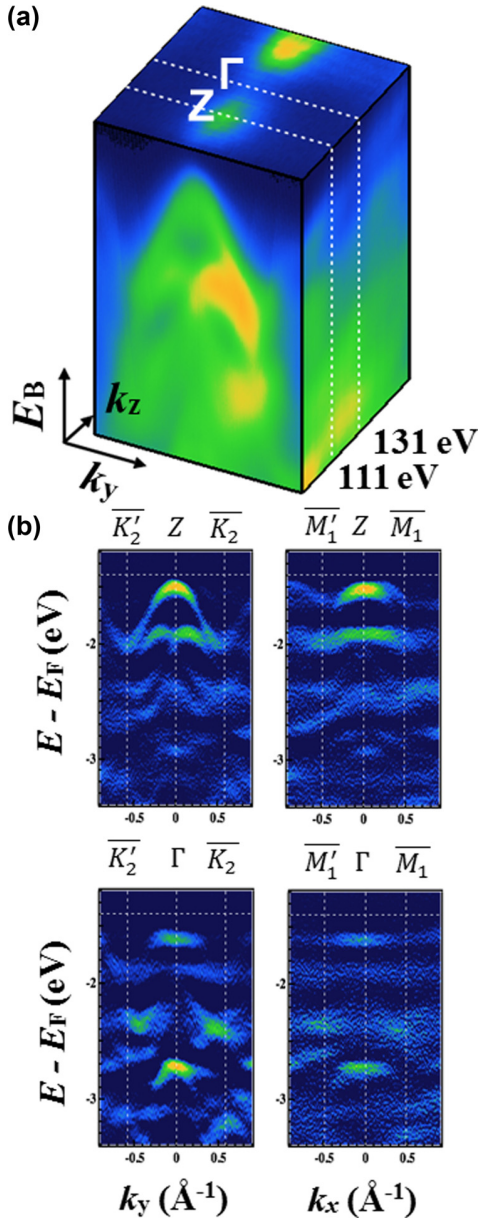

FIG. 4. (a) 3D ARPES intensity plots along the k_z, k_y versus binding energy E_B. The k_z periodicity shows that at photon energies of 131 and 111 eV, the ARPES mapping probe planes contain the Γ and the Z symmetry points, respectively. From this experimental determination we have estimated the inner potential $V_in = 16 \pm 2$ eV. (b) Second derivatives of ARPES intensity taken at Z and Γ along the $\overline{K}_2$ and $\overline{M}_1$ directions. In both cases, we see a sharper peak at Z, compared to the flatter bands in Γ, particularly in the $\overline{M}_1$ direction perpendicular to the Re chains. We see a difference in energy between the top of the valence band at Z and that at Γ of approximately 150–200 meV.

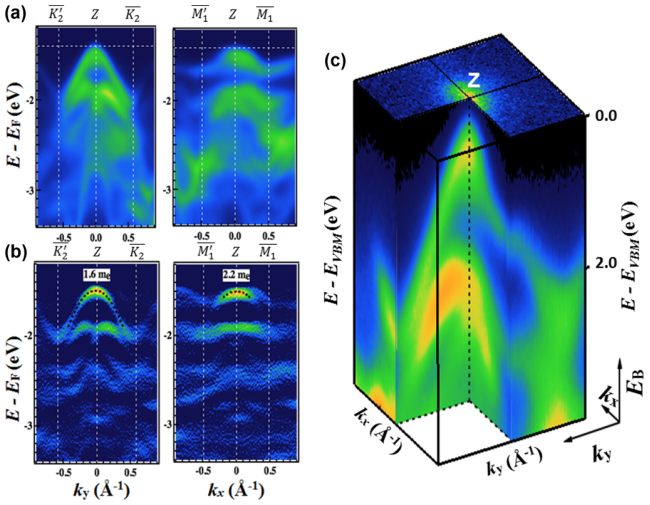

FIG. 5. (a) ARPES plots along the $\overline{K'}_2$-Z-$\overline{K}_2$ and $\overline{M'}_1$-Z-$\overline{M}_1$ directions are plotted together in (b) with the second derivative ARPES bands and the fitting curves determining the effective mass in both directions. (c) The 3D valence band dispersion along the k_x and k_y directions.

allow a precise estimation of the degree of in-plane anisotropy in the valence band. Here, effective valence band masses of $1.6 \pm 0.3 m_e$ and $2.2 \pm 0.7 m_e$ (where m_e is the free electron mass) have been directly determined along and perpendicular to the Re atomic chains, respectively (in the Supplemental Material, Fig. S1, we show fits bracketing the values above superimposed on the experimental data [27]). These values lie in the typical range for TMD materials [34].

Recently, the electrical transport properties of n-type field effect transistor devices have been reported to be strongly anisotropic [8,35,36], and the conduction band electron mobility was found to be about three times larger along the rhenium chains compared to the direction perpendicular to them [8]. In the Supplemental Material, Fig. S4, we give the conduction band effective masses derived from DFT calculations, which reflect this anisotropy [27]. The valence band masses given above would also lead to a similar degree of anisotropy in the hole mobility even if all other parameters determining the phonon-limited mobility (deformation potential constant, elastic modulus) were isotropic. However, no electrical measurements of hole mobility in ReS_2 are yet available for comparison.

To aid in interpretation of the data, we performed simulations of the present data using DFT calculations using parameters detailed in the Methods section; some results are shown in Fig. 6. We obtain qualitative agreement with the experimental data in both the $\overline{K}_2$ and the $\overline{M}_1$ directions, with the calculations matching the uppermost experimental bands best for $\overline{K}_2$-Z and worst for $\overline{M}_1$-Γ. To facilitate comparison of these simulations to experiment, Figs. S1 and S2 of the Supplemental Material show the simulations superimposed on the ARPES data for calculations using both the PBE functional (as shown in Fig. 6; Fig. S1) and a fully relativistic LDA functional (Fig. S2) [27].

Importantly, in both cases we replicate the anisotropy observed in experiment with respect to the Re chain direction. As an example, we focus on the dispersion along $\overline{K'}_2$-Γ-$\overline{K}_2$, Fig. 6(a), where the highest energy valence band has a strongly peaked and approximately parabolic form while the next valence band down in energy has a distinctive double-peak structure; this is exactly as found in experiment, as shown in Figs. 4(b) and 5(b). In these simulations, we did not take into

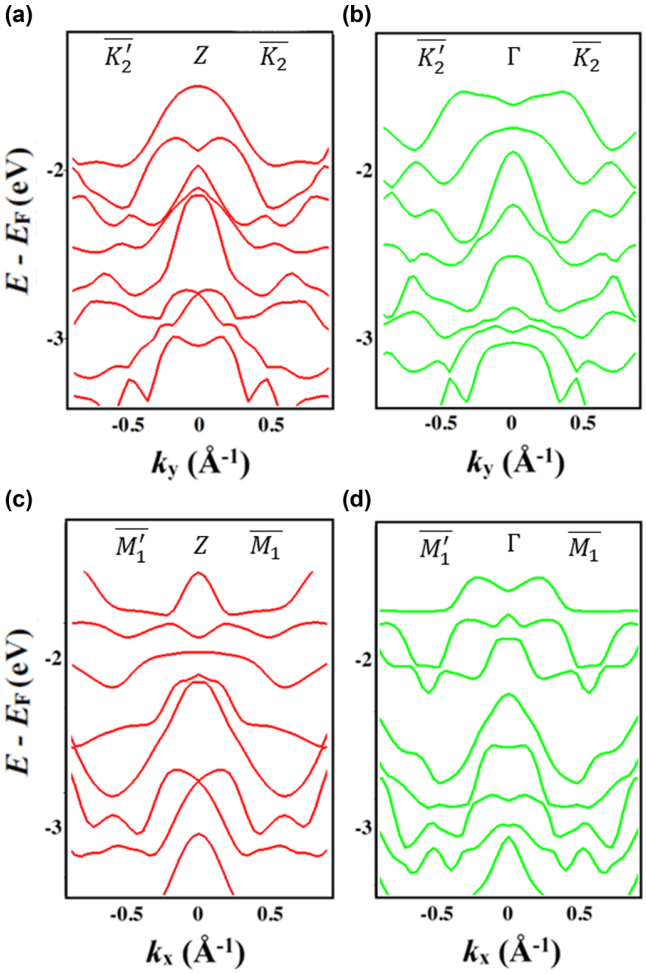

FIG. 6. Calculations of the valence bands measured by ARPES in Fig. 4 along the following directions: (a) $\overline{K'}_2$-Z-$\overline{K}_2$; (b) $\overline{K'}_2$-Γ-$\overline{K}_2$; (c) $\overline{M'}_1$-Z-$\overline{M}_1$; (d) $\overline{M'}_1$-Γ-$\overline{M}_1$ by DFT using a PBE functional (parameters given in method), showing the same anisotropy with respect to the Re chain direction.

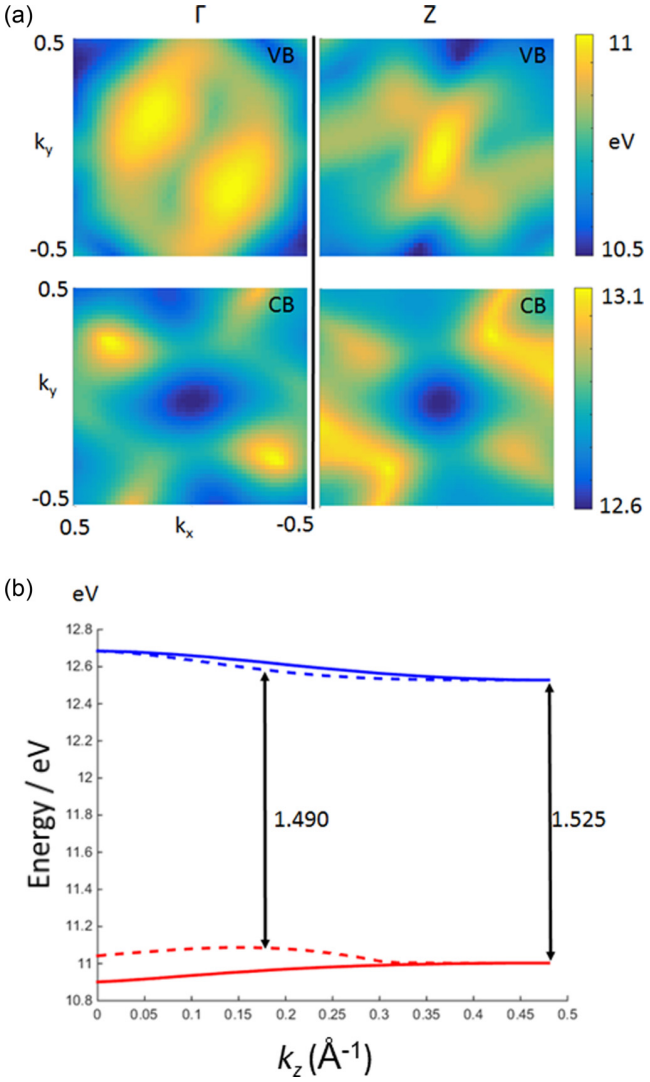

FIG. 7. Calculation of the valence band maximum (VB) and conduction band minimum (CB) at Z and Γ using a PBE functional. The calculations are performed in the shaded planes of Fig. 1(b) and here k_x and k_y are in units of the reciprocal lattice vector **a***. We see a direct gap at Z with an increasingly indirect gap towards Γ. (b) Calculation of the VB maximum and CB minimum as a function of k_z for all k_x,k_y (solid line) and restricted to the Γ-Z direction $k_x = 0$, $k_y = 0$ (dashed line). We find the minimum indirect band gap occurs at around $k_z = 0.18$, lower in energy than the direct gap at Z. We calculate again a similar change in the VB maximum from Γ to Z, as in experiment.

account the slight curvature of the plane in k space probed in ARPES that arises from the nonconservation of k_z [32]; for these rather high excitation energies, we expect that this does not introduce a significant error, but it may affect the comparison to experiment particularly for bands deeper in the valence band.

Based on these simulations of the experimental data we used DFT to calculate the full band structure of the material including the lowest-lying conduction band states. Here, both PBE (GGA) and fully relativistic PZ (LDA) functionals were used in order to estimate the effects of spin-orbit coupling due to the high atomic number of rhenium. The results are qualitatively similar apart from the well-known underestimation of the band gap in the LDA, and so we focus here on the PBE (GGA) functional as used to produce the results shown in Fig. 6. Figure 7(a) shows the calculated energy of the highest-energy VB and lowest-energy CB states, with Fig. 7(b) showing the absolute CB minimum (CBM) and VB maximum (VBM) energies (dashed) and the local CBM and VBM values moving along the direction Γ to Z, that is, as a function of k_z. We performed a full 3D calculation of the entire Brillouin zone in k_x, k_y, and k_z to obtain this data. As noted above, conduction band effective masses obtained from parabolic fits to the DFT data at the Z point are given for the k_x and k_y directions in the Supplemental Material (Fig. S4) [27]. From our calculations, we also obtained the electronic density of states for bulk ReS_2 (Supplemental Material, Fig. S3), which reproduces earlier calculations well [21,37].

At Z we obtain an estimate of the zero-temperature direct band gap as 1.525 eV. We note that a broad range of experimental band gaps exist from previous work from around

1.6 eV [15] down to around 1.3 eV [16,28] (or lower in defect-rich materials or if defect states are probed [38]). In our calculations, the band gap value obtained by the GGA is the most reliable and is in good agreement with experimental values [28]. Interestingly, towards Γ we find a transition to an indirect band gap. The conduction band minimum remains at $(k_x,k_y) = 0$ [bottom left panel of Fig. 7(a)]. We find the gap narrows at around $k_z = 0.18$ to lower energy (1.49 eV) than at Z, as indicated by the arrow on Fig. 7(b). Moving from Z to Γ and calculating at $(k_x,k_y) = 0$ (solid line on Fig. 7) we observe the valence band maximum to decrease by 125 meV for PBE (and 210 meV for PZ). This is very similar to the 100- to 200-meV drop in the valence band maximum from Z to Γ observed experimentally and can be seen in Fig. 4.

This behavior may account for some of the uncertainty in the literature regarding the direct or indirect gap nature of bulk ReS_2, with other groups reporting electrical transport properties characteristic of indirect behavior in bulk samples [28,39] or PL peaks within this range close to the direct transition [7], while one group found a direct gap via electron energy loss spectroscopy of 1.42 eV at room temperature [22], consistent with the direct gap at 100 K of ∼1.5 eV that we find [40]. Unlike here, previous calculations have often not considered the full bulk BZ and have instead focused on 2D or quasi-2D simulations of ReS_2, where calculations have predicted the gap to be direct at the 2D Γ point [15] in the monolayer form. As yet, only one brief study of ARPES measurements has been reported on a 2D monolayer of ReS_2 [11], and an important next step in this field will be to investigate few-layer structures in more detail. Use of a hybrid functional may also enhance the quality of the calculations. To confirm fully the nature of the band gap in the material, it is necessary to measure the lowest states of the conduction band (potentially through alkali-metal doping of the material).

IV. CONCLUSIONS

In conclusion, we have performed ARPES measurements on the transition-metal dichalcogenide ReS_2 in its bulk form. The anisotropic curvature of the valence band in directions perpendicular and parallel to the Re atomic chains can account for the reported anisotropic electrical properties (effective mass and mobility) of the material. We find the valence band maximum at Z to be higher in energy than that at Γ, and we obtain good agreement with DFT calculations of the band structure. Our calculations for the electronic bands over the whole bulk Brillouin zone predict a direct band gap at Z and a wider gap towards Γ with a small shift of 100–200 meV in the valence band maximum between these two points. This may account for uncertainty in the literature as to the direct or indirect nature of the band gap in bulk ReS_2. Future work to measure the conduction band directly (for example by doping to move the Fermi level into the conduction band) is required to investigate this more fully and also to map out the band structure of two-dimensional monolayer ReS_2.

Note added. Recently, two more reports of ARPES studies of ReS_2 in bulk and thin-layer forms appeared on arXiv (both now published) which confirm the three-dimensional dispersion of the valence band structure [41] and, for the bulk material, indicate via Rb-doping that the band extrema are indeed located at Z, as proposed above [42].

ACKNOWLEDGMENTS

This work was supported by the Centre for Graphene Science of the Universities of Bath and Exeter and by the EPSRC (UK) under Grants No. EP/G036101, No. EP/M022188, and No. EP/P004830; L.S.H. is supported by the Bath/Bristol Centre for Doctoral Training in Condensed Matter Physics, Grant No. EP/L015544. We thank the SOLEIL synchrotron for the provision of beam time; work at SOLEIL was supported by EPSRC Grant No. EP/P004830/1. Computational work was performed on the University of Baths High Performance Computing Facility. We thank Dr. Philip King of St. Andrews University for useful discussions and for communicating his data [42] prior to publication. M.C.A., J.A., and C.C. thank Young-Hee Lee and Matthias Bantzill for enlightening exchanges. The Synchrotron SOLEIL is supported by the Centre National de la Recherche Scientifique (CNRS). Data created during this research are freely available from the University of Bath data archive at DOI:10.15125/BATH-00331.

[1] A. K. Geim and I. V. Grigorieva, Nature (London) **499**, 419 (2013).
[2] K. F. Mak, C. Lee, J. Hone, J. Shan, and T. F. Heinz, Phys. Rev. Lett. **105**, 136805 (2010).
[3] H. R. Matte, A. Gomathi, A. K. Manna, D. J. Late, R. Datta, S. K. Pati, and C. Rao, Angew. Chem., Int. Ed. **49**, 4059 (2010).
[4] J. N. Coleman *et al.*, Science **331**, 568 (2011).
[5] N. Zibouche, P. Philipsen, A. Kuc, and T. Heine, Phys. Rev. B **90**, 125440 (2014).
[6] K. Friemelt, M. Lux-Steiner, and E. Bucher, J. Appl. Phys. **74**, 5266 (1993).
[7] O. B. Aslan, D. A. Chenet, A. M. van der Zande, J. C. Hone, and T. F. Heinz, ACS Photonics **3**, 96 (2016).
[8] E. Liu, Y. Fu, Y. Wang, Y. Feng, H. Liu, X. Wan, W. Zhou, B. Wang, L. Shao, C.-H. Ho, Y.-S. Huang, Z. Cao, L. Wang, A. Li, J. Zeng, F. Song, X. Wang, Y. Shi, H. Yuan, H. Y. Hwang, Y. Cui, F. Miao, and D. Xing, Na. Commun. **6**, 6991 (2015).
[9] Y.-C. Lin, H.-P. Komsa, C.-H. Yeh, T. Bjrkman, Z.-Y. Liang, C.-H. Ho, Y.-S. Huang, P.-W. Chiu, A. V. Krasheninnikov, and K. Suenaga, ACS Nano **9**, 11249 (2015).
[10] E. Zhang, Y. Jin, X. Yuan, W. Wang, C. Zhang, L. Tang, S. Liu, P. Zhou, W. Hu, and F. Xiu, Adv. Funct. Mater. **25**, 4076 (2015).
[11] F. Liu, S. Zheng, X. He, A. Chaturvedi, J. He, W. L. Chow, T. R. Mion, X. Wang, J. Zhou, Q. Fu *et al.*, Adv. Funct. Mater. **26**, 1169 (2016).
[12] J. O. Island, G. A. Steele, H. S. J. van der Zant, and A. Castellanos-Gomez, 2D Mater. **2**, 011002 (2015).
[13] S. Tongay, J. Zhou, C. Ataca, K. Lo, T. S. Matthews, J. Li, J. C. Grossman, and J. Wu, Nano Lett. **12**, 5576 (2012).

[14] I. G. Lezama, A. Arora, A. Ubaldini, C. Barreteau, E. Giannini, M. Potemski, and A. F. Morpurgo, Nano Lett. **15**, 2336 (2015).
[15] S. Tongay, H. Sahin, C. Ko, A. Luce, W. Fan, K. Liu, J. Zhou, Y.-S. Huang, C.-H. Ho, J. Yan, D. F. Ogletree, S. Aloni, J. Ji, S. Li, J. Li, F. M. Peeters, and J. Wu, Nat. Commun. **5**, 3252 (2014).
[16] S. P. Kelty, A. F. Ruppert, R. R. Chianelli, J. Ren, and M.-H. Whangbo, J. Am. Chem. Soc. **116**, 7857 (1994).
[17] D. A. Chenet, O. B. Aslan, P. Y. Huang, C. Fan, A. M. van der Zande, T. F. Heinz, and J. C. Hone, Nano Lett. **15**, 5667 (2015).
[18] H.-J. Lamfers, A. Meetsma, G. Wiegers, and J. de Boer, J. Alloys Compd. **241**, 34 (1996).
[19] C. H. Ho, Y. S. Huang, P. C. Liao, and K. K. Tiong, J. Phys. Chem. Solids **60**, 1797 (1999).
[20] H. H. Murray, S. P. Kelty, R. R. Chianelli, and C. S. Day, Inorg. Chem. **33**, 4418 (1994).
[21] C. H. Ho, Y. S. Huang, J. L. Chen, T. E. Dann, and K. K. Tiong, Phys. Rev. B **60**, 15766 (1999).
[22] K. Dileep, R. Sahu, S. Sarkar, S. C. Peter, and R. Datta, J. Appl. Phys. **119**, 114309 (2016).
[23] L. Hart, S. Dale, S. Hoye, J. L. Webb, and D. Wolverson, Nano Lett. **16**, 1381 (2016).
[24] P. Giannozzi *et al.*, J. Phys.: Condens. Matter **21**, 395502 (2009).
[25] J. P. Perdew, K. Burke, and M. Ernzerhof, Phys. Rev. Lett. **77**, 3865 (1996).
[26] J. P. Perdew and A. Zunger, Phys. Rev. B **23**, 5048 (1981).
[27] See Supplemental Material at http://link.aps.org/supplemental/10.1103/PhysRevB.96.115205 for comparison of calculated and measured valence band dispersions, calculated electronic densities of states, and effective mass estimates.
[28] C. H. Ho, Y. S. Huang, K. K. Tiong, and P. C. Liao, Phys. Rev. B **58**, 16130 (1998).
[29] G. Leicht, H. Berger, and F. Levy, Solid State Commun. **61**, 531 (1987).
[30] S. Hüfner, *Photoelectron Spectroscopy*, Advanced Texts in Physics (Springer-Verlag, Berlin, Heidelberg, 2003).
[31] T. Finteis, M. Hengsberger, T. Straub, K. Fauth, R. Claessen, P. Auer, P. Steiner, S. Hüfner, P. Blaha, M. Vögt, M. Lux-Steiner, and E. Bucher, Phys. Rev. B **55**, 10400 (1997).
[32] L. S. Hart, J. L. Webb, S. Dale, S. J. Bending, M. Mucha-Kruczynski, D. Wolverson, C. Chen, J. Avila, and M. C. Asensio, Sci. Rep. **7**, 5145 (2017).
[33] H.-X. Zhong, S. Gao, J.-J. Shi, and L. Yang, Phys. Rev. B **92**, 115438 (2015).
[34] F. A. Rasmussen and K. S. Thygesen, J. Phys. Chem. C **119**, 13169 (2015).
[35] C. M. Corbet, C. McClellan, A. Rai, S. S. Sonde, E. Tutuc, and S. K. Banerjee, ACS Nano **9**, 363 (2015).
[36] Z. H. Zhou, B. C. Wei, C. Y. He, Y. M. Min, C. H. Chen, L. Z. Liu, and X. L. Wu, Appl. Surf. Sci. **404**, 276 (2017).
[37] C. Fang, G. Wiegers, C. Haas, and R. De Groot, J. Phys.: Condens. Matter **9**, 4411 (1997).
[38] S. Horzum, D. Çakır, J. Suh, S. Tongay, Y.-S. Huang, C.-H. Ho, J. Wu, H. Sahin, and F. M. Peeters, Phys. Rev. B **89**, 155433 (2014).
[39] I. Gutiérrez-Lezama, B. A. Reddy, N. Ubrig, and A. F. Morpurgo, 2D Mater. **3**, 045016 (2016).
[40] C.-C. Huang, C.-C. Kao, D.-Y. Lin, C.-M. Lin, F.-L. Wu, R.-H. Horng, and Y.-S. Huang, Jpn. J. Appl. Phys. **52**, 04CH11 (2013).
[41] M. Gehlmann, I. Aguilera, G. Bihlmayer, S. Nemšák, P. Nagler, P. Gospodarič, G. Zamborlini, M. Eschbach, V. Feyer, F. Kronast, E. Młyńczak, T. Korn, L. Plucinski, C. Schüller, S. Blügel, and C. M. Schneider, Nano Lett. **17**, 5187 (2017).
[42] D. Biswas, A. M. Ganose, R. Yano, J. M. Riley, L. Bawden, O. J. Clark, J. Feng, L. Collins-Mcintyre, M. T. Sajjad, W. Meevasana, T. K. Kim, M. Hoesch, J. E. Rault, T. Sasagawa, D. O. Scanlon, and P. D. C. King, Phys. Rev. B **96**, 085205 (2017).

Electronic bandstructure of ReS_2 by high resolution angle resolved photoemission spectroscopy

James L. Webb, Lewis S. Hart, and Daniel Wolverson
Centre for Nanoscience and Nanotechnology, Department of Physics, University of Bath, Bath BA2 7AY, United Kingdom

Chaoyu Chen, Jose Avila, and Maria C. Asensio,
Synchrotron SOLEIL, Saint Aubin, and Universit_e Paris-Saclay, BP 48 91192 Gif-sur-Yvette, France

Supplemental material (four figures follow)

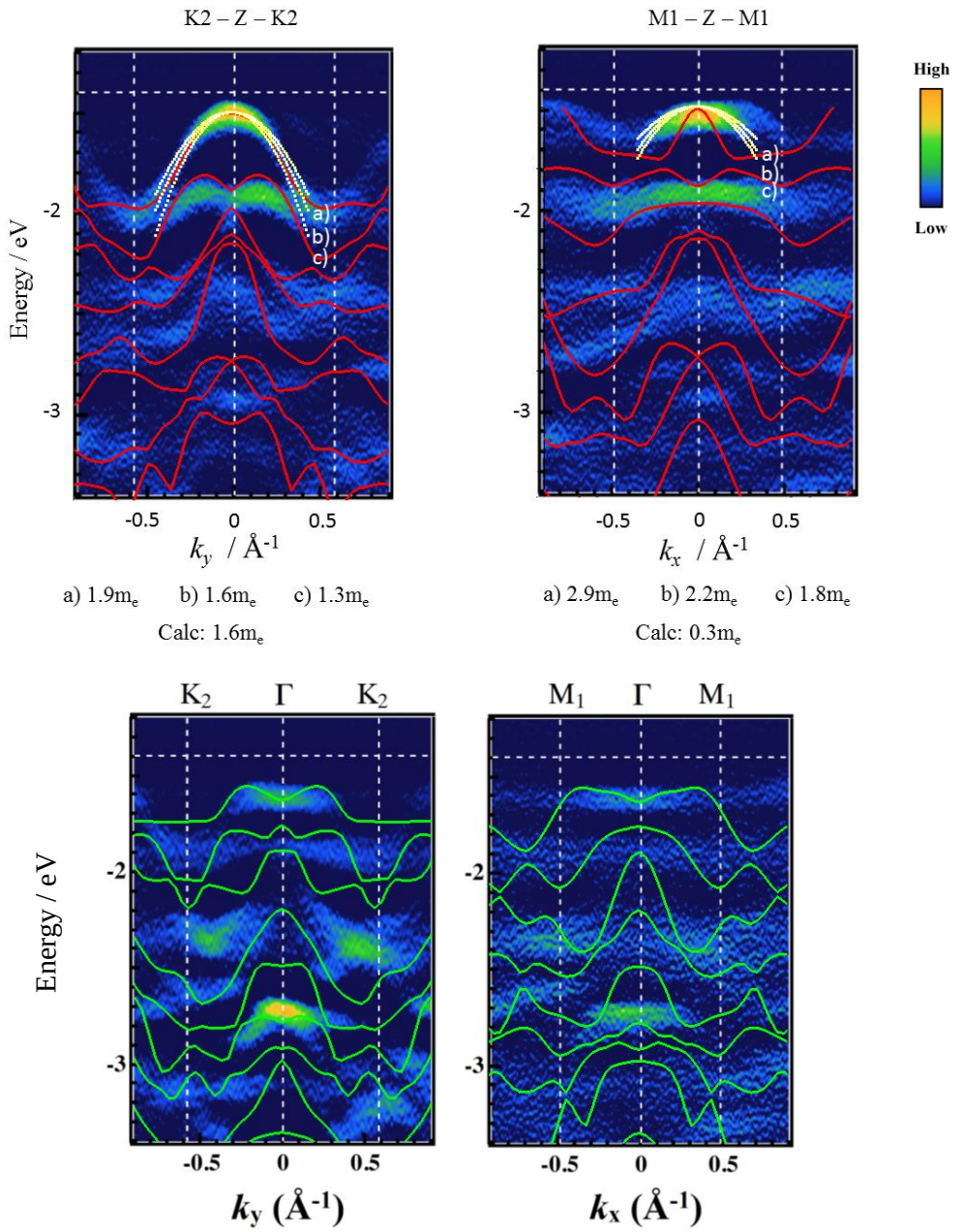

Figure S1: Calculated (solid lines) and experimental (colour map) band structures for bulk ReS_2, passing through the Z (top) and Γ (bottom) planes in the K_2 and M_1 directions as defined in the main paper. A PBE (GGA) functional was used, with identical input parameters and structural configuration as for the data presented in Fig. 6 of the main paper and in Fig. S3 below. The structure was relaxed to obtain forces of less than 10^{-3} eV/Å. The parabolae used to obtain the effective masses quoted in the main paper are shown (white dotted lines) and the values obtained from fitting the calcualted dispersions are also shown. In the K_2 direction, agreement between calculated and experimental values is good but there is a significant discrepancy in the M_1 direction. These masses are in the range of those found for TMDs [1] though no other TMDs have the ReS_2 crystal structure and so values are not directly comparable.

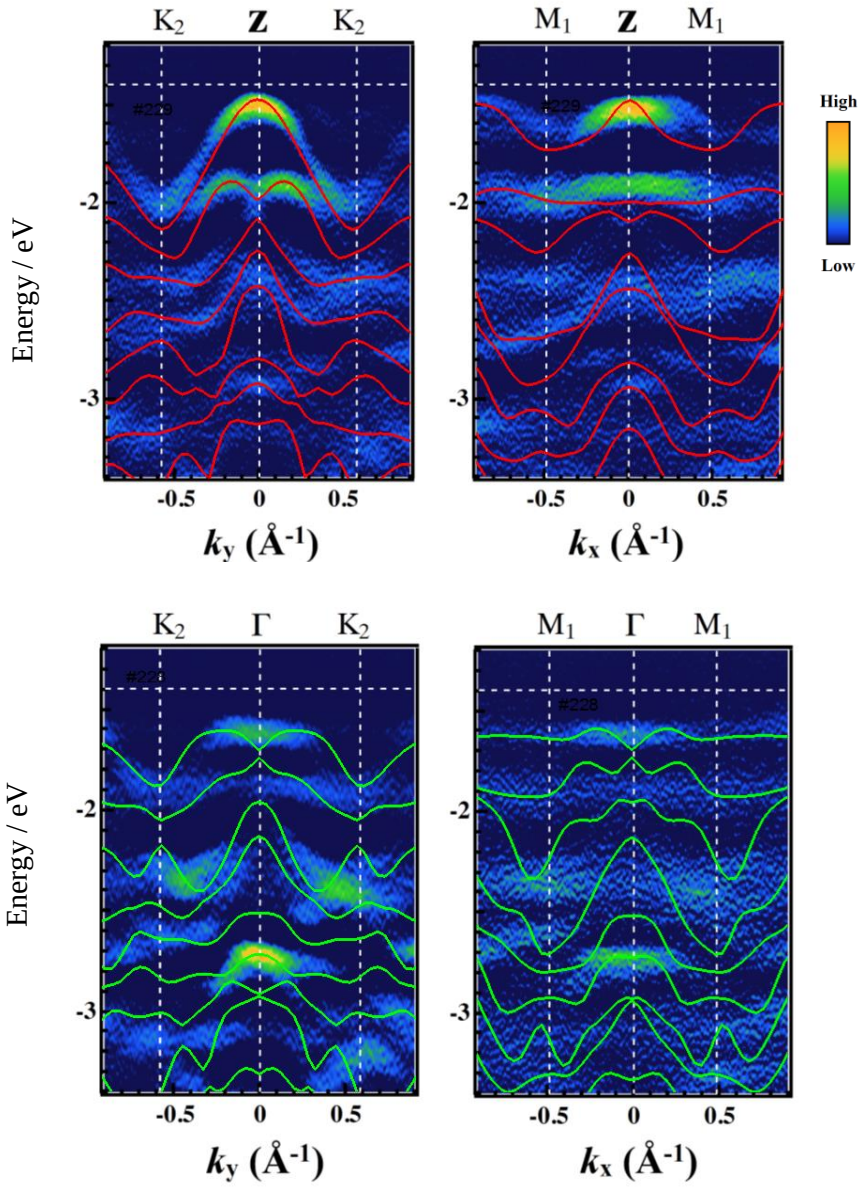

Figure S2: Calculated (solid lines) and experimental (colour map) band structures for bulk ReS_2, for the same planes and directions in reciprocal space as in Figure S1. Here, a fully-relativistic Perdew-Zunger (PZ) local density approximation (LDA) functional was used with projector-augmented wave (PAW) pseudopotentials. The starting atomic configuration was identical to that the data presented in Fig. 6 of the main paper and in Fig. S1 above and the structure was again relaxed to obtain forces of less than 10^{-3} eV/Å. This calculation, which accounts for spin-orbit coupling effects, shows an improvement in the agreement with experiment in both the Γ and Z planes; the discrepancy in the region of the Z point for the M_1-Z direction is reduced but still persists.

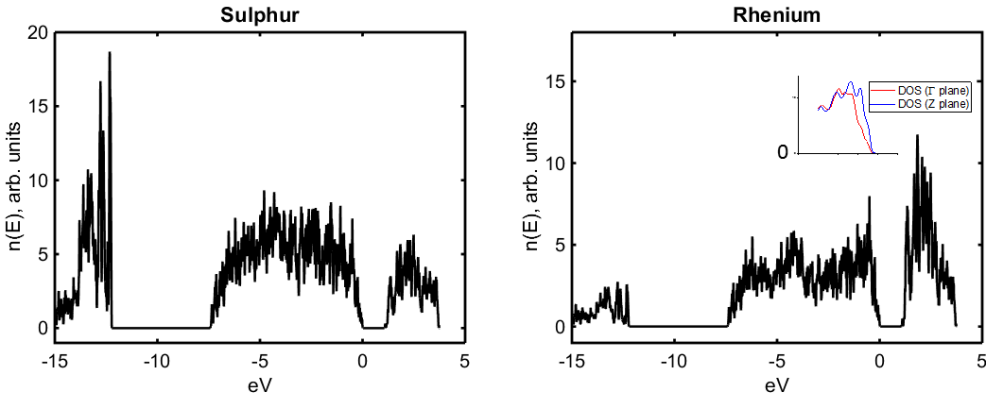

Figure S3: Calculated density of states for bulk ReS_2, plotting summed contributions from Re and S separately. Here, a PBE functional was used, with identical input parameters and structural configuration as for the data presented in Fig. 6 of the main paper and in Fig. S1 above. The top of the valence band is taken as the zero of energy. We find excellent agreement with the previous calculations performed by Ho *et al.* [2], with a valence band width of approximately 7.5eV and a large contribution from the S 3s states at approximately 12.5eV below the Fermi level. The inset shows experimental densities of states (in arb. units, kinetic energy scale shifted to align the top of the valence band with the calculated DOS) extracted from our experimental data with excitation energies corresponding to the Γ and Z planes (red and blue lines respectively) over the near-band edge range.

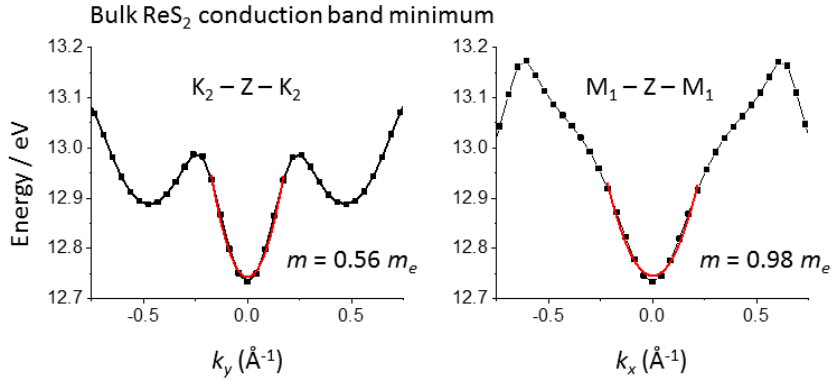

Figure S4: Calculated (black dotted lines) and fitted (red parabolae) conduction band edge dispersion for bulk ReS_2, passing through the Z plane in the K_2 and M_1 directions as defined in the main paper. Conduction band (CB) effective masses *m* at Z derived from the fits are shown. A PBE (GGA) functional was used, with the same input parameters and structural configuration as for the data presented in Fig. 6 of the main paper and in Figures S1 and S3 above. The non-equivalence of K_2 and M_1 directions in the CB is visible in the bottom two panels of Figure 7(a) in the main text.

[1] Rasmussen F A and Thygesen K S 2015 *The Journal of Physical Chemistry C* **119** 13169-13183

[2] Ho C H, Huang Y S, Chen J L, Dann T E and Tiong K K 1999 *Phys. Rev. B* **60** 15766-15771

9.4 Discussions

The results in this paper indicate that the band gap may not be along any of the high symmetry directions. It is hoped future calculations of the electronic band structure of ReS_2 will be made in regions of the Brillouin zone that are not along the high symmetry directions. This is the only way to predict the position of the true VBM and CBM. Chapter 10 contains examples of such calculations where the VBM and CBM are determined for both of the rhenium dichalcogenides.

To quantify the anisotropy in ReS_2, the effective mass of the charge carriers has been measured along and perpendicular to the direction of the rhenium chains. It is possible to compare the results in this paper to previous electronic transport studies; however such comparisons must be made with some caution. Transport experiments give an indirect measurement of the effective mass of the charge carriers, whereas obtaining these values by fitting the experimentally measured uppermost valence band with a parabola can be considered a more direct approach.

During the writing of the manuscript we were made aware of two other ARPES studies of ReS_2. This paper has a somewhat controversial result that the electronic coupling in ReS_2 is not weak, despite the large amount of literature which argue the interlayer coupling is negligible. It is therefore significant that two other independent ARPES studies of bulk ReS_2 come to the same conclusion. These other papers also agree that the effective mass of the charge carriers is smallest along the direction of the rhenium chains [55, 56].

Chapter 10

Electronic band structure of rhenium dichalcogenides

10.1 Preamble

An interesting result from the ARPES work on the bulk rhenium dichalcogenides, described in Chapter 7 and Chapter 9, is the valence band maxima of these crystals may not be along any of the high symmetry directions. All previous DFT calculations of these crystals have been along the high symmetry directions, therefore the valence band maxima might have been missed. The electronic band structures of $ReSe_2$ and ReS_2 are investigated using ab initio DFT calculations in this paper. Unlike previous work, the band energies are calculated over the entire Brillouin zone. Within this paper both the valence bands and conduction bands are calculated and used to determine whether these crystals have direct or indirect band gaps.

This chapter contains the first set of DFT calculations for both of the rhenium dichalcogenides that are not solely along high symmetry directions. By having the band structures of $ReSe_2$ and ReS_2 displayed in the same paper it is easy to compare these two materials.

The candidate was involved with the formulation of the ideas and helped with the writing of the manuscript. Miss Gunasekera and Dr Wolverson performed the DFT calculations with

help from Dr Mucha-Kruczynski.

10.2 Statement of authorship and copyright information

<table>
<tr><td colspan="5">This declaration concerns the article entitled:</td></tr>
<tr><td colspan="5">Electronic band structure of rhenium dichalcogenides</td></tr>
<tr><td colspan="5">Publication status (tick one)</td></tr>
<tr><td>Draft manuscript</td><td>Submitted</td><td>In review</td><td>Accepted</td><td>Published</td></tr>
<tr><td></td><td></td><td></td><td></td><td>✓</td></tr>
<tr><td>Publication details (reference)</td><td colspan="4">S. M. Gunasekera, D. Wolverson, L. S. Hart, and M. Mucha-Kruczynski, “Electronic band structure of rhenium dichalcogenides,” Journal of Electronic Materials, Mar 2018.</td></tr>
<tr><td>Candidate’s contribution to the paper (detailed, and also given as a percentage)</td><td colspan="4">The candidate contributed to the formulation of ideas in relation to this paper.
Formulation of ideas: 40%
Design of methodology: 0%
Experimental work: 0%
Computational work: 0%
Presentation of data in journal format: 0%</td></tr>
<tr><td>Statement from Candidate</td><td colspan="4">This paper reports on original research I conducted during the period of my Higher Degree by Research candidature.</td></tr>
<tr><td>Signature</td><td colspan="2"></td><td>Date</td><td>29/05/2018</td></tr>
</table>

Publication title: Electronic Band Structure of Rhenium Dichalcogenides

The pages of this thesis this paper spans are from 178 to 184.

Journal of ELECTRONIC MATERIALS
https://doi.org/10.1007/s11664-018-6239-0

TOPICAL COLLECTION: 18TH INTERNATIONAL CONFERENCE ON II-VI COMPOUNDS

Electronic Band Structure of Rhenium Dichalcogenides

SURANI M. GUNASEKERA,[1] DANIEL WOLVERSON ,[1,2] LEWIS S. HART,[1] and MARCIN MUCHA-KRUCZYNSKI[1]

1.—Centre for Nanoscience and Nanotechnology, Department of Physics, University of Bath, Bath BA2 7AY, UK. 2.—e-mail: d.wolverson@bath.ac.uk

The band structures of bulk transition metal dichalcogenides ReS_2 and $ReSe_2$ are presented, showing the complicated nature of interband transitions in these materials, with several close-lying band gaps. Three-dimensional plots of constant energy surfaces in the Brillouin zone at energies near the band extrema are used to show that the valence band maximum and conduction band minimum may not be located at special high symmetry points. We find that both materials are indirect gap materials and that one must be careful to consider the whole Brillouin zone volume in addressing this question.

Key words: $ReSe_2$, ReS_2, rhenium dichalcogenides, angle-resolved photoemission, band structure

INTRODUCTION

The field of two-dimensional few-layer and monolayer materials has generated intense and sustained interest since the isolation of graphene in 2004,[1] though bulk (three-dimensional) van der Waals layered materials and, in particular, the transition metal dichalcogenides (TMDs), were known and studied much earlier.[2] In the last few years, many more two-dimensional materials have been identified or proposed, and there are currently around 1000 candidates for two-dimensional metals, semiconductors, superconductors and charge density wave materials. Besides graphene, the TMDs are still the most actively studied members of this family, and many prototype devices (e.g., field effect transistors, sensors, and photo-detectors) based on MoS_2 have been demonstrated successfully and device paradigms are proposed (e.g., spin- and valleytronics) based on the band structure of mono- or few-layer MoS_2.[3,4]

Although MoS_2 is arguably the archetypal semiconducting TMD, there are many TMDs that offer contrasting properties to MoS_2 and, therefore, add significantly to the diversity of TMD devices and heterostructures that can be explored.[2] The rhenium chalcogenides ReS_2 and $ReSe_2$ are prime examples of this Ref. 5 since they differ markedly from MoS_2 in crystal structure and symmetry,[6] electronic band structure,[7] and lattice dynamics.[8] The crystal structure of these compounds is shown in Fig. 1, based on early crystal structure determinations via x-ray diffraction[6] and optimisation of the structures via first-principles calculations as described in the Methods section. In the ReX_2 structure (X = S, Se) Re atoms group into diamond-shaped clusters of four atoms, and each cluster is linked to the next one by Re–Re bonds to form chains running along the crystallographic axis direction we define as a.[9] The resulting structure has only inversion symmetry and is highly anisotropic in all physical properties in-plane, in contrast to the hexagonal TMDs. The stacking of layers is such that the c axis is not perpendicular to the layer plane, but a and b do lie in the layer plane, so that the reciprocal space c^* axis is normal to the real space layers, and thus also normal to the principal surface of bulk crystals; a^* and b^* lie out of the layer plane. Thus, angle-resolved photoemission (ARPES) experiments, which preserve information about electron momentum normal to the sample surface, will probe the valence band dispersion in an approximately planar section through the Brillouin zone that does not contain any of the reciprocal lattice vectors (this is illustrated in Ref. 10, Fig. 2).

Recently, we have presented experimental data on the electronic valence band structures of ReS_2[11]

(Received December 31, 2017; accepted March 14, 2018)

Published online: 22 March 2018

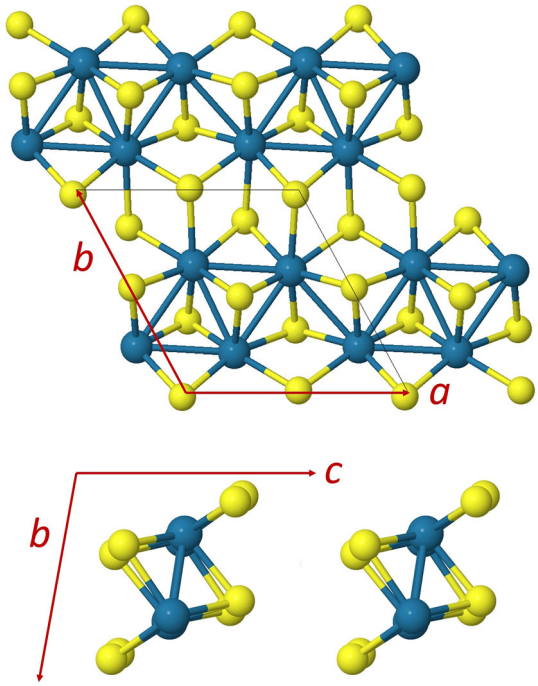

Fig. 1. Top and side views of the ReX_2 structure with rhenium (sulphur or selenium) atoms shown in blue (yellow); the rhenium atoms lie in the layer plane. The *a* and *b* crystallographic axes are in the layer plane and are defined as shown in the upper panel; the side view (lower panel) is drawn looking along *a* and shows that the *c* axis is not normal to the layer plane.

and $ReSe_2$[12] as determined by nanoscale ARPES, and closely related work has been reported also by other groups on both bulk ReS_2[13] and also few-layer ReS_2[10] This work addresses controversies over (1) the nature of the bandgaps in the ReX_2 family and (2) the degree to which the ReX_2 bulk materials can be considered as non-interacting stacked layers. It has become clear that the details of a particular first-principles calculation influence the conclusions about the existence of a direct gap and the locations of the conduction and valence band extrema; these materials present a very flat band structure with a large number of bands in a small energy range (due to the large 12-atom unit cell) and, as we shall show, the band extrema are not necessarily located at any high symmetry points of the Brillouin zone (BZ). Calculations typically focus on high symmetry paths in the BZ and may miss the true band edges; here, we take a different approach, calculating the band energies over the whole volume of the BZ and tracing out constant energy surfaces rather than dispersions. In particular, we present data for the conduction band of bulk $ReSe_2$, which has not previously been discussed in detail.

COMPUTATIONAL METHODS

Electronic band structures were calculated via plane-wave, pseudopotential methods within density functional theory (DFT) using the QUANTUM ESPRESSO package.[14] Structures were derived from published x-ray diffraction (XRD) crystallographic data[6] and were relaxed with respect to both unit cell dimensions and atomic coordinates to give atomic forces of less than 6.1×10^{-3} eV Å^{-1} (ReS_2) or 3.5×10^{-2} eV Å^{-1} ($ReSe_2$). Fully relativistic pseudopotentials were used with the projector augmented wave (PAW) method;[15] pseudopotentials and PAW datasets were constructed using the PSLibrary[16] for the local density approximation (LDA) Perdew–Zunger[17] and generalized gradient approximation (GGA) Perdew–Burke–Ernzerhof[18] exchange–correlation functionals. The valence of Re was taken as 15 (configuration $5s^2\ 5p^6\ 5d^5\ 6s^2$). Monkhorst–Pack[19] *k*-point meshes of $10 \times 10 \times 10$ (ReS_2) or $8 \times 8 \times 8$ ($ReSe_2$) were used with kinetic energy cutoffs of, typically, 60 Ry (816 eV); convergence with respect to both of these was checked. In this work we present results using fully relativistic LDA and GGA functionals; we have explored the differences between the results using the LDA and GGA levels of approximation further elsewhere.[12,20]

RESULTS AND DISCUSSION

No direct comparison of the band structures of $ReSe_2$ and ReS_2 over the whole Brillouin zone (BZ) has yet been presented and so we provide such a comparison here. This is useful as a guide to the electronic properties of these materials, but also gives insight into the difficulties in making first-principles calculations of band structure in this system; our results show that it is necessary to consider the whole BZ and not to focus only on high-symmetry paths. To make this comparison, we use consistently two types of pseudopotential; although more sophisticated calculations of band structure can be performed, and the exact positions of the band extrema depend on the choice of pseudopotential, these comments will apply at any level of approximation.

Rhenium Sulphide

We consider first ReS_2, being the more well-studied of the two materials, and the material with the wider bandgap. It should be noted that here we take the bulk unit cell to contain just one monolayer and four formula units; this contradicts the conclusions of some early XRD studies of ReS_2[6,] but is consistent with more recent XRD[21] and photon-energy dependent ARPES studies;[10,13,20] the latter technique probes the valence band dispersion in the direction normal to the sample surface (which is here the layer plane) and is thus sensitive to the lattice periodicity in that direction.

Figure 2 shows constant energy surfaces for two energies chosen to show (a, c) the conduction (CB) and (b, d) valence band (VB) structures clearly within the full three-dimensional BZ. In both cases, the smaller (red) surface encloses the band extremum and the larger (yellow) surface shows how the bands develop at energies further from the band

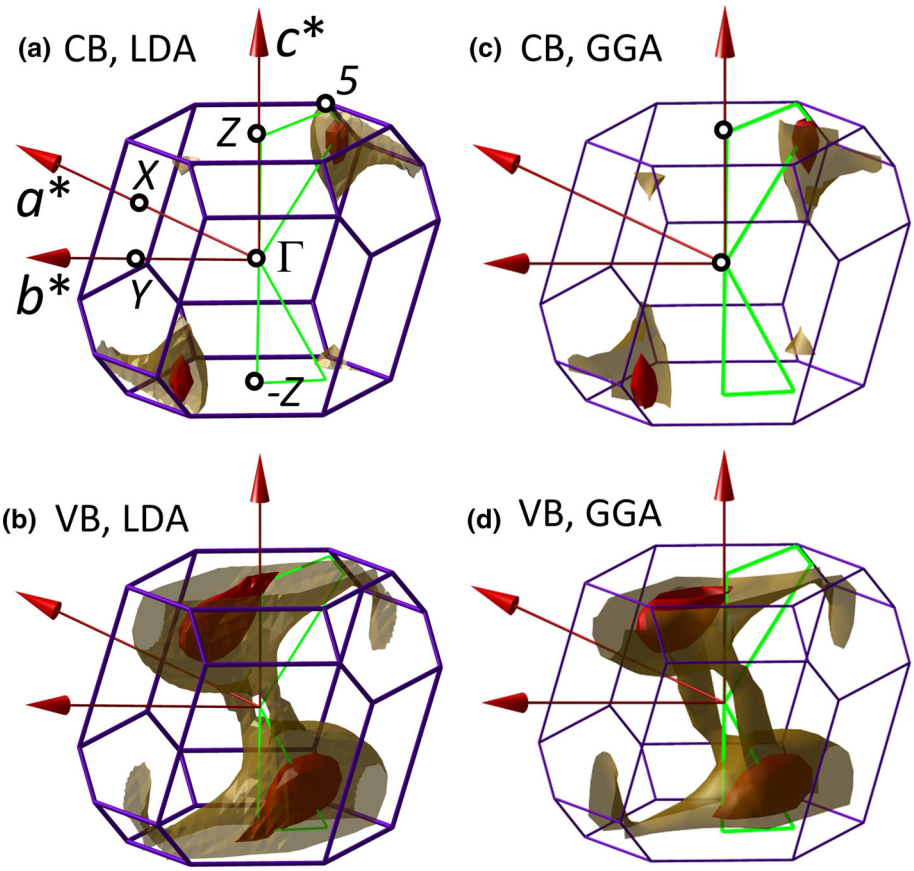

Fig. 2. Constant energy surfaces in the Brillouin zone of ReS_2. Calculations using LDA: (a) contours in the conduction band (CB) at energies of 70 meV (yellow) and 20 meV (red) above the CB minimum, and (b) contours in the valence band (VB) at energies of 310 meV (yellow) and 70 meV (red) below the VB maximum. Calculations using GGA: (c) conduction band at energies of 70 meV (yellow) and 20 meV (red) above the CB minimum, and (d) valence band at energies of 220 meV (yellow) and 70 meV (red) below the VB maximum. The red arrows indicate the reciprocal lattice vectors; the vertical arrow corresponds to the c^* axis which is normal to the layer planes and the sample surface. The green line indicates the path in the BZ used below in the LDA calculations of the band dispersion. The special points *X*, *Y*, *Z*, $-Z$, and 5[26,27] lying on the BZ boundary are indicated by circles.

extremum. To construct these figures, the band energies were calculated for a grid of points covering the whole BZ. This process is not usually required in more high-symmetry materials and can be computationally expensive; each of our datasets required 24 h with 64 processors, which is acceptable, but there is a cubic scaling with k-space resolution which makes the use of a very fine grid impractical. Therefore, we do not attempt to extract band dispersions from the same dataset, and we are only able to locate the band extrema to the resolution of our k-point grid. However, presenting the band structure in this way is useful, since one can search for the band extrema without prejudging where they are located. As Fig. 2 makes clear, this calculation implies that both the VBM and CBM are not located at Γ or at any particular high-symmetry point on the BZ boundary.

Most reported calculations of the band structure so far have presented the dispersion only along a special set of directions. In some cases, these have been chosen connecting the $\bar{\Gamma}$, $\bar{K}$ and $\bar{M}$ points of a hypothetical two-dimensional BZ; however, $\bar{K}$ and $\bar{M}$ are not special points in the three-dimensional BZ, but are projections of the latter onto the layer plane[7,22–25] (and so cannot be represented on Fig. 2). In other cases, paths have been chosen in the 3D BZ connecting three-dimensional special points, but not exploring the whole BZ.[26,27] The 2D projection onto the layer plane is very useful when considering how the band structure evolves from bulk to monolayer materials and is also necessary when modelling ARPES experiments, in which a 2D section through the 3D BZ is measured. However, by discarding the c^* component of the wavevector, it is impossible to determine whether the band extrema occur at the same crystal momentum values.

The results of Fig. 2 suggest that the lowest-energy inter-band transition is indirect in the bulk material, since the VBM and CBM do not coincide. This question has been actively discussed recently on the basis of optical, ARPES and transport measurements, and is not yet resolved. Briefly, for

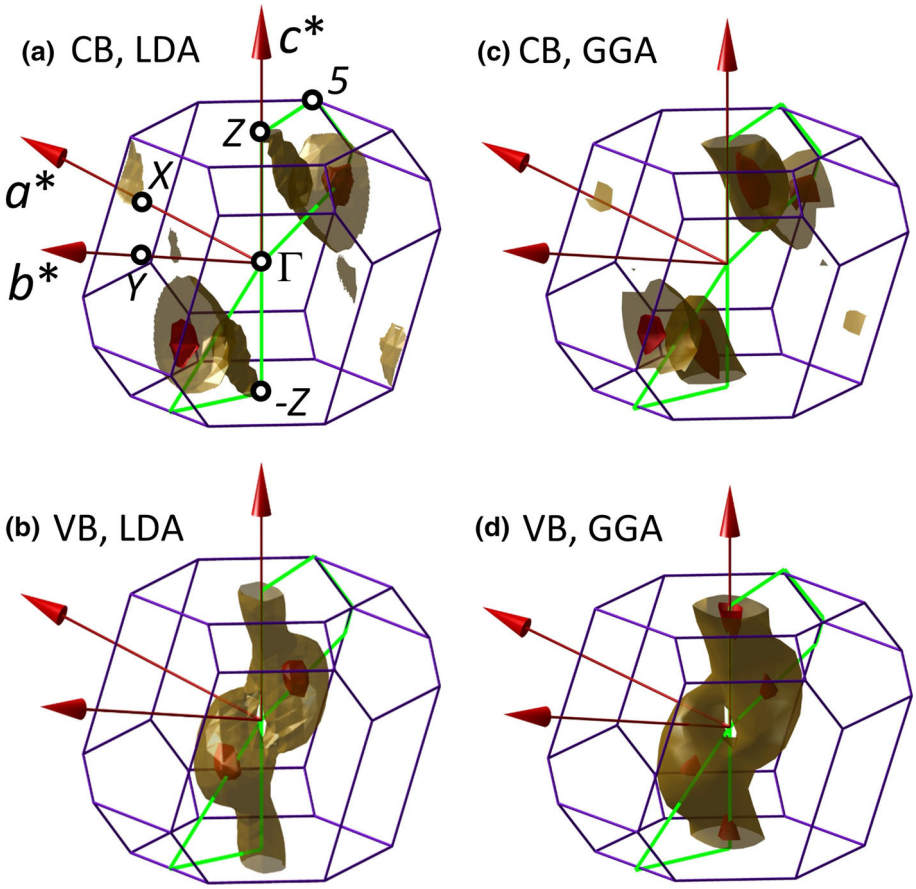

Fig. 3. Constant energy surfaces in the Brillouin zone of $ReSe_2$. Calculations using LDA: (a) contours in the conduction band (CB) at energies of 85 meV (yellow) and 20 meV (red) above the CB minimum, and (b) contours in the valence band (VB) at energies of 80 meV (yellow) and 15 meV (red) below the VB maximum. Calculations using GGA: (c) conduction band at energies of 70 meV (yellow) and 20 meV (red) above the CB minimum, and (d) valence band at energies of 85 meV (yellow) and 20 meV (red) below the VB maximum. The red arrows indicate the reciprocal lattice vectors; the vertical arrow corresponds to the c^* axis which is normal to the layer planes and the sample surface. The green line again shows the path in the BZ used in the LDA calculation of the band dispersion.

bulk ReS_2, electron energy loss spectroscopy (EELS) results gave a room-temperature direct gap of 1.42 eV[24] whilst optical absorption-edge measurements suggested indirect gaps of 1.35 eV and 1.38 eV (for polarisations parallel and perpendicular respectively to the Re chains)[28] and electroluminescence data suggested an indirect gap of 1.41 eV.[29] Recently, a combined photoacoustic and modulated reflectance spectroscopy study concluded that both ReS_2 and $ReSe_2$ have indirect bandgaps of 1.37 eV and 1.18 eV, respectively, and higher-lying direct gaps of 1.55 eV and 1.31 eV.[30] Only one ARPES study has reported observation of the CB states via rubidium doping, and found at 10–20 K a direct gap located at the BZ boundary along the c^* direction though with a substantially lower magnitude, of around 1.2 eV,[13] assumed to be due to bandgap renormalisation at the high doping levels required. This special point in the BZ, labelled Z[13,20] (as in Fig. 2) or A,[10] is the reported location of the VBM in all ARPES studies of ReS_2 to date, and this agrees reasonably well with the data of Fig. 2b and d, though the figure demonstrates the flatness of this maximum so that, in our calculations, the VBM is actually displaced away from Z to the centres of the lobes (red) which are constant energy surfaces 70 meV below the VBM; the precise location of the VBM is therefore challenging to determine via DFT, because discrepancies in energy of this magnitude easily arise from different choices of exchange–correlation functional and use of scalar versus fully relativistic pseudopotentials. To demonstrate the extent to which our choice of pseudopotential affects the conclusions, we show calculations using the LDA in Fig. 2a and b and using the GGA in Fig. 2c and d. All the essential features of the constant energy surfaces are reproduced though there are minor differences in the exact energies and positions in the BZ of the band extrema; differences in energy between LDA and GGA global indirect band gaps are of the order of 100–200 meV.

We note that our calculations are not in very good agreement with two other DFT calculations for bulk or many-layer ReS_2, which report a (T = 0 K) direct gap of 1.35 eV at the $\bar{\Gamma}$ point[7,22] (we obtain 1.495 eV), though we do find, in agreement with

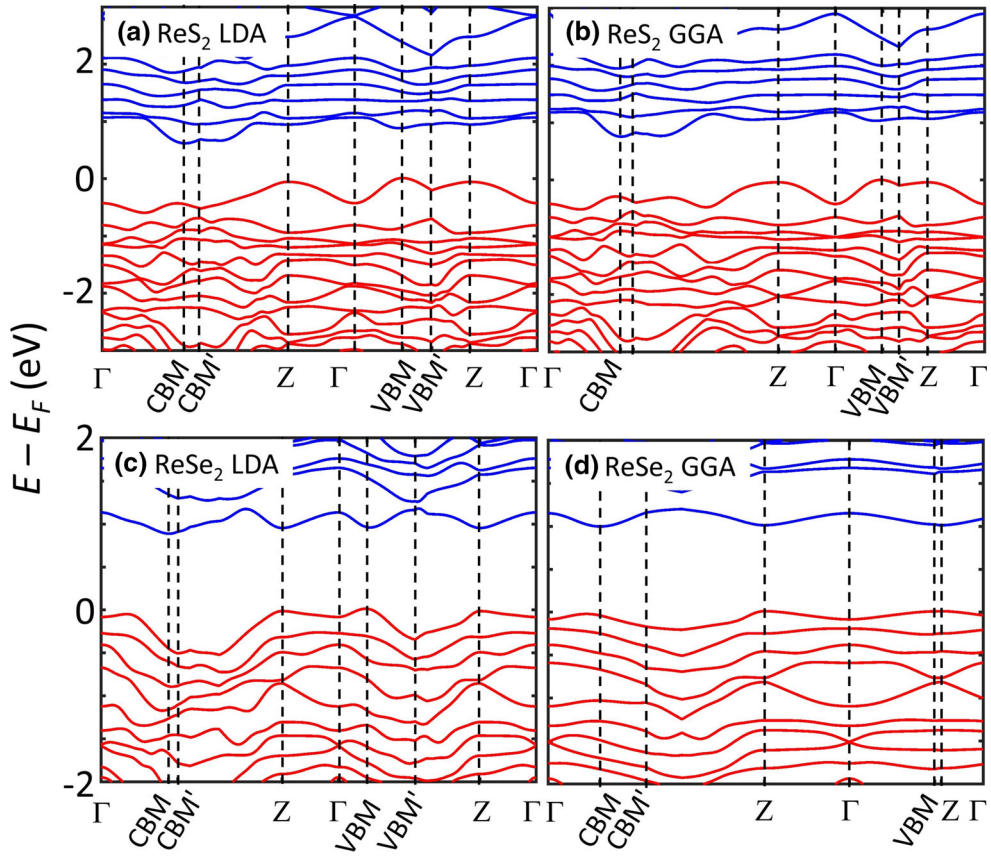

Fig. 4. Conduction and valence band edges for (a) and (b) ReS_2, and (c) and (d) $ReSe_2$ for a path around the Brillouin zone passing through the Γ and *Z* points and the band extrema (CBM and VBM). The other labels (CBM', VBM') are explained in the text. The paths through the Brillouin zone used for the LDA calculation are indicated by the green lines in Figs. 2 and 3. Data of (a) and (b) were calculated using LDA exchange–correlation functionals and GGA functionals were used for (c) and (d).

Ref. 13 that, along the c^* direction, the VB has a *local* maximum at the *Z* point. This is most clearly seen in Fig. 2b and was reported earlier, where the direct gap at *Z* was found to be 1.525 eV.[20] It is also generally found that the VB at the true Γ point shows a local minimum, giving an "M"-shaped dispersion, as shown by the bifurcation of the constant energy surface in Fig. 2b and d (yellow).

It is clear from Fig. 2a and c that the CB minimum in this level of approximation does not appear at *Z* but is indeed located near the plane containing *Z* and is displaced towards the 3D special point 5. This is in qualitative agreement with the calculations of Ref. 10 (their Fig. 4d) and is potentially compatible with the ARPES results.[13]

Rhenium Selenide

Figure 3 shows the equivalent constant energy surfaces for $ReSe_2$ and, as might be expected from the chemical similarity between S and Se, the overall structure is similar to that of ReS_2. Focusing first on the results obtained via the LDA, Fig. 3a and b (1) we find the conduction band minimum again lies within the volume of the BZ (rather than at the surface or at Γ) and is closer to the plane containing *Z* than to that containing Γ, and (2) the valence band maxima are offset either side of the Γ point. We have discussed ARPES data for $ReSe_2$ in detail elsewhere and reported the form of one constant energy surface (yellow) for its VB[12] but we show this again in Fig. 3b for comparison with the CB structure. We have also expanded Fig. 3b to include a second constant energy surface (red) closer to the calculated VBM. Just as for ReS_2, we find that the three-dimensional Γ point is a local minimum in energy with a bifurcation of the constant energy surfaces around it. This is borne out of the experimental ARPES data,[12] which shows that the VBM is displaced in the layer plane away from the projection of Γ and agrees also with other DFT calculations (Fig. S1 of the Supplementary material of Ref. 23). Turning to our results obtained in the GGA, we find that the same remarks apply, with one exception; in the GGA, two VB maxima appear, one in the same location as for the LDA results and one very close to *Z*. This does not, however, affect the conclusion that $ReSe_2$ is indirect, since the CB minimum is still not co-located with the VBM; we find global indirect gaps in LDA, GGA respectively of 0.87 eV, 0.99 eV and a direct gap at *Z* of 0.97 eV, 1.00 eV. One other recent

calculation gives an indirect gap of 0.92 eV for bulk $ReSe_2$ in the LDA with a direct quasiparticle gap at Z of 1.49 in the LDA + GdW approximation;[27] a second calculation in the GGA + GW approximation gives a direct gap at Z of 1.38 eV.[26] The recent photoacoustic spectroscopy study gives an indirect gap of 1.18 eV and direct gap of 1.31 eV.[30] However, both computational studies only report band dispersions along specific paths in the BZ and it would be interesting in future to apply these more sophisticated models to the whole BZ.

The findings of the present calculations are summarised in Fig. 4, which shows the band energies for (a), (b) ReS_2 and (c), (d) $ReSe_2$ taking a path in the Brillouin zone passing through the key points. Again, calculations for both LDA and GGA are shown. To illustrate this, the path used for the LDA calculations is shown (green lines) in Figs. 2 and 3 and is as follows: starting from Γ, it follows a straight line through the CB minimum (CBM) and continues along this line to the BZ boundary (we label this point CBM'). It then turns to run along the BZ surface up to point 5 in the plane containing the Z point, crosses that plane to Z and runs back down to Γ. The energies of both CB and VB states are plotted for this path. This accounts for the left hand halves of each panel of Fig. 4a, b, c and d; in the right hand halves, we then follow the same procedure, from Γ to the VB maximum, on to the BZ boundary (VBM') and then across the BZ surface to Z and finally back to Γ. This shows clearly that the VBM and CBM do not coincide so that, considering first ReS_2, Fig. 2a and b, the material is formally an indirect semiconductor, but there is a gap at Z which is formed between a local VB maximum and a very flat CB minimum and is, therefore, a slightly larger direct gap. In the region of the VBM, it appears that there is also a close-lying local minimum in the CB, providing another nearly direct gap. It is hardly surprising, therefore, that measurements of optical reflection or absorption have difficulty in identifying the nature of the band gap. Similar conclusions follow from the analogous data for $ReSe_2$ shown in Fig. 4c and d.

CONCLUSIONS

We have presented a detailed comparison of the band structures of bulk ReS_2 and $ReSe_2$ calculated using LDA DFT with fully relativistic pseudopotentials and use of the PAW method. We show that only a calculation of the band structure over the whole three-dimensional Brillouin zone volume can identify correctly the locations of the band extrema for a given level of computational accuracy. Our results show clearly that the task of classifying the interband optical transitions in ReS_2 via DFT calculations is very demanding since direct and indirect transitions lie close in energy and within the range of DFT results arising from different choices of pseudopotential. In the case of $ReSe_2$, computational and experimental results are in better agreement though, it should be noted, there is less experimental data available; the current consensus is that bulk $ReSe_2$ is an indirect semiconductor.

ACKNOWLEDGEMENTS

This work was supported by the Centre for Graphene Science of the Universities of Bath and Exeter and by the Engineering and Physical Sciences Research Council EPSRC (UK) under Grants Nos. EP/G036101, EP/M022188, and EP/P004830; S.M.G. and L.S.H. are supported by the Bath-Bristol Centre for Doctoral Training in Condensed Matter Physics, Grant No. EP/L015544. Associated experimental studies were supported by the award of beam time at the DIAMOND (IO5) and SOLEIL (ANTARES) synchrotron beam lines and by EPSRC Grant No. EP/P004830/1. Computational work was performed on the University of Bath's High Performance Computing Facility. Data created during this research are freely available from the University of Bath data archive at https://doi.org/10.15125/bath-00331, https://doi.org/10.15125/bath-00332.

OPEN ACCESS

REFERENCES

1. K.S. Novoselov, D. Jiang, F. Schedin, T.J. Booth, V.V. Khotkevich, S.V. Morozov, and A.K. Geim, *PNAS* 102, 10451 (2005).
2. J.A. Wilson and A.D. Yoffe, *Adv. Phys.* 18, 193 (1969).
3. J.-W. Jiang, *Front. Phys.* 10, 287 (2015).
4. S. Manzeli, D. Ovchinnikov, D. Pasquier, O.V. Yazyev, and A. Kis, *Nat. Rev. Mater.* 2, 17033 (2017).
5. M. Rahman, K. Davey, and S.-Z. Qiao, *Adv. Funct. Mater.* 27, 1606129 (2017).
6. H.J. Lamfers, A. Meetsma, G.A. Wiegers, and J.L. deBoer, *J. Alloys Compd.* 241, 34 (1996).
7. S. Tongay, H. Sahin, C. Ko, A. Luce, W. Fan, K. Liu, J. Zhou, Y.S. Huang, C.H. Ho, J.Y. Yan, D.F. Ogletree, S. Aloni, J. Ji, S.S. Li, J.B. Li, F.M. Peeters, and J.Q. Wu, *Nat. Commun.* 5, 3252 (2014).
8. D. Wolverson, S. Crampin, A.S. Kazemi, A. Ilie, and S.J. Bending, *ACS Nano* 8, 11154 (2014).
9. E. Canadell, A. LeBeuze, M.A. El Khalifa, R. Chevrel, and M.H. Whangbo, *J. Am. Chem. Soc.* 111, 3778 (1989).
10. M. Gehlmann, I. Aguilera, G. Bihlmayer, S. Nemšák, P. Nagler, P. Gospodarič, G. Zamborlini, M. Eschbach, V. Feyer, F. Kronast, E. Młyńczak, T. Korn, L. Plucinski, C. Schüller, S. Blügel, and C.M. Schneider, *Nano Lett.* 17, 5187 (2017).
11. J. L. Webb, L.S. Hart, D. Wolverson, C.Y. Chen, and J. Avila, M.C. Asensio, *Phys. Rev. B* 96, 115205 (2017).
12. L.S. Hart, J.L. Webb, S. Dale, S.J. Bending, M. Mucha-Kruczynski, D. Wolverson, C.Y. Chen, J. Avila, and M.C. Asensio, *Sci. Rep.* 7, 5145 (2017).

13. D. Biswas, A.M. Ganose, R. Yano, J.M. Riley, L. Bawden, O.J. Clark, J. Feng, L. Collins-Mcintyre, M.T. Sajjad, and W. Meevasana, *Phys. Rev. B* 96, 085205 (2017).
14. P. Giannozzi, S. Baroni, N. Bonini, M. Calandra, R. Car, C. Cavazzoni, D. Ceresoli, G.L. Chiarotti, M. Cococcioni, I. Dabo, A. Dal Corso, S. de Gironcoli, S. Fabris, G. Fratesi, R. Gebauer, U. Gerstmann, C. Gougoussis, A. Kokalj, M. Lazzeri, L. Martin-Samos, N. Marzari, F. Mauri, R. Mazzarello, S. Paolini, A. Pasquarello, L. Paulatto, C. Sbraccia, S. Scandolo, G. Sclauzero, A.P. Seitsonen, A. Smogunov, P. Umari, and R.M. Wentzcovitch, *J. Phys. Condens. Mater.* 21, 395502 (2009).
15. G. Kresse and D. Joubert, *Phys. Rev. B* 59, 1758 (1999).
16. A. Dal Corso, *Comput. Mater. Sci.* 95, 337 (2014).
17. J.P. Perdew and A. Zunger, *Phys. Rev. B* 23, 5048 (1981).
18. J.P. Perdew, K. Burke, and M. Ernzerhof, *Phys. Rev. Lett.* 77, 3865 (1996).
19. H.J. Monkhorst and J.D. Pack, *Phys. Rev. B* 13, 5188 (1976).
20. J.L. Webb, L.S. Hart, D. Wolverson, C. Chen, J. Avila, and M.C. Asensio, *Phys. Rev. B* 96, 115205 (2017).
21. C.H. Ho, Y.S. Huang, P.C. Liao, and K.K. Tiong, *J. Phys. Chem. Solids* 60, 1797 (1999).
22. E. Liu, Y. Fu, Y. Wang, Y. Feng, H. Liu, X. Wan, W. Zhou, B. Wang, L. Shao, and C.-H. Ho, *Nat. Commun.* 6, 6991 (2015).
23. H. Zhao, J. Wu, H. Zhong, Q. Guo, X. Wang, F. Xia, L. Yang, P. Tan, and H. Wang, *Nano Res.* 8, 3651 (2015).
24. K. Dileep, R. Sahu, S. Sarkar, S.C. Peter, and R. Datta, *J. Appl. Phys.* 119, 114309 (2016).
25. W. Wen, Y. Zhu, X. Liu, H.P. Hsu, Z. Fei, Y. Chen, X. Wang, M. Zhang, K.H. Lin, F.S. Huang, Y.P. Wang, Y.S. Huang, C.H. Ho, P.H. Tan, C. Jin, and L. Xie, *Small* 13, 1603788 (2017).
26. J.P. Echeverry and I.C. Gerber, *Phys. Rev. B* 97, 075123 (2018).
27. A. Arora, J. Noky, M. Drüppel, B. Jariwala, T. Deilmann, R. Schneider, R. Schmidt, O. Del Pozo-Zamudio, T. Stiehm, A. Bhattacharya, P. Krüger, S.M. de Vasconcellos, M. Rohlfing, and R. Bratschitsch, *Nano Lett.* 17, 3202 (2017).
28. C.H. Ho, Y.S. Huang, K.K. Tiong, and P.C. Liao, *Phys. Rev. B* 58, 16130 (1998).
29. I. Gutierrez-Lezama, B.A. Reddy, N. Ubrig, and A.F. Morpurgo, *2D Mater.* 3, 045016 (2016).
30. S.J. Zelewski and R. Kudrawiec, *Sci. Rep.* 7, 15365 (2017).

10.4 Discussions

The paper presented in this chapter shows that both bulk ReS_2 and $ReSe_2$ are indirect band gap semiconductors. In the case of ReS_2 two similar sized gaps that are direct and indirect are identified. Interband transitions across these gaps are possible which may explain why there has been contradictory reports for the indirect/direct nature of the band gap of ReS_2, as described in Sec 2.2.3.

Another interesting point mentioned in this chapter is that the band gaps are calculated to be indirect using LDA and GGA pseudopotentials; however, it is found that the choice of pseudopotential will affect where this band gap is predicted to be within the Brillouin zone.

There are no calculations presented in this paper for the monolayer rhenium dichalcogenides. This is because the focus of this report was to identify the band gaps of bulk ReS_2 and $ReSe_2$ by exploring the entire 3D Brillouin zones of these crystals.

A recent publication by Eickholt et al. has investigated the electronic band structure of bulk $ReSe_2$ by plotting the DFT calculated constant energy surface, which is how the results of the paper in this chapter are presented in Fig. 2 and Fig. 3. Significantly, Eickholt et al. also find a VBM that is not along a high symmetry direction, which agrees with the findings in this chapter [64].

Chapter 11

Conclusions and future work

This thesis describes investigations of the novel semiconducting van der Waals crystals, ReS_2 and $ReSe_2$. These materials are only stable in a distorted 1T structure, which is of low symmetry and these crystals have in-plane anisotropic vibrational and electronic properties. This anisotropy was explored in this body of work.

In Chapter 4, ReS_2 and $ReSe_2$ were shown to have two inequivalent vertical orientations and Raman spectroscopy was used to identify the "way up" of the flakes. The rhenium dichalcogenides are unique amongst the TMDs in that they are the only members of this family that have two non-equivalent vertical orientations. A simple ball and spring model was used to describe the lattice dynamics of these materials in Chapter 5. The results of this model demonstrate that the frequencies of the ReS_2 Raman modes are related to the $ReSe_2$ modes by a scale factor, which depends only on the chalcogen mass. Chapter 6 investigated the vibrational properties of $ReSe_2$ with low mass impurities, such as sulphur. From Raman spectroscopy and ab initio DFT calculations four different local vibrational modes are found corresponding to these sulphur impurities in four inequivalent positions of the unit cell. Furthermore, an unusual experimental geometry was utilised to enhance the intensities of some of these local vibrational modes.

Raman spectroscopy has been shown to be a very useful tool for understanding the char-

acteristics of 2D materials. In particular, this technique has been helpful for understanding the vibrational properties of ReS_2 and $ReSe_2$. Although this thesis focussed on the rhenium dichalcogenides some of the results are applicable to the other 2D materials, such as how to identify low mass impurities in the TMDs.

The electronic band structures of ReS_2 and $ReSe_2$ have been shown to be anisotropic from ARPES measurements. Moreover, the locations of the two valence band maxima of bulk $ReSe_2$ were found at positions that are not along any of the high symmetry directions. These valence band maxima were missed in DFT calculations previous to this work. From a combination of ARPES measurements and DFT calculations, bulk $ReSe_2$ and ReS_2 are predicted to be indirect band gap semiconductors. A somewhat surprising result from the ARPES measurements of the bulk crystals is, contrary to previous reports, the interlayer coupling in the rhenium dichalcogenides is non-negligible.

The electronic band structure of a monolayer of $ReSe_2$ has also been measured using ARPES. The uppermost valence band in the vicinity of the Γ point is very flat. The VBM is located somewhere in this flat band however it is not possible to determine the exact position from the data. Similar to multilayer $ReSe_2$, there is in-plane anisotropy in the electronic band structure.

11.1 Future work

The work presented in this thesis has described the electronic and vibrational properties of the pure rhenium dichalcogenides. There has also been some measurements of these materials with impurities introduced. However, there are many different dopants that can be incorporated into these crystals. From theoretical predictions the doped rhenium dichalcogenides are expected to be stable as metals, narrow band gap semiconductors and magnetic materials. Further work is required to grow and measure these exciting crystals.

With the creation of new rhenium dichalcogenide alloys comes the opportunity to explore the layer dependences of these crystals. Of course, there is a plethora of materials that can be

grown and research on monolayers and bilayers of each of these will be rather time consuming. Therefore, careful choice of which alloy to investigate should be made, by using theoretical predictions to determine the crystals that are most interesting.

There has been a lot of work in recent years involving the stacking of 2D materials to develop new and exciting electronic devices which utilise some of the remarkable properties of the layered crystals, such as the high mobility in graphene. The electronic anisotropy in the rhenium dichalcogenides could make for an interesting feature to be incorporated into future van der Waals heterostructures.

Bibliography

1. K. S. Novoselov, A. K. Geim, S. V. Morozov, D. Jiang, Y. Zhang, S. V. Dubonos, I. V. Grigorieva, and A. A. Firsov, "Electric field effect in atomically thin carbon films," *Science*, vol. 306, no. 5696, pp. 666–669, 2004.

2. K. S. Novoselov, A. K. Geim, S. V. Morozov, D. Jiang, M. I. Katsnelson, I. V. Grigorieva, S. V. Dubonos, and A. A. Firsov, "Two-dimensional gas of massless dirac fermions in graphene," *Nature*, vol. 438, no. 7065, p. 197, 2005.

3. C. Lee, X. Wei, J. W. Kysar, and J. Hone, "Measurement of the elastic properties and intrinsic strength of monolayer graphene," *Science*, vol. 321, no. 5887, pp. 385–388, 2008.

4. A. K. Geim and K. S. Novoselov, "The rise of graphene," *Nature Materials*, vol. 6, no. 3, p. 183, 2007.

5. K. S. Novoselov, V. I. Fal'ko, L. Colombo, P. R. Gellert, M. G. Schwab, K. Kim, *et al.*, "A roadmap for graphene," *Nature*, vol. 490, no. 7419, p. 192, 2012.

6. M.-W. Lin, C. Ling, Y. Zhang, H. J. Yoon, M. M.-C. Cheng, L. A. Agapito, N. Kioussis, N. Widjaja, and Z. Zhou, "Room-temperature high on/off ratio in suspended graphene nanoribbon field-effect transistors," *Nanotechnology*, vol. 22, no. 26, p. 265201, 2011.

7. R. Balog, B. Jørgensen, L. Nilsson, M. Andersen, E. Rienks, M. Bianchi, M. Fanetti, E. Lægsgaard, A. Baraldi, S. Lizzit, *et al.*, "Bandgap opening in graphene induced by patterned hydrogen adsorption," *Nature Materials*, vol. 9, no. 4, p. 315, 2010.

8. K. S. Novoselov, D. Jiang, F. Schedin, T. J. Booth, V. V. Khotkevich, S. V. Morozov, and A. K. Geim, "Two-dimensional atomic crystals," *Proceedings of the National Academy of Sciences of the United States of America*, vol. 102, no. 30, pp. 10451–10453, 2005.

9. C. Berthier, P. Molinié, and D. Jérome, "Evidence for a connection between charge density waves and the pressure enhancement of superconductivity in 2H-$NbSe_2$," *Solid State Communications*, vol. 18, no. 9-10, pp. 1393–1395, 1976.

10. A. Splendiani, L. Sun, Y. Zhang, T. Li, J. Kim, C.-Y. Chim, G. Galli, and F. Wang, "Emerging photoluminescence in monolayer MoS_2," *Nano Letters*, vol. 10, no. 4, pp. 1271–1275, 2010.

11. P. Chen, Y.-H. Chan, M.-H. Wong, X.-Y. Fang, M.-Y. Chou, S.-K. Mo, Z. Hussain, A.-V. Fedorov, and T.-C. Chiang, "Dimensional effects on the charge density waves in ultrathin films of $TiSe_2$," *Nano Letters*, vol. 16, no. 10, pp. 6331–6336, 2016.

12. T. Cheiwchanchamnangij and W. R. L. Lambrecht, "Quasiparticle band structure calculation of monolayer, bilayer, and bulk MoS_2," *Physical Review B*, vol. 85, no. 20, p. 205302, 2012.

13. K. D. Bronsema, J. L. De Boer, and F. Jellinek, "On the structure of molybdenum diselenide and disulfide," *Zeitschrift für anorganische und allgemeine Chemie*, vol. 540, no. 9-10, pp. 15–17, 1986.

14. A. V. Kolobov and J. Tominaga, *Two-Dimensional Transition-Metal Dichalcogenides*, vol. 239. Springer, 2016.

15. H. S. S. Ramakrishna Matte, A. Gomathi, A. K. Manna, D. J. Late, R. Datta, S. K. Pati, and C. N. R. Rao, "MoS_2 and WS_2 analogues of graphene," *Angewandte Chemie International Edition*, vol. 49, no. 24, pp. 4059–4062, 2010.

16. G.-B. Liu, D. Xiao, Y. Yao, X. Xu, and W. Yao, "Electronic structures and theoretical modelling of two-dimensional group-VIB transition metal dichalcogenides," *Chemical Society Reviews*, vol. 44, no. 9, pp. 2643–2663, 2015.

17. T. Li and G. Galli, "Electronic properties of MoS_2 nanoparticles," *The Journal of Physical Chemistry C*, vol. 111, no. 44, pp. 16192–16196, 2007.

18. G. Dresselhaus, "Spin-orbit coupling effects in zinc blende structures," *Physical Review*, vol. 100, no. 2, p. 580, 1955.

19. A. Chernikov, T. C. Berkelbach, H. M. Hill, A. Rigosi, Y. Li, O. B. Aslan, D. R. Reichman, M. S. Hybertsen, and T. F. Heinz, "Exciton binding energy and nonhydrogenic

rydberg series in monolayer WS_2," *Physical Review Letters*, vol. 113, no. 7, p. 076802, 2014.

20. X.-F. He, "Excitons in anisotropic solids: The model of fractional-dimensional space," *Physical Review B*, vol. 43, no. 3, p. 2063, 1991.

21. A. Thilagam, "Exciton complexes in low dimensional transition metal dichalcogenides," *Journal of Applied Physics*, vol. 116, no. 5, p. 053523, 2014.

22. J.-H. Choi and S.-H. Jhi, "Origin of distorted 1T-phase ReS_2: first-principles study," *Journal of Physics: Condensed Matter*, 2018.

23. R. E. Peierls, *Quantum Theory of Solids*. Oxford University Press, 1955.

24. B. Jariwala, A. Thamizhavel, and A. Bhattacharya, "$ReSe_2$: a reassessment of crystal structure and thermal analysis," *Journal of Physics D: Applied Physics*, vol. 50, no. 4, p. 044001, 2016.

25. N. Alcock and A. Kjekshus, "The crystal structure of $ReSe_2$," *Acta Chem. Scand*, vol. 19, no. 1, p. 79, 1965.

26. J. C. Wildervanck and F. Jellinek, "The dichalcogenides of technetium and rhenium," *Journal of the Less Common Metals*, vol. 24, no. 1, pp. 73–81, 1971.

27. C. H. Ho, Y. S. Huang, P. C. Liao, and K. K. Tiong, "Crystal structure and band-edge transitions of $ReS_{2-x}Se_x$ layered compounds," *Journal of Physics and Chemistry of Solids*, vol. 60, no. 11, pp. 1797–1804, 1999.

28. E. Liu, Y. Fu, Y. Wang, Y. Feng, H. Liu, X. Wan, W. Zhou, B. Wang, L. Shao, C.-H. Ho, *et al.*, "Integrated digital inverters based on two-dimensional anisotropic ReS_2 field-effect transistors," *Nature Communications*, vol. 6, p. 6991, 2015.

29. B. A. Parkinson, J. Ren, and M. H. Whangbo, "Relationship of STM and AFM images to the local density of states in the valence and conduction bands of rhenium selenide ($ReSe_2$)," *Journal of the American Chemical Society*, vol. 113, no. 21, pp. 7833–7837, 1991.

30. H.-J. Lamfers, A. Meetsma, G. A. Wiegers, and J. L. De Boer, "The crystal structure of some rhenium and technetium dichalcogenides," *Journal of Alloys and Compounds*, vol. 241, no. 1-2, pp. 34–39, 1996.

31. C. M. Fang, G. A. Wiegers, C. Haas, and R. A. De Groot, "Electronic structures of ReS_2, $ReSe_2$ and TcS_2 in the real and the hypothetical undistorted structures," *Journal of Physics: Condensed Matter*, vol. 9, no. 21, p. 4411, 1997.

32. R. A. Gordon, D. Yang, E. D. Crozier, D. T. Jiang, and R. F. Frindt, "Structures of exfoliated single layers of WS_2, MoS_2, and $MoSe_2$ in aqueous suspension," *Physical Review B*, vol. 65, no. 12, p. 125407, 2002.

33. S. Wu, Y. Shan, J. Guo, L. Liu, X. Liu, X. Zhu, J. Zhang, J. Shen, S. Xiong, and X. Wu, "Phase-engineering-induced generation and control of highly anisotropic and robust excitons in few-layer ReS_2," *The Journal of Physical Chemistry Letters*, vol. 8, no. 12, pp. 2719–2724, 2017.

34. Y.-C. Lin, H.-P. Komsa, C.-H. Yeh, T. Björkman, Z.-Y. Liang, C.-H. Ho, Y.-S. Huang, P.-W. Chiu, A. V. Krasheninnikov, and K. Suenaga, "Single-layer ReS_2: two-dimensional semiconductor with tunable in-plane anisotropy," *ACS Nano*, vol. 9, no. 11, pp. 11249–11257, 2015.

35. Z. Sun, H. Lv, Z. Zhuo, A. Jalil, W. Zhang, X. Wu, and J. Yang, "A new phase of two-dimensional ReS_2 sheet with tunable magnetism," *Journal of Materials Chemistry C*, 2018.

36. D. Hou, Y. Ma, J. Du, J. Yan, C. Ji, and H. Zhu, "High pressure X-ray diffraction study of ReS_2," *Journal of Physics and Chemistry of Solids*, vol. 71, no. 11, pp. 1571–1575, 2010.

37. D. Zhou, Y. Zhou, C. Pu, X. Chen, P. Lu, X. Wang, C. An, Y. Zhou, F. Miao, C.-H. Ho, *et al.*, "Pressure-induced metallization and superconducting phase in ReS_2," *npj Quantum Materials*, vol. 2, no. 1, p. 19, 2017.

38. Y.-C. Kao, T. Huang, D.-Y. Lin, Y.-S. Huang, K.-K. Tiong, H.-Y. Lee, J.-M. Lin, H.-S. Sheu, and C.-M. Lin, "Anomalous structural phase transition properties in $ReSe_2$ and Au-doped $ReSe_2$," *The Journal of Chemical Physics*, vol. 137, no. 2, p. 024509, 2012.

39. P. Blake, E. W. Hill, A. H. Castro Neto, K. S. Novoselov, D. Jiang, R. Yang, T. J. Booth, and A. K. Geim, "Making graphene visible," *Applied Physics Letters*, vol. 91, no. 6, p. 063124, 2007.

40. B. Jariwala, D. Voiry, A. Jindal, B. A. Chalke, R. Bapat, A. Thamizhavel, M. Chhowalla, M. Deshmukh, and A. Bhattacharya, "Synthesis and characterization of ReS_2 and $ReSe_2$ layered chalcogenide single crystals," *Chemistry of Materials*, vol. 28, no. 10, pp. 3352–3359, 2016.

41. E. Zhang, P. Wang, Z. Li, H. Wang, C. Song, C. Huang, Z.-G. Chen, L. Yang, K. Zhang, S. Lu, *et al.*, "Tunable ambipolar polarization-sensitive photodetectors based on high-anisotropy $ReSe_2$ nanosheets," *ACS Nano*, vol. 10, no. 8, pp. 8067–8077, 2016.

42. M. Hafeez, L. Gan, H. Li, Y. Ma, and T. Zhai, "Chemical vapor deposition synthesis of ultrathin hexagonal $ReSe_2$ flakes for anisotropic raman property and optoelectronic application," *Advanced Materials*, vol. 28, no. 37, pp. 8296–8301, 2016.

43. S. Jiang, L. Zhao, Y. Shi, C. Xie, N. Zhang, Z. Zhang, Y. Huan, P. Yang, M. Hong, X. Zhou, *et al.*, "Temperature-dependent raman spectroscopy studies of the interface coupling effect of monolayer $ReSe_2$ single crystals on Au foils," *Nanotechnology*, vol. 29, no. 20, p. 204003, 2018.

44. S. Jiang, M. Hong, W. Wei, L. Zhao, N. Zhang, Z. Zhang, P. Yang, N. Gao, X. Zhou, C. Xie, *et al.*, "Direct synthesis and in situ characterization of monolayer parallelogrammic rhenium diselenide on gold foil," *Communications Chemistry*, vol. 1, no. 1, p. 17, 2018.

45. F. Cui, X. Li, Q. Feng, J. Yin, L. Zhou, D. Liu, K. Liu, X. He, X. Liang, S. Liu, *et al.*, "Epitaxial growth of large-area and highly crystalline anisotropic $ReSe_2$ atomic layer," *Nano Research*, vol. 10, no. 8, pp. 2732–2742, 2017.

46. B. Kang, Y. Kim, J. H. Cho, and C. Lee, "Ambipolar transport based on CVD-synthesized $ReSe_2$," *2D Materials*, vol. 4, no. 2, p. 025014, 2017.

47. K. Wu, B. Chen, S. Yang, G. Wang, W. Kong, H. Cai, T. Aoki, E. Soignard, X. Marie, A. Yano, *et al.*, "Domain architectures and grain boundaries in chemical vapor deposited highly anisotropic ReS_2 monolayer films," *Nano Letters*, vol. 16, no. 9, pp. 5888–5894, 2016.

48. M. Hafeez, L. Gan, H. Li, Y. Ma, and T. Zhai, "Large-area bilayer ReS_2 film/multilayer ReS_2 flakes synthesized by chemical vapor deposition for high performance photodetectors," *Advanced Functional Materials*, vol. 26, no. 25, pp. 4551–4560, 2016.

49. F. Cui, C. Wang, X. Li, G. Wang, K. Liu, Z. Yang, Q. Feng, X. Liang, Z. Zhang, S. Liu, *et al.*, "Tellurium-assisted epitaxial growth of large-area, highly crystalline ReS_2 atomic layers on mica substrate," *Advanced Materials*, vol. 28, no. 25, pp. 5019–5024, 2016.

50. X. Li, F. Cui, Q. Feng, G. Wang, X. Xu, J. Wu, N. Mao, X. Liang, Z. Zhang, J. Zhang, *et al.*, "Controlled growth of large-area anisotropic ReS_2 atomic layer and its photodetector application," *Nanoscale*, vol. 8, no. 45, pp. 18956–18962, 2016.

51. K. Keyshar, Y. Gong, G. Ye, G. Brunetto, W. Zhou, D. P. Cole, K. Hackenberg, Y. He, L. Machado, M. Kabbani, *et al.*, "Chemical vapor deposition of monolayer rhenium disulfide (ReS_2)," *Advanced Materials*, vol. 27, no. 31, pp. 4640–4648, 2015.

52. S. Tongay, H. Sahin, C. Ko, A. Luce, W. Fan, K. Liu, J. Zhou, Y.-S. Huang, C.-H. Ho, J. Yan, *et al.*, "Monolayer behaviour in bulk ReS_2 due to electronic and vibrational decoupling," *Nature Communications*, vol. 5, p. 3252, 2014.

53. A. Arora, J. Noky, M. Drüppel, B. Jariwala, T. Deilmann, R. Schneider, R. Schmidt, O. Del Pozo-Zamudio, T. Stiehm, A. Bhattacharya, *et al.*, "Highly anisotropic in-plane excitons in atomically thin and bulklike 1T'-$ReSe_2$," *Nano Letters*, vol. 17, no. 5, pp. 3202–3207, 2017.

54. A. Molina-Sánchez, D. Sangalli, K. Hummer, A. Marini, and L. Wirtz, "Effect of spin-orbit interaction on the optical spectra of single-layer, double-layer, and bulk MoS_2," *Physical Review B*, vol. 88, no. 4, p. 045412, 2013.

55. D. Biswas, A. M. Ganose, R. Yano, J. M. Riley, L. Bawden, O. J. Clark, J. Feng, L. Collins-Mcintyre, M. T. Sajjad, W. Meevasana, *et al.*, "Narrow-band anisotropic electronic structure of ReS_2," *Physical Review B*, vol. 96, no. 8, p. 085205, 2017.

56. M. Gehlmann, I. Aguilera, G. Bihlmayer, S. Nemšák, P. Nagler, P. Gospodarič, G. Zamborlini, M. Eschbach, V. Feyer, F. Kronast, *et al.*, "Direct observation of the band gap transition in atomically thin ReS_2," *Nano Letters*, vol. 17, no. 9, pp. 5187–5192, 2017.

57. J. P. Echeverry and I. C. Gerber, "Theoretical investigations of the anisotropic optical properties of distorted 1T ReS_2 and $ReSe_2$ monolayers, bilayers, and in the bulk limit," *Physical Review B*, vol. 97, no. 7, p. 075123, 2018.

58. A. Kokalj, "Computer graphics and graphical user interfaces as tools in simulations of matter at the atomic scale," *Computational Materials Science*, vol. 28, no. 2, pp. 155–168, 2003.

59. D. Wolverson, S. Crampin, A. S. Kazemi, A. Ilie, and S. J. Bending, "Raman spectra of monolayer, few-layer, and bulk $ReSe_2$: An anisotropic layered semiconductor," *ACS Nano*, vol. 8, no. 11, pp. 11154–11164, 2014.

60. H.-X. Zhong, S. Gao, J.-J. Shi, and L. Yang, "Quasiparticle band gaps, excitonic effects, and anisotropic optical properties of the monolayer distorted 1T diamond-chain structures ReS_2 and $ReSe_2$," *Physical Review B*, vol. 92, no. 11, p. 115438, 2015.

61. H. Zhao, J. Wu, H. Zhong, Q. Guo, X. Wang, F. Xia, L. Yang, P. Tan, and H. Wang, "Interlayer interactions in anisotropic atomically thin rhenium diselenide," *Nano Research*, vol. 8, no. 11, pp. 3651–3661, 2015.

62. C. H. Ho, Y. S. Huang, P. C. Liao, and K. K. Tiong, "Piezoreflectance study of band-edge excitons of $ReS_{2-x}Se_x$ single crystals," *Physical Review B*, vol. 58, no. 19, p. 12575,

1998.

63. S. J. Zelewski and R. Kudrawiec, "Photoacoustic and modulated reflectance studies of indirect and direct band gap in van der Waals crystals," *Scientific Reports*, vol. 7, no. 1, p. 15365, 2017.

64. P. Eickholt, J. Noky, E. F. Schwier, K. Shimada, K. Miyamoto, T. Okuda, C. Datzer, M. Drüppel, P. Krüger, M. Rohlfing, *et al.*, "Location of the valence band maximum in the band structure of anisotropic 1T'- $ReSe_2$," *Physical Review B*, vol. 97, no. 16, p. 165130, 2018.

65. F. Liu, S. Zheng, A. Chaturvedi, V. Zólyomi, J. Zhou, Q. Fu, C. Zhu, P. Yu, Q. Zeng, N. D. Drummond, *et al.*, "Optoelectronic properties of atomically thin ReSSe with weak interlayer coupling," *Nanoscale*, vol. 8, no. 11, pp. 5826–5834, 2016.

66. K. Dileep, R. Sahu, S. Sarkar, S. C. Peter, and R. Datta, "Layer specific optical band gap measurement at nanoscale in MoS_2 and ReS_2 van der Waals compounds by high resolution electron energy loss spectroscopy," *Journal of Applied Physics*, vol. 119, no. 11, p. 114309, 2016.

67. O. B. Aslan, D. A. Chenet, A. M. van der Zande, J. C. Hone, and T. F. Heinz, "Linearly polarized excitons in single-and few-layer ReS_2 crystals," *ACS Photonics*, vol. 3, no. 1, pp. 96–101, 2015.

68. I. Gutiérrez-Lezama, B. A. Reddy, N. Ubrig, and A. F. Morpurgo, "Electroluminescence from indirect band gap semiconductor ReS_2," *2D Materials*, vol. 3, no. 4, p. 045016, 2016.

69. S. Yu, H. Zhu, K. Eshun, C. Shi, M. Zeng, and Q. Li, "Strain-engineering the anisotropic electrical conductance in ReS_2 monolayer," *Applied Physics Letters*, vol. 108, no. 19, p. 191901, 2016.

70. C. H. Ho, Y. S. Huang, J. L. Chen, T. E. Dann, and K. K. Tiong, "Electronic structure of ReS_2 and $ReSe_2$ from first-principles calculations, photoelectron spectroscopy, and

electrolyte electroreflectance," *Physical Review B*, vol. 60, no. 23, p. 15766, 1999.

71. C. H. Ho, P. C. Yen, Y. S. Huang, and K. K. Tiong, "Polarized electrolyte-electroreflectance study of ReS_2 and $ReSe_2$ layered semiconductors," *Journal of Physics: Condensed Matter*, vol. 13, no. 35, p. 8145, 2001.

72. S. Sim, D. Lee, A. V. Trifonov, T. Kim, S. Cha, J. H. Sung, S. Cho, W. Shim, M.-H. Jo, and H. Choi, "Ultrafast quantum beats of anisotropic excitons in atomically thin ReS_2," *Nature Communications*, vol. 9, no. 1, p. 351, 2018.

73. S. Das, H.-Y. Chen, A. V. Penumatcha, and J. Appenzeller, "High performance multilayer MoS_2 transistors with scandium contacts," *Nano Letters*, vol. 13, no. 1, pp. 100–105, 2012.

74. S. Swirhun, Y.-H. Kwark, and R. Swanson, "Measurement of electron lifetime, electron mobility and band-gap narrowing in heavily doped p-type silicon," in *Electron Devices Meeting, 1986 International*, pp. 24–27, IEEE, 1986.

75. R. Cheng, S. Jiang, Y. Chen, Y. Liu, N. Weiss, H.-C. Cheng, H. Wu, Y. Huang, and X. Duan, "Few-layer molybdenum disulfide transistors and circuits for high-speed flexible electronics," *Nature Communications*, vol. 5, p. 5143, 2014.

76. C. M. Corbet, C. McClellan, A. Rai, S. S. Sonde, E. Tutuc, and S. K. Banerjee, "Field effect transistors with current saturation and voltage gain in ultrathin ReS_2," *ACS Nano*, vol. 9, no. 1, pp. 363–370, 2014.

77. N. R. Pradhan, A. McCreary, D. Rhodes, Z. Lu, S. Feng, E. Manousakis, D. Smirnov, R. Namburu, M. Dubey, A. R. Hight Walker, *et al.*, "Metal to insulator quantum-phase transition in few-layered ReS_2," *Nano Letters*, vol. 15, no. 12, pp. 8377–8384, 2015.

78. E. Liu, M. Long, J. Zeng, W. Luo, Y. Wang, Y. Pan, W. Zhou, B. Wang, W. Hu, Z. Ni, *et al.*, "High responsivity phototransistors based on few-layer ReS_2 for weak signal detection," *Advanced Functional Materials*, vol. 26, no. 12, pp. 1938–1944, 2016.

79. D. Ovchinnikov, F. Gargiulo, A. Allain, D. J. Pasquier, D. Dumcenco, C.-H. Ho, O. V. Yazyev, and A. Kis, "Disorder engineering and conductivity dome in ReS_2 with electrolyte gating," *Nature Communications*, vol. 7, p. 12391, 2016.

80. J. Shim, A. Oh, D.-H. Kang, S. Oh, S. K. Jang, J. Jeon, M. H. Jeon, M. Kim, C. Choi, J. Lee, *et al.*, "High-performance 2D rhenium disulfide (ReS_2) transistors and photodetectors by oxygen plasma treatment," *Advanced Materials*, vol. 28, no. 32, pp. 6985–6992, 2016.

81. F. Liu, S. Zheng, X. He, A. Chaturvedi, J. He, W. L. Chow, T. R. Mion, X. Wang, J. Zhou, Q. Fu, *et al.*, "Highly sensitive detection of polarized light using anisotropic 2D ReS_2," *Advanced Functional Materials*, vol. 26, no. 8, pp. 1169–1177, 2016.

82. K. Xu, H.-X. Deng, Z. Wang, Y. Huang, F. Wang, S.-S. Li, J.-W. Luo, and J. He, "Sulfur vacancy activated field effect transistors based on ReS_2 nanosheets," *Nanoscale*, vol. 7, no. 38, pp. 15757–15762, 2015.

83. S. Yang, S. Tongay, Y. Li, Q. Yue, J.-B. Xia, S.-S. Li, J. Li, and S.-H. Wei, "Layer-dependent electrical and optoelectronic responses of $ReSe_2$ nanosheet transistors," *Nanoscale*, vol. 6, no. 13, pp. 7226–7231, 2014.

84. C. M. Corbet, S. S. Sonde, E. Tutuc, and S. K. Banerjee, "Improved contact resistance in $ReSe_2$ thin film field-effect transistors," *Applied Physics Letters*, vol. 108, no. 16, p. 162104, 2016.

85. K. K. Tiong, C. H. Ho, and Y. S. Huang, "The electrical transport properties of ReS_2 and $ReSe_2$ layered crystals," *Solid state communications*, vol. 111, no. 11, pp. 635–640, 1999.

86. H. Yang, H. Jussila, A. Autere, H.-P. Komsa, G. Ye, X. Chen, T. Hasan, and Z. Sun, "Optical waveplates based on birefringence of anisotropic two-dimensional layered materials," *ACS Photonics*, vol. 4, no. 12, pp. 3023–3030, 2017.

87. Y. Huang, H. Liu, C. Ling, X. Chen, D. Zhou, and S. Wang, "Hydrogen activation on the promoted and unpromoted ReS_2 (001) surfaces under the sulfidation conditions: A first-principles study," *The Journal of Physical Chemistry C*, vol. 119, no. 30, pp. 17092–17101, 2015.

88. L. Wang, Z. Sofer, J. Luxa, D. Sedmidubskỳ, A. Ambrosi, and M. Pumera, "Layered rhenium sulfide on free-standing three-dimensional electrodes is highly catalytic for the hydrogen evolution reaction: Experimental and theoretical study," *Electrochemistry Communications*, vol. 63, pp. 39–43, 2016.

89. Q. Zhang, S. Tan, R. G. Mendes, Z. Sun, Y. Chen, X. Kong, Y. Xue, M. H. Rümmeli, X. Wu, S. Chen, *et al.*, "Extremely weak van der Waals coupling in vertical ReS_2 nanowalls for high-current-density lithium-ion batteries," *Advanced Materials*, vol. 28, no. 13, pp. 2616–2623, 2016.

90. E. Zhang, Y. Jin, X. Yuan, W. Wang, C. Zhang, L. Tang, S. Liu, P. Zhou, W. Hu, and F. Xiu, "ReS_2-based field-effect transistors and photodetectors," *Advanced Functional Materials*, vol. 25, no. 26, pp. 4076–4082, 2015.

91. R. Bassm, M. Villarroel, F. J. Gil-Llambias, P. Baeza, J. L. García-Fierro, N. Martínez, P. Olivera, K. Leiva, and N. Escalona, "Support effect on conversion of quinoline over ReS_2 catalyst," *Journal of the Chilean Chemical Society*, vol. 61, no. 4, pp. 3170–3176, 2016.

92. Y. Huang, H. Liu, X. Chen, D. Zhou, C. Wang, J. Du, T. Zhou, and S. Wang, "Density functional theory investigation on thiophene hydrodesulfurization mechanism catalyzed by ReS_2 (001) surface," *The Journal of Physical Chemistry C*, vol. 120, no. 22, pp. 12012–12021, 2016.

93. J. Aliaga, T. Zepeda, B. Pawelec, J. Araya, J. Antúnez-García, M. Farías, S. Fuentes, D. Galván, G. Alonso-Núñez, and G. González, "Microspherical ReS_2 as a high-performance hydrodesulfurization catalyst," *Catalysis Letters*, vol. 147, no. 5, pp. 1243–1251, 2017.

94. J. A. Aliaga, T. Zepeda, J. F. Araya, F. Paraguay-Delgado, E. Benavente, G. Alonso-Núñez, S. Fuentes, and G. González, "Low-dimensional ReS_2/C composite as effective hydrodesulfurization catalyst," *Catalysts*, vol. 7, no. 12, p. 377, 2017.

95. F. Qi, X. Wang, B. Zheng, Y. Chen, B. Yu, J. Zhou, J. He, P. Li, W. Zhang, and Y. Li, "Self-assembled chrysanthemum-like microspheres constructed by few-layer $ReSe_2$ nanosheets as a highly efficient and stable electrocatalyst for hydrogen evolution reaction," *Electrochimica Acta*, vol. 224, pp. 593–599, 2017.

96. S. Jiang, Z. Zhang, N. Zhang, Y. Huan, Y. Gong, M. Sun, J. Shi, C. Xie, P. Yang, Q. Fang, *et al.*, "Application of chemical vapor–deposited monolayer $ReSe_2$ in the electrocatalytic hydrogen evolution reaction," *Nano Research*, pp. 1–11.

97. Q. Zhang, W. Wang, X. Kong, R. G. Mendes, L. Fang, Y. Xue, Y. Xiao, M. H. Rümmeli, S. Chen, and L. Fu, "Edge-to-edge oriented self-assembly of ReS_2 nanoflakes," *Journal of the American Chemical Society*, vol. 138, no. 35, pp. 11101–11104, 2016.

98. F. Qi, J. He, Y. Chen, B. Zheng, Q. Li, X. Wang, B. Yu, J. Lin, J. Zhou, P. Li, *et al.*, "Few-layered ReS_2 nanosheets grown on carbon nanotubes: A highly efficient anode for high-performance lithium-ion batteries," *Chemical Engineering Journal*, vol. 315, pp. 10–17, 2017.

99. F. Qi, Y. Chen, B. Zheng, J. He, Q. Li, X. Wang, B. Yu, J. Lin, J. Zhou, P. Li, *et al.*, "3D chrysanthemum-like ReS_2 microspheres composed of curly few-layered nanosheets with enhanced electrochemical properties for lithium-ion batteries," *Journal of Materials Science*, vol. 52, no. 7, pp. 3622–3629, 2017.

100. A. K. Geim and I. V. Grigorieva, "Van der Waals heterostructures," *Nature*, vol. 499, no. 7459, p. 419, 2013.

101. F. Withers, O. Del Pozo-Zamudio, A. Mishchenko, A. P. Rooney, A. Gholinia, K. Watanabe, T. Taniguchi, S. J. Haigh, A. K. Geim, A. I. Tartakovskii, *et al.*, "Light-emitting diodes by band-structure engineering in van der Waals heterostructures," *Nature Materials*, vol. 14, no. 3, p. 301, 2015.

102. L. Britnell, R. V. Gorbachev, R. Jalil, B. D. Belle, F. Schedin, A. Mishchenko, T. Georgiou, M. I. Katsnelson, L. Eaves, S. V. Morozov, *et al.*, "Field-effect tunneling transistor based on vertical graphene heterostructures," *Science*, vol. 335, no. 6071, pp. 947–950, 2012.

103. C.-H. Lee, G.-H. Lee, A. M. Van Der Zande, W. Chen, Y. Li, M. Han, X. Cui, G. Arefe, C. Nuckolls, T. F. Heinz, *et al.*, "Atomically thin p–n junctions with van der Waals heterointerfaces," *Nature Nanotechnology*, vol. 9, no. 9, p. 676, 2014.

104. M. Z. Bellus, M. Li, S. D. Lane, F. Ceballos, Q. Cui, X. C. Zeng, and H. Zhao, "Type-I van der Waals heterostructure formed by MoS_2 and ReS_2 monolayers," *Nanoscale Horizons*, vol. 2, no. 1, pp. 31–36, 2017.

105. M. Zhao, W. Zhang, M. Liu, C. Zou, K. Yang, Y. Yang, Y. Dong, L. Zhang, and S. Huang, "Interlayer coupling in anisotropic/isotropic van der Waals heterostructures of ReS_2 and MoS_2 monolayers," *Nano Research*, vol. 9, no. 12, pp. 3772–3780, 2016.

106. J. Shim, S. Oh, D.-H. Kang, S.-H. Jo, M. H. Ali, W.-Y. Choi, K. Heo, J. Jeon, S. Lee, M. Kim, *et al.*, "Phosphorene/rhenium disulfide heterojunction-based negative differential resistance device for multi-valued logic," *Nature Communications*, vol. 7, p. 13413, 2016.

107. B. Usha, S. Rajendra, V. Badri, S. Ankit, H. Sharona, S. Rajib, and D. Ranjan, "Distinct photoluminescence in multilayered van der waals heterostructures of $MoS_2/WS_2/ReS_2$ and BN," *Physica Status Solidi (B)*, vol. 0, no. 0, p. 1700691.

108. O. B. Mohammed, H. C. Movva, N. Prasad, A. Valsaraj, S. Kang, C. M. Corbet, T. Taniguchi, K. Watanabe, L. F. Register, E. Tutuc, *et al.*, "ReS_2-based interlayer tunnel field effect transistor," *Journal of Applied Physics*, vol. 122, no. 24, p. 245701, 2017.

109. A.-J. Cho, S. D. Namgung, H. Kim, and J.-Y. Kwon, "Electric and photovoltaic characteristics of a multi-layer $ReS_2/ReSe_2$ heterostructure," *APL Materials*, vol. 5, no. 7, p. 076101, 2017.

110. X. Wang, L. Huang, Y. Peng, N. Huo, K. Wu, C. Xia, Z. Wei, S. Tongay, and J. Li, "Enhanced rectification, transport property and photocurrent generation of multilayer $ReSe_2/MoS_2$ p–n heterojunctions," *Nano Research*, vol. 9, no. 2, pp. 507–516, 2016.

111. C. Wang, S. Yang, W. Xiong, C. Xia, H. Cai, B. Chen, X. Wang, X. Zhang, Z. Wei, S. Tongay, *et al.*, "Gate-tunable diode-like current rectification and ambipolar transport in multilayer van der Waals $ReSe_2/WS_2$ p–n heterojunctions," *Physical Chemistry Chemical Physics*, vol. 18, no. 40, pp. 27750–27753, 2016.

112. G. Agostini and C. Lamberti, *Characterization of Semiconductor Heterostructures and Nanostructures*. Elsevier, 2011.

113. G. Lucovsky, R. M. White, J. A. Benda, and J. F. Revelli, "Infrared-reflectance spectra of layered group-IV and group-VI transition-metal dichalcogenides," *Physical Review B*, vol. 7, no. 8, p. 3859, 1973.

114. A. C. Ferrari, J. C. Meyer, V. Scardaci, C. Casiraghi, M. Lazzeri, F. Mauri, S. Piscanec, D. Jiang, K. S. Novoselov, S. Roth, *et al.*, "Raman spectrum of graphene and graphene layers," *Physical Review Letters*, vol. 97, no. 18, p. 187401, 2006.

115. W. Wen, Y. Zhu, X. Liu, H.-P. Hsu, Z. Fei, Y. Chen, X. Wang, M. Zhang, K.-H. Lin, F.-S. Huang, *et al.*, "Anisotropic spectroscopy and electrical properties of 2D $ReS_{2(1-x)}Se_{2x}$ alloys with distorted 1T structure," *Small*, vol. 13, no. 12, 2017.

116. C. Rice, R. J. Young, R. Zan, U. Bangert, D. Wolverson, T. Georgiou, R. Jalil, and K. S. Novoselov, "Raman-scattering measurements and first-principles calculations of strain-induced phonon shifts in monolayer MoS_2," *Physical Review B*, vol. 87, no. 8, p. 081307, 2013.

117. C. Lee, H. Yan, L. E. Brus, T. F. Heinz, J. Hone, and S. Ryu, "Anomalous lattice vibrations of single-and few-layer MoS_2," *ACS Nano*, vol. 4, no. 5, pp. 2695–2700, 2010.

118. Y. Zhao, X. Luo, H. Li, J. Zhang, P. T. Araujo, C. K. Gan, J. Wu, H. Zhang, S. Y. Quek, M. S. Dresselhaus, *et al.*, "Interlayer breathing and shear modes in few-trilayer

MoS_2 and WSe_2," *Nano Letters*, vol. 13, no. 3, pp. 1007–1015, 2013.

119. D. A. Chenet, O. B. Aslan, P. Y. Huang, C. Fan, A. M. van der Zande, T. F. Heinz, and J. C. Hone, "In-plane anisotropy in mono-and few-layer ReS_2 probed by raman spectroscopy and scanning transmission electron microscopy," *Nano Letters*, vol. 15, no. 9, pp. 5667–5672, 2015.

120. R. He, J.-A. Yan, Z. Yin, Z. Ye, G. Ye, J. Cheng, J. Li, and C. Lui, "Coupling and stacking order of ReS_2 atomic layers revealed by ultralow-frequency raman spectroscopy," *Nano Letters*, vol. 16, no. 2, pp. 1404–1409, 2016.

121. S. Yang, Y. Liu, M. Wu, L.-D. Zhao, Z. Lin, H.-c. Cheng, Y. Wang, C. Jiang, S.-H. Wei, L. Huang, *et al.*, "Highly-anisotropic optical and electrical properties in layered SnSe," *Nano Research*, vol. 11, no. 1, pp. 554–564, 2018.

122. K. Wu, B. Chen, H. Cai, M. Blei, J. Bennett, S. Yang, D. Wright, Y. Shen, and S. Tongay, "Unusual pressure response of vibrational modes in anisotropic TaS_3," *The Journal of Physical Chemistry C*, vol. 121, no. 50, pp. 28187–28193, 2017.

123. A. Einstein, "Über einen die erzeugung und verwandlung des lichtes betreffenden heuristischen gesichtspunkt," *Annalen der physik*, vol. 322, no. 6, pp. 132–148, 1905.

124. A. Damascelli, "Probing the electronic structure of complex systems by ARPES," *Physica Scripta*, vol. 2004, no. T109, p. 61, 2004.

125. M. P. Seah and W. Dench, "Quantitative electron spectroscopy of surfaces: A standard data base for electron inelastic mean free paths in solids," *Surface and Interface Analysis*, vol. 1, no. 1, pp. 2–11, 1979.

126. J. Avila and M. C. Asensio, "First nanoARPES user facility available at SOLEIL: An innovative and powerful tool for studying advanced materials," *Synchrotron Radiation News*, vol. 27, no. 2, pp. 24–30, 2014.

127. J. Avila, I. Razado-Colambo, S. Lorcy, B. Lagarde, J.-L. Giorgetta, F. Polack, and M. C. Asensio, "ANTARES, a scanning photoemission microscopy beamline at SOLEIL," in *Journal of Physics: Conference Series*, vol. 425, p. 192023, IOP Publishing, 2013.

128. M. Cattelan and N. A. Fox, "A perspective on the application of spatially resolved ARPES for 2D materials," *Nanomaterials (Basel, Switzerland)*, vol. 8, no. 5, 2018.

129. C. R. Dean, A. F. Young, I. Meric, C. Lee, L. Wang, S. Sorgenfrei, K. Watanabe, T. Taniguchi, P. Kim, K. L. Shepard, *et al.*, "Boron nitride substrates for high-quality graphene electronics," *Nature Nanotechnology*, vol. 5, no. 10, p. 722, 2010.

130. A. Castellanos-Gomez, M. Buscema, R. Molenaar, V. Singh, L. Janssen, H. S. J. Van der Zant, and G. A. Steele, "Deterministic transfer of two-dimensional materials by all-dry viscoelastic stamping," *2D Materials*, vol. 1, no. 1, p. 011002, 2014.

131. P. Hohenberg and W. Kohn, "Inhomogeneous electron gas," *Physical Review*, vol. 136, no. 3B, p. B864, 1964.

132. W. Kohn and L. J. Sham, "Self-consistent equations including exchange and correlation effects," *Physical Review*, vol. 140, no. 4A, p. A1133, 1965.

133. R. M. Martin, *Electronic Structure: Basic Theory and Practical Methods*. Cambridge University Press, 2004.

134. P. Giannozzi, S. Baroni, N. Bonini, M. Calandra, R. Car, C. Cavazzoni, D. Ceresoli, G. L. Chiarotti, M. Cococcioni, I. Dabo, *et al.*, "QUANTUM ESPRESSO: a modular and open-source software project for quantum simulations of materials," *Journal of Physics: Condensed Matter*, vol. 21, no. 39, p. 395502, 2009.

135. G. Binnig, C. F. Quate, and C. Gerber, "Atomic force microscope," *Physical Review Letters*, vol. 56, no. 9, p. 930, 1986.

136. D. Rugar and P. Hansma, "Atomic force microscopy," *Physics Today*, vol. 43, no. 10, pp. 23–30, 1990.

137. S. Alexander, L. Hellemans, O. Marti, J. Schneir, V. Elings, P. K. Hansma, M. Longmire, and J. Gurley, "An atomic-resolution atomic-force microscope implemented using an optical lever," *Journal of Applied Physics*, vol. 65, no. 1, pp. 164–167, 1989.

138. C. I. Pearce, J. P. Icenhower, R. M. Asmussen, P. G. Tratnyek, K. M. Rosso, W. W. Lukens, and N. P. Qafoku, "Technetium stabilization in low solubility sulfide phases: A review," *ACS Earth and Space Chemistry*, 2018.

139. N. R. Wilson, P. V. Nguyen, K. Seyler, P. Rivera, A. J. Marsden, Z. P. L. Laker, G. C. Constantinescu, V. Kandyba, A. Barinov, N. D. Hine, *et al.*, "Determination of band offsets, hybridization, and exciton binding in 2D semiconductor heterostructures," *Science Advances*, vol. 3, no. 2, p. e1601832, 2017.

140. T. Uwanno, Y. Hattori, T. Taniguchi, K. Watanabe, and K. Nagashio, "Fully dry PMMA transfer of graphene on h-BN using a heating/cooling system," *2D Materials*, vol. 2, no. 4, p. 041002, 2015.

141. L. S. Hart, J. L. Webb, S. Dale, S. J. Bending, M. Mucha-Kruczynski, D. Wolverson, C. Chen, J. Avila, and M. C. Asensio, "Electronic bandstructure and van der Waals coupling of $ReSe_2$ revealed by high-resolution angle-resolved photoemission spectroscopy," *Scientific Reports*, vol. 7, no. 1, p. 5145, 2017.

142. P. Nagler, G. Plechinger, C. Schüller, and T. Korn, "Observation of anisotropic interlayer raman modes in few-layer ReS_2," *Physica Status Solidi (RRL)-Rapid Research Letters*, vol. 10, no. 2, pp. 185–189, 2016.